PARAMETRIC RESONANCE IN IMMERSED ELASTIC STRUCTURES, WITH APPLICATION TO THE COCHLEA

by

William Ko

M.Math., University of Waterloo, 2011

B.Math., University of Waterloo, 2009

Thesis Submitted in Partial Fulfillment
of the Requirements for the Degree of

Doctor of Philosophy

in the
Department of Mathematics
Faculty of Science

SIMON FRASER UNIVERSITY
Summer 2015

APPROVAL

Name: William Ko

Degree: Doctor of Philosophy

Title of Thesis: Parametric Resonance in Immersed Elastic Structures, with Application to the Cochlea

Examining Committee:

Dr. Ralf Wittenberg, Associate Professor
Chair

Dr. John Stockie, Professor
Senior Supervisor

Dr. David Muraki, Professor
Supervisor

Dr. Mary Catherine Kropinski, Professor
Internal Examiner

Dr. Charles Peskin, Professor,
Courant Institute of Mathematical Sciences,
New York University
External Examiner

Date Defended: May 5, 2015

Partial Copyright License

Abstract

Examples of fluid motion driven by immersed flexible structures abound in nature. In many biological settings, for instance a beating heart, an active material generates a time-dependent internal forcing on the surrounding fluid. Motivated by such active biological structures, this thesis investigates parametric resonance in fluid-structure systems induced by an internal forcing via periodic modulation of the material stiffness.

One particular application that we study is the cochlea which is the primary component for pitch selectivity in the mammalian hearing system. We present a 2D model of the cochlea in which a periodic internal forcing gives rise to amplification of basilar membrane (BM) oscillations. This forcing is inspired by experiments showing that outer hair cells within the cochlear partition change their lengths when stimulated, which can in turn distort the partition and modulate tension across the BM. We demonstrate the existence of resonant (unstable) solutions through a Floquet stability analysis of the linearized governing equations. Moreover, we show that an internal forcing is sufficient to produce travelling waves along the BM in the absence of any external stimulus.

We next examine parametric instabilities in a 3D system by considering a closed spherical elastic membrane (or shell) immersed in a viscous, incompressible fluid. A Floquet analysis for both inviscid and viscous systems shows that parametric resonance is possible even in the presence of fluid viscosity. Numerical simulations are presented to verify the analysis and an application to cardiac fluid dynamics is discussed.

Finally, we deviate from the topic of parametric instabilities to consider the natural oscillations of unforced spherical elastic membranes. We present a linear stability analysis to obtain a dispersion relation for immersed membrane oscillations for both inviscid and viscous fluids, as well as a nonlinear analysis of immersed membrane oscillations in an inviscid fluid. We then present an experiment where we measure oscillation frequencies of immersed water balloons in an attempt to corroborate the analytical results.

To my parents,
for their love and support.

"To explain all nature is too difficult a task for any one man or even for any one age. Tis much better to do a little with certainty and leave the rest for others that come after, than to explain all things by conjecture without making sure of any thing."

— *Sir Isaac Newton*

Acknowledgments

First and foremost, I would like to thank my advisor, John Stockie, for introducing me to the interesting projects discussed in this thesis and for being an incredible mentor. I would also like to thank David Muraki for serving on my supervisory committee and always encouraging me to be a better communicator.

There are several people I would like to acknowledge, without whom this thesis would not be possible. First, I would like to thank Brittany Froese and Jeff Wiens for letting me use their 2D immersed boundary code for simulations in Chapters 4 and 5. I am further indebted to Jeff Wiens for letting me use his 3D code (and making modifications to fit the needs of my project) and for providing comments on my thesis. It was a pleasure working with Darrell Tse on the balloon oscillation summer project discussed in section 7.4. Although the project is not yet complete, we would not have achieved so much without him. Finally, I would like to thank Sudeshna Ghosh for her comments on my thesis.

Contents

List of Tables

List of Figures

Chapter 1

Introduction

Fluid-structure interaction (FSI) problems are ubiquitous in scientific and industrial applications. Owing to the complex coupling that occurs between the fluid and moving structure, FSI presents formidable challenges to both mathematical modellers and computational scientists. Of particular interest in this thesis are systems involving a highly deformable elastic structure immersed in a viscous incompressible fluid, which is common in biofluid systems such as blood flow in the heart or arteries, dynamics of swimming or flying organisms, and organ systems [61, 75, 122].

One approach that has proven particularly effective at capturing FSI with highly deformable structures is the immersed boundary method (or IB method) [102]. This approach was initially developed by Peskin [101] to study the flow of blood in a beating heart, and has since been employed in a wide range of other biological and industrial applications. The beating heart is an example of a fluid-structure system where the immersed structure applies a periodic force onto the surrounding fluid. The heart muscle fibres repeatedly contract and relax to pump blood through its chambers without any external forcing, hence the blood flow is driven by an internal or parametric force. It is then natural to wonder if this internal periodic forcing can give rise to an instability known as *parametric resonance*.

Parametric resonance in fluid dynamics was first observed by Faraday [27] in an experiment where a fluid layer on a vertically vibrating plate revealed peculiar yet beautiful patterns. Faraday noticed that the surface of the fluid oscillates at half the frequency of the vibrating plate whenever these patterns occurred. This period-doubling phenomenon was later verified by Benjamin and Ursell [10] who performed a mathematical analysis based on an inviscid fluid and is now known to be a characteristic signature of parametric resonance. Parametric resonance has since been identified in a wide range of fluid systems.

Other examples are a liquid thread immersed in a shear flow arising in industrial polymer blending [41], interfacial dynamics of two immiscible fluids in a vibrating tank [64], and oscillatory flow of large-scale geophysical fluids [105].

Motivated by the beating heart, we investigate parametric resonance in a fluid-structure system where a spherical elastic shell is immersed in a viscous incompressible fluid. This is an extension of a study by Cortez et al. [18] where they examine parametric instabilities of an internally-forced elastic membrane in two dimensions, in which the forcing appears as a periodic modulation of the elastic stiffness parameter. These authors showed that such systems can give rise to parametric resonance, which overcomes viscous fluid damping and thereby cause the elastic structure to become unstable. Furthermore, Cottet et al. [21] presented computational evidence for the existence of parametric instabilities in 3D elastic shells, but no analysis has yet been done on the complete three-dimensional governing equations to confirm the presence of these instabilities. One of the objectives of this thesis is to extend the work of Cortez et al. [18] by presenting a rigorous mathematical analysis of the existence of parametric instabilities in 3D elastic shells. The analysis incorporates the full two-way fluid-structure coupling by formulating the model in an IB framework.

Other studies of parametric resonance in fluid-structure systems include the work by Semler and Païdoussis [115] where they examine the stability of a flow through a cantilevered pipe fixed on one end. They show that an imposed periodic velocity induces a flutter instability in the free end of the pipe. Another example is the study by Wang [126] where high-speed fluid flow causes vibrations in long, flexible vanes in a paper making machine. The purpose of the vane is to ensure a uniform distribution of fibres in the machine headbox, however a turbulent flow may induce a flutter instability in the vane which affects the quality of the paper. Both of these studies impose a periodic fluid velocity, but the solid structure has no influence on the fluid motion and so the two-way fluid-structure interaction is ignored.

Resonant instabilities arise due to an intrinsic relationship between the natural frequency of the oscillating membrane and the imposed forcing frequency, thus in this thesis we include an analysis of the natural oscillations of unforced immersed spherical elastic shells. There have been numerous studies of oscillations or vibrations of thin spherical elastic shells, for example [5, 9, 55, 78, 94], however none of these studies incorporate any hydrodynamic effects due to the surrounding fluid. In the acoustics literature, mathematical models of immersed spherical shells have been used to study the propagation of pressure waves in a fluid medium [43, 116, 132], but the fluid is often assumed to be inviscid and the fluid-structure coupling is not considered.

There is relatively little mathematical analysis on FSI problems owing to the complex

nonlinear coupling between the equations governing the elastic structure and the fluid. Stockie and Wetton [118] performed a linear stability analysis of the IB model in two dimensions for a simple geometry in which a flat fibre is immersed in fluid. They also presented asymptotic results on the frequency and rate of decay of membrane oscillations that depends on the wavenumber of the sinusoidal perturbation, as well as validating their analytical results using 2D numerical simulations with the IB method. Cortez and Varela [19] performed a nonlinear analysis of a perturbed circular elastic membrane immersed in an inviscid fluid to validate simulations using the impulse method. In this thesis, we extend the linear stability analysis in [118] to three spatial dimensions and derive a dispersion relation that describes the oscillation frequencies and decay rates of immersed spherical shells. Furthermore, we extend the nonlinear analysis of [19] to investigate nonlinear effects in spherical shells immersed in an inviscid fluid.

Some researchers have studied oscillations of spherical elastic shells experimentally. Kuo and Hunt [65] performed an experiment with a helium-filled rubber balloon and contrasted their results with a soap bubble model by Grinfeld [40]. However, they found that the theory consistently under-predicted the experimental results. They later develop a new model that incorporates the nonlinear elasticity of the balloon material and achieve a better agreement between model and experiment [66]. Lund and Dalziel [79] examined the fluid dynamic phenomena that are present at different stages of a bursting water balloon. In their experiments, they found that the oscillation frequencies of the surface waves on a water balloon in its "pre-burst" stage are consistent with the dispersion relation derived by Lamb [69] for spherical drops in an inviscid fluid. In this thesis, we present our own experiment on the oscillations of immersed water balloons in an attempt to validate our analytical results with data.

1.1 Thesis Outline

In Chapter 2, we define parametric resonance and introduce Floquet theory with an illustrative model problem: a pendulum with a vertically moving support. Next we provide an overview of the immersed boundary method in Chapter 3.

The following three chapters delve into parametric resonance in fluid-structure systems. In Chapter 4, we revisit the paper by Cortez et al. [18] where they investigate parametric resonance in immersed elastic fibres in 2D. Next we explore an application of parametric resonance to a biological system in Chapter 5 where we develop and analyze a 2D model of the cochlea (inner ear) with internal forcing. In Chapter 6, we extend the work of [18] to

spherical immersed elastic shells in 3D.

In Chapter 7, we present some results on the natural oscillations of unforced immersed spherical elastic shells. Finally, we present conclusions and discuss future work in Chapter 8.

Chapter 2

Parametric Resonance and Floquet Theory

Parametric resonance is an instability in a dynamical system that is caused by periodic variations in a system parameter. In this chapter, we illustrate parametric resonance and introduce Floquet theory by examining a simple model problem that exhibits parametric instability: a pendulum with vertically moving support [8].

2.1 A Pendulum with Vertically Moving Support

Consider a rigid pendulum with length ℓ connecting a point mass m to a support at position $y(t)$ as illustrated in figure 2.1. The angle that the pendulum makes with the vertical, $u(t)$, is governed by the second-order differential equation

$$m\ell\frac{\mathrm{d}^2u}{\mathrm{d}t^2} + m\left(g + \frac{\mathrm{d}^2y}{\mathrm{d}t^2}\right)\sin u = 0, \tag{2.1}$$

where g is the acceleration due to gravity. If the support of the pendulum is fixed (i.e. $y(t) = y_0$) and the initial angle is small then the pendulum swings with natural frequency $\omega_0 = \sqrt{g/\ell}$. Now suppose the support is moving vertically with a prescribed periodic motion $y(t) = A\sin(\omega t) + y_0$. *How does the moving support affect the dynamics of the swinging pendulum?* The vertically moving support induces an *internal* or *parametric force* by periodically modulating the gravitational restoring force of the pendulum. This parametric force can lead to an instability depending on the specific relationship between the forcing frequency ω and the natural oscillation frequency ω_0. We shall conduct an analysis to elucidate these instabilities.

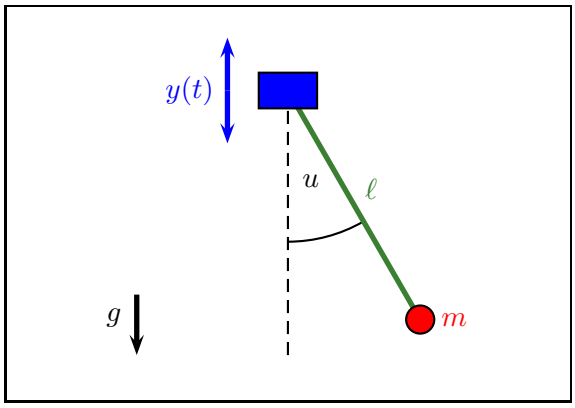

Figure 2.1: A rigid pendulum with a vertically moving support. Here, ℓ is the rod length, m is the mass, $u(t)$ is the angle measured from the rest position, $y(t)$ is the position of the support, and g is the acceleration due to gravity.

2.2 The Mathieu Equation

Consider the small angle approximation ($u \approx 0$) to the pendulum equation (2.1)

$$\frac{\mathrm{d}^2 u}{\mathrm{d}t^2} + \kappa(1 + 2\tau \sin t)u = 0, \tag{2.2}$$

where we have performed a change of variable $\tilde{t} = \omega t$, dropped the tilde, and introduced two nondimensional parameters

$$\kappa = \frac{g}{\ell\omega^2} \quad \text{and} \quad \tau = -\frac{A\omega^2}{2g}.$$

Equation (2.2) is the well-known Mathieu equation [84, 91] which determines the stability of the pendulum when the initial angle is small. Specifically, an unbounded solution to the linear equation implies a resonant solution to the original nonlinear problem.

The Mathieu equation is a second-order ODE which can be written as a first-order system

$$\frac{\mathrm{d}}{\mathrm{d}t}\begin{bmatrix} u \\ v \end{bmatrix} = \begin{bmatrix} 0 & 1 \\ -\kappa(1 + 2\tau \sin t) & 0 \end{bmatrix}\begin{bmatrix} u \\ v \end{bmatrix}, \tag{2.3}$$

with a coefficient matrix that is a periodic function of time. We now invoke Floquet theory [16, 31].

Theorem. *(Floquet's Theorem [54]) Consider the ODE system*

$$\frac{\mathrm{d}\boldsymbol{u}}{\mathrm{d}t} = \mathbf{C}(t)\boldsymbol{u}(t),$$

where $\mathbf{C}(t)$ *is a periodic matrix function with minimal period* T*. There exists a nontrivial solution of the form*

$$\boldsymbol{u}(t) = e^{\gamma t}\boldsymbol{P}(t), \tag{2.4}$$

where $\boldsymbol{P}(t)$ *is periodic with period* T *and* $\gamma \in \mathbb{C}$*.*

The Floquet exponent γ determines the stability of the system (2.3) as $t \to \infty$. In particular, if $\Re\{\gamma\} > 0$ then the solutions to the Mathieu equation are unbounded, which in turn leads to unstable motions in the pendulum problem. We apply Floquet theory to the Mathieu equation and look for nontrivial solutions of the form

$$u(t) = e^{\gamma t}\sum_{n=-\infty}^{\infty} u_n e^{\mathrm{i}nt}, \tag{2.5a}$$

$$v(t) = e^{\gamma t}\sum_{n=-\infty}^{\infty} v_n e^{\mathrm{i}nt}, \tag{2.5b}$$

where we have written the components of the periodic function $\boldsymbol{P}(t)$ in (2.4) as a Fourier series. Substituting the Floquet-Fourier solution into the system (2.3) and writing $\sin t$ in terms of complex exponentials yield

$$\begin{aligned}\gamma u_n &= -\mathrm{i}nu_n + v_n,\\ \gamma v_n &= -\mathrm{i}nv_n - \kappa u_n + \mathrm{i}\kappa\tau(u_{n-1} - u_{n+1})\end{aligned}$$

for $n \in \mathbb{Z}$. This system has the form of an eigenvalue problem with eigenvector $[\ldots, u_n, v_n, \ldots]^{\mathrm{T}}$ and eigenvalue γ, and so we can immediately determine the stability of the Mathieu equation (2.2) by truncating the above linear system at some finite n, solving the resulting eigenvalue problem, and examining the computed eigenvalues. Another approach is to treat the forcing amplitude τ as an unknown and γ as a parameter. This approach is more suitable when the Floquet exponent appears nonlinearly in the analysis [18, 64, 88] and thus will be the method used in this thesis. The above system can be rearranged to eliminate v_n to obtain

$$-\mathrm{i}\left(\frac{(\gamma + \mathrm{i}n)^2}{\kappa} + 1\right)u_n = \tau(u_{n-1} - u_{n+1}), \tag{2.6}$$

which is a generalized eigenvalue problem with eigenvalue τ and eigenvector $[\ldots, u_n, u_{n+1}, \ldots]^{\mathrm{T}}$.

When choosing a value for the parameter γ, we restrict ourselves to periodic solutions with $\Re\{\gamma\} = 0$. In particular, we choose from two special values: $\gamma = 0$, referred to as *harmonic* solutions; and $\gamma = \frac{1}{2}\mathrm{i}$, called *subharmonic*. These choices of harmonic and subharmonic γ can be justified as follows. The Floquet-Fourier solution form (2.5) implies

$$u(t + kT) = e^{\gamma(t+kT)}\sum_{n=-\infty}^{\infty} u_n e^{\mathrm{i}n(t+kT)} = e^{\gamma kT}e^{\gamma t}\sum_{n=-\infty}^{\infty} u_n e^{\mathrm{i}nt} = q^k u(t)$$

for any positive integer k where $T = 2\pi$ is the period and $q = e^{\gamma T}$ with $q \in \mathbb{R}$. As $k \to \infty$, the long-term behaviour of the solution depends on the value of q. We conclude that solutions are stable if $|q| < 1$ and unstable if $|q| > 1$, where the special values $q = \pm 1$ correspond to periodic solutions that define the marginal stability boundaries separating stable and unstable solutions. If $\gamma = 0$, then $q = 1$ and

$$u(t + T) = u(t),$$

which is the T-periodic harmonic solution. If $\gamma = \frac{1}{2}\mathrm{i}$, then $q = -1$ and

$$\begin{aligned} u(t + \ \ T) &= -u(t), \\ u(t + 2T) &= \ \ \ u(t), \end{aligned}$$

which is the period-doubling subharmonic solution.

To ensure that the resulting solutions are real-valued functions, we impose a set of *reality conditions* on the Fourier series coefficients, which for the harmonic case are

$$u_{-n} = \overline{u}_n, \tag{2.7}$$

whereas for the subharmonic case

$$u_{-n} = \overline{u}_{n-1}, \tag{2.8}$$

for all $n \in \mathbb{Z}$, where the overbar denotes the complex conjugate. Either set of reality conditions implies that it is only necessary to consider nonnegative values of n.

In practice, we approximate the infinite linear system (2.6) by truncating at a finite number of Fourier modes $n = 0, 1, \ldots, N$. The resulting equations may be written compactly in matrix form as

$$\mathbf{A}\boldsymbol{v} = \tau \mathbf{B}\boldsymbol{v},$$

where the unknown series coefficients are collected together in a vector of length $2(N + 1)$

$$\boldsymbol{v} = \begin{bmatrix} \vdots \\ \Re\{u_n\} \\ \Im\{u_n\} \\ \vdots \end{bmatrix},$$

and $\mathbf{A} = \mathrm{diag}\{\mathbf{A}_0, \mathbf{A}_1, \ldots, \mathbf{A}_N\}$ is a block diagonal matrix consisting of 2×2 blocks. If $\gamma = 0$, then the block matrices are

$$\mathbf{A}_0 = \mathbf{I}_2, \qquad \mathbf{A}_n = \begin{bmatrix} 0 & -\frac{n^2}{\kappa} + 1 \\ \frac{n^2}{\kappa} - 1 & 0 \end{bmatrix} \quad \text{for } n > 0,$$

whereas if $\gamma = \frac{1}{2}\mathrm{i}$ we have

$$\mathbf{A}_n = \begin{bmatrix} 0 & -\frac{(n+\frac{1}{2})^2}{\kappa} + 1 \\ \frac{(n+\frac{1}{2})^2}{\kappa} - 1 & 0 \end{bmatrix} \quad \text{for } n \geq 0.$$

Matrix $\mathbf{B}$ has a block tridiagonal structure of the form

$$\mathbf{B} = \begin{bmatrix} \widehat{\mathbf{B}} & \widetilde{\mathbf{B}} & & & \\ \mathbf{I}_2 & \mathbf{0}_2 & -\mathbf{I}_2 & & \\ & \ddots & \ddots & \ddots & \\ & & \mathbf{I}_2 & \mathbf{0}_2 & -\mathbf{I}_2 \\ & & & \mathbf{I}_2 & \mathbf{0}_2 \end{bmatrix},$$

where $\mathbf{0}_2$ and $\mathbf{I}_2$ denote the 2×2 zero and identity matrices respectively. The sub-matrices making up the first block row depend on the value of γ, so that for the harmonic case ($\gamma = 0$) we have

$$\widehat{\mathbf{B}} = \mathbf{0}_2 \qquad \text{and} \qquad \widetilde{\mathbf{B}} = \begin{bmatrix} 0 & 2 \\ 0 & 0 \end{bmatrix},$$

while for the subharmonic case ($\gamma = \frac{1}{2}\mathrm{i}$) we have

$$\widehat{\mathbf{B}} = \begin{bmatrix} 1 & 0 \\ 0 & -1 \end{bmatrix} \qquad \text{and} \qquad \widetilde{\mathbf{B}} = -\mathbf{I}_2.$$

Determining the stability of the Mathieu equation reduces to finding all values of τ and $\boldsymbol{v}$ for the two Floquet exponents $\gamma = 0$ and $\frac{1}{2}\mathrm{i}$.

An effective way of visualizing these solutions is to vary κ and to consider the *stability regions* that are generated as the eigenvalues trace out curves in parameter space. This diagram is referred to as an *Ince-Strutt diagram* [16], and is depicted in figure 2.2 as a plot of κ versus τ. The stability boundaries take the form of "fingers" or "tongues" that extend downward in parameter space. There are clearly two distinct sets of alternating fingers corresponding to harmonic and subharmonic modes, which we denote using the two point types $+$ and $\circ$ respectively. Parameter values lying above and inside any given finger correspond to unstable solutions, whereas all parameters lying below the fingers correspond to stable solutions. The left-most contour is called the *principal subharmonic mode* and tends to be the most prominent instability.

For the Mathieu problem, the eigenvalues touch the κ-axis ($\tau = 0$) at well-defined locations $\sqrt{\kappa} = \frac{k}{2}$, where k is any positive integer. From these points, slightly increasing

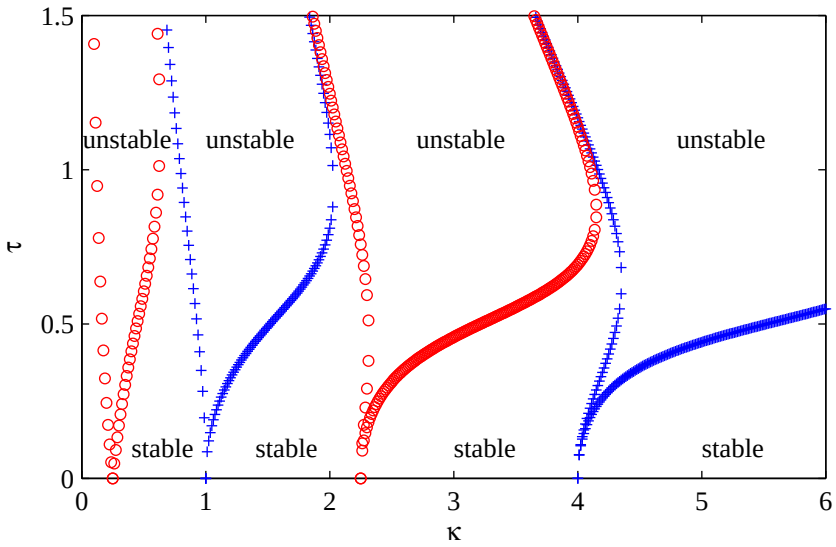

Figure 2.2: Ince-Strutt diagram for the Mathieu equation. Periodic solutions trace out stability contours in parameter space. Harmonic solutions are denoted by + and subharmonic solutions are denoted by ○. Unstable or resonant solutions of the Mathieu equation lie within each stability "finger".

τ brings us into the region in parameter space where unstable solutions to the Mathieu equation reside. This implies that for $|\tau| \ll 1$, resonance occurs when

$$\omega_0 = \frac{k}{2}\omega$$

for any positive integer k; that is, the natural frequency of the unforced pendulum is an integer multiple of half the parametric forcing frequency. Subharmonic modes (odd k), where the response frequency is half the forcing frequency, are a characteristic feature of parametric resonance.

2.3 The Damped Mathieu Equation

Now suppose we include the effect of damping in the pendulum problem that is proportional to the angular velocity by a damping coefficient μ:

$$m\ell\frac{\mathrm{d}^2u}{\mathrm{d}t^2} + \mu\frac{\mathrm{d}u}{\mathrm{d}t} + m\left(g + \frac{\mathrm{d}^2y}{\mathrm{d}t^2}\right)\sin u = 0.$$

The corresponding linearized equation is the damped Mathieu equation [54]

$$\frac{\mathrm{d}^2u}{\mathrm{d}t^2} + \nu\frac{\mathrm{d}u}{\mathrm{d}t} + \kappa(1 + 2\tau\sin t)u = 0, \tag{2.9}$$

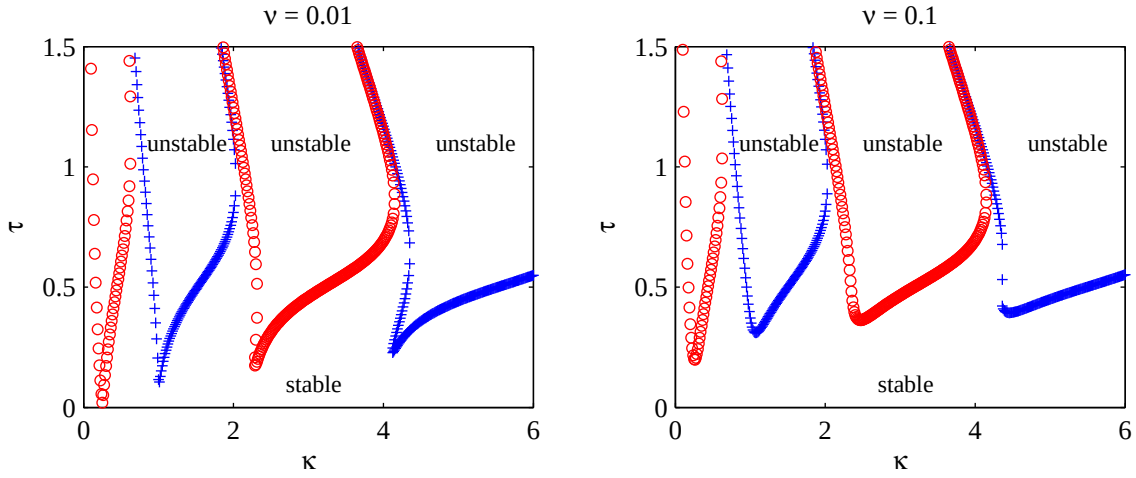

Figure 2.3: Ince-Strutt diagrams for the damped Mathieu equation with damping parameter $\nu = 10^{-2}$ (left) and $\nu = 10^{-1}$ (right). Harmonic and subharmonic solutions are denoted by $+$ and $\circ$, respectively. Observe that stable region increases with ν but unstable solutions still exist.

where $\nu = \mu/m$ is a scaled damping parameter. Following the same procedure as the previous section, we obtain the infinite linear system

$$-\mathrm{i}\left(\frac{(\gamma+\mathrm{i}n)^2}{\kappa}+\nu\frac{\gamma+\mathrm{i}n}{\kappa}+1\right)u_n=\tau(u_{n-1}-u_{n+1})$$

for $n \in \mathbb{Z}$. Truncating this system, imposing reality conditions and solving the generalized eigenvalue problem results in the Ince-Strutt diagram for the damped Mathieu equation in figure 2.3. We observe similar stability fingers as in the undamped case, however these fingers no longer touch the κ-axis. The region in parameter space where stable solutions exist increases in size as the viscosity coefficient ν increases. Furthermore, we see that unstable solutions persist at sufficiently high forcing amplitudes in spite of damping forces. Therefore, the damped Mathieu equation can exhibit instabilities with unbounded amplitude, even in the presence of damping. Moreover, the principal subharmonic mode always extends downward the furthest and is therefore the most prevalent response observed. This ability to overcome damping is a characteristic feature of parametric resonance. In contrast, a pendulum with external or additive forcing always exhibits bounded oscillations if damping is present.

Chapter 3

The Immersed Boundary Method

Fluid-structure interaction problems present formidable challenges to both mathematical modellers and computational scientists. One approach that has proven effective at capturing fluid-structure interactions is the immersed boundary method (or IB method) [102]. This approach was initially developed to study the flow of blood in a beating heart [101], and has since been employed in a wide range of other biological and industrial applications, for example, biofilm aggregation [25], sperm motility [28], parachute descent [59], insect flight [86], and pulp fibre suspensions [117]. The primary advantage of the IB method is its ability to capture the full two-way interaction between an elastic structure and a surrounding fluid in a simple manner using Dirac delta function source terms, which leads to a simple and efficient numerical algorithm.

This thesis is concerned with incompressible, Newtonian fluids and we restrict our attention to structures having co-dimension one (that is, curves in 2D or surfaces in 3D). The fluid dynamics are described by the incompressible Navier-Stokes equations

$$\rho\left(\frac{\partial \boldsymbol{u}}{\partial t} + \boldsymbol{u}\cdot\nabla\boldsymbol{u}\right) = -\nabla p + \mu\Delta\boldsymbol{u} + \boldsymbol{f}, \tag{3.1}$$

$$\nabla\cdot\boldsymbol{u} = 0 \quad \text{for } \boldsymbol{x}\in\Omega, \tag{3.2}$$

where $\boldsymbol{u}(\boldsymbol{x},t)$ is the velocity, $p(\boldsymbol{x},t)$ is the pressure, ρ is the density, μ is the viscosity and $\boldsymbol{f}(\boldsymbol{x},t)$ is the force exerted on the fluid by the immersed boundary. The density and viscosity are assumed constant and the fluid domain, denoted Ω, is taken to be a subset of either $\mathbb{R}^2$ or $\mathbb{R}^3$. The external force is due to deformations of the elastic structure and is given by

$$\boldsymbol{f}(\boldsymbol{x},t) = \int_\Gamma \boldsymbol{F}(\boldsymbol{X},\boldsymbol{s},t)\,\delta(\boldsymbol{x}-\boldsymbol{X})\,\mathrm{d}\Gamma, \tag{3.3}$$

where $\boldsymbol{X}(\boldsymbol{s},t)\in\Gamma$ is the position of the elastic solid, $\boldsymbol{F}(\boldsymbol{X},\boldsymbol{s},t)$ is the force density, $\delta(\boldsymbol{x})$

is the Dirac delta function, and $\boldsymbol{s}$ is a Lagrangian variable that parametrizes the elastic solid. Owing to the Dirac delta function in (3.3), the force is singular and is only applied where the immersed structure is present. The force density, $\boldsymbol{F}(\boldsymbol{X},t)$, comes from taking a variational derivative of an energy functional [102]

$$\boldsymbol{F}(\boldsymbol{X},t) = -\frac{\wp E}{\wp \boldsymbol{X}}. \tag{3.4}$$

Here, $E(\boldsymbol{X},t)$ denotes an energy functional and we use $\wp$ to denote the variation of the functional as opposed to the conventional δ which we have already used for the Dirac delta function. The energy functional incorporates the physics of the elastic structure and depends on the problem at hand. Finally, the evolution of the immersed boundary is described by

$$\frac{\partial \boldsymbol{X}}{\partial t} = \boldsymbol{u}(\boldsymbol{X},t) = \int_\Omega \boldsymbol{u}(\boldsymbol{x},t)\,\delta(\boldsymbol{x}-\boldsymbol{X})\,\mathrm{d}\Omega, \tag{3.5}$$

which implies that the structure moves with the local fluid velocity, and effectively imposes a no-penetration flow condition across the boundary and a no-slip condition tangential to the boundary. Equations (3.1)–(3.5) are referred to as the *delta function formulation* of the IB method.

In lieu of singular force terms, the IB method can be reformulated in terms of jump conditions across the boundary which is more amenable to analysis. In this formulation, the fluid equations are satisfied away from the immersed structure

$$\rho\left(\frac{\partial \boldsymbol{u}}{\partial t} + \boldsymbol{u}\cdot\nabla\boldsymbol{u}\right) = -\nabla p + \mu\Delta\boldsymbol{u},$$
$$\nabla\cdot\boldsymbol{u} = 0 \quad \text{for } \boldsymbol{x}\in\Omega\setminus\Gamma.$$

In a two-dimensional fluid, the immersed boundary is a one-dimensional fibre parametrized by a single Lagrangian variable, $\boldsymbol{X} = \boldsymbol{X}(s,t)$. The jump conditions across the fibre are [72, 103]

$$[\![\boldsymbol{u}]\!] = \boldsymbol{0},$$
$$\mu\hat{\boldsymbol{\tau}}\cdot[\![\hat{\boldsymbol{n}}\cdot\nabla\boldsymbol{u}]\!] = -\frac{\boldsymbol{F}\cdot\hat{\boldsymbol{\tau}}}{\left\|\frac{\partial \boldsymbol{X}}{\partial s}\right\|},$$
$$[\![p]\!] = \frac{\boldsymbol{F}\cdot\hat{\boldsymbol{n}}}{\left\|\frac{\partial \boldsymbol{X}}{\partial s}\right\|},$$

where $\hat{\boldsymbol{n}}$ is the outward unit normal vector, and $\hat{\boldsymbol{\tau}}$ is the unit tangent vector. The double brackets $[\![\cdot]\!]$ indicate the jump in a quantity across the fibre Γ, which can be written more precisely as

$$[\![\cdot]\!] := \lim_{\varrho\to 0}\left((\cdot)|_{\boldsymbol{x}^+} - (\cdot)|_{\boldsymbol{x}^-}\right),$$

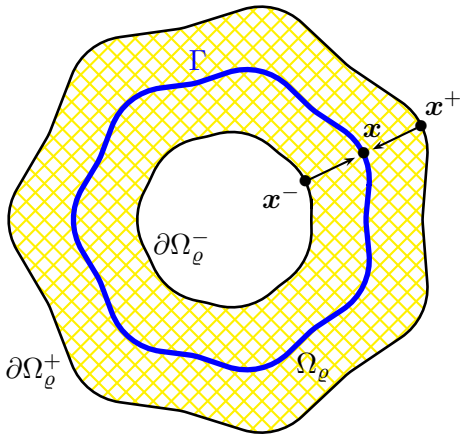

Figure 3.1: Diagram of the immersed boundary Γ and subdomain $\Omega_\varrho(t)$, having inner and outer boundaries $\partial\Omega_\varrho^-(t)$ and $\partial\Omega_\varrho^+(t)$ respectively, which illustrates the limiting process $\boldsymbol{x}^+, \boldsymbol{x}^- \to \boldsymbol{x}$ as $\varrho \to 0$.

where we have introduced a thin strip region $\Omega_\varrho(t)$ surrounding Γ that extends a distance ϱ on either side of the fibre, with inner boundary $\partial\Omega_\varrho^-(t)$ and outer boundary $\partial\Omega_\varrho^+(t)$ as illustrated in figure 3.1. The jump in a quantity at location $\boldsymbol{x} \in \Gamma$ is the difference between values at $\boldsymbol{x}^+ \in \partial\Omega_\varrho^+(t)$ and $\boldsymbol{x}^- \in \partial\Omega_\varrho^-(t)$, taken in the limit as $\varrho \to 0$ where both $\boldsymbol{x}^+, \boldsymbol{x}^- \to \boldsymbol{x}$. In three dimensions, the elastic structure is a surface parametrized by two variables, $\boldsymbol{s} = (\xi, \eta)$ with $\boldsymbol{X} = \boldsymbol{X}(\xi, \eta, t)$, and the appropriate jump conditions are [67, 131]

$$\begin{aligned}
[\![\boldsymbol{u}]\!] &= \boldsymbol{0}, \\
\mu[\![\hat{\boldsymbol{n}} \cdot \nabla \boldsymbol{u}]\!] &= \frac{(\boldsymbol{F} \cdot \hat{\boldsymbol{n}})\hat{\boldsymbol{n}} - \boldsymbol{F}}{\left\| \frac{\partial \boldsymbol{X}}{\partial \xi} \times \frac{\partial \boldsymbol{X}}{\partial \eta} \right\|}, \\
[\![p]\!] &= \frac{\boldsymbol{F} \cdot \hat{\boldsymbol{n}}}{\left\| \frac{\partial \boldsymbol{X}}{\partial \xi} \times \frac{\partial \boldsymbol{X}}{\partial \eta} \right\|}.
\end{aligned}$$

The presence of the Dirac delta kernel in the external force (3.3) and the fibre evolution equation (3.5) provide a means for developing a numerical scheme for computing fluid-structure interaction problems. The external force is approximated by replacing the Dirac delta function with a smooth regularization and applying a quadrature scheme to approximate the integral. Once the force is obtained, the fluid variables can be computed using any fluid solver such as Chorin's projection algorithm [17]. Finally, the membrane is evolved by interpolating the fluid velocity onto the immersed structure locations using the regularized Dirac delta function. Numerous implementations of the IB method exist

in the literature, many of which combat issues such as fluid leakage, and numerical stiffness [39, 68, 87, 103, 128]. This thesis is not concerned directly with addressing these algorithmic issues although numerical simulations will be used to verify the analytical results.

Chapter 4

Parametric Resonance in Circular Fibres

In this chapter, we revisit the paper by Cortez et al. [18] where they investigate parametric resonance in a circular elastic fibre immersed in a two-dimensional fluid. The elastic fibre is given a time-periodic elastic stiffness parameter which introduces an internal (parametric) forcing in the problem. This fluid-structure system exhibits parametric instabilities, which were uncovered through a Floquet stability analysis and validated in numerical simulations. We reproduce the analytical results obtained by Cortez et al., however our analysis differs in two key aspects. First, we describe the fluid using a velocity-pressure formulation, instead of a streamfunction-vorticity formulation used in [18]. Second, we derive the necessary jump conditions across the fibre by multiplying the governing equations with a smooth test function, instead of directly integrating the equations. These changes provide a framework that is more easily extended to three dimensions, as seen in Chapter 6. Furthermore, by reproducing the analysis, we uncover several errors in the original paper [18] which are discussed in section 4.3.

4.1 Immersed Boundary Model

We consider a circular elastic fibre with radius R that is immersed in a viscous incompressible fluid occupying the domain $\Omega = \mathbb{R}^2$. The same fluid is present both inside and outside the fibre and the material making up the fibre is assumed to be neutrally buoyant. The fibre location is given by $\boldsymbol{X}(s,t) \in \Gamma$ and is parametrized by the Lagrangian coordinate $s \in [0, 2\pi)$. The governing equations in the delta function formulation described in

Chapter 3 are

$$\rho\left(\frac{\partial \boldsymbol{u}}{\partial t}+\boldsymbol{u}\cdot\nabla\boldsymbol{u}\right)=-\nabla p+\mu\Delta\boldsymbol{u}+\boldsymbol{f}, \tag{4.1a}$$

$$\nabla\cdot\boldsymbol{u}=0, \tag{4.1b}$$

$$\boldsymbol{f}(\boldsymbol{x},t)=\int_0^{2\pi}\boldsymbol{F}(\boldsymbol{X},t)\,\delta(\boldsymbol{x}-\boldsymbol{X})\,\mathrm{d}s, \tag{4.1c}$$

$$\frac{\partial \boldsymbol{X}}{\partial t}=\boldsymbol{u}(\boldsymbol{X},t), \tag{4.1d}$$

$$\boldsymbol{F}(\boldsymbol{X},t)=-\frac{\wp E}{\wp \boldsymbol{X}}. \tag{4.1e}$$

We choose a simple energy functional

$$E(\boldsymbol{X},t)=\frac{1}{2}K(t)\int_0^{2\pi}\left\|\frac{\partial \boldsymbol{X}}{\partial s}\right\|^2\mathrm{d}s, \tag{4.2}$$

which describes a fibre that resists stretching but not bending. Therefore, the force density becomes

$$\boldsymbol{F}(\boldsymbol{X},t)=K(t)\frac{\partial^2\boldsymbol{X}}{\partial s^2}. \tag{4.3}$$

with the time-dependent stiffness function $K(t)$. We define the stiffness function as

$$K(t)=\sigma\big(1+2\tau\sin(\omega t)\big),$$

where σ is the elastic stiffness parameter, ω is the forcing frequency and τ is the forcing amplitude.

4.1.1 Nondimensionalization

To simplify the analytical derivation to follow, we first nondimensionalize the problem by introducing the scalings

$$\boldsymbol{x}=R\,\widetilde{\boldsymbol{x}},\quad \boldsymbol{X}=R\,\widetilde{\boldsymbol{X}},\quad t=\frac{1}{\omega}\,\widetilde{t},\quad \boldsymbol{u}=U\,\widetilde{\boldsymbol{u}},\quad p=P\,\widetilde{p},$$

where the variables with tildes denote nondimensional quantities. The characteristic velocity and pressure scales are chosen to be

$$U=R\omega \qquad \text{and} \qquad P=\rho R^2\omega^2.$$

Substituting the above quantities into the governing equations (4.1) and (4.3) yields

$$\frac{\partial \widetilde{\boldsymbol{u}}}{\partial \widetilde{t}} + \widetilde{\boldsymbol{u}} \cdot \widetilde{\nabla} \widetilde{\boldsymbol{u}} = -\widetilde{\nabla} \widetilde{p} + \nu \widetilde{\Delta} \widetilde{\boldsymbol{u}} + \widetilde{\boldsymbol{f}}, \tag{4.4a}$$

$$\widetilde{\nabla} \cdot \widetilde{\boldsymbol{u}} = 0, \tag{4.4b}$$

$$\frac{\partial \widetilde{\boldsymbol{X}}}{\partial \widetilde{t}} = \widetilde{\boldsymbol{u}}(\widetilde{\boldsymbol{X}}, \widetilde{t}), \tag{4.4c}$$

$$\widetilde{\boldsymbol{f}}(\widetilde{\boldsymbol{x}}, \widetilde{t}) = \int_0^{2\pi} \widetilde{\boldsymbol{F}}(\widetilde{\boldsymbol{X}}, \widetilde{t})\, \widetilde{\delta}(\widetilde{\boldsymbol{x}} - \widetilde{\boldsymbol{X}})\, \mathrm{d}s, \tag{4.4d}$$

$$\widetilde{\boldsymbol{F}}(\widetilde{\boldsymbol{X}}, \widetilde{t}) = \widetilde{K}(\widetilde{t})\, \frac{\partial^2 \widetilde{\boldsymbol{X}}}{\partial s^2}, \tag{4.4e}$$

$$\widetilde{K}(\widetilde{t}) = \kappa(1 + 2\tau \sin \widetilde{t}), \tag{4.4f}$$

where

$$\nu = \frac{1}{Re} = \frac{\mu}{\rho R^2 \omega} \tag{4.5}$$

is the dimensionless viscosity (or reciprocal Reynolds number) and

$$\kappa = \frac{\sigma}{\rho R^2 \omega^2} \tag{4.6}$$

is the dimensionless IB stiffness parameter. To simplify our notation, we drop the tildes from all variables from this point onward.

4.1.2 Linearization

To make the problem more tractable, we linearize the governing equations by considering small perturbations of the fibre from its equilibrium state. The equilibrium state of the system is a circular fibre with a pressurized interior immersed in a motionless fluid and is given by

$$\boldsymbol{u}_0 = \boldsymbol{0}, \qquad p_0 = K(t)H(1-r) + p_a, \qquad \boldsymbol{X}_0 = \hat{\boldsymbol{r}},$$

where $H(r)$ is the Heaviside step function and p_a represents some constant ambient pressure. We wish to investigate the stability of the fibre when its initial configuration is of the form

$$\boldsymbol{X}(s, 0) = \big(1 + \epsilon g(s)\big)\hat{\boldsymbol{r}}(s)$$

for an arbitrary function $g(s)$ and $|\epsilon| \ll 1$ is a perturbation parameter. We then assume a solution in the form of a regular perturbation expansion

$$\begin{aligned} \boldsymbol{u} &= \boldsymbol{u}_0 + \epsilon \boldsymbol{u}_1 + O\big(\epsilon^2\big), \\ p &= p_0 + \epsilon p_1 + O\big(\epsilon^2\big), \\ \boldsymbol{X} &= \boldsymbol{X}_0 + \epsilon \boldsymbol{X}_1 + O\big(\epsilon^2\big). \end{aligned}$$

Substituting these expressions into the governing equations and retaining only those terms of $O(\epsilon)$, we obtain the following system for the perturbations

$$\frac{\partial \boldsymbol{u}_1}{\partial t} = -\nabla p_1 + \nu \Delta \boldsymbol{u}_1 + \boldsymbol{f}_1, \tag{4.7a}$$

$$\nabla \cdot \boldsymbol{u}_1 = 0, \tag{4.7b}$$

$$\frac{\partial \boldsymbol{X}_1}{\partial t} = \boldsymbol{u}_1(\boldsymbol{X}_0, t). \tag{4.7c}$$

4.1.3 Jump Condition Formulation

We next reformulate the equations by replacing the singular forcing term in lieu of suitable jump conditions across the fibre. We follow the approach used by LeVeque and Li [72] where a smooth test function is used to eliminate the Dirac delta functions from the momentum equations. We first present the jump condition for the fluid variables $\boldsymbol{u}$ and p, and then extract the jump conditions for the perturbation quantities $\boldsymbol{u}_1$ and p_1. Furthermore, the jumps in velocity are written in terms of components in polar coordinates

$$\boldsymbol{u}_1(r, \theta, t) = u^r(r, \theta, t)\, \hat{\boldsymbol{r}} + u^\theta(r, \theta, t)\, \hat{\boldsymbol{\theta}}.$$

Observe that equation (4.1d) implies that the fibre must move with the local fluid velocity. Because the fibre is infinitesimally thin, the velocity must be continuous across Γ, or

$$[\![\boldsymbol{u}]\!] = 0.$$

For the perturbation quantities, continuity of velocity across the fibre implies that

$$[\![u^r]\!] = [\![u^\theta]\!] = 0. \tag{4.8}$$

Note the jump condition for the $O(\epsilon)$ quantities are taken across a circular fibre defined by $r = 1$ and $\theta = s$. The divergence-free condition (4.4b) must be zero everywhere, so that

$$[\![\nabla \cdot \boldsymbol{u}]\!] = 0.$$

In terms of the components of the perturbation we have

$$\left[\!\!\left[\frac{\partial u^r}{\partial r} + \frac{2}{r}\, u^r + \frac{1}{r}\, \frac{\partial u^\theta}{\partial \theta} \right]\!\!\right] = 0.$$

The jump (4.8) eliminates the second term in the above expression. The third term also reduces to zero since u^θ is continuous and the jump is taken across a circular fibre, so that

derivatives with respect to θ are continuous. We are then left with

$$\left[\!\left[\frac{\partial u^r}{\partial r}\right]\!\right] = 0. \tag{4.9}$$

The remaining jump conditions are derived from the momentum equations (4.4a). Let $\Omega_\varrho(t)$ be a subdomain that encompasses the fibre as in figure 3.1. Let $\varphi(\boldsymbol{x})$ be a smooth test function with compact support. Multiply the momentum equations by $\varphi(\boldsymbol{x})$ and integrate over $\Omega_\varrho(t)$ to obtain

$$\int_{\Omega_\varrho(t)} \left(\frac{\partial \boldsymbol{u}}{\partial t} + \boldsymbol{u}\cdot\nabla\boldsymbol{u}\right)\varphi(\boldsymbol{x})\,\mathrm{d}A = \int_{\Omega_\varrho(t)} \left(-\nabla p + \nu\Delta\boldsymbol{u} + \boldsymbol{f}\right)\varphi(\boldsymbol{x})\,\mathrm{d}A. \tag{4.10}$$

We now examine each term in this equation in the limit as $\varrho \to 0$. Starting with the left-hand side, we apply the Reynolds transport theorem to rewrite the acceleration term:

$$\int_{\Omega_\varrho(t)} \left(\frac{\partial \boldsymbol{u}}{\partial t} + \boldsymbol{u}\cdot\nabla\boldsymbol{u}\right)\varphi(\boldsymbol{x})\,\mathrm{d}A = \frac{\mathrm{d}}{\mathrm{d}t}\int_{\Omega_\varrho(t)} \boldsymbol{u}\,\varphi(\boldsymbol{x})\,\mathrm{d}A - \int_{\Omega_\varrho(t)} \boldsymbol{u}(\boldsymbol{u}\cdot\nabla\varphi)\,\mathrm{d}A.$$

Because $\varphi(\boldsymbol{x})$ is smooth and $\boldsymbol{u}$ is continuous, we have that

$$\lim_{\varrho\to 0}\frac{\mathrm{d}}{\mathrm{d}t}\int_{\Omega_\varrho(t)} \boldsymbol{u}\,\varphi(\boldsymbol{x})\,\mathrm{d}A = 0 \quad \text{and} \quad \lim_{\varrho\to 0}\int_{\Omega_\varrho(t)} \boldsymbol{u}(\boldsymbol{u}\cdot\nabla\varphi)\,\mathrm{d}A = 0,$$

hence

$$\int_{\Omega_\varrho(t)} \left(\frac{\partial \boldsymbol{u}}{\partial t} + \boldsymbol{u}\cdot\nabla\boldsymbol{u}\right)\varphi(\boldsymbol{x})\,\mathrm{d}A \to 0 \quad \text{as } \varrho \to 0.$$

Considering next the pressure term in the right-hand side of (4.10), integrate by parts to obtain

$$\begin{aligned}\int_{\Omega_\varrho(t)} -\nabla p\,\varphi(\boldsymbol{x})\,\mathrm{d}A = &-\int_{\partial\Omega_\varrho^+(t)} p\,\hat{\boldsymbol{n}}\,\varphi(\boldsymbol{x})\,\mathrm{d}\ell \\ &+ \int_{\partial\Omega_\varrho^-(t)} p\,\hat{\boldsymbol{n}}\,\varphi(\boldsymbol{x})\,\mathrm{d}\ell + \int_{\Omega_\varrho(t)} p\,\nabla\varphi(\boldsymbol{x})\,\mathrm{d}A,\end{aligned} \tag{4.11}$$

where $\hat{\boldsymbol{n}}$ is the outward unit normal vector and $\partial\Omega_\varrho^-(t)$ and $\partial\Omega_\varrho^+(t)$ are the inner and outer surfaces of $\Omega_\varrho(t)$, respectively. Because p is also bounded, the last term in (4.11) vanishes as $\varrho \to 0$ and we are left with the difference between two boundary integrals, which reduces to a jump in pressure; in other words,

$$\int_{\Omega_\varrho(t)} -\nabla p\,\varphi(\boldsymbol{x})\,\mathrm{d}A \quad \to \quad -\int_\Gamma [\![p]\!]\,\hat{\boldsymbol{n}}\,\varphi(\boldsymbol{x})\,\mathrm{d}\ell \qquad \text{as } \varrho \to 0.$$

In an analogous manner, the viscous term in (4.10) can be integrated by parts to yield

$$\int_{\Omega_\varrho(t)} \nu\Delta\boldsymbol{u}\,\varphi(\boldsymbol{x})\,\mathrm{d}A \quad \to \quad \int_\Gamma \nu[\![\hat{\boldsymbol{n}}\cdot\nabla\boldsymbol{u}]\!]\,\varphi(\boldsymbol{x})\,\mathrm{d}\ell \qquad \text{as } \varrho \to 0.$$

Finally, we consider the forcing term in (4.10) and apply the sifting property of the Dirac delta function to obtain

$$\int_{\Omega_\varrho(t)} \boldsymbol{f}\,\varphi(\boldsymbol{x})\,\mathrm{d}A = \int_{\Omega_\varrho(t)} \left(\int_0^{2\pi} \boldsymbol{F}\,\delta(\boldsymbol{x}-\boldsymbol{X})\,\mathrm{d}s\right)\varphi(\boldsymbol{x})\,\mathrm{d}A = \int_0^{2\pi} \boldsymbol{F}\,\varphi(\boldsymbol{X})\,\mathrm{d}s.$$

Taking the limit as $\varrho \to 0$ and making use of the identity

$$\mathrm{d}\ell = \left\|\frac{\partial \boldsymbol{X}}{\partial s}\right\| \mathrm{d}s,$$

the integral (4.10) becomes

$$0 = \int_0^{2\pi} \left(-[\![p]\!]\left\|\frac{\partial \boldsymbol{X}}{\partial s}\right\|\hat{\boldsymbol{n}} + \nu[\![\hat{\boldsymbol{n}}\cdot\nabla\boldsymbol{u}]\!]\left\|\frac{\partial \boldsymbol{X}}{\partial s}\right\| + \boldsymbol{F}\right)\varphi(\boldsymbol{X})\,\mathrm{d}s.$$

Since $\varphi(\boldsymbol{x})$ is arbitrary and smooth, the integrand must be identically zero, so that

$$0 = -[\![p]\!]\left\|\frac{\partial \boldsymbol{X}}{\partial s}\right\|\hat{\boldsymbol{n}} + \nu[\![\hat{\boldsymbol{n}}\cdot\nabla\boldsymbol{u}]\!]\left\|\frac{\partial \boldsymbol{X}}{\partial s}\right\| + \boldsymbol{F}. \tag{4.12}$$

Before proceeding further, we need to derive the perturbation expansion for the unit normal vector $\hat{\boldsymbol{n}}$, and the force density $\boldsymbol{F}$, in order to find the remaining jump conditions for the $O(\epsilon)$ quantities. To find an expansion for the normal vector, we first find the expansion for the tangent vector $\hat{\boldsymbol{\tau}}$, which is given by

$$\hat{\boldsymbol{\tau}} = \frac{\frac{\partial \boldsymbol{X}}{\partial s}}{\left\|\frac{\partial \boldsymbol{X}}{\partial s}\right\|}.$$

Substituting the perturbation expansion for $\boldsymbol{X}$ and writing

$$\boldsymbol{X}_1(s,t) = X^r(s,t)\,\hat{\boldsymbol{r}} + X^\theta(s,t)\,\hat{\boldsymbol{\theta}}$$

gives

$$\left\|\frac{\partial \boldsymbol{X}}{\partial s}\right\|\hat{\boldsymbol{\tau}} = \hat{\boldsymbol{\theta}} + \epsilon\left[\left(\frac{\partial X^r}{\partial s} - X^\theta\right)\hat{\boldsymbol{r}} + \left(X^r + \frac{\partial X^\theta}{\partial s}\right)\hat{\boldsymbol{\theta}}\right] + O(\epsilon^2).$$

The outward pointing normal must satisfy $\hat{\boldsymbol{n}}\cdot\hat{\boldsymbol{\tau}} = 0$, and so using the above expansion for the tangent vector, we get

$$\left\|\frac{\partial \boldsymbol{X}}{\partial s}\right\|\hat{\boldsymbol{n}} = \hat{\boldsymbol{r}} + \epsilon\left[\left(X^r + \frac{\partial X^\theta}{\partial s}\right)\hat{\boldsymbol{r}} - \left(\frac{\partial X^r}{\partial s} - X^\theta\right)\hat{\boldsymbol{\theta}}\right] + O(\epsilon^2).$$

Furthermore, the expansion for the force density is

$$\begin{aligned}\boldsymbol{F} &= K(t)\frac{\partial^2}{\partial s^2}\left[\hat{\boldsymbol{r}} + \epsilon\left(X^r\hat{\boldsymbol{r}} + X^\theta\hat{\boldsymbol{\theta}}\right) + O(\epsilon^2)\right],\\ &= -K(t)\hat{\boldsymbol{r}} + \epsilon K(t)\left[\left(\frac{\partial^2 X^r}{\partial s^2} - 2\frac{\partial X^\theta}{\partial s} - X^r\right)\hat{\boldsymbol{r}} + \left(\frac{\partial^2 X^\theta}{\partial s^2} + 2\frac{\partial X^r}{\partial s} - X^\theta\right)\hat{\boldsymbol{\theta}}\right] + O(\epsilon^2).\end{aligned}$$

The leading order quantities in (4.12) give

$$[\![p_0]\!] = -K(t), \tag{4.13}$$

which agrees with the equilibrium state. The $O(\epsilon)$ quantities in equation (4.12) satisfy

$$0 = -[\![p_1]\!]\,\hat{\boldsymbol{r}} + \nu\left[\!\!\left[\frac{\partial \boldsymbol{u}_1}{\partial r}\right]\!\!\right] + K(t)\left[\left(\frac{\partial^2 X^r}{\partial s^2} - \frac{\partial X^\theta}{\partial s}\right)\hat{\boldsymbol{r}} + \left(\frac{\partial X^r}{\partial s} + \frac{\partial^2 X^\theta}{\partial s^2}\right)\hat{\boldsymbol{\theta}}\right]. \tag{4.14}$$

The radial component of the above equation, along with the jump (4.9), gives a jump condition for pressure

$$[\![p_1]\!] = K(t)\left(\frac{\partial^2 X^r}{\partial s^2} - \frac{\partial X^\theta}{\partial s}\right). \tag{4.15}$$

The angular component of (4.14) gives the jump condition for the radial derivative of u^θ

$$\nu\left[\!\!\left[\frac{\partial u^\theta}{\partial r}\right]\!\!\right] = -K(t)\left(\frac{\partial X^r}{\partial s} + \frac{\partial^2 X^\theta}{\partial s^2}\right). \tag{4.16}$$

We now have a complete set of equations for the $O(\epsilon)$ quantities. To summarize, the linearized system of equations in component form is

$$\frac{\partial u^r}{\partial t} = -\frac{\partial p}{\partial r} + \nu\left(\Delta u^r - \frac{u^r}{r^2} - \frac{2}{r^2}\frac{\partial u^\theta}{\partial \theta}\right), \tag{4.17a}$$

$$\frac{\partial u^\theta}{\partial t} = -\frac{1}{r}\frac{\partial p}{\partial \theta} + \nu\left(\Delta u^\theta - \frac{u^\theta}{r^2} + \frac{2}{r^2}\frac{\partial u^r}{\partial \theta}\right), \tag{4.17b}$$

$$\nabla \cdot \boldsymbol{u}_1 = \frac{1}{r}\frac{\partial}{\partial r}(r u^r) + \frac{1}{r}\frac{\partial u^\theta}{\partial \theta} = 0, \tag{4.17c}$$

$$\frac{\partial X^r}{\partial t} = u^r(1, s, t), \tag{4.17d}$$

$$\frac{\partial X^\theta}{\partial t} = u^\theta(1, s, t), \tag{4.17e}$$

subject to jump conditions (4.8), (4.9), (4.15) and (4.16) where the linearized immersed boundary is a unit circle. Moving forward, we omit the subscript '1' when referring the $O(\epsilon)$ variables.

4.2 Floquet Analysis

Our next goal is to investigate the stability of solutions to the linearized system (4.17). Owing to the presence of a time-periodic parameter in the jump conditions, we invoke Floquet theory and adopt the Floquet-Fourier form for the time-dependence in our solutions.

For the angular dependence, we consider a single Fourier mode with integer wavenumber m. Since we are only interested in real-valued solutions, the Fourier modes are written as trigonometric functions instead of complex exponentials. Moreover, to allow the incompressibility condition (4.17c) to be satisfied, we write the radial component of velocity as a cosine mode and the angular component as a sine mode. Consequently, we look for solutions of the form

$$u^r(r,\theta,t) = e^{\gamma t} \sum_{n=-\infty}^{\infty} u_n^r(r) e^{\mathrm{i}nt} \cos(m\theta), \tag{4.18a}$$

$$u^\theta(r,\theta,t) = e^{\gamma t} \sum_{n=-\infty}^{\infty} u_n^\theta(r) e^{\mathrm{i}nt} \sin(m\theta), \tag{4.18b}$$

$$p(r,\theta,t) = e^{\gamma t} \sum_{n=-\infty}^{\infty} p_n(r) e^{\mathrm{i}nt} \cos(m\theta), \tag{4.18c}$$

$$X^r(s,t) = e^{\gamma t} \sum_{n=-\infty}^{\infty} X_n^r e^{\mathrm{i}nt} \cos(ms), \tag{4.18d}$$

$$X^\theta(s,t) = e^{\gamma t} \sum_{n=-\infty}^{\infty} X_n^\theta e^{\mathrm{i}nt} \sin(ms). \tag{4.18e}$$

The Fourier coefficients in the the above series are functions of r (or constant) that remain to be determined.

We begin by first finding the Fourier coefficients for the pressure $p_n(r)$. Away from the fibre these coefficients satisfy

$$\left(\frac{1}{r}\frac{\mathrm{d}}{\mathrm{d}r}\left(r\frac{\mathrm{d}p_n}{\mathrm{d}r}\right) - \frac{m^2}{r^2}p_n\right)\cos(m\theta) = 0,$$

which yields an ODE for $p_n(r)$ that must be satisfied for $r < 1$ and $r > 1$. The pressure solution that is bounded for all r is

$$p_n(r) = \begin{cases} a_n r^m, & \text{if } r < 1, \\ b_n r^{-m}, & \text{if } r > 1, \end{cases} \tag{4.19}$$

where a_n and b_n are coefficients yet to be determined. We next solve for the radial velocity coefficients u_n^r. Substituting the Floquet-Fourier series (4.18a) into the radial momentum equation (4.17a) yields

$$(\gamma + \mathrm{i}n)u_n^r = -\frac{\mathrm{d}p_n}{\mathrm{d}r} + \nu\left(\frac{1}{r}\frac{\mathrm{d}}{\mathrm{d}r}\left(r\frac{\mathrm{d}u_n^r}{\mathrm{d}r}\right) - \frac{m^2+1}{r^2}u_n^r + \frac{2m}{r^2}u_n^\theta\right).$$

To obtain an ODE for u_n^r only, we use the incompressibility condition

$$\left(\frac{1}{r}\frac{\mathrm{d}}{\mathrm{d}r}(ru_n^r) - \frac{m}{r}u_n^\theta\right)\cos(m\theta) = 0.$$

By orthogonality, we find the expression for u_n^θ in terms of u_n^r to be

$$u_n^\theta(r) = \frac{1}{m}\frac{\mathrm{d}}{\mathrm{d}r}(ru_n^r). \tag{4.20}$$

Hence, the Fourier coefficients u_n^r satisfy

$$r^2\frac{\mathrm{d}^2u_n^r}{\mathrm{d}r^2} + 3r\frac{\mathrm{d}u_n^r}{\mathrm{d}r} + \left(-\beta_n^2r^2 + 1 - m^2\right)u_n^r = \frac{r^2}{\nu}\frac{\mathrm{d}p_n}{\mathrm{d}r},$$

where

$$\beta_n = \sqrt{\frac{\gamma + in}{\nu}} \quad \text{with} \quad \Re\{\beta_n\} > 0.$$

We first consider the case $\beta_n \neq 0$. The solution of the the radial velocity is given by

$$u_n^r(r) = \int_0^\infty G(r,z)\frac{z^2}{\nu}\frac{\mathrm{d}p_n(z)}{\mathrm{d}z}\,\mathrm{d}z, \tag{4.21}$$

where $G(r,z)$ is the Green's function that satisfies

$$r^2\frac{\partial^2G}{\partial r^2} + 3r\frac{\partial G}{\partial r} + \left(-\beta_n^2r^2 + 1 - m^2\right)G = \delta(r-z), \tag{4.22}$$

with jump conditions

$$G|_{r=z^-}^{r=z+} = 0 \quad \text{and} \quad r^2\frac{\partial G}{\partial r}\bigg|_{r=z^-}^{r=z+} = 1. \tag{4.23}$$

Applying the change of variable $G(r,z) = w(r,z)/r$ transforms ODE (4.22) into

$$r^2\frac{\partial^2w}{\partial r^2} + 2r\frac{\partial w}{\partial r} + \left(-\beta_n^2r^2 - m^2\right)w = r\delta(r-z),$$

which yields *Bessel's equation* [1] on the left-hand side. The Green's function is found to be

$$G(r,z) = \begin{cases} c_1\dfrac{J_m(\mathrm{i}\beta_nr)}{r}, & \text{if } r < z, \\ c_2\dfrac{H_m(\mathrm{i}\beta_nr)}{r}, & \text{if } r > z, \end{cases}$$

where c_1 and c_2 are undetermined constants, J_m and H_m denote the mth-order Bessel and Hankel functions of the first kind respectively (see Appendix A for a list of useful properties and identities). The constants c_1 and c_2 can be found by imposing the jump conditions for the Green's function (4.23):

$$c_1 = \frac{H_m(\mathrm{i}\beta_nz)}{\mathrm{i}\beta_n(H_m'(\mathrm{i}\beta_nz)J_m(\mathrm{i}\beta_nz) - H_m(\mathrm{i}\beta_nz)J_m'(\mathrm{i}\beta_nz))},$$
$$c_2 = \frac{J_m(\mathrm{i}\beta_nz)}{\mathrm{i}\beta_n(H_m'(\mathrm{i}\beta_nz)J_m(\mathrm{i}\beta_nz) - H_m(\mathrm{i}\beta_nz)J_m'(\mathrm{i}\beta_nz))}.$$

These coefficients can be simplified using the Wronskian identity for Bessel functions (A.13) to

$$c_1 = -\frac{\mathrm{i}\pi}{2} H_m(\mathrm{i}\beta_n z), \qquad c_2 = -\frac{\mathrm{i}\pi}{2} J_m(\mathrm{i}\beta_n z),$$

which gives a simpler form of the Green's function

$$G(r,z) = \begin{cases} -\dfrac{\mathrm{i}\pi}{2r} J_m(\mathrm{i}\beta_n r) H_m(\mathrm{i}\beta_n z), & \text{if } r < z, \\ -\dfrac{\mathrm{i}\pi}{2r} H_m(\mathrm{i}\beta_n r) J_m(\mathrm{i}\beta_n z), & \text{if } r > z. \end{cases}$$

Owing to the pressure discontinuity (4.19), we must consider two cases when solving for $u_n^r(r)$. For $r < 1$, we have

$$\begin{aligned} u_n^r(r) = \int_0^r & -\frac{\mathrm{i}\pi}{2} \frac{H_m(\mathrm{i}\beta_n r)}{r} J_m(\mathrm{i}\beta_n z) a_n \frac{1}{\nu} m z^{m+1} \,\mathrm{d}z \\ & + \int_r^1 -\frac{\mathrm{i}\pi}{2} \frac{J_m(\mathrm{i}\beta_n r)}{r} H_m(\mathrm{i}\beta_n z) a_n \frac{1}{\nu} m z^{m+1} \,\mathrm{d}z \\ & + \int_1^\infty -\frac{\mathrm{i}\pi}{2} \frac{J_m(\mathrm{i}\beta_n r)}{r} H_m(\mathrm{i}\beta_n z) b_n \frac{1}{\nu} (-m) z^{-m+1} \,\mathrm{d}z. \end{aligned}$$

The above integrals can be simplified using the identities (A.8) and (A.9) to obtain

$$\begin{aligned} u_n^r(r) = -a_n \frac{\pi m}{2\nu\beta_n} & \left[r^m H_m(\mathrm{i}\beta_n r) J_{m+1}(\mathrm{i}\beta_n r) + J_m(\mathrm{i}\beta_n r) \left(\frac{H_{m+1}(\mathrm{i}\beta_n)}{r} - r^m H_{m+1}(\mathrm{i}\beta_n r) \right) \right] \\ & + b_n \frac{\pi m}{2\nu\beta_n} \left[\frac{J_m(\mathrm{i}\beta_n r)}{r} H_{m-1}(\mathrm{i}\beta_n) \right]. \end{aligned}$$

A similar procedure for the case $r > 1$ yields

$$\begin{aligned} u_n^r(r) = - b_n \frac{\pi m}{2\nu\beta_n} & \left[H_m(\mathrm{i}\beta_n r) \left(\frac{J_{m-1}(\mathrm{i}\beta_n r)}{r^m} - J_{m-1}(\mathrm{i}\beta_n) \right) - \frac{J_m(\mathrm{i}\beta_n r)}{r^m} H_{m-1}(\mathrm{i}\beta_n r) \right] \\ & - a_n \frac{\pi m}{2\nu\beta_n} \left[\frac{H_m(\mathrm{i}\beta_n r)}{r} J_{m+1}(\mathrm{i}\beta_n) \right]. \end{aligned}$$

The above solutions can be simplified further using (A.11) and expressed more compactly as

$$u_n^r(r) = \begin{cases} \dfrac{\pi m}{2\nu\beta_n} \dfrac{J_m(\mathrm{i}\beta_n r)}{r} \big(b_n H_{m-1}(\mathrm{i}\beta_n) - a_n H_{m+1}(\mathrm{i}\beta_n) \big) - a_n \dfrac{m}{\nu\beta_n^2} \, r^{m-1}, & \text{if } r < 1, \\ \dfrac{\pi m}{2\nu\beta_n} \dfrac{H_m(\mathrm{i}\beta_n r)}{r} \big(b_n J_{m-1}(\mathrm{i}\beta_n) - a_n J_{m+1}(\mathrm{i}\beta_n) \big) + b_n \dfrac{m}{\nu\beta_n^2} \, r^{-m-1}, & \text{if } r > 1. \end{cases}$$

We check to ensure that this result is indeed continuous and satisfies the first jump condition (4.8):

$$u_n^r(1^+) = u_n^r(1^-) = -\frac{\pi m}{2\nu\beta_n} \big(a_n H_m(\mathrm{i}\beta_n) J_{m+1}(\mathrm{i}\beta_n) - b_n J_m(\mathrm{i}\beta_n) H_{m-1}(\mathrm{i}\beta_n) \big).$$

The coefficients $u_n^\theta(r)$ can be found using equation (4.20) and therefore

$$u_n^\theta(r) = \begin{cases} \dfrac{\mathrm{i}\pi}{2\nu} J_m'(\mathrm{i}\beta_n r)\big(b_n H_{m-1}(\mathrm{i}\beta_n) - a_n H_{m+1}(\mathrm{i}\beta_n)\big) - a_n \dfrac{m}{\nu\beta_n^2} r^{m-1}, & \text{if } r < 1, \\ \dfrac{\mathrm{i}\pi}{2\nu} H_m'(\mathrm{i}\beta_n r)\big(b_n J_{m-1}(\mathrm{i}\beta_n) - a_n J_{m+1}(\mathrm{i}\beta_n)\big) - b_n \dfrac{m}{\nu\beta_n^2} r^{-m-1}, & \text{if } r > 1. \end{cases}$$

Calculating the limit of $u_n^\theta(r)$ as $r \to 1^-$ and $r \to 1^+$ yields

$$u_n^\theta(1^+) = u_n^\theta(1^-) = -\frac{\mathrm{i}\pi}{2\nu}\big(a_n H_m'(\mathrm{i}\beta_n) J_{m+1}(\mathrm{i}\beta_n) - b_n J_m'(\mathrm{i}\beta_n) H_{m-1}(\mathrm{i}\beta_n)\big).$$

which verifies that the angular velocity is also continuous.

The next step is to solve for the undetermined coefficients a_n and b_n. The evolution equations for the membrane, (4.17d) and (4.17e), lead to an algebraic system

$$\begin{aligned} (\gamma + \mathrm{i}n) X_n^r &= -\frac{\pi m}{2\nu\beta_n}\big(a_n H_m(\mathrm{i}\beta_n) J_{m+1}(\mathrm{i}\beta_n) - b_n J_m(\mathrm{i}\beta_n) H_{m-1}(\mathrm{i}\beta_n)\big), \\ (\gamma + \mathrm{i}n) X_n^\theta &= -\frac{\mathrm{i}\pi}{2\nu}\big(a_n H_m'(\mathrm{i}\beta_n) J_{m+1}(\mathrm{i}\beta_n) - b_n J_m'(\mathrm{i}\beta_n) H_{m-1}(\mathrm{i}\beta_n)\big). \end{aligned}$$

This is a 2×2 linear system that can be inverted to find a_n and b_n

$$\begin{aligned} a_n &= \frac{\nu^2\beta_n^4}{m}\frac{J_m'(\mathrm{i}\beta_n)}{J_{m+1}(\mathrm{i}\beta_n)} X_n^r + \nu^2 \mathrm{i}\beta_n^3 \frac{J_m(\mathrm{i}\beta_n)}{J_{m+1}(\mathrm{i}\beta_n)} X_n^\theta, \\ b_n &= \frac{\nu^2\beta_n^4}{m}\frac{H_m'(\mathrm{i}\beta_n)}{H_{m-1}(\mathrm{i}\beta_n)} X_n^r + \nu^2 \mathrm{i}\beta_n^3 \frac{H_m(\mathrm{i}\beta_n)}{H_{m-1}(\mathrm{i}\beta_n)} X_n^\theta. \end{aligned}$$

We are now ready to impose the jump conditions. The Floquet-Fourier solution for pressure implies

$$\begin{aligned} [\![p]\!] &= e^{\gamma t} \sum_{n=-\infty}^{\infty} e^{\mathrm{i}nt}\big(p_n(1^+) - p_n(1^-)\big)\cos(ms), \\ &= e^{\gamma t} \sum_{n=-\infty}^{\infty} e^{\mathrm{i}nt}(b_n - a_n)\cos(ms). \end{aligned}$$

Furthermore, by rewriting the stiffness function $K(t)$ in terms of complex exponentials as

$$K(t) = \kappa\big(1 - \mathrm{i}\tau e^{\mathrm{i}t} + \mathrm{i}\tau e^{-\mathrm{i}t}\big),$$

the right-hand side of the pressure jump (4.15) can be simplified as

$$\begin{aligned}
[\![p]\!] &= K(t)\left(\frac{\partial^2 X^r}{\partial s^2} - \frac{\partial X^\theta}{\partial s}\right), \\
&= \kappa\left(1 - \mathrm{i}\tau e^{\mathrm{i}t} + \mathrm{i}\tau e^{-\mathrm{i}t}\right) e^{\gamma t} \sum_{n=-\infty}^{\infty} e^{\mathrm{i}nt}\left(-m^2 X_n^r + m X_n^\theta\right)\cos(ms), \\
&= \kappa e^{\gamma t} \sum_{n=-\infty}^{\infty} \left(e^{\mathrm{i}nt} - \mathrm{i}\tau e^{\mathrm{i}(n+1)t} + \mathrm{i}\tau e^{\mathrm{i}(n-1)t}\right)\left(-m^2 X_n^r + m X_n^\theta\right)\cos(ms), \\
&= \kappa e^{\gamma t} \sum_{n=-\infty}^{\infty} \Big[-m^2\Big(X_n^r - \mathrm{i}\tau X_{n-1}^r + \mathrm{i}\tau X_{n+1}^r\Big) + m\Big(X_n^\theta - \mathrm{i}\tau X_{n-1}^\theta + \mathrm{i}\tau X_{n+1}^\theta\Big)\Big]\cos(ms).
\end{aligned}$$

By orthogonality, the pressure jump reduces to

$$b_n - a_n = -m^2\kappa(X_n^r - \mathrm{i}\tau X_{n-1}^r + \mathrm{i}\tau X_{n+1}^r) + m\kappa(X_n^\theta - \mathrm{i}\tau X_{n-1}^\theta + \mathrm{i}\tau X_{n+1}^\theta).$$

To apply the next jump condition (4.16), we first need to find $\frac{\mathrm{d}u_n^\theta}{\mathrm{d}r}$

$$\frac{\mathrm{d}u_n^\theta}{\mathrm{d}r} = \begin{cases} -\dfrac{\pi\beta_n}{2\nu} J_m''(\mathrm{i}\beta_n r)(b_n H_{m-1}(\mathrm{i}\beta_n) - a_n H_{m+1}(\mathrm{i}\beta_n)) - a_n \dfrac{m(m-1)}{\nu\beta_n^2} r^{m-2}, & \text{if } r < 1, \\ -\dfrac{\pi\beta_n}{2\nu} H_m''(\mathrm{i}\beta_n r)(b_n J_{m-1}(\mathrm{i}\beta_n) - a_n J_{m+1}(\mathrm{i}\beta_n)) + b_n \dfrac{m(m+1)}{\nu\beta_n^2} r^{-m-2}, & \text{if } r > 1. \end{cases}$$

Upon simplifying the Bessel function derivatives, the jump (4.16) reduces to

$$-(b_n + a_n) = m\kappa(X_n^r - \mathrm{i}\tau X_{n-1}^r + \mathrm{i}\tau X_{n+1}^r) + m^2\kappa(X_n^\theta - \mathrm{i}\tau X_{n-1}^\theta + \mathrm{i}\tau X_{n+1}^\theta).$$

Substituting a_n and b_n into the simplified jump conditions yields

$$\begin{aligned}
&\left[\mathrm{i}\frac{\beta_n^4}{2m}\frac{\nu^2}{\kappa}\left(2 - \frac{H_{m+1}(\mathrm{i}\beta_n)}{H_{m-1}(\mathrm{i}\beta_n)} - \frac{J_{m-1}(\mathrm{i}\beta_n)}{J_{m+1}(\mathrm{i}\beta_n)}\right) + \mathrm{i}m^2\right] X_n^r \\
&\qquad + \left[-\mathrm{i}\frac{\beta_n^4}{2m}\frac{\nu^2}{\kappa}\left(\frac{H_{m+1}(\mathrm{i}\beta_n)}{H_{m-1}(\mathrm{i}\beta_n)} - \frac{J_{m-1}(\mathrm{i}\beta_n)}{J_{m+1}(\mathrm{i}\beta_n)}\right) - \mathrm{i}m\right] X_n^\theta \\
&\qquad\qquad = -m^2\tau(X_{n-1}^r - X_{n+1}^r) + k\tau(X_{n-1}^\theta - X_{n+1}^\theta),
\end{aligned} \tag{4.24}$$

$$\begin{aligned}
&\left[-\beta_n^3\frac{\nu^2}{\kappa}\left(\frac{H_m(\mathrm{i}\beta_n)}{H_{m-1}(\mathrm{i}\beta_n)} - \frac{J_m(\mathrm{i}\beta_n)}{J_{m+1}(\mathrm{i}\beta_n)}\right) - \mathrm{i}m\right] X_n^r \\
&\qquad + \left[\beta_n^3\frac{\nu^2}{\kappa}\left(\frac{H_m(\mathrm{i}\beta_n)}{H_{m-1}(\mathrm{i}\beta_n)} + \frac{J_m(\mathrm{i}\beta_n)}{J_{m+1}(\mathrm{i}\beta_n)}\right) - \mathrm{i}m^2\right] X_n^\theta \\
&\qquad\qquad = m\tau(X_{n-1}^r - X_{n+1}^r) + m^2\tau(X_{n-1}^\theta - X_{n+1}^\theta).
\end{aligned} \tag{4.25}$$

Now consider the special case $\beta_n = 0$ which only occurs when both $\gamma = 0$ and $n = 0$. The equation for the radial velocity in this case reduces to

$$\frac{\mathrm{d}^2 u_0^r}{\mathrm{d}r^2} + \frac{3}{r}\frac{\mathrm{d}u_0^r}{\mathrm{d}r} - \left(\frac{m^2-1}{r^2}\right) u_0^r = \frac{1}{\nu}\frac{\mathrm{d}p_0}{\mathrm{d}r}.$$

Following the same steps as before, we first find the Green's function

$$G(r,z) = -\frac{1}{2k}\begin{cases} \dfrac{r^{m-1}}{z^{m-1}}, & \text{if } r < z, \\ \dfrac{z^{m+2}}{r^{m+1}}, & \text{if } r > z, \end{cases}$$

and then the coefficient for the radial velocity using the integral (4.21)

$$u_0^r(r) = \begin{cases} \dfrac{a_0}{\nu}\left(\dfrac{m}{4m+4}\, r^{m+1} - \dfrac{1}{4}\, r^{m-1}\right) - \dfrac{b_0}{\nu}\dfrac{1}{4m-4}\, r^{m-1}, & \text{if } r < 1, \\ -\dfrac{a_0}{\nu}\dfrac{1}{4m+4}\, r^{-m-1} + \dfrac{b_0}{\nu}\left(\dfrac{m}{4m-4}\, r^{-m+1} - \dfrac{1}{4}\, r^{-m-1}\right), & \text{if } r > 1. \end{cases}$$

From the incompressibility condition (4.20) we obtain the angular velocity component

$$u_0^\theta(r) = \begin{cases} \dfrac{a_0}{\nu}\left(\dfrac{m+2}{4m+4}\, r^{m+1} - \dfrac{1}{4}\, r^{m-1}\right) - \dfrac{b_0}{\nu}\dfrac{1}{4m-4}\, r^{m-1}, & \text{if } r < 1, \\ \dfrac{a_0}{\nu}\dfrac{1}{4m+4}\, r^{-m-1} - \dfrac{b_0}{\nu}\left(\dfrac{m-2}{4m-4}\, r^{-m+1} - \dfrac{1}{4}\, r^{-m-1}\right), & \text{if } r > 1. \end{cases}$$

To ensure continuity at the interface $r = 1$ we must have $a_0 = b_0 = 0$. Hence the jump conditions (4.15) and (4.16) are simply

$$0 = -m^2(X_0^r - \mathrm{i}\tau X_{-1}^r + \mathrm{i}\tau X_1^r) + m(X_0^\theta - \mathrm{i}\tau X_{-1}^\theta + \mathrm{i}\tau X_1^\theta), \tag{4.26}$$

$$0 = m(X_0^r - \mathrm{i}\tau X_{-1}^r + \mathrm{i}\tau X_1^r) + m^2(X_0^\theta - \mathrm{i}\tau X_{-1}^\theta + \mathrm{i}\tau X_1^\theta). \tag{4.27}$$

Our aim now is to determine for which parameters (if any) instabilities occur. We follow the approach illustrated in Chapter 2 and in other studies of parametric instabilities [64]. The linear system of equations equations (4.24)–(4.27) can be written in the form

$$\begin{aligned} A_n X_n^r + B_n X_n^\theta &= -m^2\tau(X_{n+1}^r - X_{n-1}^r) + m\tau(X_{n+1}^\theta - X_{n-1}^\theta), \\ C_n X_n^r + D_n X_n^\theta &= m\tau(X_{n+1}^r - X_{n-1}^r) + m^2\tau(X_{n+1}^\theta - X_{n-1}^\theta). \end{aligned}$$

where A_n, B_n, C_n and D_n depend on m, β_n, ν and κ. To ensure real-valued solutions, we impose reality conditions to the Fourier series coefficients:

$$\begin{aligned} &X_{-n}^r = \overline{X}_n^r, \qquad X_{-n}^\theta = \overline{X}_n^\theta \qquad \text{for the harmonic case } (\gamma = 0), \\ &X_{-n}^r = \overline{X}_{n-1}^r, \qquad X_{-n}^\theta = \overline{X}_{n-1}^\theta \qquad \text{for the subharmonic case } (\gamma = \tfrac{1}{2}\mathrm{i}). \end{aligned}$$

To solve the linear system numerically, we truncate the number of temporal modes in the Floquet-Fourier series such that $0 \leq n \leq N$. We now have a generalized eigenvalue problem

$$\mathbf{A}\boldsymbol{v} = \tau \mathbf{B}\boldsymbol{v}, \tag{4.28}$$

where

$$\boldsymbol{v} = \begin{bmatrix} \vdots \\ \Re\{X_n^r\} \\ \Im\{X_n^r\} \\ \Re\{X_n^\theta\} \\ \Im\{X_n^\theta\} \\ \vdots \end{bmatrix}$$

is a vector of length $4N + 4$ and $\mathbf{A}$ and $\mathbf{B}$ are $(4N + 4) \times (4N + 4)$ matrices. The matrix $\mathbf{A} = \text{diag}\{\mathbf{A}_0, \mathbf{A}_1, \ldots, \mathbf{A}_N\}$ is block diagonal consisting of 4×4 blocks

$$\mathbf{A}_n = \begin{bmatrix} \Re\{A_n\} & -\Im\{A_n\} & \Re\{B_n\} & -\Im\{B_n\} \\ \Im\{A_n\} & \Re\{A_n\} & \Im\{B_n\} & \Re\{B_n\} \\ \Re\{C_n\} & -\Im\{C_n\} & \Re\{D_n\} & -\Im\{D_n\} \\ \Im\{C_n\} & \Re\{C_n\} & \Im\{D_n\} & \Re\{D_n\} \end{bmatrix},$$

except in the harmonic case where

$$\mathbf{A}_0 = \begin{bmatrix} -m^2 & 0 & m & 0 \\ 0 & -m^2 & 0 & m \\ m & 0 & m^2 & 0 \\ 0 & m & 0 & m^2 \end{bmatrix}.$$

The matrix $\mathbf{B}$ is a block tridiagonal matrix of the form

$$\mathbf{B} = \begin{bmatrix} \widehat{\mathbf{B}} & \widetilde{\mathbf{B}} & & & \\ \breve{\mathbf{B}} & \mathbf{0}_4 & -\breve{\mathbf{B}} & & \\ & \ddots & \ddots & \ddots & \\ & & \breve{\mathbf{B}} & \mathbf{0}_4 & -\breve{\mathbf{B}} \\ & & & \breve{\mathbf{B}} & \mathbf{0}_4 \end{bmatrix},$$

where $\mathbf{0}_4$ denotes the 4×4 zero matrix. The first block row depends on the choice of γ. In

the harmonic case

$$\widehat{\mathbf{B}} = \mathbf{0}_4 \qquad \text{and} \qquad \widetilde{\mathbf{B}} = \begin{bmatrix} 0 & -2m^2 & 0 & 2m \\ 0 & 0 & 0 & 0 \\ 0 & 2m & 0 & 2m^2 \\ 0 & 0 & 0 & 0 \end{bmatrix},$$

whereas in the subharmonic case

$$\widehat{\mathbf{B}} = \begin{bmatrix} -m^2 & 0 & m & 0 \\ 0 & m^2 & 0 & -m \\ m & 0 & m^2 & 0 \\ 0 & -m & 0 & -m^2 \end{bmatrix} \qquad \text{and} \qquad \widetilde{\mathbf{B}} = -\breve{\mathbf{B}}.$$

Below the first block row we have

$$\breve{\mathbf{B}} = \begin{bmatrix} -m^2 & 0 & m & 0 \\ 0 & -m^2 & 0 & m \\ m & 0 & m^2 & 0 \\ 0 & m & 0 & m^2 \end{bmatrix}.$$

Figure 4.1 shows the Ince-Strutt diagrams for wavenumbers $m = 2$, 3 and 4 and with viscosity parameter $\nu = 2 \times 10^{-4}$ and 10^{-3}. Because $m = 1$ corresponds to a translation and hence remains in equilibrium, we do not consider its stability. The generalized eigenvalue problem (4.28) is computed using MATLAB's built-in linear system solver. The harmonic and subharmonic solutions are marked by the point types $+$ and $\circ$ respectively. In these diagrams, only parameters lying below the horizontal line $\tau = \frac{1}{2}$ are physically relevant, since these values of τ correspond to a fibre stiffness $K(t)$ that remains positive for all time. Within the physically relevant region, we observe stability fingers that extend downward in parameter space similar to what was seen for the damped Mathieu equation in Chapter 2. As ν increases, the stability fingers lift up away from the axis and eventually only stable solutions remain in the physically relevant region. Hence, parametric instabilities arise for sufficiently small ν (or high Reynolds number).

In the jump formulation of the IB model, there are actually two sources of internal forcing induced by the time-variation in the elastic stiffness: the jump in pressure (4.15) and the jump in the tangential stress (4.16). For this reason there lies a secondary instability in the unphysical region ($\tau > \frac{1}{2}$) the boundary of which is depicted by the subharmonic modes that sweep across parameter space. To illustrate the source of the secondary instability, we "turn off" the time-variation in the jump in tangential stress, and then recompute the

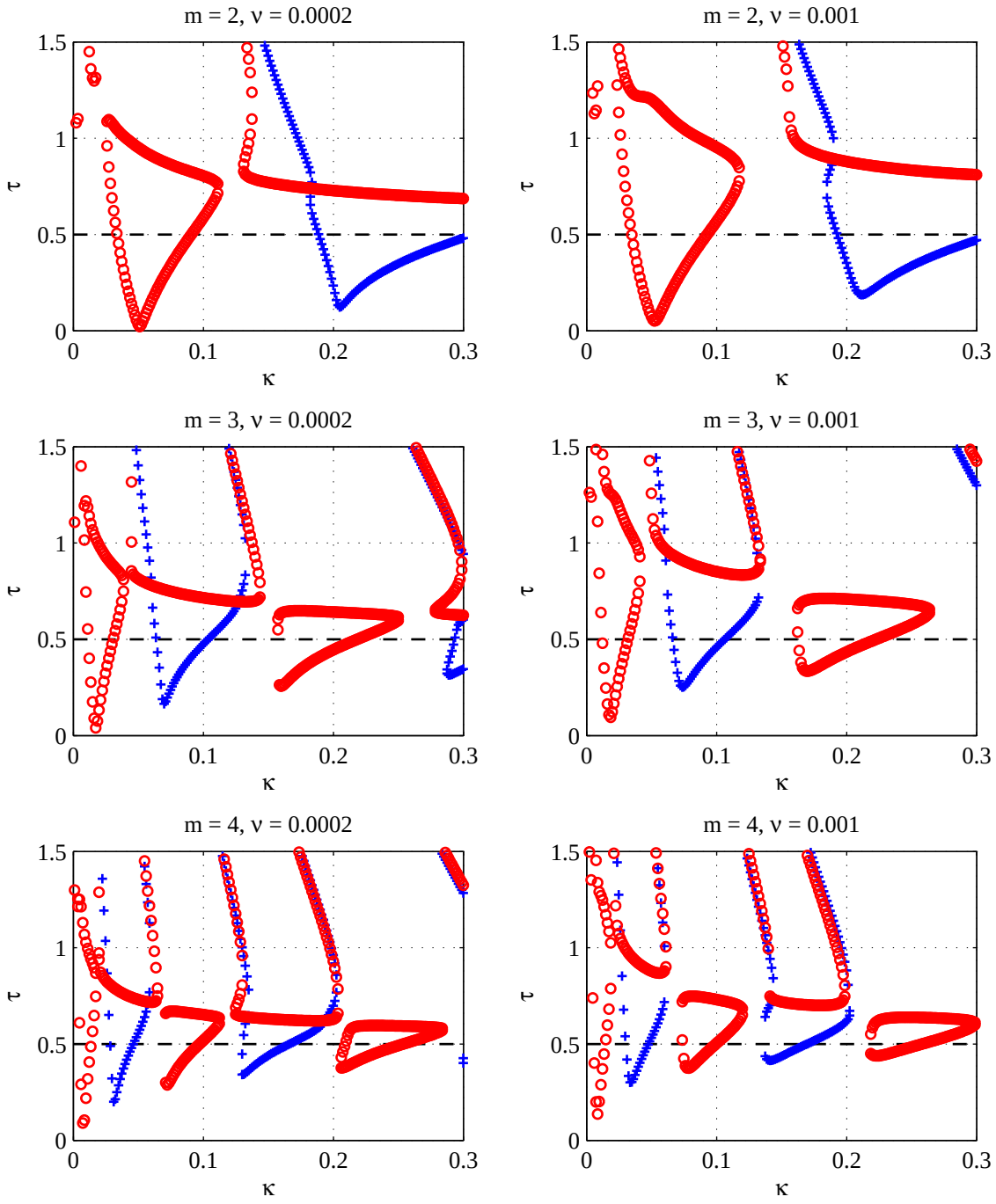

Figure 4.1: Ince-Strutt diagrams for a 2D immersed fibre undergoing a periodic modulation in elastic stiffness. Results are plotted on for dimensionless viscosity parameters $\nu = 2\times10^{-4}$ (left) and 10^{-3} (right) with wavenumbers $m = 2$ (top), 3 (middle) and 4 (bottom). Only the $\tau < \frac{1}{2}$ region correspond to positive stiffness.

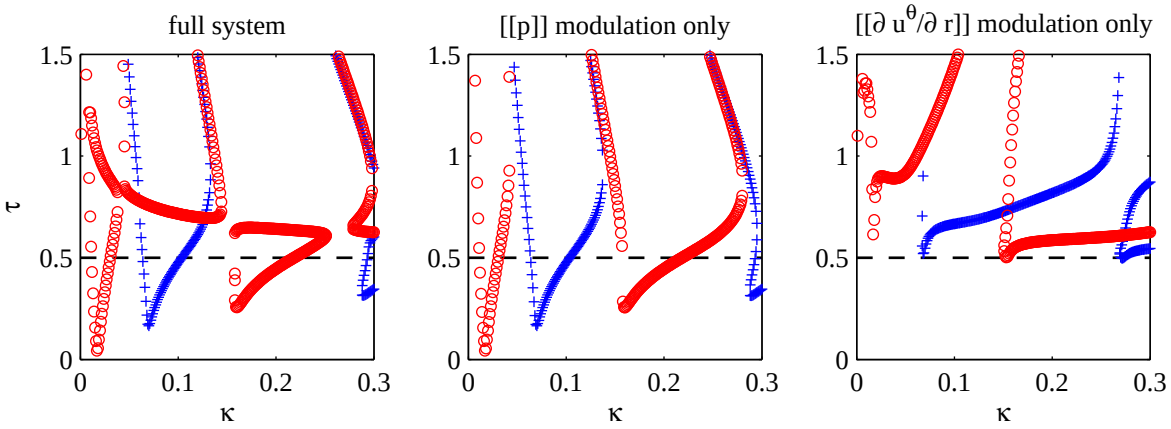

Figure 4.2: Left: Ince-Strutt diagram for the 2D IB system with $m = 3$ and $\nu = 0.0002$. Centre: Ince-Strutt diagram for periodic modulation in pressure jump only. Right: Ince-Strutt diagram for periodic modulation in tangential stress only.

eigenvalue τ. The resulting Ince-Strutt diagrams are shown in figure 4.2. When we only consider variations in the pressure jump, the result is an Ince-Strutt diagram with disjoint stability contours similar to the damped Mathieu equation. Furthermore, the physically relevant stability fingers match that of the full system. If we only consider periodic variation in the jump in tangential stress, the instabilities tend to occur in unphysical region. Hence we conclude that the physical instabilities are due to the variation in the pressure jump.

4.3 Corrections to "Parametric Resonance in Immersed Elastic Boundaries" [18]

During the course of this work, three errors were uncovered in the paper by Cortez et al. [18]. The first error is a bug in the original MATLAB code to generate the Ince-Strutt diagrams which results in the principal subharmonic mode (left-most subharmonic contour) to be absent. Figures 4.3 and 4.4 reproduce figures from the earlier paper [18, Fig. 8.2] and [18, Fig. 8.3] alongside the corrected plots. The Ince-Strutt diagrams are plotted here against wavenumber m, rather than stiffness κ. This alternate view shows which integer mode number is unstable for given values of parameters ν and κ. It is clear that the original paper misses the principal subharmonic mode, although the remaining physical modes appear to agree qualitatively with our corrected analysis.

The second error is found in Appendix B of [18], where the gradient of the Dirac delta

function is improperly transformed from Cartesian to polar coordinates, leading to an error in the perturbation expansion of the immersed boundary forcing term. The correct transformation [46] is

$$\nabla\delta(\boldsymbol{x}-\hat{\boldsymbol{r}}) = \frac{1}{r}\nabla\big(\delta(r-1)\delta(\theta-s)\big).$$

This modifies the second equation in Claim 1, from

$$(\hat{\boldsymbol{z}}\cdot\nabla\times\boldsymbol{f}^{(1)}) = K(t)(X^{\theta}_{ss}+X^{r}_{s})\left(\frac{\delta(r-1)}{r}\right)_r - K(t)(X^{r}_{sss}-X^{\theta}_{ss})\frac{\delta(r-1)}{r},$$

to

$$(\hat{\boldsymbol{z}}\cdot\nabla\times\boldsymbol{f}^{(1)}) = K(t)(X^{\theta}_{ss}+X^{r}_{s})\frac{\delta_r(r-1)}{r} - K(t)(X^{r}_{sss}-X^{\theta}_{ss})\frac{\delta(r-1)}{r},$$

where the only change is the location of the r-derivative in the first instance of the Dirac delta function. In our analysis, we derive the jump conditions via multiplying by test functions and removing the Dirac delta functions which eliminates this coordinate transformation altogether.

Lastly, a third error was introduced in the imposed reality condition. The spatial mode in the original analysis is written as a complex exponential and therefore the reality condition for the harmonic case

$$X^{r}_{-n} = \overline{X}^{r}_{n},$$

is not suitable. For harmonic solutions ($\gamma = 0$), the complex-valued mode should be viewed as a single mode in a double Fourier series

$$X^{r}(s,t) = \sum_{n=-\infty}^{\infty}\sum_{k=-\infty}^{\infty} X^{r}_{n,k}\, e^{\mathrm{i}nt+\mathrm{i}ks},$$

and for this reason the appropriate reality condition is

$$X^{r}_{-n,-k} = \overline{X}^{r}_{n,k},$$

which involves both spatial and temporal mode numbers. A similar argument holds for the subharmonic solutions ($\gamma = \frac{1}{2}\mathrm{i}$). In our analysis, we employ real-valued Fourier modes (trigonometric functions) in space which only requires a reality condition in the temporal modes.

The errors in the original analysis only result in minor changes to the results so that other than the missing principal subharmonic mode, the Ince-Strutt diagrams from [18] are still qualitatively correct.

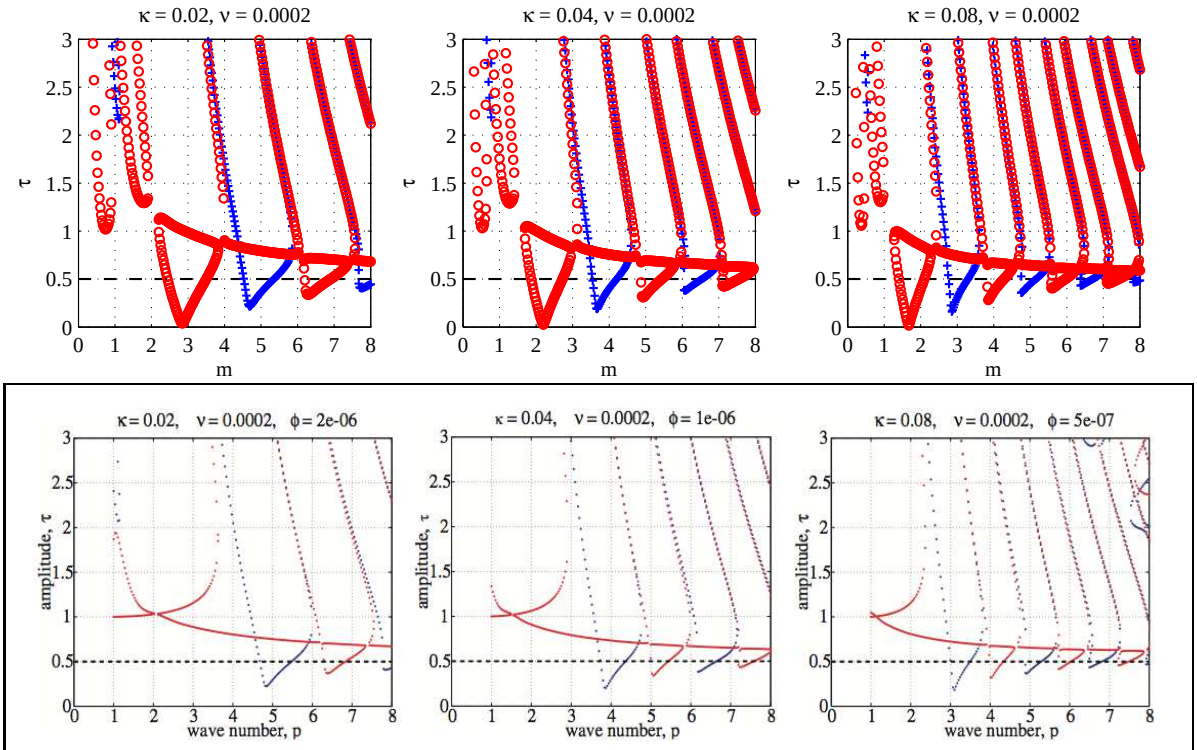

FIG. 8.2. *A series of three plots showing the impact of changes in the stiffness on the stability boundaries in the p, τ-plane, with viscosity $\nu = 0.0002$ and three different values of stiffness: $\kappa = 0.02$ (left), 0.04 (middle), and 0.08 (right).*

Figure 4.3: Top: Ince-Strutt diagrams for a 2D immersed fibre undergoing a periodic modulation in elastic stiffness. Results are plotted for $\nu = 2 \times 10^{-4}$ and $\kappa = 0.02$, 0.04 and 0.08. Bottom: Ince-Strutt diagrams by Cortez et al. [18, Fig. 8.2] (Copyright © 2004 Society for Industrial and Applied Mathematics. Reprinted with permission. All rights reserved). Note the wavenumber is denoted by p instead of m.

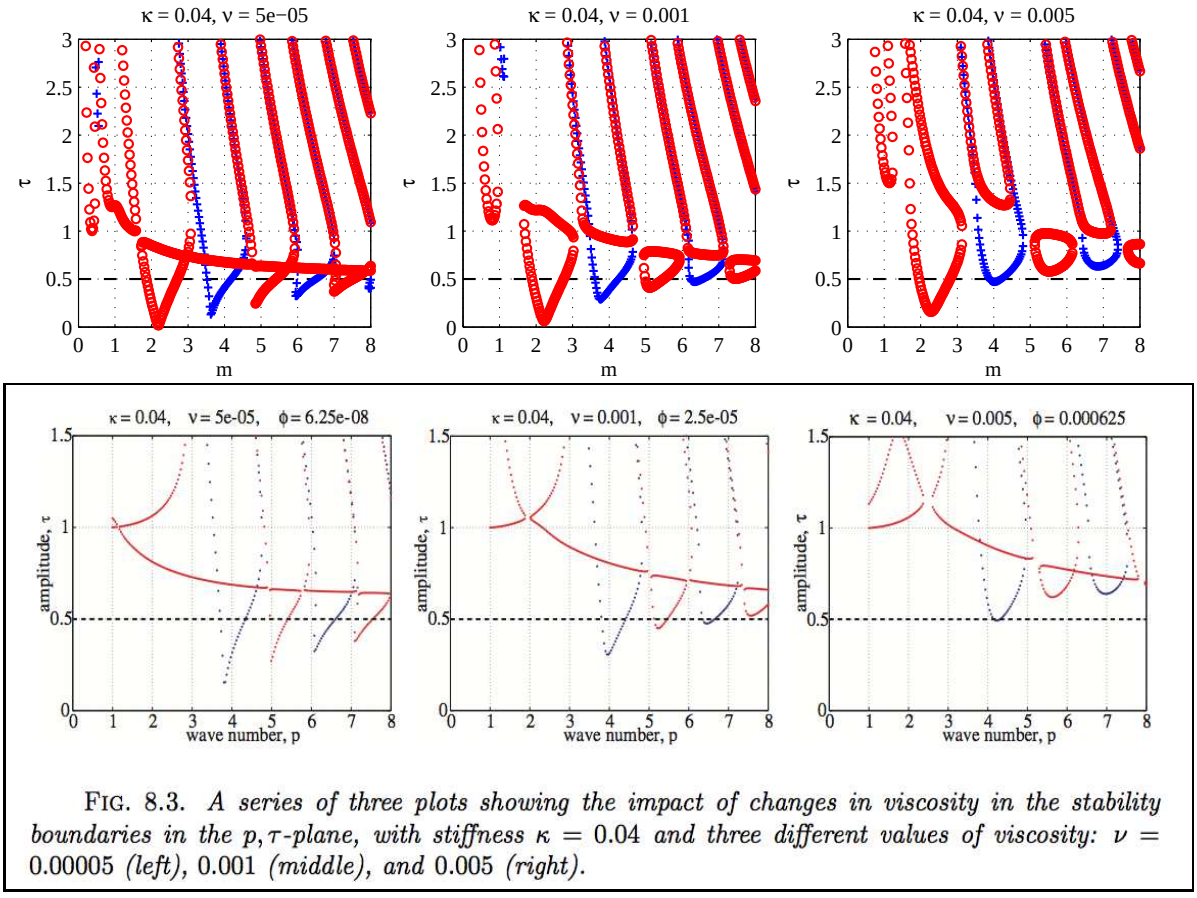

FIG. 8.3. *A series of three plots showing the impact of changes in viscosity in the stability boundaries in the p,τ-plane, with stiffness $\kappa = 0.04$ and three different values of viscosity: $\nu =$ 0.00005 (left), 0.001 (middle), and 0.005 (right).*

Figure 4.4: Top: Ince-Strutt diagrams for a 2D immersed fibre undergoing a periodic modulation in elastic stiffness. Results are plotted for $\kappa = 0.04$ and $\nu = 5 \times 10^{-5}$, 10^{-3} and 5×10^{-3}. Bottom: Ince-Strutt diagrams by Cortez et al. [18, Fig. 8.3] (Copyright © 2004 Society for Industrial and Applied Mathematics. Reprinted with permission. All rights reserved). Note the wavenumber is denoted by p instead of m.

	ν	κ	τ	ρ (g/cm^3)	R (cm)	ω (1/s)	μ (g/cm s)	σ (g cm/s^2)
Case 1	0.0002	0.02	0.45	1	0.2	2500	0.02	5×10^3
Case 2	0.0002	0.08	0.45	1	0.2	2500	0.02	2×10^4

Table 4.1: Physical parameters used in numerical simulations of the 2D immersed boundary equations.

4.4 Numerical Simulations

We perform numerical simulations of the full IB equations (4.1) to verify our analytical stability results. In particular, we wish to confirm the existence of the principal subharmonic mode that was uncovered in this chapter but missing in [18]. We use the IB algorithm implemented in the freely-available MATLAB software package `MatIB` developed by Froese and Wiens [33]. The fluid domain is chosen to be $[-1.5, 1.5]$ and is discretized uniformly with 256 grid points in each direction. The elastic fibre is discretized with 768 IB nodes and the time step is 5×10^{-6} s for each simulation. We consider two cases listed in table 4.1 which correspond to the left and right Ince-Strutt diagrams in figure 4.3. The fibre is given the initial configuration

$$\boldsymbol{X}(s,0) = R(1 + 0.05\cos(ms))\hat{\boldsymbol{r}},$$

with m chosen as the resonant mode number predicted by our analysis. From figure 4.5, we expect $m = 3$ to be resonant in case 1 and $m = 2$ to be resonant in case 2. Figure 4.5 also shows the simulated growth in the radial component of the resonant m-mode, which we depict using

$$\widehat{X}^r(t) = \frac{1}{\pi}\int_0^{2\pi} |\boldsymbol{X}(s,t)|\cos(ms)\,\mathrm{d}s.$$

From the simulations, we see the expected growth in the mode with a period-doubling response that is consistent with the principal subharmonic mode. For more numerical simulations of resonant elastic fibres, the reader is referred to the original paper [18].

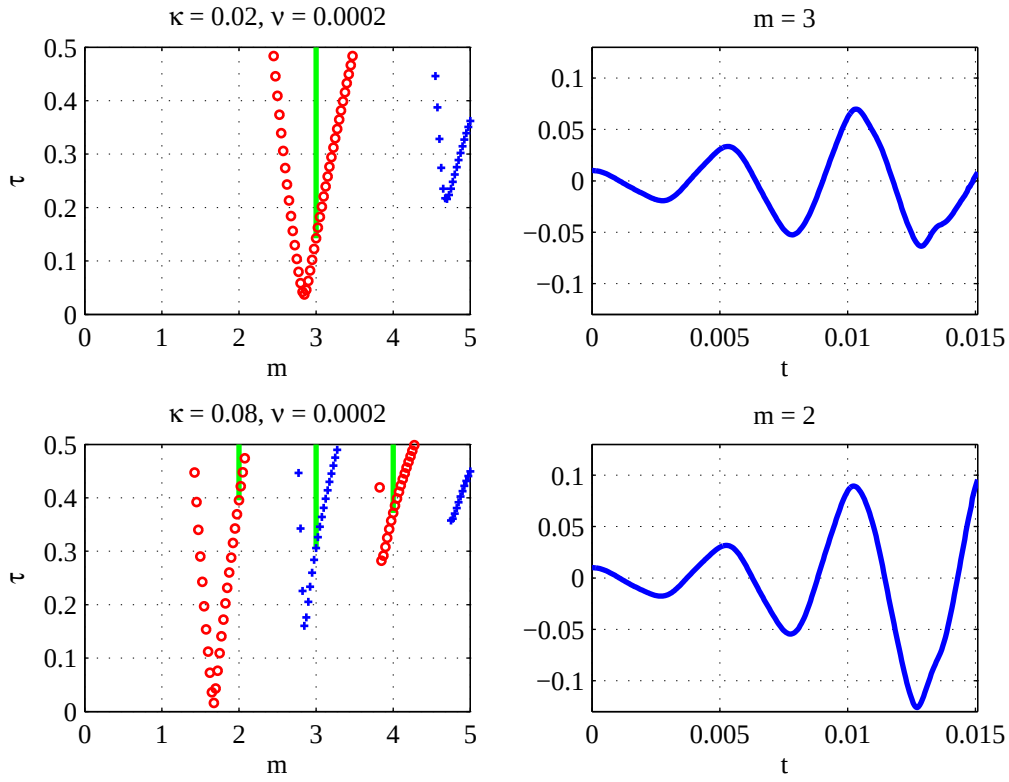

Figure 4.5: Left: Ince-Strutt diagrams for the parameters in table 4.1, zoomed in on the principal subharmonic mode. The physically relevant instabilities (for integer m) are highlighted by a vertical green line. Right: Plots of $\widehat{X}^r(t)$ depicting the expected period-doubling response, where the period of the stiffness modulation is $2\pi/\omega \approx 2.51 \times 10^{-3}$ s.

Chapter 5

A Cochlea Model with Parametric Forcing

The cochlea is a fluid-filled, spiral-wound cavity in the inner ear and is the central source of frequency selectivity in the hearing system of humans and many other animals. The cochlea is divided length-wise into three fluid chambers as illustrated in figure 5.1. The scala vestibuli and the scala media are separated by the Reissner's membrane (RM), and between the scala media and the scala tympani is a structure known as the cochlear partition (CP). The CP itself consists of an elastic membrane known as the basilar membrane (BM), on top of which is mounted the organ of Corti containing the mechano-sensitive outer hair cells (OHC) that are the primary sensory receptors in the ear. Figure 5.2 depicts the structure of the CP.

Sound vibrations entering the outer ear are transferred to the cochlear duct by the stapes, and then propagate from base to apex along the basilar membrane and the surrounding fluid. The cochlea has a remarkable ability to amplify self-induced oscillations of the basilar membrane in spite of viscous forces arising from the cochlear fluid. Many authors have attributed this amplification ability to some active process related to resonance, which experiments have connected with mechanical properties of various structures making up the CP [22, 49, 50, 95]. In particular, the OHC in the organ of Corti are stimulated by BM deflections caused by pressure waves travelling through the cochlear fluid. The hair cell stimulation leads to either *somatic motility*, wherein the hair cell changes its length in response to electrical signals induced when the hair bundle on its tip is deflected; or *active hair bundle motility* in which the hair bundle itself generates additional forces that initiate a shearing action between the BM and the overlying tectorial membrane. Both

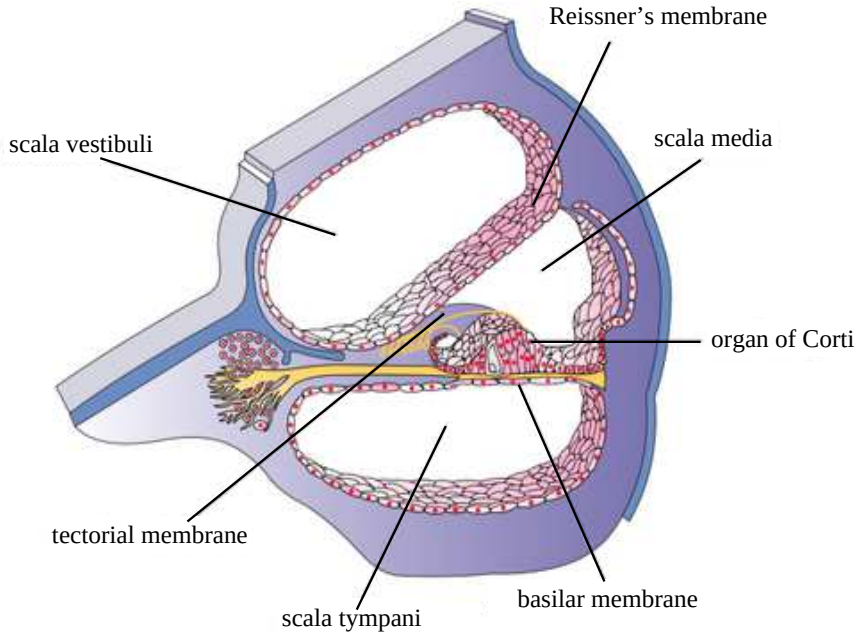

Figure 5.1: Diagram of a cross-section of the cochlear duct showing the the three fluid chambers: scala vestibuli, scala media and scala tympani. These chambers are separated by the Reissner's membrane and the cochlear partition which consists of the basilar membrane, the orgran of Corti and the tectorial membrane. Source: [97, Fig. 21.8]

of these effects are believed to contribute to the cochlear active process, but the precise causes of BM amplification remain a topic of debate [4, 111]. Hence we explore the idea of parametric resonance as a possible mechanism that amplifies BM oscillations. We extend the two-dimensional IB model of the cochlea from LeVeque et al. [74] by introducing a parametric or internal forcing via a periodic time-variation of the BM stiffness. This forcing is inspired by experiments showing that the OHC within the CP change their lengths when the ear is stimulated, which can in turn cause periodic distortions of the BM and modify the membrane tension [80, 83]. We present a Floquet analysis of the linearized equations that demonstrates the existence of resonant solutions within the range of physical parameters corresponding to human and other mammalian auditory systems.

Another notable feature of the cochlea is its ability to distinguish between different frequencies by localizing the peak amplitude of incident travelling waves wherein the peak location is closer to the base for high frequencies and to the apex for low frequencies, as illustrated in figure 5.3. This "place principle" was validated by von Békésy [124] and is primarily due to the spatially varying stiffness of the BM. Hence, an additional contribution of this chapter is to extend the parametric resonance analysis from [18] for an elastic fibre

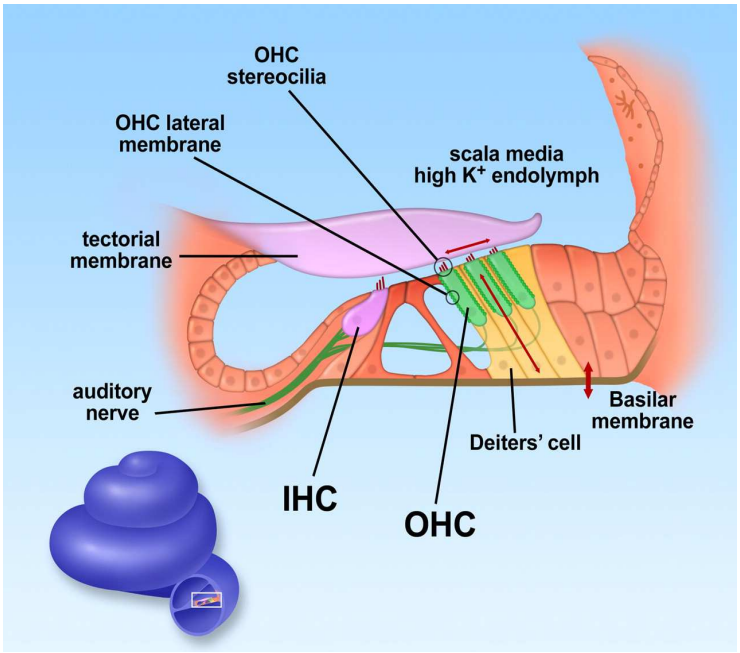

Figure 5.2: Diagram showing a close-up of the cochlear partition. The outer hair cells are embedded in the organ of Corti which sits on top of the basilar membrane. Source: [3, Fig. 1]

to the case where stiffness depends on both time and space. The spatial dependence of stiffness leads to coupling of spatial modes that introduces new challenges in the Floquet analysis.

The results in this chapter will appear in the SIAM Journal on Applied Mathematics [62].

5.1 Background on the Cochlea

The first prominent resonance theory of hearing was developed by Helmholtz [44] in the mid-1800's. His theory was based on a place principle where he assumed that the cochlea consists of an array of resonating elements, much like the strings in a piano. When stimulated, resonanting elements will vibrate in synchrony with the input sound and their locations determine the pitch. However, a flaw in Helmholtz's theory is that it requires the BM to be under high tension which does not match the actual anatomical structure of the cochlea. In the early 1900's, travelling wave theory began to succeed resonance theory in the hearing literature, the most famous work being by von Békésy [123] who was the first to observe travelling waves in the cochlea in human and animal cadavers. He also observed travelling waves in large-scale physical models using rubber membranes in a water

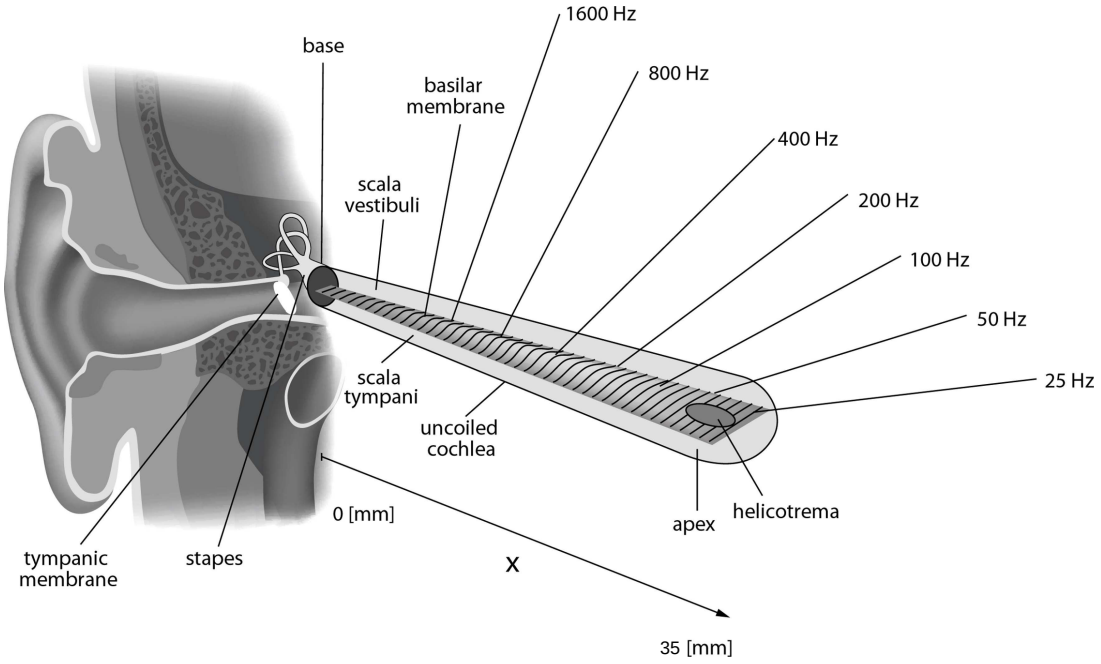

Figure 5.3: Diagram of a simplified view of an uncoiled cochlea and BM, showing the relative location of maximal BM response for several sound frequencies in the human audible range. Source: [58, Fig. 2]

tank [124]. Moreover, von Békésy's experiments show that a place principle still holds in travelling wave theory in that the wave peak systematically shifts from the base to the apex with decreasing excitation frequency. As a result, Helmholtz's resonance theory began to wane and travelling wave theory became the prevailing opinion on the theory of hearing.

A proponent for a resonance theory of hearing was Gold who claimed that resonance must account for the acute frequency differentiation ability of the ear [37, 38]. Gold hypothesized that the cochlea is an active system that employs positive feedback to overcome damping due to the cochlear fluid and achieve its fine frequency tuning ability. Gold and Pumphrey [38] performed an experiment to test this new resonance theory by exposing listeners to a sequence of pulsating and continuous tones, and assessing the volume gain. If hearing depends on resonating elements that build strength with incoming sound, like the swing of an externally forced pendulum, then the amplitude gain can be predicted. A consequence of Gold's theory is the "ringing in the ear" phenomenon or *otoacoustic emission*, wherein the ear itself produces a sound. This prediction was verified by Kemp [57] who recorded sounds emitted by the ear in several human subjects and therefore further supported a resonance theory of hearing. The state of the art of cochlea modelling combines von Békésy's travelling wave theory with an active process proposed by Gold [4, 95, 111].

Many mathematical and computational models of the cochlea have appeared since the seminal work of von Békésy [124]. The earliest two-dimensional models of the cochlea describe the BM as a collection of damped mass-spring systems and also reduce the fluid dynamics to a simple linear potential flow [2, 71, 93]. The spring constant decreases exponentially along the BM from base to apex, which coincides with BM stiffness values measured in experiments [124]. The BM is treated as a passive structure to which is applied a sinusoidal external forcing term that mimics the input of sound energy from the stapes. These models give predictions of BM dynamics that agree qualitatively with the behaviours observed by von Békésy. Inselberg and Chadwick [51] proposed a similar model in which the BM is represented as an Euler-Bernoulli beam, and showed not only that the place principle still holds but also that fluid viscosity is required to obtain travelling wave solutions along the BM as opposed to standing waves [15]. Pozrikidis [106] revisited this last approach by replacing the sinusoidal stapes motion with a point source at the stapes position and a point sink at the round window, and then solving the resulting equations using a boundary integral method. Another noteworthy class of models based on transmission line equations was introduced in the pioneering work of Zweig [133] and de Boer [23] and has since been applied in many more recent studies such as [26, 121].

To obtain a more realistic model of the fluid dynamics in the cochlea as well as the hydrodynamic interactions between the fluid and BM, several authors have exploited the IB method. LeVeque et al. [73, 74] employed an IB model in which the fluid obeys the unsteady Stokes equations and the elasticity of the cochlea is treated using simple springs. They derived an asymptotic solution for travelling waves along the BM, from which they drew conclusions regarding the effects of fluid viscosity on these waves. Beyer [11] performed numerical simulations of a related IB model, with the primary difference being that their fluid obeys the full (nonlinear) Navier-Stokes equations. All of the aforementioned immersed boundary models approximate the geometry of the cochlea and BM by a straight (uncoiled) configuration. Although the curvature of the cochlear duct has a relatively small influence on the fluid dynamics [34], there is nonetheless some evidence to suggest that within the most tightly coiled apical region of the BM that is stimulated by the lowest frequency sounds, curvature cannot be ignored [82]. To this end, a much more detailed IB model capturing the full 3D geometry of the cochlea was developed in [36] that reproduced important features of BM dynamics.

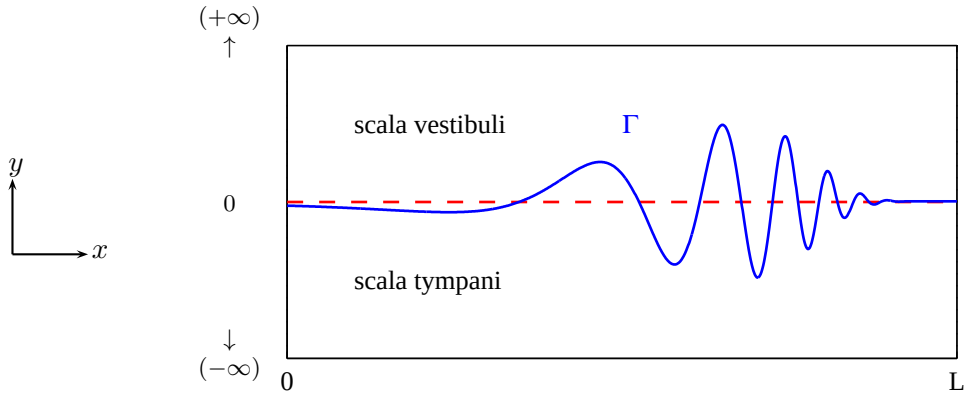

Figure 5.4: Geometry of the 2D immersed boundary model for the cochlea. The deformed BM is represented by a solid line Γ, and the flat equilibrium state by a dashed line. The depth of the cochlear chambers are taken to be infinite and Neumann boundary conditions are imposed at $x = 0$ and $x = L$.

5.2 Immersed Boundary Model

The IB cochlea model was first derived by Peskin in [100] and developed in more detail by LeVeque et al. [73, 74]. We consider a simple 2D geometry pictured in figure 5.4 in which the cochlear duct of length L is treated as a rectangular strip $\Omega = [0, L] \times \mathbb{R}$, along the centre of which lies the BM. Another simplification in our model is that we neglect the structural components of the organ of Corti in the CP and only consider the BM. Furthermore, we only consider two fluid-filled chambers, the scala vestibuli (above) and the scala tympani (below), and ignore the scala media. In other cochlea models, the scala media is either merged with the scala vestibuli or neglected entirely since the RM that separates these two chambers is thin and soft and is thought by many to have little influence on the fluid and BM motion [51, 81]. However, a recent study [112] has shown that wave motions on the Reissner's membrane may play a role in otoacoustic emissions in the ear, hence including the Reissner's membrane in our IB model is an interesting possible extension for future study.

This work is primarily concerned with the effects of parametric forcing on BM oscillations and so we simplify the model by isolating the membrane from any boundary effects due to the cochlear walls. For the purposes of the mathematical analysis, we take the depth of the cochlear chambers to be infinite in the vertical direction ($y \to \pm\infty$) as various authors [56, 73] have shown that taking the depth beyond the physical value has little influence on the BM motion. Furthermore, we impose Neumann boundary conditions in

the x-direction to permit solutions to be written as an even Fourier series which simplifies the analysis in section 5.3. This choice is in lieu of the more physical Dirichlet condition, however it has been shown that this change in boundary condition has little influence on the BM motion [93, 130].

The delta function formulation of the IB equations in physical variables is

$$\rho\left(\frac{\partial \boldsymbol{u}}{\partial t} + \boldsymbol{u}\cdot\nabla\boldsymbol{u}\right) = -\nabla p + \mu\Delta\boldsymbol{u} + \boldsymbol{f}, \tag{5.1a}$$

$$\nabla\cdot\boldsymbol{u} = 0, \tag{5.1b}$$

$$\frac{\partial \boldsymbol{X}}{\partial t} = \boldsymbol{u}(\boldsymbol{X}, t). \tag{5.1c}$$

The elastic force exerted on the fluid by the membrane is given by

$$\boldsymbol{f}(\boldsymbol{x}, t) = \int_0^L K(s,t)\,(\boldsymbol{X}_0 - \boldsymbol{X})\,\delta(\boldsymbol{x} - \boldsymbol{X})\,\mathrm{d}s, \tag{5.2}$$

where $\boldsymbol{X}(s,t)$ is the position of the BM parameterized by the Lagrangian coordinate $s \in [0, L]$, and $\boldsymbol{X}_0(s) = s\,\hat{\boldsymbol{x}}$ is the horizontal equilibrium or rest state. This force was derived by Peskin [100] using an elastic plate model which was then reduced to the above form in the narrow plate limit. Hence this force can be thought of as arising from a membrane that is connected to its resting position via a series of Hookean springs with "spring constant" or stiffness $K(s,t)$. The elastic stiffness parameter is a function of time and space given by

$$K(s,t) = \sigma e^{-\lambda_c s}\big(1 + 2\tau\sin(\omega t)\big), \tag{5.3}$$

where σ is the time-averaged elastic stiffness constant (units of $\mathrm{g\,cm^{-2}\,s^{-2}}$) and λ_c captures the spatial variation in stiffness along the BM. The value of $\lambda_c \approx 1.4\ \mathrm{cm^{-1}}$ has been determined for a human cochlea experimentally by von Békésy [124], based on the observation that the BM stiffness at the apex is approximately two orders of magnitude smaller than that at the base, and that it decays roughly exponentially. The time-dependent factor in the stiffness encapsulates the parametric forcing with amplitude τ and frequency ω arising from OHC that contract/expand in response to BM oscillations [14, 47, 49]. Note in particular that the forcing frequency ω is taken to be the same as that of the input sound signal and is also constant in space, which assumes that the outer hair cells contract in synchrony along the entire CP. This is in contrast with most other models of the cochlea that consider hair cell contractions in response to local stimuli, which would correspond to a stiffness parameter having spatiotemporal dependence that is not separable. The values of the remaining physical parameters are taken from [74] (listed in table 5.1) that are also consistent with parameters reported elsewhere in the literature for the human cochlea, with

Physical parameters (cgs units):	
fluid density	$\rho = 1.0\ \mathrm{g\,cm^{-3}}$
fluid viscosity	$\mu = 0.02\ \mathrm{g\,cm^{-1}\,s^{-1}}$
elastic stiffness	$\sigma = 6 \times 10^5\ \mathrm{g\,cm^{-2}\,s^{-2}}$
elastic stiffness decay rate	$\lambda_c = 1.4\ \mathrm{cm^{-1}}$
basilar membrane length	$L = 3.5\ \mathrm{cm}$
forcing frequency	$\omega \in [400,\ 1600]\ \mathrm{s^{-1}}$
Dimensionless parameters:	
dimensionless decay rate	$\alpha = 1.56$
forcing amplitude	$\tau \in [0, 0.5]$
dimensionless viscosity	$\nu \in [8.06 \times 10^{-6},\ 1.61 \times 10^{-4}]$
dimensionless stiffness	$\kappa \in [0.135,\ 53.9]$

Table 5.1: Parameter values (or ranges) used in the analysis and simulation of the cochlea model. Values are taken from [74] and (with the exception of σ) correspond to the human cochlea.

the only exception being the elastic stiffness value. Other cochlea models take values of σ that range from 1×10^7 [71] to $2 \times 10^9\ \mathrm{g\,cm^{-2}\,s^{-2}}$ [2]; however, in this chapter we use $\sigma = 6 \times 10^5\ \mathrm{g\,cm^{-2}\,s^{-2}}$ to permit a direct comparison with the results in [74] for a similar IB model.

For the purpose of making the Floquet analysis tractable, we linearize the governing equations. The typical vertical displacement of the BM is approximately 10^{-6} cm which is six orders of magnitude smaller than its length of 3.5 cm [124]. Therefore a typical velocity scale characterizing BM oscillations is $U = \epsilon L\omega$, where $\epsilon \ll 1$ is the ratio between the typical BM displacement size and the BM length. This implies that the flow Reynolds number is low, on the order of 10^{-6} or less, and the Strouhal number

$$St = \frac{L\omega}{U} = \frac{1}{\epsilon}$$

is high and so the nonlinear term in the Navier-Stokes equations can be ignored [106] to yield the unsteady Stokes equations

$$\rho \frac{\partial \boldsymbol{u}}{\partial t} = -\nabla p + \mu \Delta \boldsymbol{u} + \boldsymbol{f}.$$

We next proceed to nondimensionalize the problem by introducing the following scalings

$$\boldsymbol{x} = \frac{L\widetilde{\boldsymbol{x}}}{\pi}, \quad t = \frac{\widetilde{t}}{\omega}, \quad \boldsymbol{u} = \frac{L\omega}{\pi}\widetilde{\boldsymbol{u}}, \quad p = \frac{\rho L^2\omega^2}{\pi^2}\widetilde{p}, \quad \boldsymbol{X} = \frac{L\widetilde{\boldsymbol{X}}}{\pi}, \quad s = \frac{L\widetilde{s}}{\pi},$$

where a tilde denotes a nondimensional quantity. The horizontal extent of the rescaled domain $\widetilde{\Omega} = [0, \pi] \times \mathbb{R}$ is chosen for reasons of mathematical convenience, in order to eliminate a factor of π that would otherwise appear in the solutions derived in section 5.3.

Substituting the above variables into the governing equations (5.1)–(5.3) yields

$$\begin{aligned}
\frac{\partial \widetilde{\boldsymbol{u}}}{\partial \widetilde{t}} &= -\widetilde{\nabla}\widetilde{p} + \nu\widetilde{\Delta}\widetilde{\boldsymbol{u}} + \widetilde{\boldsymbol{f}},\\
\widetilde{\nabla}\cdot\widetilde{\boldsymbol{u}} &= 0,\\
\widetilde{\boldsymbol{f}}(\,\widetilde{\boldsymbol{x}},\widetilde{t}\,) &= \int_0^{\pi} \widetilde{K}(\widetilde{\boldsymbol{X}}_0 - \widetilde{\boldsymbol{X}})\,\widetilde{\delta}(\widetilde{\boldsymbol{x}} - \widetilde{\boldsymbol{X}})\,\mathrm{d}\widetilde{s},\\
\widetilde{K}(\widetilde{s},\widetilde{t}) &= \kappa e^{-\alpha\widetilde{s}}(1 + 2\tau\sin\widetilde{t}\,),\\
\frac{\partial \widetilde{\boldsymbol{X}}}{\partial \widetilde{t}} &= \widetilde{\boldsymbol{u}}(\,\widetilde{\boldsymbol{X}},\widetilde{t}\,).
\end{aligned}$$

We reduce the number of dimensionless parameters appearing in the equations to four, consisting of τ plus the three new quantities

$$\nu = \frac{\mu\pi^2}{\rho L^2\omega}, \qquad \kappa = \frac{\sigma\pi}{\rho L\omega^2}, \qquad \alpha = \frac{\lambda_c L}{\pi}.$$

From this point onwards, the tildes will be dropped.

Assuming that there is negligible coupling in the membrane along the longitudinal (x) direction, we only consider membrane displacements in the y-direction. Another simplification is achieved by eliminating the delta functions and reformulating the problem in terms of linearized jump conditions across the BM. To do so, we integrate the governing equations across the membrane at its linearized rest state $y = 0$ [103], yielding the unsteady Stokes equations

$$\frac{\partial \boldsymbol{u}}{\partial t} = -\nabla p + \nu\Delta\boldsymbol{u}, \tag{5.4a}$$

$$\nabla\cdot\boldsymbol{u} = 0, \tag{5.4b}$$

on either side of the BM which are linked by a normal jump condition for the pressure

$$[\![p]\!] = -\kappa e^{-\alpha x}(1 + 2\tau\sin t)\,h(s,t), \tag{5.5a}$$

and

$$u(x,0,t) = 0, \tag{5.5b}$$

$$v(x,0,t) = \frac{\partial h}{\partial t}. \tag{5.5c}$$

Here, $h(s,t)$ represents the vertical membrane displacement, $[\![p]\!](s,t) = p(s,0^+,t) - p(s,0^-,t)$ is the jump in pressure across the membrane, and $u(x,y,t)$ and $v(x,y,t)$ are the horizontal and vertical components of the vector velocity $\boldsymbol{u}$. Equations (5.4)–(5.5) were studied analytically in [74] without the time-varying stiffness parameter (that is, with $\tau = 0$).

5.3 Floquet Analysis

Owing to the presence of a time-varying parameter in the system, we invoke Floquet theory to analyze the stability of perturbations of the membrane from its resting state. For the purposes of our analysis, we extend the x-domain to $[-\pi, \pi]$ and impose even symmetry across $x = 0$. We then take the dependent variables to be of the form

$$u(x,y,t) = e^{\gamma t} \sum_{n=-\infty}^{\infty} \sum_{k=-\infty}^{\infty} u_k^n(y)\, e^{\mathrm{i}nt} e^{\mathrm{i}kx}, \tag{5.6a}$$

$$v(x,y,t) = e^{\gamma t} \sum_{n=-\infty}^{\infty} \sum_{k=-\infty}^{\infty} v_k^n(y)\, e^{\mathrm{i}nt} e^{\mathrm{i}kx}, \tag{5.6b}$$

$$p(x,y,t) = e^{\gamma t} \sum_{n=-\infty}^{\infty} \sum_{k=-\infty}^{\infty} p_k^n(y)\, e^{\mathrm{i}nt} e^{\mathrm{i}kx}, \tag{5.6c}$$

$$h(s,t) = e^{\gamma t} \sum_{n=-\infty}^{\infty} \sum_{k=-\infty}^{\infty} h_k^n\, e^{\mathrm{i}nt} e^{\mathrm{i}ks}. \tag{5.6d}$$

Our solution approach is similar to that of Cortez et al. [18] and the previous chapter. In contrast, here we must represent each solution mode as an infinite Fourier series because of the mode-coupling through the spatial non-uniformity in the stiffness parameter which will be shown later in this section. However, the simple rectangular geometry permits writing solutions in terms of elementary functions rather than Bessel and Hankel functions.

We begin by finding solutions for the y-dependent Fourier coefficients $u_k^n(y)$, $v_k^n(y)$ and $p_k^n(y)$. Take the divergence of the momentum equations (5.4a) and apply the incompressibility condition (5.4b) to arrive at a Poisson problem for pressure

$$\Delta p = \sum_{n,k=-\infty}^{\infty} \left(\frac{\mathrm{d}^2 p_k^n}{\mathrm{d}y^2} - k^2 p_k^n(y) \right) \mathcal{E}_k^n = 0.$$

Here we have simplified notation by setting $\mathcal{E}_k^n(x,t) := \exp[(\gamma + \mathrm{i}n)t + \mathrm{i}kx]$. The exponentials $\mathcal{E}_k^n$ are all linearly independent and so we have a decoupled system of ordinary differential equations for the coefficients $p_k^n(y)$, that is

$$\frac{\mathrm{d}^2 p_k^n}{\mathrm{d}y^2} - k^2 p_k^n(y) = 0 \qquad \text{for all } n, k \in \mathbb{Z},$$

which after imposing boundedness in y yields the pressure solution

$$p_k^n(y) = \begin{cases} a_k^n\, e^{ky}, & \text{if } y < 0, \\ b_k^n\, e^{-ky}, & \text{if } y > 0, \end{cases}$$

for each $n, k \in \mathbb{Z}$, with constants a_k^n and b_k^n yet to be determined. Note that taking $k = 0$ is valid in the above expression since this implies simply a constant pressure in each subdomain.

We can now solve for the Fourier coefficients of the vertical velocity component $v_k^n(y)$ by substituting the series (5.6b) into the momentum equation to obtain

$$\sum_{n,k=-\infty}^{\infty} (\gamma + \mathrm{i}n) v_k^n(y) \mathcal{E}_k^n = \sum_{n,k=-\infty}^{\infty} \left[-\frac{\mathrm{d}p_k^n}{\mathrm{d}y} + \nu \left(\frac{\mathrm{d}^2 v_k^n}{\mathrm{d}y^2} - k^2 v_k^n(y) \right) \right] \mathcal{E}_k^n.$$

This is equivalent to the infinite system of linear ordinary differential equations

$$\frac{\mathrm{d}^2 v_k^n}{\mathrm{d}y^2} - (\beta_k^n)^2 v_k^n(y) = \frac{1}{\nu} \frac{\mathrm{d}p_k^n}{\mathrm{d}y} \qquad \text{for all } n, k \in \mathbb{Z},$$

where

$$\beta_k^n = \sqrt{\frac{\gamma + \mathrm{i}n}{\nu} + k^2} \quad \text{with} \quad \Re\{\beta_k^n\} > 0.$$

The solution is given by

$$v_k^n(y) = \int_{-\infty}^{\infty} G(y, z) \frac{1}{\nu} \frac{\mathrm{d}p_k^n(z)}{\mathrm{d}z} \, \mathrm{d}z,$$

where $G(y, z)$ is the Green's function satisfying

$$\frac{\partial^2 G}{\partial y^2} - (\beta_k^n)^2 G = \delta(y - z),$$

with jump conditions

$$G|_{y=z^-}^{y=z+} = 0 \quad \text{and} \quad \left. \frac{\partial G}{\partial y} \right|_{y=z^-}^{y=z+} = 1.$$

Assuming that $\gamma + \mathrm{i}n \neq 0$ and $k \neq 0$, the Green's function is

$$G(y, z) = -\frac{1}{2\beta_k^n} \begin{cases} e^{\beta_k^n (y-z)}, & \text{if } y < z, \\ e^{-\beta_k^n (y-z)}, & \text{if } y > z, \end{cases}$$

and the solution to the vertical velocity is

$$v_k^n(y) = \frac{1}{2\nu\beta_k^n} \begin{cases} -\dfrac{2k\beta_k^n a_k^n}{(\beta_k^n)^2 - k^2} e^{ky} + \left(\dfrac{k a_k^n}{\beta_k^n - k} + \dfrac{k b_k^n}{\beta_k^n + k} \right) e^{\beta_k^n y}, & \text{if } y < 0, \\ \dfrac{2\beta_k^n b_k^n}{(\beta_k^n)^2 - k^2} e^{-ky} - \left(\dfrac{k b_k^n}{\beta_k^n - k} + \dfrac{k a_k^n}{\beta_k^n + k} \right) e^{-\beta_k^n y}, & \text{if } y > 0. \end{cases}$$

The incompressibility condition (5.4b) reduces to

$$\mathrm{i}ku_k^n(y) + \frac{\mathrm{d}v_k^n}{\mathrm{d}y} = 0 \quad \text{for all } n, k \in \mathbb{Z},$$

from which $u_k^n(y)$ are found to be

$$u_k^n(y) = -\frac{\mathrm{i}}{2k\nu} \begin{cases} -\dfrac{2k^2 a_k^n}{(\beta_k^n)^2 - k^2}\, e^{ky} + \left(\dfrac{ka_k^n}{\beta_k^n - k} + \dfrac{kb_k^n}{\beta_k^n + k}\right) e^{\beta_k^n y}, & \text{if } y < 0, \\ -\dfrac{2kb_k^n}{(\beta_k^n)^2 - k^2}\, e^{-ky} + \left(\dfrac{kb_k^n}{\beta_k^n - k} + \dfrac{ka_k^n}{\beta_k^n + k}\right) e^{-\beta_k^n y}, & \text{if } y > 0. \end{cases}$$

We then impose the membrane evolution equations (5.5b) and (5.5c) to obtain

$$\begin{aligned} u_k^n(0^+) = u_k^n(0^-) &= \frac{\mathrm{i}}{2\nu}\left(\frac{a_k^n}{\beta_k^n + k} + \frac{b_k^n}{\beta_k^n + k}\right) = 0, \\ v_k^n(0^+) = v_k^n(0^-) &= \frac{1}{2\nu\beta_k^n}\left(\frac{-ka_k^n}{\beta_k^n + k} + \frac{kb_k^n}{\beta_k^n + k}\right) = (\gamma + \mathrm{i}n)h_k^n, \end{aligned}$$

which can be solved in terms of the h_k^n as

$$\begin{aligned} a_k^n &= -\nu(\gamma + \mathrm{i}n)\,\frac{\beta_k^n + k}{k}\,\beta_k^n\, h_k^n, \\ b_k^n &= \quad \nu(\gamma + \mathrm{i}n)\,\frac{\beta_k^n + k}{k}\,\beta_k^n\, h_k^n. \end{aligned}$$

Using the jump condition (5.5a), we can now formulate an infinite system of linear equations that connects all of the membrane coefficients h_k^n. Substituting the solution for pressure into (5.5a), we obtain

$$\sum_{n,k=-\infty}^{\infty} 2\nu(\gamma + \mathrm{i}n)\,\frac{\beta_k^n + k}{k}\,\beta_k^n\, h_k^n\, \mathcal{E}_k^n = \sum_{n,k=-\infty}^{\infty} -\kappa e^{-\alpha x}\,(1 + 2\tau\sin t)\, h_k^n\, \mathcal{E}_k^n,$$

provided that $\gamma + \mathrm{i}n \neq 0$ and $k \neq 0$.

We next consider two special cases, the first of which is $\gamma + \mathrm{i}n = 0$ (both $\gamma = 0$ and $n = 0$) and $k \in \mathbb{Z}$. The vertical velocity coefficients satisfy

$$\frac{\mathrm{d}^2 v_k^0}{\mathrm{d}y^2} - k^2 v_k^0(y) = \frac{1}{\nu}\frac{\mathrm{d}p_k^0}{\mathrm{d}y} \qquad \text{for all } k \in \mathbb{Z}.$$

Following the Green's functions approach as in the previous case, the solution is

$$v_k^n(y) = \begin{cases} \dfrac{ka_k^0}{2\nu} y e^{ky} + c_k^0 e^{ky}, & \text{if } y < 0, \\ -\dfrac{kb_k^0}{2\nu} y e^{-ky} + c_k^0 e^{-ky}, & \text{if } y > 0, \end{cases}$$

where we have introduced a third set of undetermined coefficients c_k^0. From the incompressibility condition, we find the horizontal velocity coefficient to be

$$u_k^n(y) = \begin{cases} \dfrac{\mathrm{i}a_k^0}{2\nu}\Big(e^{ky} + yke^{ky}\Big) + c_k^0 ke^{ky}, & \text{if } y < 0, \\ -\dfrac{\mathrm{i}b_k^0}{2\nu}\Big(e^{-ky} - yke^{-ky}\Big) - c_k^0 ke^{-ky}, & \text{if } y > 0. \end{cases}$$

The membrane evolution equations (5.5b) and (5.5c) imply $a_k^0 = b_k^0 = c_k^0 = 0$ for all k, hence the pressure jump condition (5.5a) reduces to

$$0 = \sum_{n,k=-\infty}^{\infty} -\kappa e^{-\alpha x}(1 + 2\tau \sin t) h_k^0 \, \mathcal{E}_k^0.$$

The second special case to consider is $\gamma + \mathrm{i}n \neq 0$ and $k = 0$. The pressure coefficients p_0^n reduce to a piece-wise constant function and thus the Fourier coefficients for the vertical velocity component satisfy

$$\frac{\mathrm{d}^2 v_0^n}{\mathrm{d}y^2} - (\beta_0^n)^2 v_0^n(y) = 0 \qquad \text{for } n \neq 0,$$

away from the membrane. The solution for the velocity coefficients is

$$v_0^n(y) = \begin{cases} c_0^n e^{\beta_0^n y}, & \text{if } y < 0, \\ c_0^n e^{-\beta_0^n y}, & \text{if } y > 0. \end{cases}$$

The incompressibility condition leads to $c_0^n = 0$ and so the vertical velocity component is zero. Therefore the $k = 0$ mode is motionless and $h_0^n = 0$.

In order to proceed any further, we need to expand the exponential ($e^{-\alpha x}$) and sinusoidal ($\sin t$) terms in their respective Fourier series. For the time-dependent factor, we can write $1 + 2\tau \sin t = 1 - \mathrm{i}\tau e^{\mathrm{i}t} + \mathrm{i}\tau e^{-\mathrm{i}t}$, but the Fourier series for the exponential function does not converge uniformly because $e^{-\alpha x}$ is not a periodic function on $[0, \pi]$. It is for this reason that we have extended the spatial domain to $[-\pi, \pi]$ and have chosen to impose Neumann boundary conditions. We instead use the even periodic extension $e^{-\alpha|x|}$ of the elastic stiffness function on this extended interval. We then simply need to remember that only the portion with $x \in [0, \pi]$ that is of physical interest. Then, for $\gamma + \mathrm{i}n \neq 0$ and $k \neq 0$ we have

$$\begin{aligned} &\sum_{n,k=-\infty}^{\infty} 2\nu(\gamma + \mathrm{i}n) \frac{\beta_k^n + k}{k} \beta_k^n \, h_k^n \, \mathcal{E}_k^n \\ &\qquad = \sum_{n,k=-\infty}^{\infty} -\kappa \left(\sum_{j=-\infty}^{\infty} c_j e^{\mathrm{i}jx} \right) (1 - \mathrm{i}\tau e^{\mathrm{i}t} + \mathrm{i}\tau e^{-\mathrm{i}t}) h_k^n \, \mathcal{E}_k^n, \end{aligned} \tag{5.7}$$

while for $\gamma + \mathrm{i}n = 0$,

$$0 = \sum_{n,k=-\infty}^{\infty} -\kappa \left(\sum_{j=-\infty}^{\infty} c_j e^{\mathrm{i}jx} \right) (1 - \mathrm{i}\tau e^{\mathrm{i}t} + \mathrm{i}\tau e^{-\mathrm{i}t}) h_k^0 \, \mathcal{E}_k^0, \tag{5.8}$$

where

$$c_j = \alpha \frac{1 - (-1)^j e^{-\alpha\pi}}{\pi(\alpha^2 + j^2)}$$

are the Fourier coefficients of $e^{-\alpha|x|}$ on $[-\pi, \pi]$. The complex exponential terms involving x and t in equations (5.7) and (5.8) introduce a shift in the indices of $\mathcal{E}_k^n$ in both n and k, which has the effect of coupling the corresponding modes. We can then rearrange the sum in order to gather together all terms involving the common expression $\mathcal{E}_k^n$, and hence obtain

$$\frac{2\nu^2}{\kappa} (\beta_k^n - k) \, (\beta_k^n + k)^2 \, \frac{\beta_k^n}{k} h_k^n + \sum_{j=-\infty}^{\infty} c_{k-j} h_j^n = \mathrm{i}\tau \sum_{j=-\infty}^{\infty} c_{k-j} (h_j^{n-1} - h_j^{n+1}) \tag{5.9}$$

for $\gamma + \mathrm{i}n \neq 0$ and $k \neq 0$ and

$$\sum_{j=-\infty}^{\infty} c_{k-j} h_j^0 = \mathrm{i}\tau \sum_{j=-\infty}^{\infty} c_{k-j} (h_j^{-1} - h_j^1) \tag{5.10}$$

for the special cases $\gamma + \mathrm{i}n = 0$. These last two equations comprise an infinite linear system for the h_j^n in which the spatially dependent stiffness introduces a simultaneous coupling between all spatial modes that is not present in the spatially uniform ($\alpha = 0$) case from [18].

Because we are interested in investigating the stability of the parametrically forced problem, and in particular finding the stability boundary in parameter space, we look for harmonic ($\gamma = 0$) and subharmonic ($\gamma = \frac{1}{2}\mathrm{i}$) solutions of equations (5.9)–(5.10). To ensure that the solution $h(s,t)$ is real-valued, we impose reality conditions for the Fourier coefficients that apply to both time and space indices. In general, the reality condition for a two-dimensional Fourier series is $h_k^n = \bar{h}_{-k}^{-n}$, however, we have to consider the harmonic and subharmonic cases separately when applying the condition in the temporal modes. Furthermore, we want to ensure an even spatial symmetry in our solutions which leads to a decoupling in the reality condition. Consequently, the reality conditions that we impose are

$$h_{-k}^n = h_k^n,$$
$$h_k^{-n} = \begin{cases} \bar{h}_k^n & \text{for the harmonic case } (\gamma = 0), \\ \bar{h}_k^{n-1} & \text{for the subharmonic case } (\gamma = \frac{1}{2}\mathrm{i}). \end{cases}$$

As a result, the reality conditions introduce a certain symmetry between the Fourier coefficients such that we only need to consider nonnegative values of n and k.

To solve the system (5.9)–(5.10), we truncate at values of $n = 0, 1, \ldots, N$ and $k = 1, 2, \ldots, M$ and then approximate the solutions numerically. Recall that for $k = 0$, we have that $h_0^n = 0$ for each n and so there is no need to include them in the linear system. The truncated system of equations can therefore be represented as a matrix equation

$$\mathbf{A}\boldsymbol{v} = \tau \mathbf{B}\boldsymbol{v}, \tag{5.11}$$

where

$$\boldsymbol{v} = \begin{bmatrix} \vdots \\ \Re\{h_k^n\} \\ \Im\{h_k^n\} \\ \Re\{h_{k+1}^n\} \\ \Im\{h_{k+1}^n\} \\ \vdots \end{bmatrix}$$

is a vector of length $2M(N+1)$ containing all unknown coefficients, $\mathbf{A}$ is a block diagonal matrix and $\mathbf{B}$ is a block tridiagonal matrix. Both $\mathbf{A}$ and $\mathbf{B}$ have block dimension $(N+1) \times (N+1)$ where each block is size $2M \times 2M$. The block diagonal matrix $\mathbf{A}$ can be expressed as $\mathbf{A} = \text{diag}\{\mathbf{A}^0, \mathbf{A}^1, \ldots, \mathbf{A}^N\}$ where each block has the form

$$\mathbf{A}^n = \begin{bmatrix} \mathbf{C}_{1,1} + \mathbf{D}_1^n & \mathbf{C}_{1,2} & \cdots & \mathbf{C}_{1,M} \\ \mathbf{C}_{2,1} & \mathbf{C}_{2,2} + \mathbf{D}_2^n & & \mathbf{C}_{2,M} \\ \vdots & & \ddots & \vdots \\ \mathbf{C}_{M,1} & \mathbf{C}_{M,2} & \cdots & \mathbf{C}_{M,M} + \mathbf{D}_M^n \end{bmatrix},$$

with

$$\begin{aligned} \mathbf{C}_{k,j} &= \begin{bmatrix} c_{k-j} + c_{k+j} & 0 \\ 0 & c_{k-j} + c_{k+j} \end{bmatrix}, \\ \mathbf{D}_k^n &= \frac{2\nu^2}{k\kappa} \begin{bmatrix} \Re\{(\beta_k^n - k)(\beta_k^n + k)^2 \beta_k^n\} & -\Im\{(\beta_k^n - k)(\beta_k^n + k)^2 \beta_k^n\} \\ \Im\{(\beta_k^n - k)(\beta_k^n + k)^2 \beta_k^n\} & \Re\{(\beta_k^n - k)(\beta_k^n + k)^2 \beta_k^n\} \end{bmatrix}. \end{aligned} \tag{5.12}$$

For the harmonic case, $\mathbf{D}_k^0$ is simply the 2×2 zero matrix. The block tridiagonal matrix $\mathbf{B}$

has the form

$$\mathbf{B} = \begin{bmatrix} \breve{\mathbf{B}} & \widetilde{\mathbf{B}} & & & \\ \widehat{\mathbf{B}} & \mathbf{0} & -\widehat{\mathbf{B}} & & \\ & \ddots & \ddots & \ddots & \\ & & \widehat{\mathbf{B}} & \mathbf{0} & -\widehat{\mathbf{B}} \\ & & & \widehat{\mathbf{B}} & \mathbf{0} \end{bmatrix},$$

where

$$\widehat{\mathbf{B}} = \begin{bmatrix} \widehat{\mathbf{C}}_{1,1} & \widehat{\mathbf{C}}_{1,2} & \dots & \widehat{\mathbf{C}}_{1,M} \\ \widehat{\mathbf{C}}_{2,1} & \widehat{\mathbf{C}}_{2,2} & & \widehat{\mathbf{C}}_{2,M} \\ \vdots & & \ddots & \vdots \\ \widehat{\mathbf{C}}_{M,1} & \widehat{\mathbf{C}}_{M,2} & \dots & \widehat{\mathbf{C}}_{M,M} \end{bmatrix}, \tag{5.13}$$

$$\widehat{\mathbf{C}}_{k,j} = \begin{bmatrix} 0 & -c_{k-j} - c_{k+j} \\ c_{k-j} + c_{k+j} & 0 \end{bmatrix}.$$

The reality conditions determine the first block row of $\mathbf{B}$. For harmonic solutions, $\breve{\mathbf{B}}$ is the $2M \times 2M$ zero matrix while $\widetilde{\mathbf{B}}$ has the same form as $\widehat{\mathbf{B}}$ in (5.13) except that the 2×2 sub-blocks are

$$\widetilde{\mathbf{C}}_{k,j} = \begin{bmatrix} 0 & 2c_{k-j} + 2c_{k+j} \\ 0 & 0 \end{bmatrix}.$$

For subharmonic solutions, $\widetilde{\mathbf{B}} = -\widehat{\mathbf{B}}$ and $\breve{\mathbf{B}}$ consists of the 2×2 sub-blocks

$$\breve{\mathbf{C}}_{k,j} = \begin{bmatrix} 0 & c_{k-j} + c_{k+j} \\ c_{k-j} + c_{k+j} & 0 \end{bmatrix}.$$

Next we investigate the convergence behaviour of the eigenvalues in equation (5.11). Let τ_M^N denote the lowest eigenvalue computed for a series truncation $n = 0, 1, \dots, N$ and $k = 1, 2, \dots, M$. To examine how the computed eigenvalue depends on N, we fix $M = 100$ and compute τ_M^N with $N = 4 \times 2^j$ for $j = 0, \dots, 4$, and estimate the error by

$$\varepsilon^N = \left| \tau_M^{2N} - \tau_M^N \right|.$$

Figure 5.5 shows the error using parameters from table 5.1 with $\omega = 1600$ s^{-1}. Similarly, figure 5.6 shows the error estimate defined by

$$\varepsilon_M = \left| \tau_{2M}^N - \tau_M^N \right|,$$

when fixing $N = 20$ and taking $M = 16 \times 2^j$ for $j = 0, \ldots, 4$. It is clear from the plots that the error reduces more quickly when increasing the number of temporal modes than increasing the number of spatial modes. Hence, we take a larger value of M than N in our eigenvalue calculations.

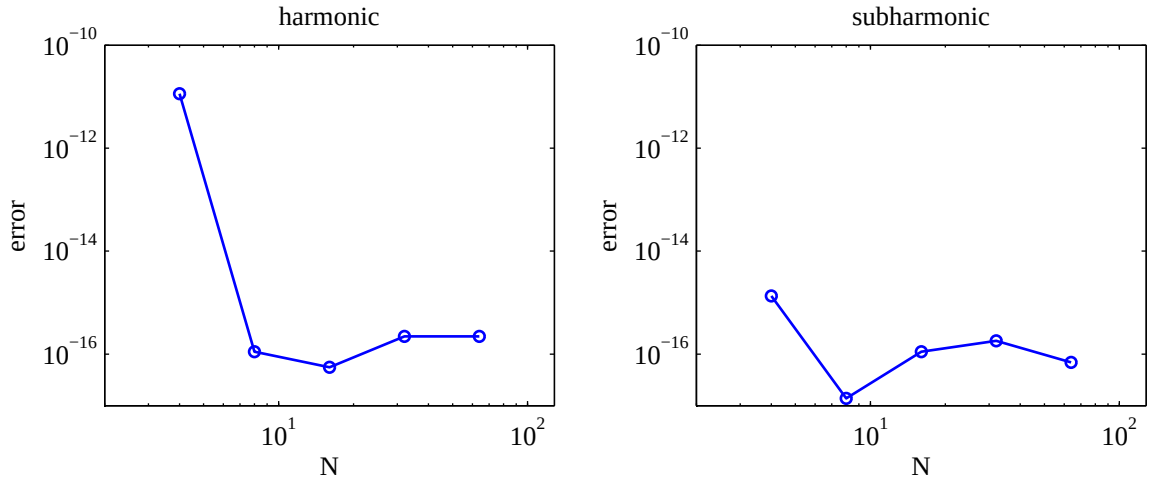

Figure 5.5: Error in the computed eigenvalue τ_M^N for the harmonic (left) and subharmonic (right) cases. The matrix truncation is chosen to be $M = 100$ and $N = 4{\times}2^j$ for $j = 0, \ldots, 4$. The error is estimated by $\left|\tau_M^{2N} - \tau_M^N\right|$.

5.4 Natural Modes for an Unforced Membrane

Before solving the parametrically forced problem, we first examine the stability of the unforced membrane corresponding to $\tau = 0$. Previous stability analyses of the immersed boundary method showed that unforced membranes are always stable [18, 118] and we expect a similar result here. The Fourier coefficients of the unforced solution satisfy

$$\frac{2\zeta\gamma}{k\sqrt{\kappa}}\sqrt{\frac{\gamma}{\zeta\sqrt{\kappa}}+k^2}\left(k+\sqrt{\frac{\gamma}{\zeta\sqrt{\kappa}}+k^2}\right)h_k^0+\sum_{j=-\infty}^{\infty}c_{k-j}h_j^0=0 \tag{5.14}$$

when $k \neq 0$ and

$$\sum_{j=-\infty}^{\infty}c_{k-j}h_j^0=0 \tag{5.15}$$

when $k = 0$. We have introduced the new dimensionless parameter

$$\zeta=\frac{\nu}{\sqrt{\kappa}}=\frac{\mu}{\sqrt{\rho\sigma(L/\pi)^3}},$$

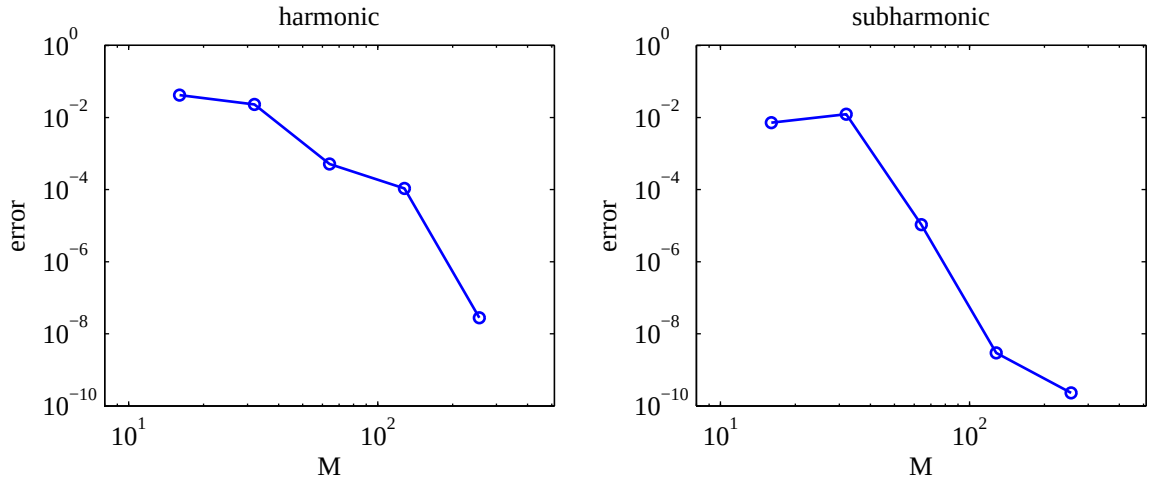

Figure 5.6: Error in the computed eigenvalue τ_M^N for the harmonic (left) and subharmonic (right) cases. The matrix truncation is chosen to be $N = 20$ and $M = 16{\times}2^j$ for $j = 0, \ldots, 4$. The error is estimated by $\left|\tau_{2M}^N - \tau_M^N\right|$.

which is a measure of the relative importance of viscous fluid force relative to elastic membrane force. The system of equations (5.14) and (5.15) can be written simply as a matrix system $\mathbf{T}\boldsymbol{v}^0 = \mathbf{0}$, where the entries of the matrix $\mathbf{T}$ depend on the parameters ζ, $\gamma/\sqrt{\kappa}$ and α. This linear system has non-trivial solutions only if $\det(\mathbf{T}) = 0$, and so by fixing values of ζ and α we can determine values of $\gamma/\sqrt{\kappa}$ such that solutions to the homogeneous system exist. In practice, we proceed by first truncating the infinite series in (5.14) and (5.15) to M terms and then computing the determinant numerically.

Figure 5.7 depicts the zero contours of the real and imaginary parts of $\det(\mathbf{T})$ for the specific choice of parameters $\alpha = 1.56$ and $M = 20$, and two values of $\zeta = 2 \times 10^{-5}$ (using parameters from table 5.1) and 10^{-2}. The points where the contours intersect correspond to the natural modes of the system. Observe that $\Re\{\gamma\}$ at the intersection points is always negative, from which we conclude that all solution modes are stable. We see next how the behaviour of the natural modes depends on ζ, the relative strength of fluid viscosity to membrane stiffness. For the relatively small value of $\zeta = 2 \times 10^{-5}$, the dominant modes (which are slowest to decay) have non-zero $\Im\{\gamma\}$ and are therefore oscillatory. When ζ is increased to 10^{-2}, viscosity has a much stronger influence and the dominant (lowest wavenumber) modes decay without oscillations, although decaying oscillatory solutions still do exist. In both cases, the unforced modes always decay in time and hence any periodic or unstable solutions must arise from a periodic modulation of the membrane stiffness.

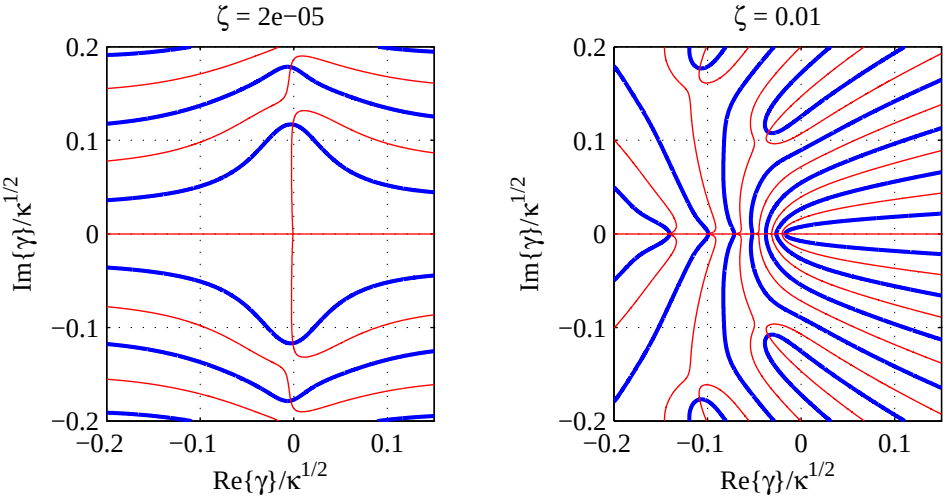

Figure 5.7: Zero contours of the real (thick, blue) and imaginary parts (thin, red) of $\det(\mathbf{T})$ for: $\zeta = 2 \times 10^{-5}$ (left) and $\zeta = 10^{-2}$ (right). In both cases, $\alpha = 1.56$ and $M = 20$. The natural modes correspond to intersection points between the real and imaginary contours.

5.5 Parametrically Forced Pure-Tone Response

In this section, we demonstrate that an internally-forced membrane can generate travelling wave solutions that are similar to solutions obtained from another model [74] that imposes an external forcing. We compute solutions to (5.9)–(5.10) numerically and then choose the smallest physically-allowable value of τ along with its corresponding eigenvector. We can reconstruct a periodic solution for $h(s,t)$ using the series representation (5.6d), which is then compared to the travelling wave solutions from LeVeque et al. [74] obtained when a pure-tone external forcing is applied.

Figure 5.8 shows solution profiles of the BM displacement curve $h(x, t_{peak})$ for forcing frequencies $\omega = 400$, 800, 1200 and 1600 s^{-1}, where t_{peak} represents the time when the maximum vertical BM displacement occurs. The wave envelope is determined by computing the absolute value of a complex-valued function whose real part is the BM profile and the imaginary part is its Hilbert transform [12, 60]. The envelope is normalized so that the maximum height is one. These wave envelopes have the characteristic asymmetric shape seen in experiments [110], exhibiting an amplitude that increases gradually from base to peak, followed by a sharp decline at the apical end. The solid curve in each case corresponds to the harmonic mode for which the response frequency is equal to the forcing frequency. A qualitatively similar result is obtained for subharmonic solutions (dashed curves) except that the response occurs at a frequency equal to half that of the internal forcing and so the

wave profiles are shifted. This indicates that the location of the envelope peak depends on the response frequency and not the forcing frequency.

Through a combination of experiments and analysis, von Békésy [124] showed that the peak location of the travelling wave envelope depends logarithmically on the external stimulus frequency. Figure 5.9 depicts the computed peak locations at various response frequencies, and our results lie nearly on a straight line which is consistent with the logarithmic dependence. This plot also includes the asymptotic results derived from the model in [74] as a solid line, which is clearly very close to our own results. As a further validation, figure 5.10 compares our BM displacement curve with the corresponding result from [74] for the frequency $\omega = 400$ s^{-1}. Both profiles are shifted so that the wave envelope peak occurs at $x = 0$, after which we can see that the qualitative shape and solution envelope are quite similar. These numerical results demonstrate that external forcing is not required to obtain a realistic travelling wave solution on the BM, and indeed that parametric (internal) forcing in the BM stiffness can generate pure-tone solutions that are consistent with results of another model [74].

5.6 Parametric Resonance in the Cochlea Model

5.6.1 Spatially Uniform Stiffness

To gain more insight into solutions of the eigenvalue problem (5.11), we begin by considering the simple case $\alpha = 0$ where the elastic stiffness does not depend on BM location and thus the spatial Fourier modes are decoupled. For each spatial wavenumber k we have

$$\frac{2\nu^2}{k\kappa}(\beta_k^n - k)(\beta_k^n + k)^2\beta_k^n\, h_k^n + h_k^n = \mathrm{i}\tau(h_k^{n-1} - h_k^{n+1}),$$

for $n = 0, 1, \ldots, N$. This equation may be rewritten in matrix form as

$$\mathbf{A}_k \boldsymbol{v}_k = \tau \mathbf{B}_k \boldsymbol{v}_k,$$

where for each value of k we have

$$\boldsymbol{v}_k = \left[\, \Re\{h_k^0\},\ \Im\{h_k^0\},\ \ldots,\ \Re\{h_k^N\},\ \Im\{h_k^N\} \,\right]^{\mathrm{T}},$$
$$\mathbf{A}_k = \mathrm{diag}\{\mathbf{I}_2 + \mathbf{D}_k^0,\ \mathbf{I}_2 + \mathbf{D}_k^1,\ \ldots\ , \mathbf{I}_2 + \mathbf{D}_k^N\},$$

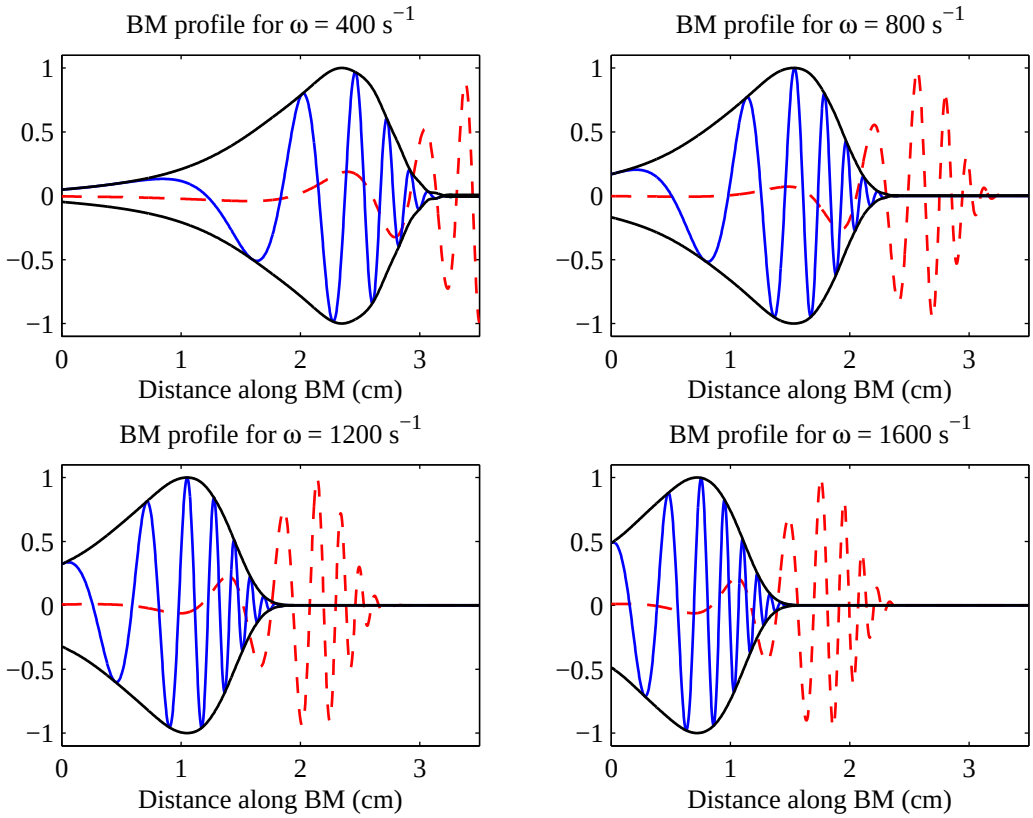

Figure 5.8: Normalized BM displacement profiles for the harmonic (solid) and subharmonic (dashed) cases at forcing frequencies $\omega = 400$, 800, 1200 and 1600 s^{-1}.

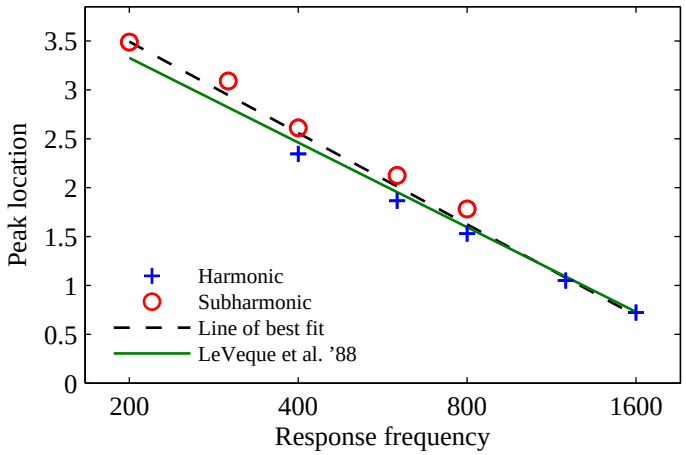

Figure 5.9: BM envelope peak location plotted against response frequency, with the horizontal axis (frequency) plotted on a log scale. Harmonic (+) and subharmonic (○) solutions have response frequencies ω and $\omega/2$ respectively.

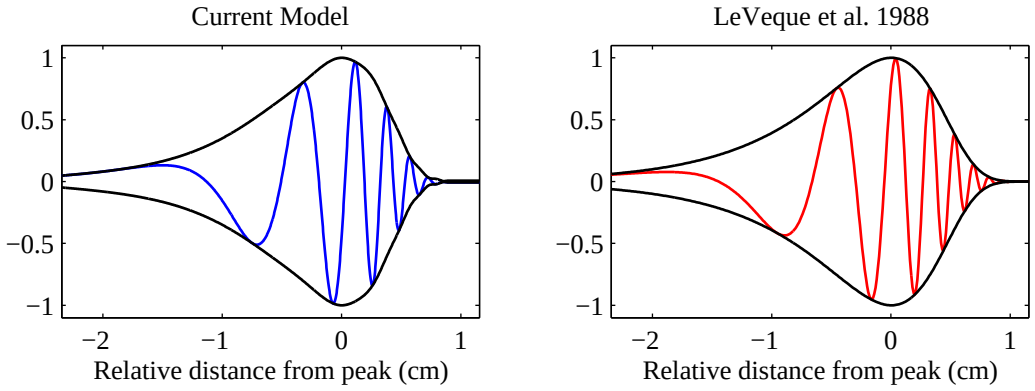

Figure 5.10: Normalized BM displacement profiles from the current IB model (left) and the model by LeVeque et al. [74] (right) at a frequency of $\omega = 400$ s^{-1}.

$\mathbf{D}_k^n$ defined by (5.12), and $\mathbf{I}_2$ is the 2×2 identity matrix. The matrix $\mathbf{B}_k$ has the form

$$\mathbf{B}_k = \begin{bmatrix} \breve{\mathbf{B}}_k & \widetilde{\mathbf{B}}_k & & & \\ \widehat{\mathbf{B}}_k & \mathbf{0} & -\widehat{\mathbf{B}}_k & & \\ & \ddots & \ddots & \ddots & \\ & & \widehat{\mathbf{B}}_k & \mathbf{0} & -\widehat{\mathbf{B}}_k \\ & & & \widehat{\mathbf{B}}_k & \mathbf{0} \end{bmatrix},$$

and we need to consider separately the two cases corresponding to harmonic solutions where

$$\breve{\mathbf{B}}_k = \begin{bmatrix} 0 & 0 \\ 0 & 0 \end{bmatrix}, \quad \widehat{\mathbf{B}}_k = \begin{bmatrix} 0 & 2 \\ 0 & 0 \end{bmatrix} \quad \text{and} \quad \widetilde{\mathbf{B}}_k = \begin{bmatrix} 0 & -1 \\ 1 & 0 \end{bmatrix},$$

and subharmonic solutions where

$$\breve{\mathbf{B}}_k = \begin{bmatrix} 0 & 1 \\ 1 & 0 \end{bmatrix}, \quad \widehat{\mathbf{B}}_k = \begin{bmatrix} 0 & 1 \\ -1 & 0 \end{bmatrix} \quad \text{and} \quad \widetilde{\mathbf{B}}_k = \begin{bmatrix} 0 & -1 \\ 1 & 0 \end{bmatrix}.$$

Figure 5.11 contains Ince-Strutt diagrams that depict τ plotted against the spatial wavenumber k for two values of the frequency $\omega = 500$ and 1000 s^{-1}. Harmonic and subharmonic solutions are labelled $+$ and $\circ$ respectively. Although we can expect parametric resonance to occur for any choice of parameters located inside one of the unstable fingers, the parameters are further constrained by the fact that the forcing amplitude must satisfy $\tau \leq \frac{1}{2}$ so that the BM stiffness $K(s,t)$ remains nonnegative. To get a clearer idea of the unstable modes that correspond to physical BM oscillations, we fix k at integer values ranging from 1 through 6 and display in figure 5.12 the stability plots as a function of

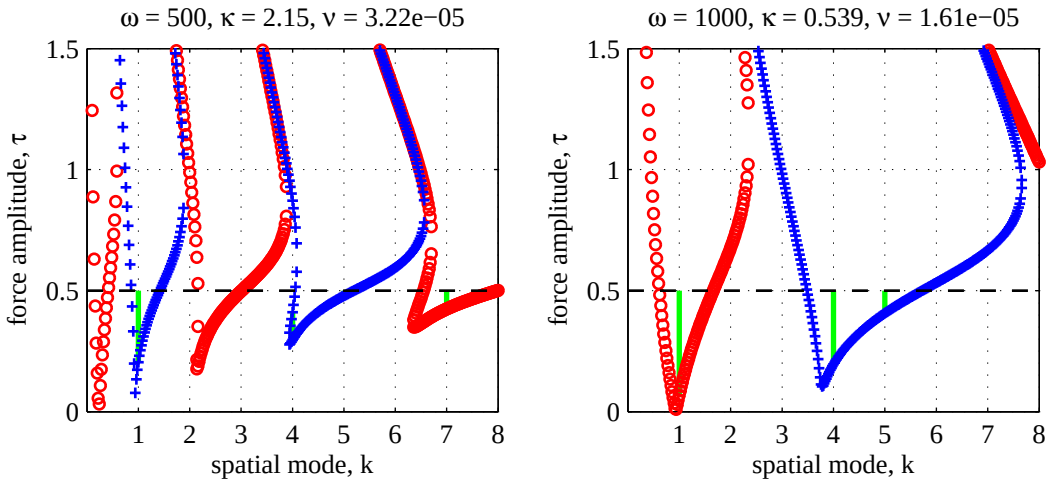

Figure 5.11: Ince-Strutt diagrams showing the eigenvalues τ (corresponding to the critical forcing amplitude) for $\alpha = 0$ plotted against spatial wavenumber when $\omega = 500$ s^{-1} (left) and $\omega = 1000$ s^{-1} (right). Harmonic and subharmonic solutions are labelled $+$ and $\circ$, respectively. The physically relevant parameters for instability are highlighted by the vertical solid green lines.

frequency ω on the horizontal axis. In each case the right-most contour or finger is the principal subharmonic mode and the subsequent fingers moving to the left alternate between harmonic and subharmonic modes. We observe that as k increases, the contours tend to widen and shift downward and to the right; consequently, it is higher frequency modes that are more susceptible to resonant instabilities. Indeed, the lowest wavenumber modes can be excited at very low values of the forcing amplitude τ provided the forcing frequency is high enough.

To verify the existence of these resonant solutions from our linear analysis in the case $\alpha = 0$, we next perform numerical simulations of the full governing IB equations (5.1), that now include nonlinearities from both the advection terms and the Dirac delta function integral terms. We use the MATLAB implementation of the IB method, `MatIB` [33]. Simulations are performed on a doubly-periodic fluid domain of size $[-L, L] \times [-L, L]$ and we use the forcing parameters $\omega = 900, 1000, 1100$ s^{-1} and $\tau = 0.1, 0.2$, with all other parameters listed in table 5.1. Although the analysis assumes an infinite domain in the vertical direction, we find that the square domain is sufficiently large to avoid significant interference from the neighbouring periodic copies of the membrane. The fluid grid is chosen to be 128×128 while the BM is discretized with 384 IB points. Figure 5.13 depicts the time evolution of the peak BM amplitude for an initial membrane displacement corresponding to a $k = 1$ cosine wave with amplitude 10^{-6} cm. For the parameter values chosen, the results exhibit a

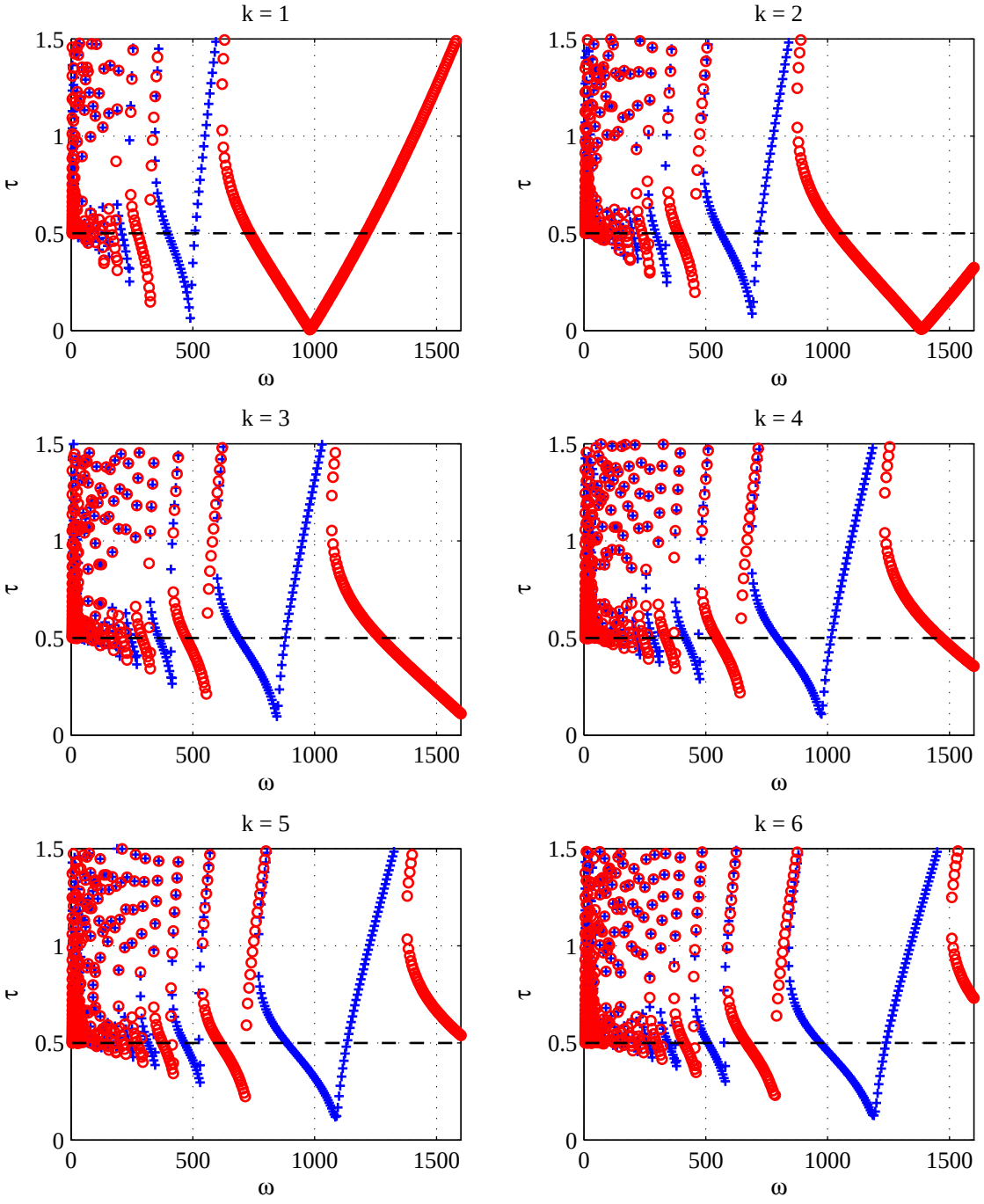

Figure 5.12: Ince-Strutt diagram showing the eigenvalues τ (corresponding to the critical forcing amplitude) for $\alpha = 0$ plotted against forcing frequency when k varies from 1 to 6. Harmonic and subharmonic solutions are labelled $+$ and $\circ$ respectively.

	$\omega = 900$ s^{-1}	$\omega = 1000$ s^{-1}	$\omega = 1100$ s^{-1}
$\tau = 0.1$	stable	unstable	stable
$\tau = 0.2$	stable	unstable	unstable

Table 5.2: Analytical stability behaviour predicted for the $k = 1$ mode and the parameters used in figure 5.13 for spatially uniform membrane stiffness $\alpha = 0$.

range of behaviour including stable (non-resonant) solutions in which the amplitude decays over time, as well as resonant solutions that experience growth in amplitude by up to two orders of magnitude for the largest values of forcing frequency ω and amplitude τ. The Ince-Strutt diagram corresponding to $k = 1$ from figure 5.12 may be used to predict the solution stability in these simulations, and the expected solution behaviour is summarized in table 5.2 for the parameter values corresponding to the simulations. Clearly, the linear analysis matches the stability behaviour observed in simulations. Most notably, for the case of amplitude $\tau = 0.1$ we capture for increasing ω how the $k = 1$ mode transitions from stable, through the marginal stability boundary into an unstable finger, and then returns again to the stable region.

5.6.2 Exponentially Varying Stiffness

We next investigate the stability of solutions in the spatially coupled case ($\alpha \neq 0$) where the BM stiffness varies exponentially along its length. The stability contours are shown as plots of τ versus ω in figure 5.14 using the same parameters listed in table 5.1. Here we present three sets of results that truncate the series solutions at different numbers of spatial modes, $M = 5$, 10 and 250 (in all cases using $N = 20$ temporal modes), and have displayed the harmonic and subharmonic mode plots separately for $M = 5$ and 10. In contrast with the $\alpha = 0$ results from the previous section where stability contours are disjoint and the behaviour of a given mode is easy to identify, we observe that contours overlap due to the coupling between spatial modes. A similar "mode-mixing" effect has been observed in another physical system: the double pendulum [52]. Furthermore, we find that the number of stability contours depends strongly on the number of spatial modes M included in the truncated series expansion; in particular, increasing M gives rise to more stability contours that tend to pack more closely together. As M gets large, the contour "finger tips" sweep out a smooth curve that divides parameter space into stable and unstable solutions as seen in the bottom plot in figure 5.14 for $M = 250$. We note that convergence in the time modes is much faster than in the spatial modes, thereby requiring that M be taken significantly larger than N in order to achieve accurate results. We note in particular that when either

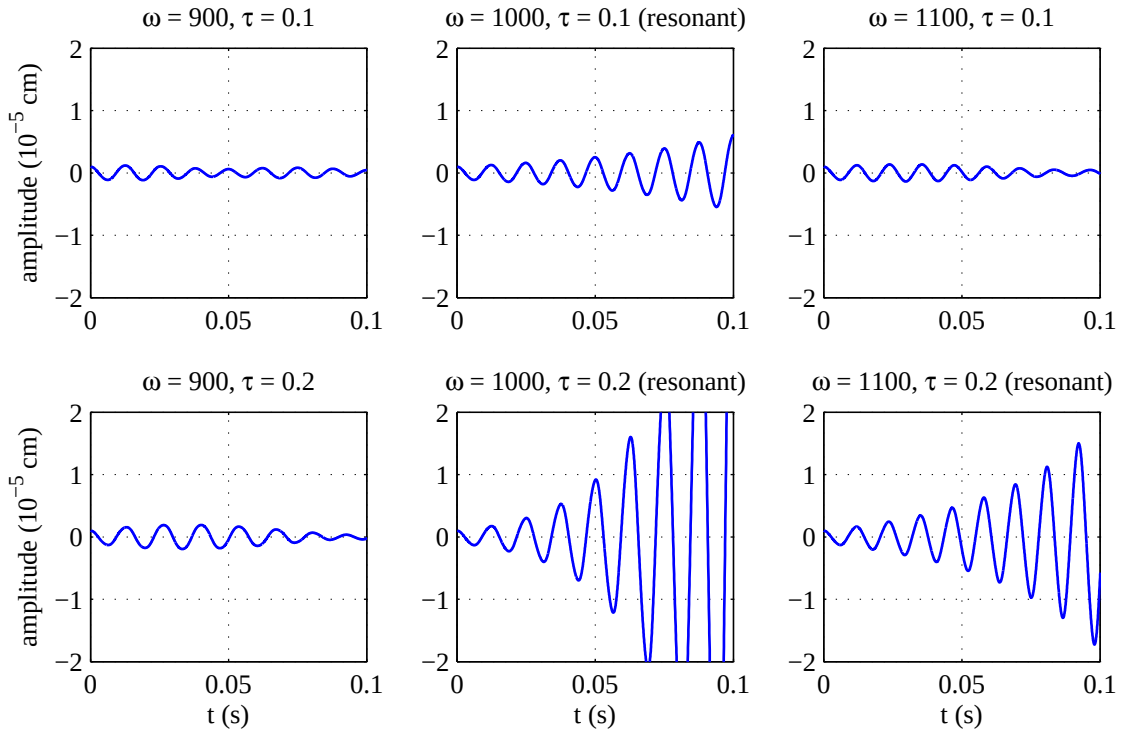

Figure 5.13: Time evolution of the IB peak amplitude when $\alpha = 0$ given an initial $k = 1$ mode cosine wave profile, for various values of parameters: ω increases from left to right, and τ increases from top to bottom.

$k > 250$ or $n > 20$, all coefficients satisfy $|h_k^n| < 10^{-4}$ and so the neglected modes have negligible effect on our computed results.

Although it is no longer possible to predict the growth or decay of a single given wavenumber mode as in the $\alpha = 0$ case, we can nevertheless still identify the region in parameter space corresponding to stable solutions. Figure 5.14 (bottom plot) shows that for each forcing frequency there is a critical value of τ_o in the interval $[0, \frac{1}{2}]$ for which a forcing amplitude $0 < \tau < \tau_o$ yields a stable solution whereas amplitudes $\tau_o < \tau < \frac{1}{2}$ lead to resonance. Again, viscosity acts as a stabilizing mechanism in the sense that increasing μ will increase τ_o and consequently increase the size of the region in parameter space where solutions are stable. Varying σ has the effect of changing the range of resonant frequencies: increasing σ causes the contours to spread out, thereby increase the range of frequencies that result in unstable solutions.

Once again, we use numerical simulations of the full IB model equations to validate the existence of resonant modes found analytically. We compute on the same domain and grid resolution as in the spatially uniform case. For the initial membrane configuration, we use the same cosine wave with amplitude 10^{-6} cm and wavenumber $k = 1$. Figures 5.15, 5.16 and 5.17 display the time variation of the amplitude for the first three Fourier cosine modes with forcing frequencies $\omega = 400, 600$ and 800 s^{-1} respectively. In each case we also choose three different values of the forcing amplitude, $\tau = 0.05$, 0.08 and 0.1. Even though the initial condition contains a pure wavenumber $k = 1$ mode, all k-modes are eventually excited because of the mode-coupling that arises through the spatially dependent stiffness. According to figure 5.14, we expect the $\tau = 0.05$ cases to be stable (since the tips of all fingers lie above this value of τ) while taking τ any larger should destabilize the solution. Indeed, numerical simulations with $\tau = 0.05$ do show that BM oscillations decay in time and that the parametric forcing is insufficient to initiate an instability. Furthermore, when τ is increased to 0.08, the solutions become unstable and sustained oscillations appear, and for the largest value of $\tau = 0.1$ the peak amplitude grows even larger. It is important to note that in all of the resonant cases simulated, the oscillation frequency is half of the internal forcing frequency, which is a common signature of parametric resonance.

Slight differences arise from the fact that our numerical simulations are on a doubly-periodic domain of finite length, whereas the analysis assumes a fluid domain of infinite extent in y. Although we have chosen the domain size to be large enough that boundary effects are kept to a minimum, there are still interactions between periodic BM copies that cannot be completely eliminated in our simulations.

We conclude by discussing the existence of parametric resonances in our cochlea model

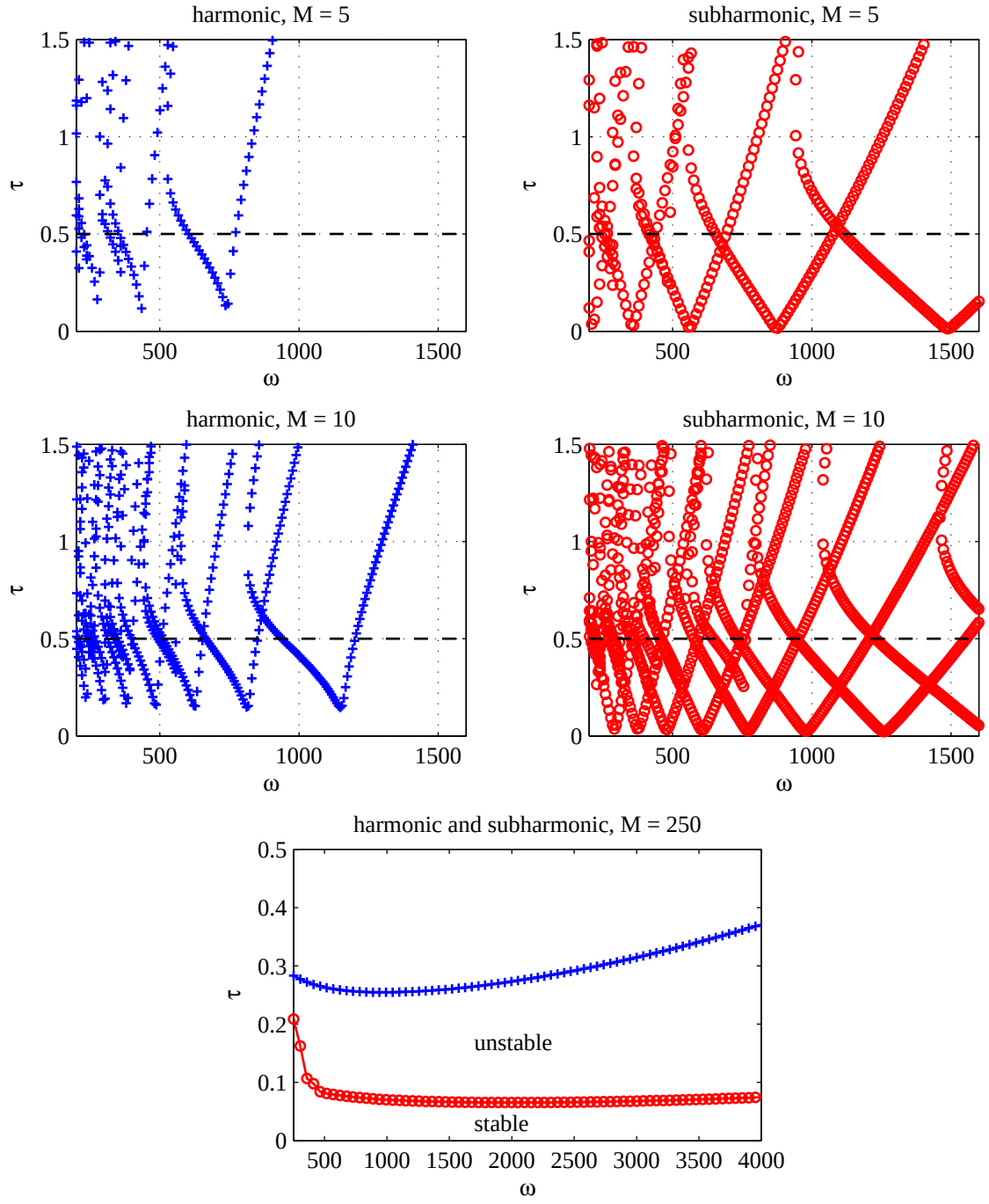

Figure 5.14: Ince-Strutt diagrams for the case $\alpha \neq 0$, depicting the convergence of the eigenvalues as the number of spatial modes M is increased from 5 (top) to 10 (middle) to 250 (bottom). The eigenvalues are separated into harmonic (left) and subharmonic (right) modes for $M = 5$ and $M = 10$. Note the change axis range for the $M = 250$ case.

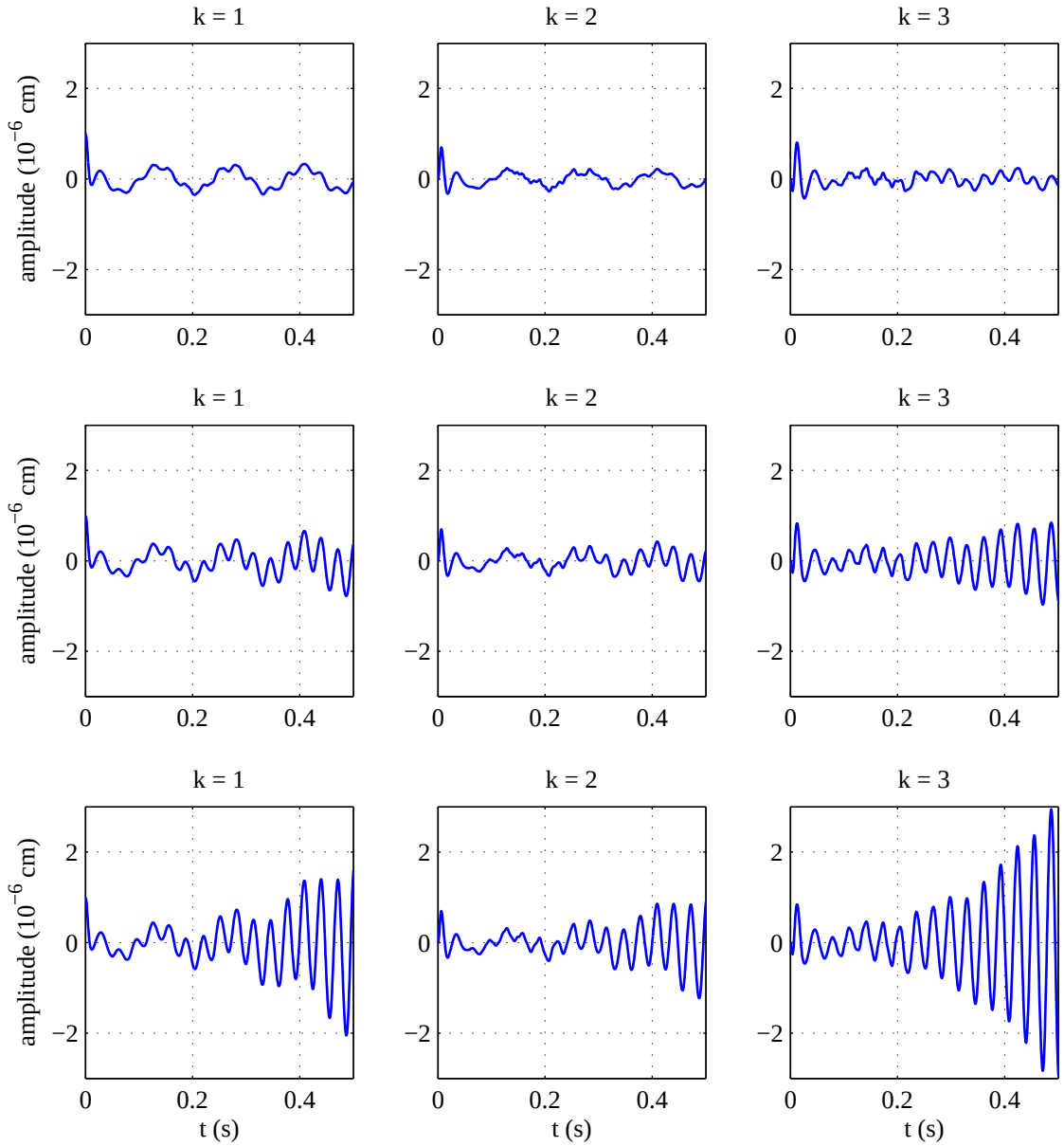

Figure 5.15: Time evolution of the amplitude of Fourier cosine coefficients from numerical simulations for internal forcing frequency $\omega = 400$ s^{-1} and stiffness forcing amplitude $\tau = 0.05, 0.08$ and 0.1 (top, middle, bottom).

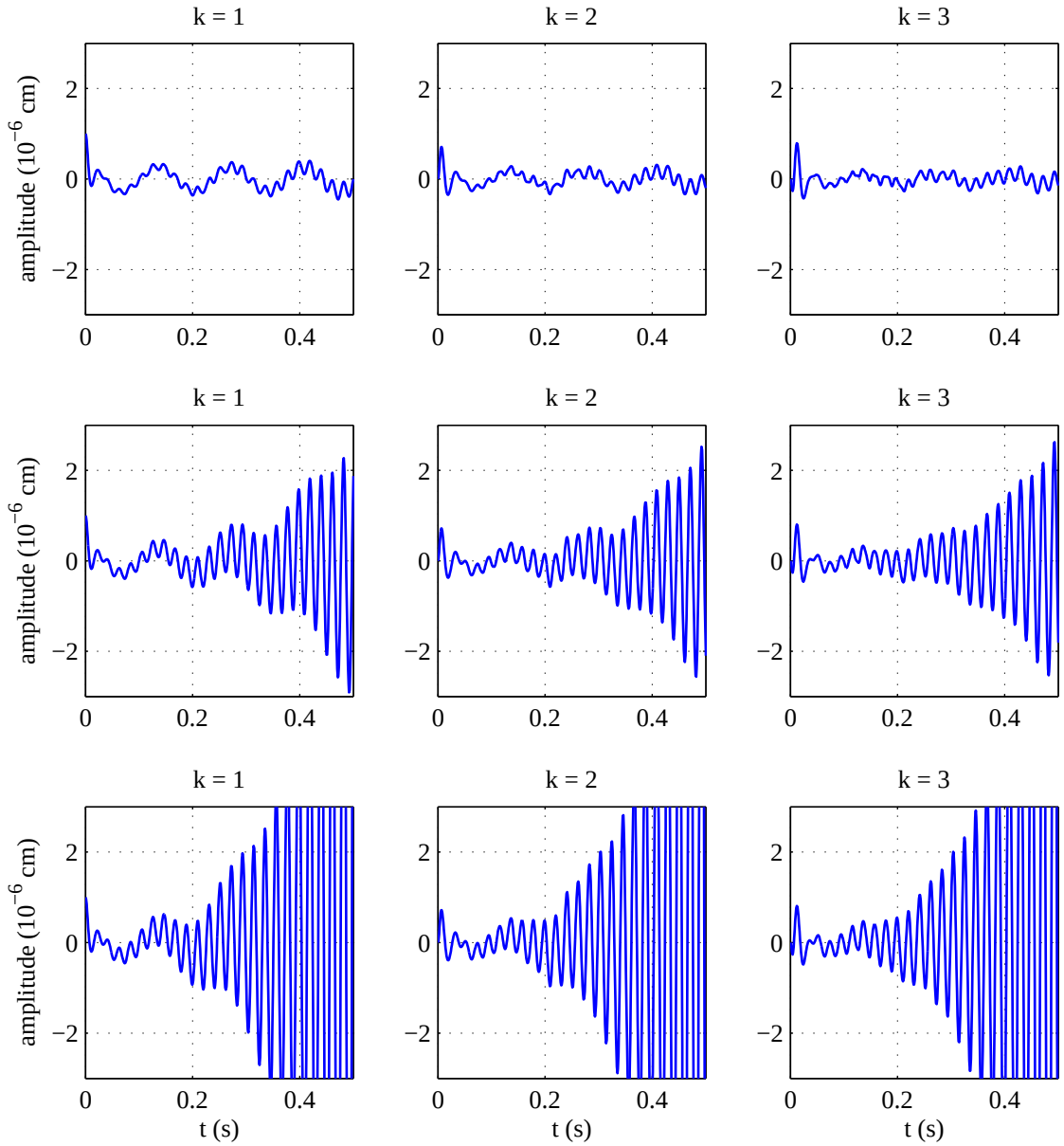

Figure 5.16: Time evolution of the amplitude of Fourier cosine coefficients from numerical simulations for internal forcing frequency $\omega = 600$ s^{-1} and stiffness forcing amplitude $\tau = 0.05, 0.08$ and 0.1 (top, middle, bottom).

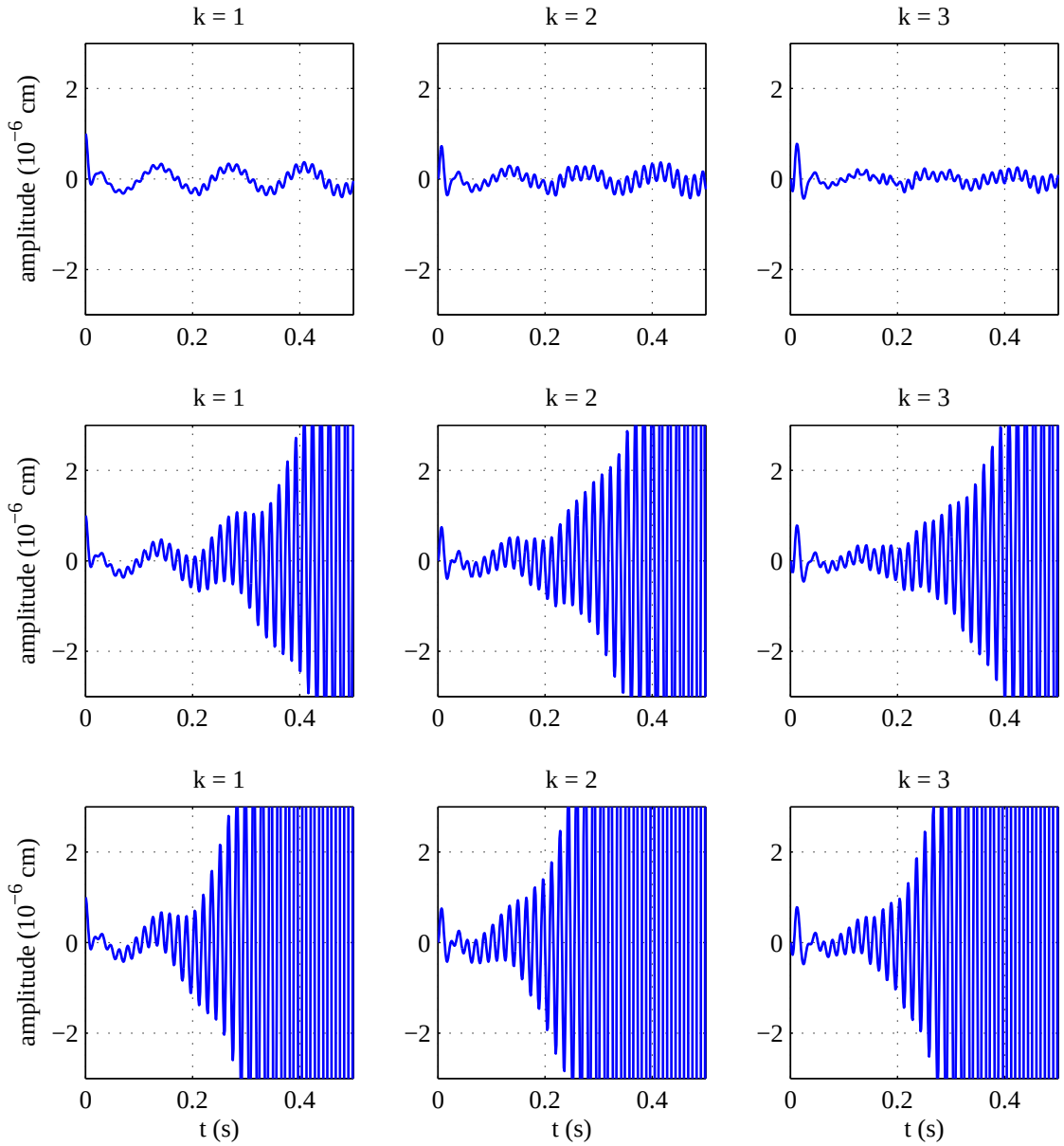

Figure 5.17: Time evolution of the amplitude of Fourier cosine coefficients from numerical simulations for internal forcing frequency $\omega = 800$ s^{-1} and stiffness forcing amplitude $\tau = 0.05, 0.08$ and 0.1 (top, middle, bottom).

for the full range of physically-relevant BM parameters (namely σ). Figure 5.18 displays the smallest τ resulting in resonance predicted by our analysis using $N = 20$, $M = 250$ for a human cochlea (top) and a gerbil cochlea (bottom). The parameters for the human cochlea are taken from table 5.1 except for the membrane stiffness. Experimental values for σ reported in the literature for human cochleas exhibit a large variation, ranging from $\sigma = 1 \times 10^7$ $\mathrm{g\,cm^{-2}\,s^{-2}}$ from [71] to as high as 2×10^9 $\mathrm{g\,cm^{-2}\,s^{-2}}$ in other two-dimensional models (see [93, Table 1], for example). We consider this entire range on the vertical axis of figure 5.18, while the horizontal axis covers the entire range of audible frequencies $\omega \in [50, 20000]$ Hz for humans. Stiffness values for the gerbil cochlea were extracted from [96, Fig. 8] where several experiments are summarized and show $\sigma \in [1.5\times10^8, 2.0\times10^9]$ $\mathrm{g\,cm^{-2}\,s^{-2}}$ (a wider range is plotted). The stiffness decay parameter for the gerbil BM is approximately $\lambda_c = 3.7$ $\mathrm{cm^{-1}}$ and the length is $L = 1.3$ cm [90]. The horizontal axis of the right plot covers the audible range for a gerbil $\omega \in [100, 50000]$ Hz. The dark (blue) region in each plot correspond to parameters where a small value of τ leads to resonance, whereas the light (green) region require larger values of τ, but still within the physically relevant range. Any regions in parameter space where the BM oscillations are not resonant are coloured white. From these plots, we observe that parametric resonance is possible ($\tau < \frac{1}{2}$) for nearly all parameter values corresponding to the human cochlea, except at the highest frequencies and the lowest values of σ. Therefore, we can conclude that parametric resonance arising from fluid-structure interaction effects is possible in our cochlea model for most sounds in the human audible range, similarly for the gerbil cochlea.

5.7 Summary and Future Work

An immersed boundary model was developed for the basilar membrane in the cochlea, for the purpose of investigating the relevance of parametric resonance as a novel mechanism for amplification of BM oscillations. Our model captures the fluid-structure interaction that occurs between the basilar membrane and the surrounding cochlear fluid. The proposed model is based on the model from [74], but includes the additional effects of internal (parametric) forcing due to variations in the elastic properties of the BM. The prime motivation for introducing such a parametric forcing derives from the work of Mammano and Ashmore [80] who have uncovered experimental evidence that oscillations of the outer hair cells embedded in the CP can lead to periodic modulation of the tension across the BM.

We demonstrated that a parametrically-forced membrane can produce travelling wave solutions that are similar to those observed in [74] for a passive BM. A Floquet stability

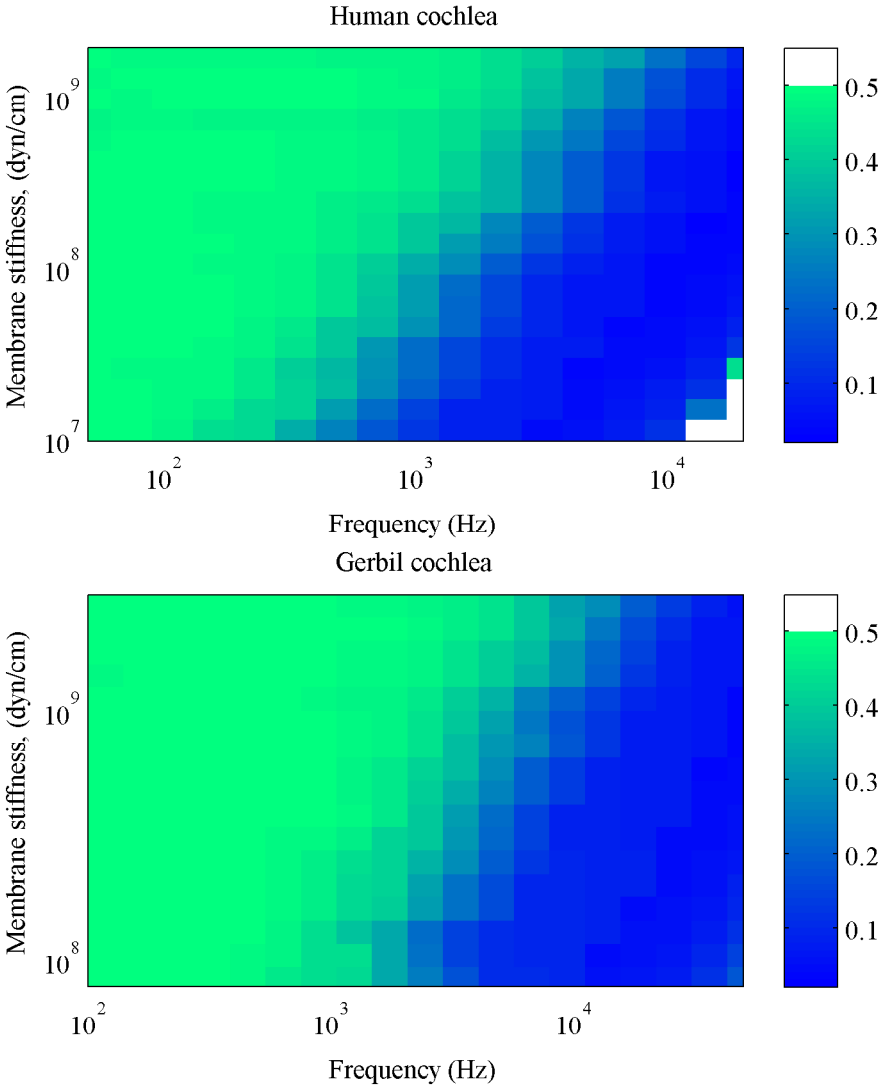

Figure 5.18: Plot of minimum τ required for parametric resonance with physically relevant parameters for the human cochlea (top) and the gerbil cochlea (bottom). The parameters for which resonance does not occur are coloured white and so only those parameters lying in the lower right corner of the diagram for the human cochlea (small stiffness, large frequency) correspond to stable or non-resonant solutions.

analysis was then used to demonstrate the existence of resonant solutions in the linearized IB equations. The results were presented as plots of the marginal stability contours in τ-ω (forcing amplitude-frequency) parameter space. For a spatially homogeneous membrane with a constant value of stiffness, the stability contours in the corresponding Ince-Strutt diagram are disjoint for each Fourier mode similar to the damped Mathieu equation. However, for the realistic case of a BM stiffness that varies exponentially along its length, there is a mode-mixing effect in which the stability contours overlap in parameter space. We conclude that internal forcing through via the BM stiffness at sufficiently large amplitudes can induce parametric instability for any frequency in the physiological range of human hearing. These existence of these resonances is verified using numerical simulations of a full two-dimensional immersed boundary model of the cochlea.

Our main conclusion is that parametric resonances arising from fluid-structure interactions in the cochlea are worthy of further study as a possible contributing factor in the amplification ability of human and other mammalian hearing systems. One focus for future research is to develop a more complete cochlea model that couples the fluid-structure interaction effects (giving rise to parametric resonance) along with an existing model for BM amplification [80, 83, 93, 107, 110], which would thereby allow a comparison of the relative importance of the combined effects. Furthermore, this will permit us to replace the BM stiffness parameter (5.3) with a more physiologically relevant (non-separable) function of the form

$$K(s,t) = \sigma e^{-\lambda_c s}\big(1 + 2\tau \sin(\omega t)\chi(s)\big)$$

in which the spatial dependence $\chi(s)$ is determined by an existing model that has been validated against experiments.

Our 2D IB model is an ideal framework to investigate other features of a cochlea. For example, we can impose more realistic Dirchlet conditions on the ends of the BM and include the helicotrema which is a small opening near the apex that joins the scala vestibuli to the scala tympani (see figure 5.3). Another extension that can be easily included in our IB framework is the RM which is a passive, spatially uniform elastic structure. The motion of the RM is often neglected in cochlear models, however there is evidence that wave motion on the RM plays a role in otoacoustic emissions [112] which merits further study of RM dynamics.

Chapter 6

Parametric Resonance in Spherical Shells

In this chapter, we extend the analysis for immersed 2D fibres from [18] to three dimensions where we consider parametric resonance in immersed spherical elastic shells. We perform a Floquet stability analysis, considering both inviscid and viscous fluids, and demonstrate that a parametrically forced fluid-structure system gives rise to resonances in which the linear solution becomes unbounded even in the presence of viscosity. The analytical results are validated using numerical simulations with a 3D immersed boundary code for a range of mode numbers and physical parameter values. Finally, a potential application to cardiac fluid dynamics is discussed.

The results in this chapter have been submitted for publication to the SIAM Journal on Applied Mathematics [63].

6.1 Immersed Boundary Model

We consider a closed elastic membrane that encompasses a region of viscous, incompressible fluid and is immersed in an infinite domain containing the same fluid ($\Omega = \mathbb{R}^3$). At equilibrium, the membrane takes the form of a pressurized sphere with radius R that is centred at the origin. Considering the geometry of the equilibrium state, it is natural to formulate the governing equations in a spherical coordinate system. We therefore introduce coordinates (r, θ, ϕ), where $r \in [0, \infty)$ is the distance from the origin, $\theta \in [0, 2\pi)$ is the azimuth angle in the horizontal plane, and $\phi \in [0, \pi]$ is the polar angle measured downward from the vertical axis. The elastic membrane, $\boldsymbol{X}(\xi, \eta, t)$, is parametrized by two Lagrangian

coordinates; $\xi \in [0, 2\pi)$ and $\eta \in [0, \pi]$, that are analogous to spherical coordinates (θ, ϕ). The IB equations are

$$\rho\left(\frac{\partial \boldsymbol{u}}{\partial t} + \boldsymbol{u}\cdot\nabla\boldsymbol{u}\right) = -\nabla p + \mu\Delta\boldsymbol{u} + \boldsymbol{f}, \tag{6.1a}$$

$$\nabla\cdot\boldsymbol{u} = 0, \tag{6.1b}$$

$$\boldsymbol{f}(\boldsymbol{x}, t) = \int_0^{\pi}\int_0^{2\pi} \boldsymbol{F}(\boldsymbol{X}, t)\,\delta(\boldsymbol{x} - \boldsymbol{X})\sin\eta\,\mathrm{d}\xi\,\mathrm{d}\eta, \tag{6.1c}$$

$$\frac{\partial \boldsymbol{X}}{\partial t} = \boldsymbol{u}(\boldsymbol{X}, t), \tag{6.1d}$$

for $\boldsymbol{x} \in \Omega$. Recall that the force density can be derived by taking a variational derivative of the membrane elastic energy functional $E(\boldsymbol{X}, t)$

$$\boldsymbol{F}(\boldsymbol{X}, t) = -\frac{\wp E}{\wp \boldsymbol{X}}.$$

As in the 2D case, we choose an energy functional that incorporates the effect of membrane stretching but ignores any resistance to bending motions. Hence, we assume the form

$$E(\boldsymbol{X}, t) = \frac{1}{2}K(t)\int_0^{\pi}\int_0^{2\pi}\left(\left\|\frac{1}{\sin\eta}\frac{\partial \boldsymbol{X}}{\partial \xi}\right\|^2 + \left\|\frac{\partial \boldsymbol{X}}{\partial \eta}\right\|^2\right)\sin\eta\,\mathrm{d}\xi\,\mathrm{d}\eta,$$

together with

$$K(t) = \sigma\big(1 + 2\tau\sin(\omega t)\big).$$

This choice of functional was motivated by Terzopoulos and Fleischer [119] who simulated deformable sheets in computer graphics. This expression for $E(\boldsymbol{X}, t)$ is also a simplified version of other energy functionals used in fluid-structure interaction problems [48]. As a result

$$\boldsymbol{F}(\boldsymbol{X}, t) = K(t)\Delta_{\mathrm{S}}\boldsymbol{X}, \tag{6.2}$$

where

$$\Delta_{\mathrm{S}} = \frac{1}{\sin^2\eta}\frac{\partial^2}{\partial \xi^2} + \frac{1}{\sin\eta}\frac{\partial}{\partial \eta}\left(\sin\eta\frac{\partial}{\partial \eta}\right)$$

denotes the spherical (or angular) Laplacian operator, which is clearly a natural generalization of (4.3) for an elastic fibre in 2D.

6.1.1 Nondimensionalization

To simplify the model and the analysis, we nondimensionalize the problem by introducing the following scalings

$$\boldsymbol{x} = R\,\widetilde{\boldsymbol{x}}, \quad \boldsymbol{X} = R\,\widetilde{\boldsymbol{X}}, \quad t = \frac{1}{\omega}\,\widetilde{t}, \quad \boldsymbol{u} = U\,\widetilde{\boldsymbol{u}}, \quad p = P\,\widetilde{p},$$

where a tilde denotes a nondimensional quantity and the characteristic velocity and pressure scales are

$$U = R\omega \qquad \text{and} \qquad P = \rho R^2\omega^2.$$

Substituting the above quantities into the governing equations (6.1)–(6.2) yields

$$\frac{\partial\widetilde{\boldsymbol{u}}}{\partial\widetilde{t}} + \widetilde{\boldsymbol{u}}\cdot\widetilde{\nabla}\widetilde{\boldsymbol{u}} = -\widetilde{\nabla}\widetilde{p} + \nu\widetilde{\Delta}\widetilde{\boldsymbol{u}} + \widetilde{\boldsymbol{f}}, \tag{6.3a}$$

$$\widetilde{\nabla}\cdot\widetilde{\boldsymbol{u}} = 0, \tag{6.3b}$$

$$\frac{\partial\widetilde{\boldsymbol{X}}}{\partial\widetilde{t}} = \widetilde{\boldsymbol{u}}(\,\widetilde{\boldsymbol{X}},\widetilde{t}\,), \tag{6.3c}$$

$$\widetilde{\boldsymbol{f}}(\,\widetilde{\boldsymbol{x}},\widetilde{t}\,) = \int_0^{\pi}\!\!\int_0^{2\pi} \widetilde{\boldsymbol{F}}(\,\widetilde{\boldsymbol{X}},\widetilde{t}\,)\,\widetilde{\delta}(\,\widetilde{\boldsymbol{x}} - \widetilde{\boldsymbol{X}}\,)\sin\eta\,\mathrm{d}\xi\,\mathrm{d}\eta, \tag{6.3d}$$

$$\widetilde{\boldsymbol{F}}(\,\widetilde{\boldsymbol{X}},\widetilde{t}\,) = \widetilde{K}(\,\widetilde{t}\,)\,\Delta_{\mathrm{S}}\widetilde{\boldsymbol{X}}, \tag{6.3e}$$

$$\widetilde{K}(\,\widetilde{t}\,) = \kappa(1 + 2\tau\sin\widetilde{t}\,), \tag{6.3f}$$

where we have introduced the dimensionless viscosity (or reciprocal Reynolds number)

$$\nu = \frac{1}{Re} = \frac{\mu}{\rho R^2\omega}, \tag{6.4}$$

and the dimensionless IB stiffness parameter

$$\kappa = \frac{\sigma}{\rho R^3\omega^2}. \tag{6.5}$$

Note that ν is the same as equation (4.5) in the 2D case but κ has an extra factor of R in the denominator of (6.5) in contrast with the 2D case in equation (4.6) due to the increase in dimension of the Dirac delta function.

6.1.2 Linearized Vector Spherical Harmonic Expansion

Consider small deformations to the spherical equilibrium configuration characterized by the parameter $|\epsilon| \ll 1$. We assume a solution in the form of a regular perturbation expansion

$$\begin{aligned}
\boldsymbol{u} &= \boldsymbol{u}_0 + \epsilon\boldsymbol{u}_1 + O(\epsilon^2),\\
p &= p_0 + \epsilon p_1 + O(\epsilon^2),\\
\boldsymbol{X} &= \boldsymbol{X}_0 + \epsilon\boldsymbol{X}_1 + O(\epsilon^2),
\end{aligned}$$

where the 0 subscript denotes the equilibrium solution

$$\boldsymbol{u}_0 = \mathbf{0}, \qquad p_0 = 2K(t)\,H(1-r) + p_a, \qquad \boldsymbol{X}_0 = \hat{\boldsymbol{r}}(\xi,\eta).$$

Here, $H(r)$ is the Heaviside step function and p_a is some constant ambient pressure. Substituting these expressions into the governing equations and retaining only those terms of $O(\epsilon)$, we obtain the following system for the first-order quantities:

$$\frac{\partial \boldsymbol{u}_1}{\partial t} = -\nabla p_1 + \nu \Delta \boldsymbol{u}_1 + \boldsymbol{f}_1, \tag{6.6a}$$

$$\nabla \cdot \boldsymbol{u}_1 = 0, \tag{6.6b}$$

$$\frac{\partial \boldsymbol{X}_1}{\partial t} = \boldsymbol{u}_1(\boldsymbol{X}_0, t). \tag{6.6c}$$

The stability of the fluid-membrane system may then be determined by studying solutions of this simpler linearized system for the $O(\epsilon)$ variables. Owing to the rotational symmetry in the problem we look for solutions in terms of spherical harmonics, which are eigenfunctions of the spherical Laplacian operator Δ_{S} and form an orthonormal basis for sufficiently smooth functions of (θ, ϕ). The normalized scalar spherical harmonic of degree m and order k is

$$Y_{m,k}(\theta,\phi) = (-1)^k \sqrt{\frac{2m+1}{4\pi}\frac{(m-k)!}{(m+k)!}}\; e^{\mathrm{i}k\theta}\, P_{m,k}(\cos\phi), \tag{6.7}$$

where $P_{m,k}$ denotes the associated Legendre polynomial [1]. The natural generalization to vector-valued functions (in our case, the fluid velocity and IB position) are the *vector spherical harmonics* (or VSH) for which various definitions have been proposed in the literature [7, 42, 45, 53]. For example, the VSH proposed by Hill [45] are eigenfunctions of the angular Laplacian and thus fully decouple the components of the vector Laplacian in the diffusion term in equation (6.6a). For this reason, Hill's VSH has proven effective in studying problems in fluid dynamics [29, 32] and other areas of physics [24, 129]. However, the VSH basis derived by Barrera et al. [7] decomposes vectors into a normal component and two tangential components to the sphere, which provides a more intuitive geometric interpretation of the basis vectors. This is a more fitting choice for our analysis since the jump conditions in the IB model naturally separate the force density into a normal component and tangential components [67]. Therefore, we use the VSH by Barrera et al. that is

defined in terms of the scalar spherical harmonics (6.7) as follows:

$$\begin{aligned}
\boldsymbol{Y}_{m,k}(\theta,\phi) &= Y_{m,k}\,\hat{\boldsymbol{r}},\\
\boldsymbol{\Psi}_{m,k}(\theta,\phi) &= r\,\nabla Y_{m,k} = \frac{\mathrm{i}k}{\sin\phi}\,Y_{m,k}\hat{\boldsymbol{\theta}} + \frac{\partial Y_{m,k}}{\partial\phi}\,\hat{\boldsymbol{\phi}},\\
\boldsymbol{\Phi}_{m,k}(\theta,\phi) &= \hat{\boldsymbol{r}}\times\boldsymbol{\Psi}_{m,k} = \frac{\partial Y_{m,k}}{\partial\phi}\,\hat{\boldsymbol{\theta}} - \frac{\mathrm{i}k}{\sin\phi}Y_{m,k}\,\hat{\boldsymbol{\phi}},
\end{aligned}$$

where $\hat{\boldsymbol{\theta}}$ and $\hat{\boldsymbol{\phi}}$ are the other two unit vectors in spherical coordinates. This choice of basis re-introduces a coupling between velocity components in the momentum equations but we will see later on that it has the advantage of decoupling the jump conditions. Finally, because we require real-valued solutions, we write the velocity, IB position and pressure variables, without loss of generality, as

$$\begin{aligned}
\boldsymbol{u}_1 &= u^r(r,t)\boldsymbol{Y}^c_{m,k} + u^\Psi(r,t)\boldsymbol{\Psi}^c_{m,k} + u^\Phi(r,t)\boldsymbol{\Phi}^c_{m,k},\\
p_1 &= \hat{p}(r,t)Y^c_{m,k},\\
\boldsymbol{X}_1 &= X^r(t)\boldsymbol{Y}^c_{m,k} + X^\Psi(t)\boldsymbol{\Psi}^c_{m,k} + X^\Phi(t)\boldsymbol{\Phi}^c_{m,k},
\end{aligned}$$

where the superscript c denotes the real (cosine) part of each spherical harmonic. We then consider a particular initial membrane configuration with the form

$$\boldsymbol{X}(\xi,\eta,0) = \big(1+\epsilon Y^c_{m,k}(\xi,\eta)\big)\hat{\boldsymbol{r}}(\xi,\eta),$$

and examine the stability of each (m,k)-mode. Several possible membrane configurations corresponding to spherical harmonics are illustrated in figure 6.1. Note that $m=0$ corresponds to a radial expansion of the membrane which is forbidden due to the incompressibility condition. Moreover, $m=1$ is a simple translation of the spherical membrane for which the system remains in equilibrium. Therefore we are only concerned with modes with $m\geq 2$ that are capable of generating nontrivial oscillations.

6.1.3 Jump Condition Formulation

We next reformulate the equations by eliminating the delta function forcing term and replacing it with suitable jump conditions across the membrane, following the approach used by Lai and Li [67].

The evolution equation (6.1d) is a statement that the membrane must move with the local fluid velocity. Because the membrane is infinitesimally thin, the velocity must be continuous across the membrane, which leads immediately to the jump conditions

$$[\![u^r]\!] = [\![u^\Psi]\!] = [\![u^\Phi]\!] = 0. \tag{6.8}$$

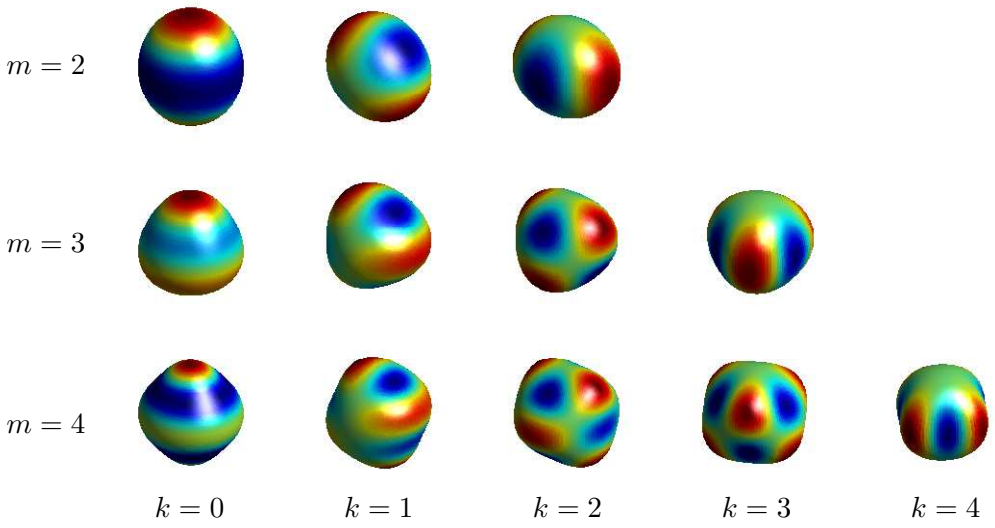

Figure 6.1: Spherical shells perturbed by a spherical harmonic mode (real part) with non-negative order k.

Next, consider the divergence condition (6.3b) which must be satisfied identically on either side of the membrane so that

$$[\![\nabla \cdot \boldsymbol{u}]\!] = 0.$$

Rewriting this condition in terms of the components of $\boldsymbol{u}_1$, we have

$$\left[\!\!\left[\frac{\partial u^r}{\partial r} + \frac{2}{r}\, u^r - \frac{m(m+1)}{r}\, u^\Psi \right]\!\!\right] = \left[\!\!\left[\frac{\partial u^r}{\partial r} \right]\!\!\right] = 0, \tag{6.9}$$

where the last equality follows from (6.8).

The remaining jump conditions are derived from the momentum equations (6.3a). Let $\Omega_\varrho(t)$ be a thin annular shell surrounding the membrane Γ with ϱ characterizing the thickness of the shell. Letting $\varphi(\boldsymbol{x})$ be a smooth test function with compact support, we multiply the momentum equations by $\varphi(\boldsymbol{x})$ and integrate over $\Omega_\varrho(t)$ to obtain

$$\int_{\Omega_\varrho(t)} \left(\frac{\partial \boldsymbol{u}}{\partial t} + \boldsymbol{u} \cdot \nabla \boldsymbol{u} \right) \varphi(\boldsymbol{x}) \,\mathrm{d}V = \int_{\Omega_\varrho(t)} \left(-\nabla p + \nu \Delta \boldsymbol{u} + \boldsymbol{f} \right) \varphi(\boldsymbol{x}) \,\mathrm{d}V. \tag{6.10}$$

Following the same procedure as in section 4.1.3, we arrive at the limits

$$\int_{\Omega_\varrho(t)} \left(\frac{\partial \boldsymbol{u}}{\partial t} + \boldsymbol{u} \cdot \nabla \boldsymbol{u} \right) \varphi(\boldsymbol{x}) \,\mathrm{d}V \quad \to \quad 0, \tag{6.11}$$

$$\int_{\Omega_\varrho(t)} -\nabla p\, \varphi(\boldsymbol{x}) \,\mathrm{d}V \quad \to \quad -\int_\Gamma [\![p]\!]\, \hat{\boldsymbol{n}}\, \varphi(\boldsymbol{x}) \,\mathrm{d}A, \tag{6.12}$$

$$\int_{\Omega_\varrho(t)} \nu \Delta \boldsymbol{u}\, \varphi(\boldsymbol{x}) \,\mathrm{d}V \quad \to \quad \int_\Gamma \nu [\![\hat{\boldsymbol{n}} \cdot \nabla \boldsymbol{u}]\!]\, \varphi(\boldsymbol{x}) \,\mathrm{d}A, \tag{6.13}$$

as $\varrho \to 0$ where

$$\hat{\boldsymbol{n}} = \frac{\frac{\partial \boldsymbol{X}}{\partial \eta} \times \frac{\partial \boldsymbol{X}}{\partial \xi}}{\left\| \frac{\partial \boldsymbol{X}}{\partial \eta} \times \frac{\partial \boldsymbol{X}}{\partial \xi} \right\|} \tag{6.14}$$

is the outward unit normal vector to the membrane surface. Furthermore, the sifting property of the Dirac delta function simplifies the forcing term in (6.10) to

$$\begin{aligned} \int_{\Omega_\varrho(t)} \boldsymbol{f} \varphi(\boldsymbol{x}) \, \mathrm{d}V &= \int_{\Omega_\varrho(t)} \left(\int_0^\pi \int_0^{2\pi} \boldsymbol{F} \delta(\boldsymbol{x} - \boldsymbol{X}) \sin\eta \, \mathrm{d}\xi \, \mathrm{d}\eta \right) \varphi(\boldsymbol{x}) \, \mathrm{d}V, \\ &= \int_0^\pi \int_0^{2\pi} \boldsymbol{F} \, \varphi(\boldsymbol{X}) \sin\eta \, \mathrm{d}\xi \, \mathrm{d}\eta. \end{aligned} \tag{6.15}$$

The limits (6.11)–(6.13) and equation (6.15) reduce the integral (6.10) to

$$0 = \int_0^\pi \int_0^{2\pi} \left(-[\![p]\!] \, \hat{\boldsymbol{n}} \left\| \frac{\partial \boldsymbol{X}}{\partial \eta} \times \frac{\partial \boldsymbol{X}}{\partial \xi} \right\| + \nu [\![\hat{\boldsymbol{n}} \cdot \nabla \boldsymbol{u}]\!] \left\| \frac{\partial \boldsymbol{X}}{\partial \eta} \times \frac{\partial \boldsymbol{X}}{\partial \xi} \right\| + \boldsymbol{F} \sin\eta \right) \varphi(\boldsymbol{X}) \, \mathrm{d}\xi \, \mathrm{d}\eta$$

as $\varrho \to 0$, where we have also made use of the identity for the area element

$$\mathrm{d}A = \left\| \frac{\partial \boldsymbol{X}}{\partial \eta} \times \frac{\partial \boldsymbol{X}}{\partial \xi} \right\| \mathrm{d}\xi \, \mathrm{d}\eta.$$

Because $\varphi(\boldsymbol{x})$ is arbitrary and smooth, the integrand must be identically zero which yields

$$0 = -[\![p]\!] \left(\frac{\partial \boldsymbol{X}}{\partial \eta} \times \frac{\partial \boldsymbol{X}}{\partial \xi} \right) + \nu \left[\!\!\left[\left(\frac{\partial \boldsymbol{X}}{\partial \eta} \times \frac{\partial \boldsymbol{X}}{\partial \xi} \right) \cdot \nabla \boldsymbol{u} \right]\!\!\right] + \boldsymbol{F} \sin\eta, \tag{6.16}$$

where the normal vector has been replaced using (6.14). Decomposing the above expression into its normal and tangential components leads to the jump conditions derived by Lai and Li [67]. However, our aim is to derive jump conditions for the VSH components so we further linearize equation (6.16).

We now make use of the perturbation expansion for $\boldsymbol{X}$ to write the terms arising from the normal vector as

$$\begin{aligned} \frac{\partial \boldsymbol{X}}{\partial \eta} \times \frac{\partial \boldsymbol{X}}{\partial \xi} &= \frac{\partial}{\partial \eta}\Big(\hat{r} + \epsilon \boldsymbol{X}_1 + O(\epsilon^2)\Big) \times \frac{\partial}{\partial \xi}\Big(\hat{r} + \epsilon \boldsymbol{X}_1 + O(\epsilon^2)\Big), \\ &= \sin\eta \, \hat{r} + \epsilon \sin\eta \Big[\Big(2X^r - m(m+1) X^\Psi \Big) \boldsymbol{Y}^c_{m,k} \\ &\qquad + \Big(X^\Psi - X^r \Big) \boldsymbol{\Psi}^c_{m,k} + X^\Phi \boldsymbol{\Phi}^c_{m,k} \Big] + O(\epsilon^2). \end{aligned}$$

Similarly, the force density can be expanded as

$$\begin{aligned} \boldsymbol{F} &= K(t) \Delta_{\mathrm{S}} \Big(\hat{r} + \epsilon \boldsymbol{X}_1 + O(\epsilon^2) \Big), \\ &= -2K(t)\hat{r} + \epsilon K(t) \Big[\Big(2m(m+1) X^\Psi - (m^2 + m + 2) X^r \Big) \boldsymbol{Y}^c_{m,k} \\ &\qquad + \Big(2X^r - m(m+1) X^\Psi \Big) \boldsymbol{\Psi}^c_{m,k} - m(m+1) X^\Phi \boldsymbol{\Phi}^c_{m,k} \Big] + O(\epsilon^2). \end{aligned}$$

The remaining jump conditions are obtained by substituting these last two equations along with the perturbation expansions for $\boldsymbol{u}$ and p into (6.16). The radial component of (6.16) gives two jump conditions for the pressure variables

$$\begin{aligned}\llbracket p_0 \rrbracket &= -2K(t),\\ \llbracket p_1 \rrbracket &= -K(t)(m-1)(m+2)X^r Y^c_{m,k},\end{aligned} \tag{6.17}$$

while the $\boldsymbol{\Psi}_{m,k}$ and $\boldsymbol{\Phi}_{m,k}$ components give jump conditions for the radial derivatives of u^Ψ and u^Φ

$$\nu\left\llbracket \frac{\partial u^\Psi}{\partial r} \right\rrbracket = K(t)(m-1)(m+2)X^\Psi, \tag{6.18}$$

$$\nu\left\llbracket \frac{\partial u^\Phi}{\partial r} \right\rrbracket = K(t)(m-1)(m+2)X^\Phi. \tag{6.19}$$

Note that the jump conditions (6.17)–(6.19) are separated into normal and tangential components, and as a result are decoupled from each other, which is the advantage to our particular choice of VSH basis that we referred to earlier in section 6.1.2.

We can now summarize the system of equations that will be analyzed in this chapter:

$$\frac{\partial u^r}{\partial t} = -\frac{\partial \hat{p}}{\partial r} + \nu\left(\frac{\partial^2 u^r}{\partial r^2} + \frac{2}{r}\frac{\partial u^r}{\partial r} - \frac{m(m+1)}{r^2}u^r - \frac{2}{r^2}\,u^r + \frac{2m(m+1)}{r^2}\,u^\Psi\right), \tag{6.20a}$$

$$\frac{\partial u^\Psi}{\partial t} = -\frac{\hat{p}}{r} + \nu\left(\frac{\partial^2 u^\Psi}{\partial r^2} + \frac{2}{r}\frac{\partial u^\Psi}{\partial r} - \frac{m(m+1)}{r^2}\,u^\Psi + \frac{2}{r^2}\,u^r\right), \tag{6.20b}$$

$$\frac{\partial u^\Phi}{\partial t} = \nu\left(\frac{\partial^2 u^\Phi}{\partial r^2} + \frac{2}{r}\frac{\partial u^\Phi}{\partial r} - \frac{m(m+1)}{r^2}\,u^\Phi\right), \tag{6.20c}$$

$$\nabla\cdot\boldsymbol{u}_1 = \left(\frac{1}{r^2}\frac{\partial}{\partial r}(r^2u^r) - \frac{m(m+1)}{r}\,u^\Psi\right)Y^c_{m,k} = 0, \tag{6.20d}$$

$$\frac{\partial \boldsymbol{X}_1}{\partial t} = \boldsymbol{u}_1|_{r=1}. \tag{6.20e}$$

The $O(\epsilon)$ quantities $\boldsymbol{X}_1$, $\boldsymbol{u}_1$ and p_1 are subject to the jump conditions (6.8), (6.9) and (6.17)–(6.19). Note that the equation for u^Φ only involved $\boldsymbol{\Phi}_{m,k}$ quantities which is another advantage of our choice of VSH basis. We also observe that the dynamics of the linearized solution depend only on the degree m of the spherical harmonic and not on its order k; hence solution modes are characterized by a single integer m.

In the remainder of this chapter, we will drop the subscript "1" that until now has distinguished the $O(\epsilon)$ quantities.

6.2 Floquet Analysis for an Inviscid Fluid

To afford some insight into parametric instabilities occurring in a simpler version of the immersed membrane problem, we first consider an inviscid fluid for which the governing equations reduce to

$$\frac{\partial u^r}{\partial t} = -\frac{\partial \hat{p}}{\partial r}, \tag{6.21a}$$

$$\frac{\partial u^\Psi}{\partial t} = -\frac{\hat{p}}{r}, \tag{6.21b}$$

$$\frac{\partial u^\Phi}{\partial t} = 0, \tag{6.21c}$$

$$\nabla \cdot \boldsymbol{u} = 0, \tag{6.21d}$$

$$\frac{\mathrm{d}X^r}{\mathrm{d}t} = u^r(1,t), \tag{6.21e}$$

$$[\![u^r]\!] = 0, \tag{6.21f}$$

$$[\![\hat{p}]\!] = -K(t)(m-1)(m+2)X^r. \tag{6.21g}$$

Notice that in the absence of viscosity, we are only permitted to impose the zero normal flow condition (6.21e) at the fluid-membrane interface instead of the usual no-slip condition.

We begin by solving for the pressure away from the membrane, which satisfies

$$r^2\frac{\partial^2 \hat{p}}{\partial r^2} + 2r\frac{\partial \hat{p}}{\partial r} - m(m+1)\hat{p} = 0. \tag{6.22}$$

Imposing the requirement that the pressure be bounded at $r = 0$ and as $r \to \infty$ yields

$$\hat{p}(r,t) = \begin{cases} a(t)\, r^m, & \text{if } r < 1, \\ b(t)\, r^{-m-1}, & \text{if } r > 1, \end{cases}$$

where $a(t)$ and $b(t)$ are as-yet undetermined functions of time. Substituting the pressure solution into the inviscid momentum equation (6.21a) yields the radial fluid acceleration

$$\frac{\partial u^r}{\partial t} = \begin{cases} -ma(t)\, r^{m-1}, & \text{if } r < 1, \\ (m+1)b(t)\, r^{-m-2}, & \text{if } r > 1. \end{cases}$$

Since the fluid cannot pass through the membrane, the radial acceleration of the fluid and membrane must match and

$$\frac{\mathrm{d}^2 X^r}{\mathrm{d}t^2} = \left.\frac{\partial u^r}{\partial t}\right|_{r=1} = -ma(t) = (m+1)b(t),$$

where the last equality follows from continuity of u^r at the interface. This allows us to determine the functions

$$a(t) = -\frac{1}{m}\frac{\mathrm{d}^2 X^r}{\mathrm{d}t^2} \qquad \text{and} \qquad b(t) = \frac{1}{m+1}\frac{\mathrm{d}^2 X^r}{\mathrm{d}t^2},$$

after which the pressure jump (6.21g) may be expressed as

$$b(t) - a(t) = -K(t)(m-1)(m+2)X^r(t).$$

We then have the following equation for the membrane location

$$\frac{\mathrm{d}^2 X^r}{\mathrm{d}t^2} + \lambda_0^2(1 + 2\tau \sin t)X^r = 0, \tag{6.23}$$

where

$$\lambda_0^2 = \frac{\kappa m(m+1)(m-1)(m+2)}{2m+1}.$$

Here, λ_0 is the dimensionless natural oscillation frequency. Recalling the definition of κ in (6.5), we may write $\lambda_0 = \omega_0/\omega$ as the ratio of the natural frequency ω_0 for the unforced problem to the forcing frequency ω, where

$$\omega_0^2 = \frac{\sigma m(m+1)(m-1)(m+2)}{\rho R^3(2m+1)}. \tag{6.24}$$

This natural oscillation frequency matches with the classical result by Lamb [69, Art. 253] for oscillations of a spherical liquid drop, with the only difference being that a surface tension force replaces the elastic restoring force in our IB context.

We now focus on (6.23) which takes the form of the Mathieu equation which we know from Chapter 2 exhibits parametric resonance. Figure 6.2 shows the Ince-Strutt diagrams as plots of κ versus τ for three different spherical harmonics, $m = 2$, 3 and 4. In each plot, the eigenvalues τ divide parameter space into stable and unstable regions as for the Mathieu equation. It is essential to keep in mind that only parameters lying below the horizontal line $\tau = \frac{1}{2}$ are physically relevant, since these values of τ correspond to a membrane stiffness $K(t)$ that remains positive. It is evident from these diagrams that for a given forcing amplitude τ, an immersed spherical shell can experience parametric instability for a disjoint set of κ ranges (with corresponding ranges of the physical parameters ω, ρ, R and σ according to (6.5)). For example, different unstable modes (corresponding to different integer values of m) can be excited by forcing the system within a given range of ω. Furthermore, there is an infinite number of unstable modes that can be excited since the harmonic and subharmonic fingers continue to alternate to the right forever as κ increases.

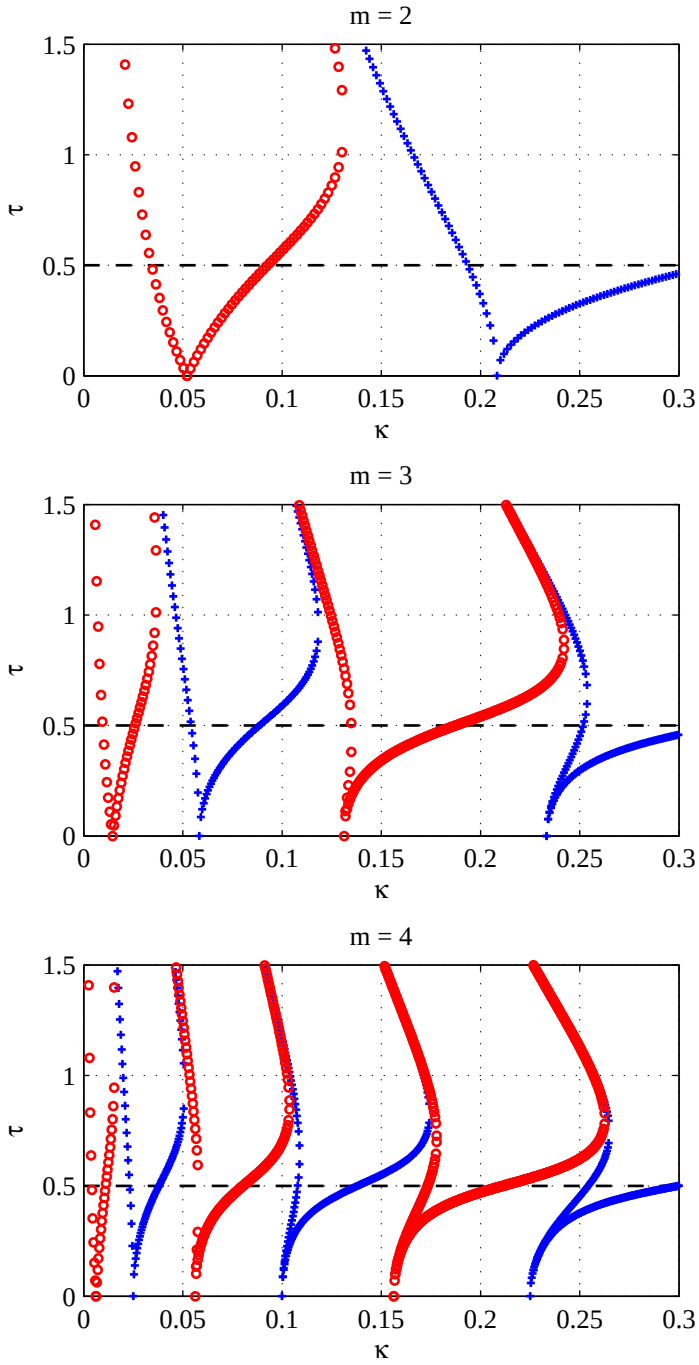

Figure 6.2: Ince-Strutt diagrams for the inviscid problem, showing stability contours for spherical harmonics $m = 2$ (top), 3 (middle) and 4 (bottom). Harmonic modes are denoted with $+$ and subharmonic modes with $\circ$, and only modes with $\tau < \frac{1}{2}$ are physically relevant.

These membrane instabilities exist for all values of forcing amplitude $0 < \tau < \frac{1}{2}$ since each of the stability fingers extends downward and touches the κ-axis as $\tau \to 0$. The points at which the fingers touch the κ-axis correspond to the natural oscillation frequencies ω_0 for the unforced problem given in (6.24). Indeed, we see that for $|\tau| \ll 1$, resonances occur at forcing frequencies that satisfy

$$\omega_0 \approx \frac{\ell\omega}{2}$$

for any positive integer ℓ; that is, the natural frequency for a given m-mode is an integer multiple of half the parametric forcing frequency.

6.3 Floquet Analysis for a Viscous Fluid

We next apply Floquet theory to the original governing equations with viscosity by looking for series solutions of the form

$$\boldsymbol{u}(r,\theta,\phi,t) = e^{\gamma t} \sum_{n=-\infty}^{\infty} e^{\mathrm{i}nt} \left(u_n^r(r)\boldsymbol{Y}_{m,k}^c + u_n^\Psi(r)\boldsymbol{\Psi}_{m,k}^c + u_n^\Phi(r)\boldsymbol{\Phi}_{m,k}^c \right), \tag{6.25a}$$

$$p(r,\theta,\phi,t) = e^{\gamma t} \sum_{n=-\infty}^{\infty} e^{\mathrm{i}nt} p_n(r) Y_{m,k}^c, \tag{6.25b}$$

$$\boldsymbol{X}(\xi,\eta,t) = e^{\gamma t} \sum_{n=-\infty}^{\infty} e^{\mathrm{i}nt} \left(X_n^r\boldsymbol{Y}_{m,k}^c + X_n^\Psi\boldsymbol{\Psi}_{m,k}^c + X_n^\Phi\boldsymbol{\Phi}_{m,k}^c \right). \tag{6.25c}$$

The pressure coefficients $p_n(r)$ satisfy the same ODE (6.22) and boundedness conditions as in the inviscid case, and so the solution has the same form

$$p_n(r) = \begin{cases} a_n r^m, & \text{if } r < 1, \\ b_n r^{-m-1}, & \text{if } r > 1, \end{cases}$$

with the only difference being that a_n and b_n are constants. Next, combining the radial momentum equation (6.20a) with the divergence-free condition (6.20d) and then substituting the Floquet-Fourier series (6.25a) and (6.25b) yields the ODE

$$r^2 \frac{\mathrm{d}^2 u_n^r}{\mathrm{d}r^2} + 4r\frac{\mathrm{d}u_n^r}{\mathrm{d}r} + \left(2 - m(m+1) - \beta_n^2 r^2\right) u_n^r - \frac{r^2}{\nu}\frac{\mathrm{d}p_n}{\mathrm{d}r} = 0,$$

where

$$\beta_n = \sqrt{\frac{\gamma + \mathrm{i}n}{\nu}} \qquad \text{with} \qquad \Re\{\beta_n\} > 0.$$

We first consider the situation where the quantity $\beta_n \neq 0$, in which case the radial velocity components can be expressed as

$$u_n^r(r) = \int_0^\infty G(r,z)\,\frac{z^2}{\nu}\frac{\mathrm{d}p_n(z)}{\mathrm{d}z}\,\mathrm{d}z, \tag{6.26}$$

where $G(r,z)$ is the Green's function satisfying

$$r^2\frac{\partial^2 G}{\partial r^2} + 4r\frac{\partial G}{\partial r} + \Big(2 - m(m+1) - \beta_n^2 r^2\Big)\,G = \delta(r-z)$$

along with the two jump conditions

$$G|_{r=z^-}^{r=z^+} = 0 \qquad \text{and} \qquad r^2\frac{\partial G}{\partial r}\bigg|_{r=z^-}^{r=z^+} = 1.$$

The Green's function can be obtained explicitly as

$$G(r,z) = \begin{cases} z\beta_n h_m(\mathrm{i}\beta_n z)\,\dfrac{j_m(\mathrm{i}\beta_n r)}{r}, & \text{if } r < z, \\[2ex] z\beta_n j_m(\mathrm{i}\beta_n z)\,\dfrac{h_m(\mathrm{i}\beta_n r)}{r}, & \text{if } r > z, \end{cases}$$

where j_m and h_m denote the mth-order spherical Bessel and Hankel functions of the first kind, respectively. The expression in (6.26) can be integrated explicitly to obtain the radial velocity as

$$u_n^r(r) = \begin{cases} -\dfrac{\mathrm{i}j_m(\mathrm{i}\beta_n r)}{\nu r}\Big(ma_n h_{m+1}(\mathrm{i}\beta_n) - (m+1)b_n h_{m-1}(\mathrm{i}\beta_n)\Big) \\ \qquad\qquad - \dfrac{ma_n}{\nu\beta_n^2}r^{m-1}, & \text{if } r < 1, \\[2ex] -\dfrac{\mathrm{i}h_m(\mathrm{i}\beta_n r)}{\nu r}\Big(ma_n j_{m+1}(\mathrm{i}\beta_n) - (m+1)b_n j_{m-1}(\mathrm{i}\beta_n)\Big) \\ \qquad\qquad + \dfrac{(m+1)b_n}{\nu\beta_n^2}r^{-m-2}, & \text{if } r > 1. \end{cases}$$

It is then straightforward to show that radial velocity coefficients are continuous across the membrane and satisfy

$$u_n^r(1^+) = u_n^r(1^-) = -\frac{\mathrm{i}ma_n}{\nu}\,h_m(\mathrm{i}\beta_n)j_{m+1}(\mathrm{i}\beta_n) + \frac{\mathrm{i}(m+1)b_n}{\nu}\,j_m(\mathrm{i}\beta_n)h_{m-1}(\mathrm{i}\beta_n).$$

The coefficient u_n^Ψ can be obtained from the incompressibility condition

$$\left(\frac{1}{r^2}\frac{\mathrm{d}}{\mathrm{d}r}(r^2 u_n^r) - \frac{m(m+1)}{r}u_n^\Psi\right)Y_{m,k}^c = 0,$$

so that

$$
\begin{aligned}
u_n^{\Psi}(r) &= \frac{1}{rm(m+1)}\frac{\mathrm{d}}{\mathrm{d}r}(r^2 u_n^r), \\
&= \begin{cases}
-\dfrac{\mathrm{i}}{\nu}\left(\dfrac{j_m(\mathrm{i}\beta_n r)}{r} + \mathrm{i}\beta_n j_m'(\mathrm{i}\beta_n r)\right)\left(\dfrac{a_n}{m+1}\,h_{m+1}(\mathrm{i}\beta_n) - \dfrac{b_n}{m}\,h_{m-1}(\mathrm{i}\beta_n)\right) \\
\qquad\qquad - \dfrac{a_n}{\nu\beta_n^2}\,r^{m-1}, & \text{if } r<1, \\
-\dfrac{\mathrm{i}}{\nu}\left(\dfrac{h_m(\mathrm{i}\beta_n r)}{r} + \mathrm{i}\beta_n h_m'(\mathrm{i}\beta_n r)\right)\left(\dfrac{a_n}{m+1}\,j_{m+1}(\mathrm{i}\beta_n) - \dfrac{b_n}{m}\,j_{m-1}(\mathrm{i}\beta_n)\right) \\
\qquad\qquad - \dfrac{b_n}{\nu\beta_n^2}\,r^{-m-2}, & \text{if } r>1.
\end{cases}
\end{aligned}
$$

Here, primes denote derivatives with respect to the argument. The analogous equation for the third velocity coefficient $u_n^{\Phi}(r)$ is

$$
r^2\frac{\mathrm{d}^2 u_n^{\Phi}}{\mathrm{d}r^2} + 2r\frac{\mathrm{d}u_n^{\Phi}}{\mathrm{d}r} - (\beta_n^2 r^2 + m(m+1))u_n^{\Phi} = 0,
$$

which can be solved to obtain

$$
u_n^{\Phi}(r) = \begin{cases}
c_n j_m(\mathrm{i}\beta_n r), & \text{if } r<1, \\
c_n\dfrac{j_m(\mathrm{i}\beta_n)}{h_m(\mathrm{i}\beta_n)}\,h_m(\mathrm{i}\beta_n r), & \text{if } r>1,
\end{cases}
$$

where c_n are arbitrary constants.

The next major step is to determine values of the constants a_n, b_n and c_n by imposing the interface conditions (6.20e). By orthogonality, the radial coefficients for the membrane position satisfy

$$
\begin{aligned}
(\gamma + \mathrm{i}n)X_n^r &= u_n^r(1), \\
&= -\frac{\mathrm{i}ma_n}{\nu}\,h_m(\mathrm{i}\beta_n)j_{m+1}(\mathrm{i}\beta_n) + \frac{\mathrm{i}(m+1)b_n}{\nu}\,j_m(\mathrm{i}\beta_n)h_{m-1}(\mathrm{i}\beta_n),
\end{aligned}
$$

with similar expressions holding for the other two sets of coefficients

$$
\begin{aligned}
(\gamma + \mathrm{i}n)X_n^{\Psi} &= -\frac{\mathrm{i}a_n}{(m+1)\nu}\Big(h_m(\mathrm{i}\beta_n) + \mathrm{i}\beta_n h_m'(\mathrm{i}\beta_n)\Big)j_{m+1}(\mathrm{i}\beta_n) \\
&\qquad + \frac{\mathrm{i}b_n}{m\nu}\Big(j_m(\mathrm{i}\beta_n) + \mathrm{i}\beta_n h_m'(\mathrm{i}\beta_n)\Big)h_{m-1}(\mathrm{i}\beta_n), \\
(\gamma + \mathrm{i}n)X_n^{\Phi} &= c_n j_m(\mathrm{i}\beta_n).
\end{aligned}
$$

These three equations may then be solved to obtain

$$a_n = -\frac{\mathrm{i}\nu^2\beta_n^3}{m}\,\frac{j_m(\mathrm{i}\beta_n)+\mathrm{i}\beta_n j_m'(\mathrm{i}\beta_n)}{j_{m+1}(\mathrm{i}\beta_n)}\,X_n^r + \mathrm{i}\nu^2\beta_n^3(m+1)\,\frac{j_m(\mathrm{i}\beta_n)}{j_{m+1}(\mathrm{i}\beta_n)}\,X_n^\Psi, \tag{6.27a}$$

$$b_n = -\frac{\mathrm{i}\nu^2\beta_n^3}{m+1}\,\frac{h_m(\mathrm{i}\beta_n)+\mathrm{i}\beta_n\, h_m'(\mathrm{i}\beta_n)}{h_{m-1}(\mathrm{i}\beta_n)}\,X_n^r + \mathrm{i}\nu^2\beta_n^3 m\,\frac{h_m(\mathrm{i}\beta_n)}{h_{m-1}(\mathrm{i}\beta_n)}\,X_n^\Psi, \tag{6.27b}$$

$$c_n = \frac{\nu\beta_n^2}{j_m(\mathrm{i}\beta_n)}\,X_n^\Phi. \tag{6.27c}$$

We are now prepared to impose the jump conditions (6.18) and (6.19), which yield

$$\nu\left(-\frac{a_n}{m+1}-\frac{b_n}{m}\right) = \kappa(m-1)(m+2)(X_n^\Psi - \mathrm{i}\tau X_{n-1}^\Psi + \mathrm{i}\tau X_{n+1}^\Psi),$$

$$\nu\left(\mathrm{i}\beta_n\frac{j_m(\mathrm{i}\beta_n)}{h_m(\mathrm{i}\beta_n)}h_m'(\mathrm{i}\beta_n) - \mathrm{i}\beta_n j_m'(\mathrm{i}\beta_n)\right)c_n = \kappa(m-1)(m+2)(X_n^\Phi - \mathrm{i}\tau X_{n-1}^\Phi + \mathrm{i}\tau X_{n+1}^\Phi).$$

After replacing a_n, b_n and c_n in these last two expressions with (6.27), we obtain the following linear system of equations relating the coefficients X_n^r, X_n^Ψ and X_n^Φ:

$$\begin{aligned}\frac{\beta_n^3}{(m-1)(m+2)}\frac{\nu^2}{\kappa}\left(\frac{h_m(\mathrm{i}\beta_n)}{(m+1)h_{m-1}(\mathrm{i}\beta_n)} - \frac{j_m(\mathrm{i}\beta_n)}{m j_{m+1}(\mathrm{i}\beta_n)}\right)X_n^r \\ + \left[\frac{\beta_n^3}{(m-1)(m+2)}\frac{\nu^2}{\kappa}\left(\frac{h_m(\mathrm{i}\beta_n)}{h_{m-1}(\mathrm{i}\beta_n)} + \frac{j_m(\mathrm{i}\beta_n)}{j_{m+1}(\mathrm{i}\beta_n)}\right) - \mathrm{i}\right]X_n^\Psi \\ = \tau(X_{n-1}^\Psi - X_{n+1}^\Psi),\end{aligned} \tag{6.28}$$

$$\left[\frac{\mathrm{i}\beta_n}{(m-1)(m+2)j_m(\mathrm{i}\beta_n)h_m(\mathrm{i}\beta_n)}\frac{\nu^2}{\kappa} - \mathrm{i}\right]X_n^\Phi = \tau(X_{n-1}^\Phi - X_{n+1}^\Phi). \tag{6.29}$$

In a similar manner, the final jump condition for the pressure (6.17) yields

$$\begin{aligned}\left[-\frac{\mathrm{i}\beta_n^4}{(2m+1)(m-1)(m+2)}\frac{\nu^2}{\kappa}\left(2 - \frac{m}{m+1}\frac{h_{m+1}(\mathrm{i}\beta_n)}{h_{m-1}(\mathrm{i}\beta_n)} - \frac{m+1}{m}\frac{j_{m-1}(\mathrm{i}\beta_n)}{j_{m+1}(\mathrm{i}\beta_n)}\right) - \mathrm{i}\right]X_n^r \\ - \frac{\mathrm{i}\beta_n^4}{(2m+1)(m-1)(m+2)}\frac{\nu^2}{\kappa}\left(1 - m\frac{h_{m+1}(\mathrm{i}\beta_n)}{h_{m-1}(\mathrm{i}\beta_n)} + (m+1)\frac{j_{m-1}(\mathrm{i}\beta_n)}{j_{m+1}(\mathrm{i}\beta_n)}\right)X_n^\Psi \\ = \tau\left(X_{n-1}^r - X_{n+1}^r\right).\end{aligned} \tag{6.30}$$

When taken together, equations (6.28)–(6.30) represent a system for X_n^r, X_n^Ψ and X_n^Φ in the case when $\beta_n \neq 0$.

We now consider the special case $\beta_n = 0$, which occurs only when $n = 0$ and $\gamma = 0$ (i.e., for harmonic modes) and the equation for radial velocity reduces to

$$r^2\frac{\mathrm{d}^2u_0^r}{\mathrm{d}r^2} + 4r\frac{\mathrm{d}u_0^r}{\mathrm{d}r} + \big(2 - m(m+1)\big)u_0^r - r^2\frac{\mathrm{d}p_0}{\mathrm{d}r}\nu = 0.$$

The corresponding Green's function is

$$G(r,z) = -\frac{1}{2m+1}\begin{cases} \dfrac{r^{m-1}}{z^m}, & \text{if } r < z, \\ \dfrac{z^{m+1}}{r^{m+2}}, & \text{if } r > z, \end{cases}$$

from which we obtain

$$u_0^r(r) = \begin{cases} \dfrac{ma_0}{\nu(2m+3)} r^{m+1} \\ \qquad - \dfrac{1}{\nu(2m+1)}\left(\dfrac{ma_0}{2} - \dfrac{(m+1)b_0}{2m-1}\right) r^{m-1}, & \text{if } r < 1, \\ \dfrac{(m+1)b_0}{\nu(2m-1)} r^{-m} \\ \qquad - \dfrac{1}{\nu(2m+1)}\left(\dfrac{ma_0}{2m+3} + \dfrac{(m+1)b_0}{2}\right) r^{-m-2}, & \text{if } r > 1. \end{cases}$$

Applying the incompressibility condition as before, we find that

$$u_0^\Psi(r) = \begin{cases} \dfrac{(m+3)a_0}{\nu(2m+3)(m+1)}\, r^{m+1} \\ \qquad - \dfrac{1}{\nu m(2m+1)}\left(\dfrac{ma_0}{2} - \dfrac{(m+1)b_0}{2m-1}\right) r^{m-1}, & \text{if } r < 1, \\ -\dfrac{(m-1)b_0}{\nu m(2m-1)}\, r^{-m} \\ \qquad + \dfrac{1}{\nu(m+1)(2m+1)}\left(\dfrac{ma_0}{2m+3} + \dfrac{(m+1)b_0}{2}\right) r^{-m-2}, & \text{if } r > 1. \end{cases}$$

To ensure continuity across the membrane, we must have $a_0 = b_0 = 0$. The remaining velocity coefficients are given simply by

$$u_0^\Phi(r) = \begin{cases} c_0\, r^m, & \text{if } r < 1, \\ c_0\, r^{-m-1}, & \text{if } r > 1. \end{cases}$$

From the membrane evolution equation (6.20e), we find that $c_0 = 0$. Therefore, in the special case $\beta_n = 0$, the jump conditions (6.17)–(6.19) reduce to

$$X_n^r - \mathrm{i}\tau X_{n-1}^r + \mathrm{i}\tau X_{n+1}^r = 0, \tag{6.31}$$

$$X_n^\Psi - \mathrm{i}\tau X_{n-1}^\Psi + \mathrm{i}\tau X_{n+1}^\Psi = 0, \tag{6.32}$$

$$X_n^\Phi - \mathrm{i}\tau X_{n-1}^\Phi + \mathrm{i}\tau X_{n+1}^\Phi = 0. \tag{6.33}$$

To investigate the stability of a parametrically-forced elastic shell, we now need only consider the $\boldsymbol{Y}_{m,k}$ and $\boldsymbol{\Psi}_{m,k}$ solution components. This is because the $\boldsymbol{\Phi}_{m,k}$ component is

completely decoupled in the momentum equations and neither is it driven by a pressure gradient, so that it evolves independently. In particular, if the $\mathbf{\Phi}_{m,k}$ component of the initial membrane position is zero, then it will remain zero for all time (this is closely related to the fact that the linear equations (6.29) and (6.33) for X_n^Φ are decoupled from the other equations). As a result, it is only necessary to consider equations (6.28), (6.30), (6.31) and (6.32), which can be written as

$$A_n X_n^r + B_n X_n^\Psi = \tau(X_{n-1}^r - X_{n+1}^r), \tag{6.34a}$$
$$C_n X_n^r + D_n X_n^\Psi = \tau(X_{n-1}^\Psi - X_{n+1}^\Psi), \tag{6.34b}$$

for suitably defined constants A_n, B_n, C_n and D_n. We again impose reality conditions for either harmonic solutions ($\gamma = 0$)

$$X_{-n}^r = \overline{X}_n^r,$$
$$X_{-n}^\Psi = \overline{X}_n^\Psi,$$

or subharmonic solutions ($\gamma = \frac{1}{2}\mathrm{i}$)

$$X_{-n}^r = \overline{X}_{n-1}^r,$$
$$X_{-n}^\Psi = \overline{X}_{n-1}^\Psi.$$

We only need to consider nonnegative integer values of $n = 0, 1, \ldots, N$, so that system (6.34) take the form of a generalized eigenvalue problem $\mathbf{A}\boldsymbol{v} = \tau\mathbf{B}\boldsymbol{v}$, where the solution vector

$$\boldsymbol{v} = \begin{bmatrix} \vdots \\ \Re\{X_n^r\} \\ \Im\{X_n^r\} \\ \Re\{X_n^\Psi\} \\ \Im\{X_n^\Psi\} \\ \vdots \end{bmatrix}$$

is of length $4(N+1)$. The matrix $\mathbf{A} = \mathrm{diag}(\mathbf{A_0}, \mathbf{A_1}, \ldots, \mathbf{A_N})$ is block diagonal consisting of 4×4 blocks

$$\mathbf{A}_n = \begin{bmatrix} \Re\{A_n\} & -\Im\{A_n\} & \Re\{B_n\} & -\Im\{A_n\} \\ \Im\{A_n\} & \Re\{A_n\} & \Im\{B_n\} & \Re\{B_n\} \\ \Re\{C_n\} & -\Im\{C_n\} & \Re\{D_n\} & -\Im\{D_n\} \\ \Im\{C_n\} & \Re\{C_n\} & \Im\{D_n\} & \Re\{D_n\} \end{bmatrix},$$

and $\mathbf{B}$ is a block tridiagonal matrix of the form

$$\mathbf{B} = \begin{bmatrix} \widehat{\mathbf{B}} & \widetilde{\mathbf{B}} & & & \\ \mathbf{I}_4 & \mathbf{0}_4 & -\mathbf{I}_4 & & \\ & \ddots & \ddots & \ddots & \\ & & \mathbf{I}_4 & \mathbf{0}_4 & -\mathbf{I}_4 \\ & & & \mathbf{I}_4 & \mathbf{0}_4 \end{bmatrix},$$

where in the harmonic case

$$\widehat{\mathbf{B}} = \mathbf{0}_4 \qquad \text{and} \qquad \widetilde{\mathbf{B}} = \begin{bmatrix} 0 & 2 & 0 & 0 \\ 0 & 0 & 0 & 0 \\ 0 & 0 & 0 & 2 \\ 0 & 0 & 0 & 0 \end{bmatrix},$$

whereas in the subharmonic case

$$\widehat{\mathbf{B}} = \begin{bmatrix} 1 & 0 & 0 & 0 \\ 0 & -1 & 0 & 0 \\ 0 & 0 & 1 & 0 \\ 0 & 0 & 0 & -1 \end{bmatrix} \qquad \text{and} \qquad \widetilde{\mathbf{B}} = -\mathbf{I}_4.$$

To illustrate the stability of the viscous problem, we solve the eigenvalue equations for two values of dimensionless viscosity, $\nu = 10^{-3}$ and 6×10^{-3}, and for spherical harmonics with degree $m = 2, 3, 4$. In the numerical calculations, we use a truncation size of $N = 80$ so that all neglected coefficients of $\{X_n^r, X_n^\Psi\}$ for $n > 80$ are smaller than 10^{-9} and so can be neglected. The corresponding Ince-Strutt diagrams are shown in figure 6.3 where again we observe a clearly defined sequence of alternating harmonic and subharmonic fingers of instability in parameter space. These results reinforce one of the defining characteristics of parametric resonance, namely that such linear systems can experience instabilities leading to unbounded growth even in the presence of damping.

There are a few key comparisons that can be drawn with the inviscid results from section 6.2. First of all, the stability fingers do not touch the κ-axis as they did in the inviscid case, but instead are shifted vertically upwards. As a result, there is a minimum forcing amplitude required to initiate resonance for any given value of κ. For the value of viscosity $\nu = 10^{-3}$ the fingers appear most similar to the inviscid case, while for larger ν the fingers deform upwards away from the κ-axis and shift outward to the right. Indeed, for large enough values of either viscosity or mode number m the fingers can lift entirely above

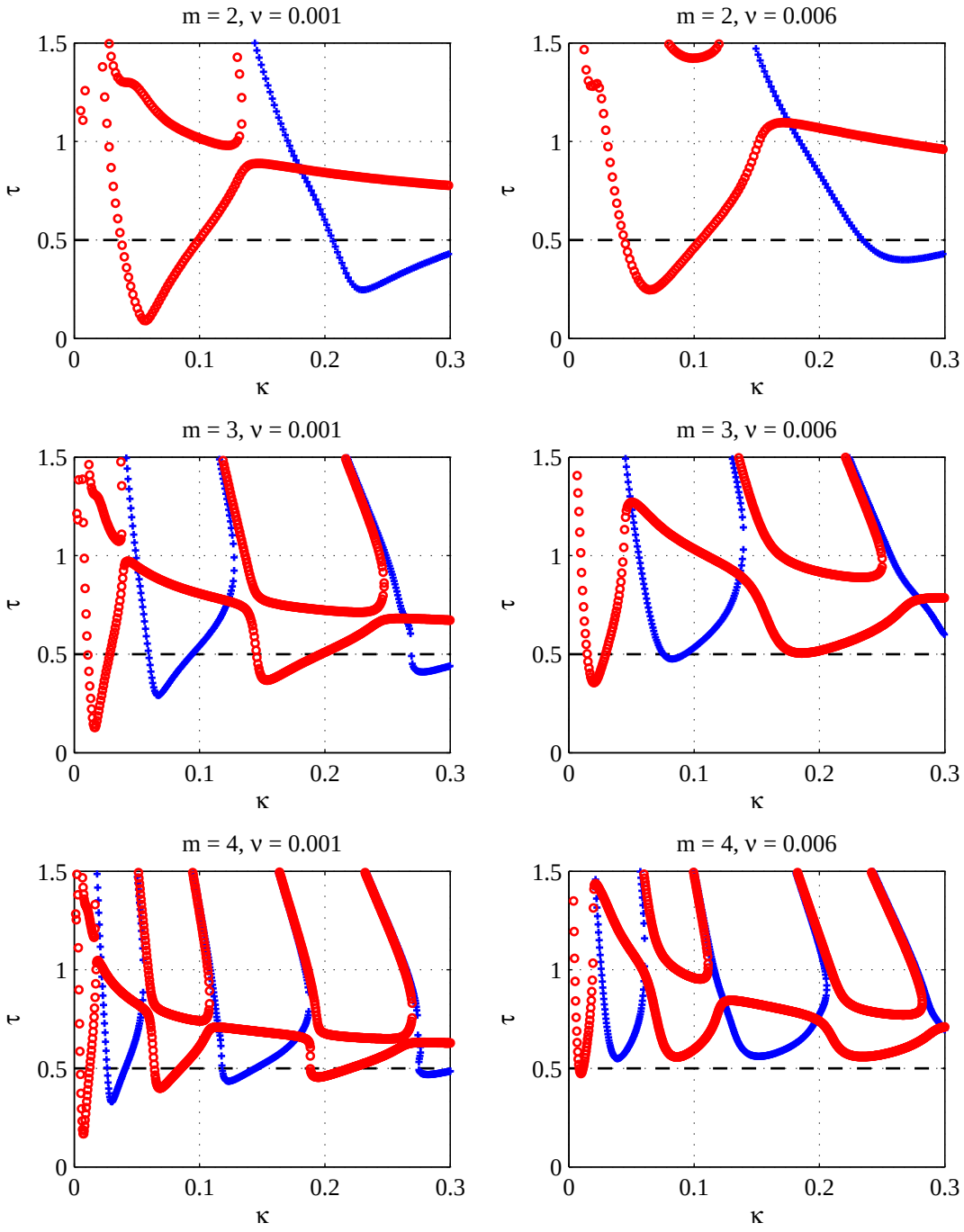

Figure 6.3: Ince-Strutt diagrams for the viscous problem with dimensionless viscosities $\nu = 10^{-3}$ (left) and $\nu = 6 \times 10^{-3}$ (right). Stability contours are shown for spherical harmonics $m = 2$ (top), 3 (middle) and 4 (bottom). Subharmonic solutions are denoted with $\circ$ and harmonic solutions with $+$.

the line $\tau = \frac{1}{2}$ so that resonance is no longer possible. This should be contrasted with the inviscid case where resonances exist for any value of m.

The second distinction from the inviscid results is that within the non-physical region $\tau > \frac{1}{2}$, an additional subharmonic solution appears as a curve of circular points that cuts across the finger-shaped contours. These unstable modes occur due to the periodic modulation in the tangential stress across the membrane (6.19) and thus are not observed in the inviscid case. However, all of these modes are restricted to the non-physical region $\tau > \frac{1}{2}$ and so they can be considered as spurious and safely ignored. A similar result was observed in the 2D case in Chapter 4 where we have have showed that the physical instabilities are due to periodic modulation of the pressure jump, and the same conclusion holds in the 3D case.

6.4 Numerical Simulations

Our next aim is to verify the existence of parametric instabilities for an internally forced spherical membrane using numerical simulations of the full governing equations (6.3). We use a parallel implementation of the immersed boundary algorithm developed by Wiens [127, 128] that utilizes a pseudo-compressible Navier-Stokes solver having particular advantages in terms of parallel speed-up on distributed clusters. The algorithm exploits a rectangular fluid domain with periodic boundary conditions, but we found that a cubic computational domain with side length $6R$ is sufficiently large to avoid significant interference from the adjacent periodic shells, where R is the equilibrium radius of the spherical membrane. The fluid domain is discretized uniformly with 128 grid points in each direction.

The spherical shell is discretized using a triangulated mesh generated with the MATLAB code `distmesh` [99] (see figure 6.4), wherein each vertex is an IB node and each edge in the triangulation is a force-generating spring link that joins adjacent nodes. The discretized shell in our simulation consists of 30054 IB nodes with mean equilibrium spring length $0.022R$. The elastic force generated by the deformed membrane is then simply the sum of all spring forces arising from this network of stretched springs. However, the spring constant used in the numerical simulation is not necessarily equivalent to elastic stiffness parameter σ in the analysis. Hence, in order for the numerical simulations to agree with the analysis, we must derive a relationship between the analytical membrane stiffness and the numerical spring constant.

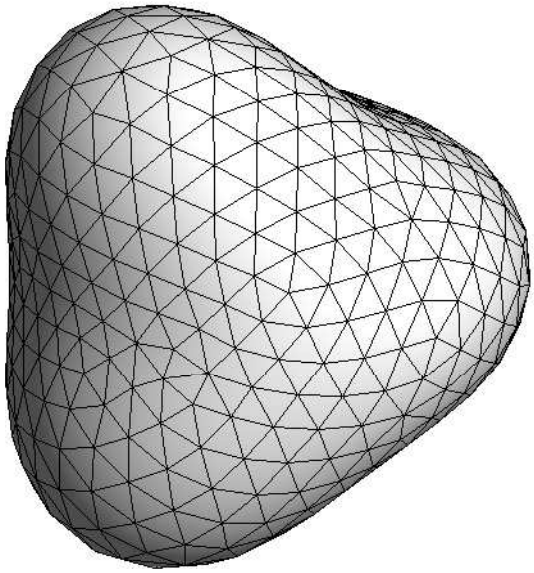

Figure 6.4: An example of a discretized membrane, where the mesh triangulation is generated using `distmesh` [99]

6.4.1 Relating the Membrane Stiffness to the Numerical Spring Constant

Let $\mathcal{H}$ be a connected subset of the membrane Γ and let $\mathcal{S}$ be a parameterization of $\mathcal{H}$. In other words, for $\mathcal{H} \subset \Gamma$, we have

$$\mathcal{S} = \{(\xi, \eta) \mid \boldsymbol{X}(\xi, \eta) \in \mathcal{H}\}.$$

The force density in the IB framework is defined such that the net force acting on the surface patch $\mathcal{H}$ is given by

$$\iint_{\mathcal{S}} \boldsymbol{F}(\boldsymbol{X}, t) \sin\eta \, \mathrm{d}\xi \, \mathrm{d}\eta. \tag{6.35}$$

Now suppose the set of nodes $\{\boldsymbol{X}_j^*\}_{j=0}^{N_{\mathrm{IB}}}$ represent a membrane discretization where we use the superscript $*$ to denote numerical quantities and distinguish them from their continuous counterparts. The elastic force in the 3D code [128] is generated by a network of Hookean springs that connect adjacent IB nodes. That is, the force density (assuming constant spring constant σ^*) between node i and node j is simply

$$\boldsymbol{F}_{ij}^* = \sigma^*(\boldsymbol{X}_i^* - \boldsymbol{X}_j^*),$$

and so the total force acting on node $\boldsymbol{X}_j^*$ is

$$\boldsymbol{f}_j^* = \sum_i \sigma^*(\boldsymbol{X}_i^* - \boldsymbol{X}_j^*), \tag{6.36}$$

where the sum is taken over all i such that $\boldsymbol{X}_i^*$ is connected to $\boldsymbol{X}_j^*$. Our aim now is to find an approximate relationship between the membrane stiffness σ and the spring constant σ^*. To this end, we derive a discretization of the integral (6.35) and contrast it with the sum (6.36).

Let Γ^* be a piecewise linear surface that represents the discretization of the membrane Γ. Moreover, we subdivide Γ^* into pyramidal surfaces, denoted $\mathcal{H}_j^*$, with node $\boldsymbol{X}_j^*$ at its apex such that

$$\Gamma^* = \bigcup_{j=0}^{N_{\mathrm{IB}}} \mathcal{H}_j^* \qquad \text{and} \qquad \bigcap_{j=0}^{N_{\mathrm{IB}}} \mathcal{H}_j^* = \emptyset.$$

Each vertex of $\mathcal{H}_j^*$ is the centroid of the triangle formed by the apex $\boldsymbol{X}_j^*$ and its surrounding nodes as in figure 6.5. Furthermore, the surface $\mathcal{H}_j^*$ is the effective area in which the net force $\boldsymbol{f}_j^*$ is applied to the membrane. Now let $\mathcal{H}_j$ be a smooth patch of Γ with a parameterization given by $\mathcal{S}_j$, and having the same boundary as $\mathcal{H}_j^*$. Then the net force acting on $\mathcal{H}_j$ is approximated by

$$\sigma \iint_{\mathcal{S}_j} \Delta_{\mathrm{S}} \boldsymbol{X} \sin\eta \, \mathrm{d}\xi \, \mathrm{d}\eta \approx \sigma^* \sum_i (\boldsymbol{X}_i^* - \boldsymbol{X}_j^*),$$

where the sum is taken over all i such that $\boldsymbol{X}_i^*$ is connected to $\boldsymbol{X}_j^*$. Now consider a single node, say $\boldsymbol{X}_0^*$, as in figure 6.5. Without loss of generality, suppose $\boldsymbol{X}_0^*$ is located on the positive z-axis. Moreover we assume

- The spring length, denoted Δs, is small.
- The membrane is in near equilibrium (sphere with radius R).
- The membrane stiffness is spatially uniform.
- Each X_j^* is connected to six other nodes.

In practice, the last two assumptions do not always hold as there are nodes that have either five or seven connections that can be seen in figure 6.4. This will cause a non-uniformity in the force induced by the springs, however the vast majority of the nodes have six connections and so we assume that the force is spatially uniform.

For nodes near the z-axis, that is $\eta \approx 0$, the following approximation of the spherical Laplacian operator holds

$$\sin\eta \, \Delta_{\mathrm{S}} = \frac{1}{\sin\eta} \frac{\partial^2}{\partial \xi^2} + \sin\eta \frac{\partial^2}{\partial \eta^2} + \cos\eta \frac{\partial}{\partial \eta} \approx \frac{\partial}{\partial \eta}.$$

This is justified by the fact that

$$\left.\frac{\partial \boldsymbol{X}}{\partial \xi}\right|_{\eta=0} = \lim_{\Delta\xi\to 0} \frac{\boldsymbol{X}(\xi+\Delta\xi,0)-\boldsymbol{X}(\xi,0)}{\Delta\xi} = 0,$$

since $\boldsymbol{X}(\xi+\Delta\xi,0)=\boldsymbol{X}(\xi,0)$ at the pole $\eta=0$ for any choice of $\xi\in[0,2\pi)$, and so

$$\left.\frac{\partial^2 \boldsymbol{X}}{\partial \xi^2}\right|_{\eta=0} = \lim_{\Delta\xi\to 0} \frac{\frac{\partial \boldsymbol{X}}{\partial \xi}(\xi+\Delta\xi,0)-\frac{\partial \boldsymbol{X}}{\partial \xi}(\xi,0)}{\Delta\xi} = 0.$$

Therefore, the numerical force density is estimated by

$$\boldsymbol{f}_0^* \approx \sigma \iint_{\mathcal{S}_0} \frac{\partial \boldsymbol{X}}{\partial \eta}\,\mathrm{d}\xi\,\mathrm{d}\eta.$$

The above integral can be approximated on each planar face of $\mathcal{H}_0^*$. For example, if we assume that Δs is small and $\mathcal{H}_0$ is nearly flat, then we can roughly parametrize the shaded triangular region in figure 6.5 by

$$-\frac{\pi}{6} \le \xi \le \frac{\pi}{6} \quad \text{and} \quad 0 \le \eta \le \frac{\Delta s}{2R}\sec\xi.$$

In this region, the net force can be approximated using the midpoint quadrature rule

$$\sigma \int_{-\frac{\pi}{6}}^{\frac{\pi}{6}} \int_0^{\frac{\Delta s}{2R}\sec\xi} \frac{\partial \boldsymbol{X}}{\partial \eta}\,\mathrm{d}\eta\,\mathrm{d}\xi \;\approx\; \sigma \frac{\ln 3}{2}\frac{\Delta s}{R}\left.\frac{\partial \boldsymbol{X}}{\partial \eta}\right|_{(\xi,\eta)=(0,0^+)}.$$

Using finite differences, the derivative can be approximated by

$$\left.\frac{\partial \boldsymbol{X}}{\partial \eta}\right|_{(\xi,\eta)=(0,0^+)} \approx \frac{\boldsymbol{X}_1-\boldsymbol{X}_0}{\Delta\eta},$$

where $\Delta\eta$ is the polar angle measured between $\boldsymbol{X}_0^*$ (or the z-axis) and $\boldsymbol{X}_1^*$. A similar result is obtained for all of the other nodes connected to $\boldsymbol{X}_0^*$. So the total force on node $\boldsymbol{X}_0^*$ is estimated by

$$\boldsymbol{f}_0^* \approx \sigma \frac{\ln 3}{2}\sum_{i=1}^{6}(\boldsymbol{X}_i^*-\boldsymbol{X}_0^*).$$

where we use $\Delta\eta \approx \frac{\Delta s}{R}$. Comparing this result with the sum (6.36) we get

$$\sigma^* \approx \frac{\ln 3}{2}\sigma.$$

This implies that a desired membrane stiffness σ must be scaled by $\frac{\ln 3}{2}$ in order for the analysis to agree with the simulation. Since the membrane force is assumed to be uniform, this approximation holds for any node on the mesh for small spring size Δs.

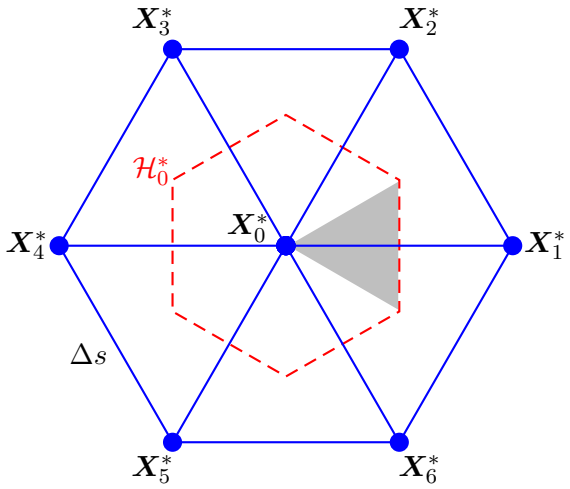

Figure 6.5: The node $\boldsymbol{X}_0^*$ connected to six other nodes $\boldsymbol{X}_j^*$ for $j = 1, \ldots, 6$. The solid lines represent the springs and the dashed hexagon represents the effective pyramidal surface $\mathcal{H}_0^*$.

6.4.2 Simulation Results

The membrane is given an initial configuration

$$\boldsymbol{X}(\xi, \eta, 0) = R(1 + \epsilon Y_{m,k}^c(\xi, \eta))\, \hat{\boldsymbol{r}}(\xi, \eta),$$

corresponding to a chosen scalar spherical harmonic of degree m and order k with perturbation amplitude

$$\epsilon = \frac{0.05}{\max_{\xi,\eta} \left| Y_{m,k}^c(\xi, \eta) \right|}.$$

We then performed numerical simulations for four different sets of parameters listed in table 6.1, which we refer to as cases 1–4. This table lists the physical parameters used in the simulations (ρ, μ, R, ω, σ) as well as the corresponding dimensionless parameters appearing in our analytical results (ν, κ). The corresponding stability contours for each case 1 to 4 are shown in figure 6.6, this time in terms of plots of τ versus m holding the values of ν and κ fixed. This alternate view of the stability regions allows us to identify the unstable modes that correspond to physical oscillations, since only modes with integer values of m are actually observable.

Numerical simulations are performed by initializing the membrane with various (m,k)-modes lying inside and outside the highlighted unstable fingers so that direct comparisons can be drawn with our analytical results. Figure 6.7 depicts several snapshots of the numerical solution for case 1, where the membrane was perturbed by a $(3, 0)$-mode. The

Case	ν	κ	ρ (g/cm^3)	R (cm)	ω (1/s)	μ (g/cm s)	σ (g/s^2)
1	0.006	0.02	1	1	1	0.006	0.02
2	0.002	0.06	1	0.5	20	0.01	3
3	0.001	0.0075	1	0.5	20	0.005	0.375
4	0.004	0.25	1	10	0.05	0.02	0.625

Table 6.1: Dimensionless and physical parameters for the four cases used in the numerical simulations of the 3D immersed boundary equations.

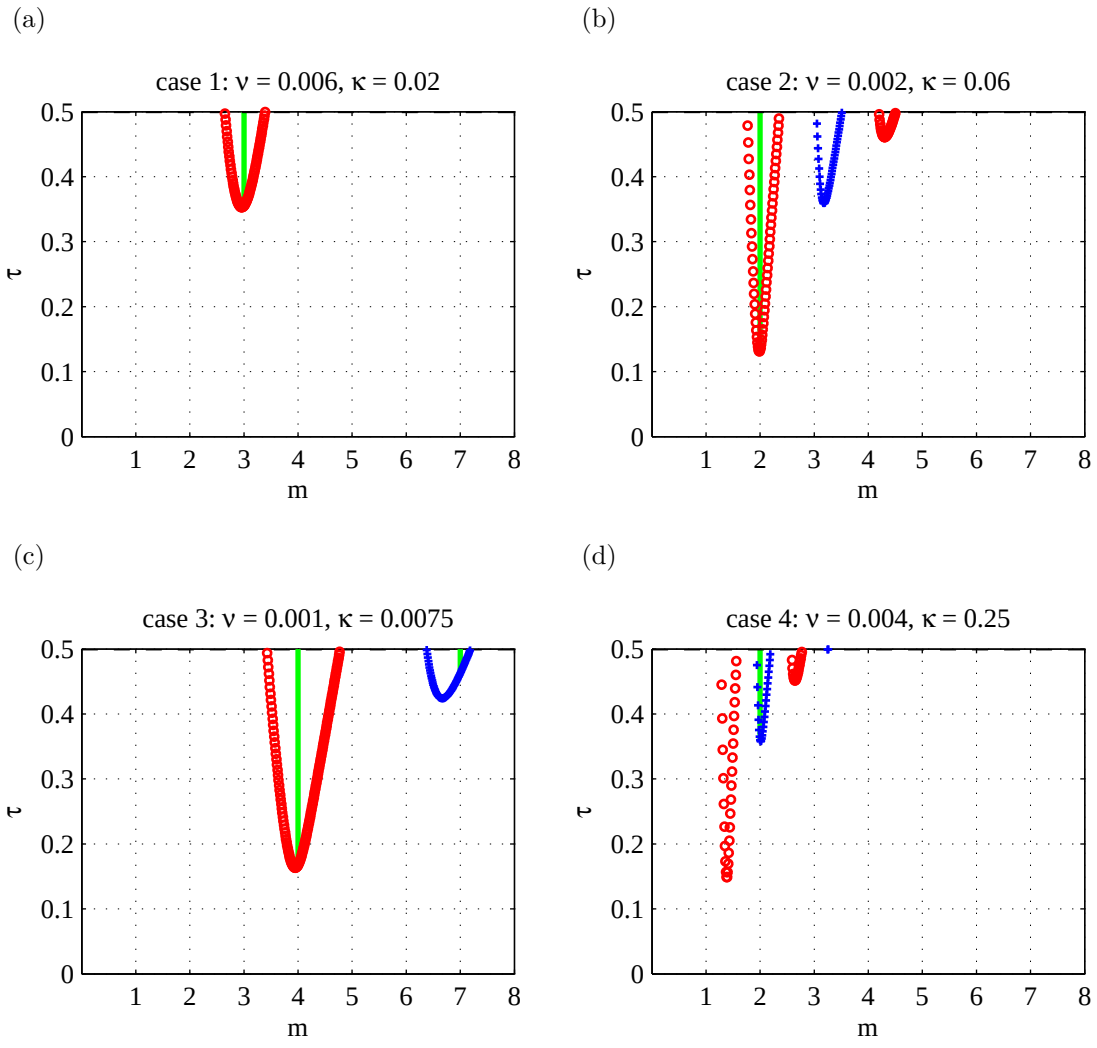

Figure 6.6: Ince-Strutt plots showing stability contours for each test case 1–4. Parameters that give rise to observable instabilities (i.e., corresponding to integer values of m) are highlighted by a vertical green line.

parametric forcing amplitude was set to $\tau = 0.45$ which is well within the stability finger in figure 6.6a. Over time, the small initial perturbation grows and oscillates with a frequency equal to one-half that of the forcing frequency, as expected from the $(3, 0)$ subharmonic response predicted by the linear analysis. To help visualize the growth of this mode over time, we compute the radial projection

$$X^r(t) = \int_0^{\pi}\int_0^{2\pi} \boldsymbol{X} \cdot \boldsymbol{Y}^c_{m,k} \sin\eta \, \mathrm{d}\xi \, \mathrm{d}\eta$$

at each time. This integral is computed by first interpolating the IB mesh values of $\boldsymbol{X}$ onto a regular (ξ, η) grid and then approximating the integral numerically using a Fast Fourier Transform in ξ and Gauss-Legendre quadrature in η. Figure 6.8 depicts the evolution of $X^r(t)$ for the $(3, 0)$-mode, from which it is easy to see the expected period-doubling response to a waveform with period 4π. To illustrate that the membrane instability depends sensitively on the choice of mode, figure 6.8 also shows simulations that were perturbed with $(2, 0)$ and $(4, 0)$-modes; neither of these two other modes exhibits any evidence of instability, which is also predicted by the stability plots in figure 6.6a.

One conclusion from our analysis is that for each m, the stability of the linearized dynamics does not depend on the order k of the spherical harmonic. This result is investigated in figure 6.9, where we display the projected radial amplitude X^r for two simulations using the case 1 parameters and two initial membrane shapes corresponding to modes $(3, 0)$ and $(3, 1)$. The analytical solution is provided for comparison, and we observe that the behaviour of all three solution curves is nearly indistinguishable at early times. However, as time goes on the perturbations grow and nonlinear effects come into play in the simulations, so that the growth rates eventually deviate from the linear analysis.

As another illustration of the dependence of stability on system parameters, we perform a series of simulations to investigate the "sharpness" of the stability fingers. Using parameters from case 2, we fix $\tau = 0.25$ and then investigate the behaviour of the numerical solution as κ is varied. Based on figure 6.6b, we expect case 2 to be unstable if the membrane configuration is an $m = 2$ mode, but if parameters are changed sufficiently then the stability fingers can shift enough that the 2-mode stabilizes. Figure 6.10a shows the Ince-Strutt diagram as a plot of τ versus κ for $\nu = 0.002$ and $m = 2$. The parameter values used in this series of tests are denoted by $\triangle$ in figure 6.10a, with the centre point located in the middle of the subharmonic finger corresponding to case 2, and the remaining parameters lying either on the border of the stability region ($\kappa \approx 0.048$ and 0.074) or outside. Figures 6.10b-6.10f depict the radial projection X^r for each of the five simulations from which we can clearly see that as κ increases the solutions transition from stable to unstable and then back to stable

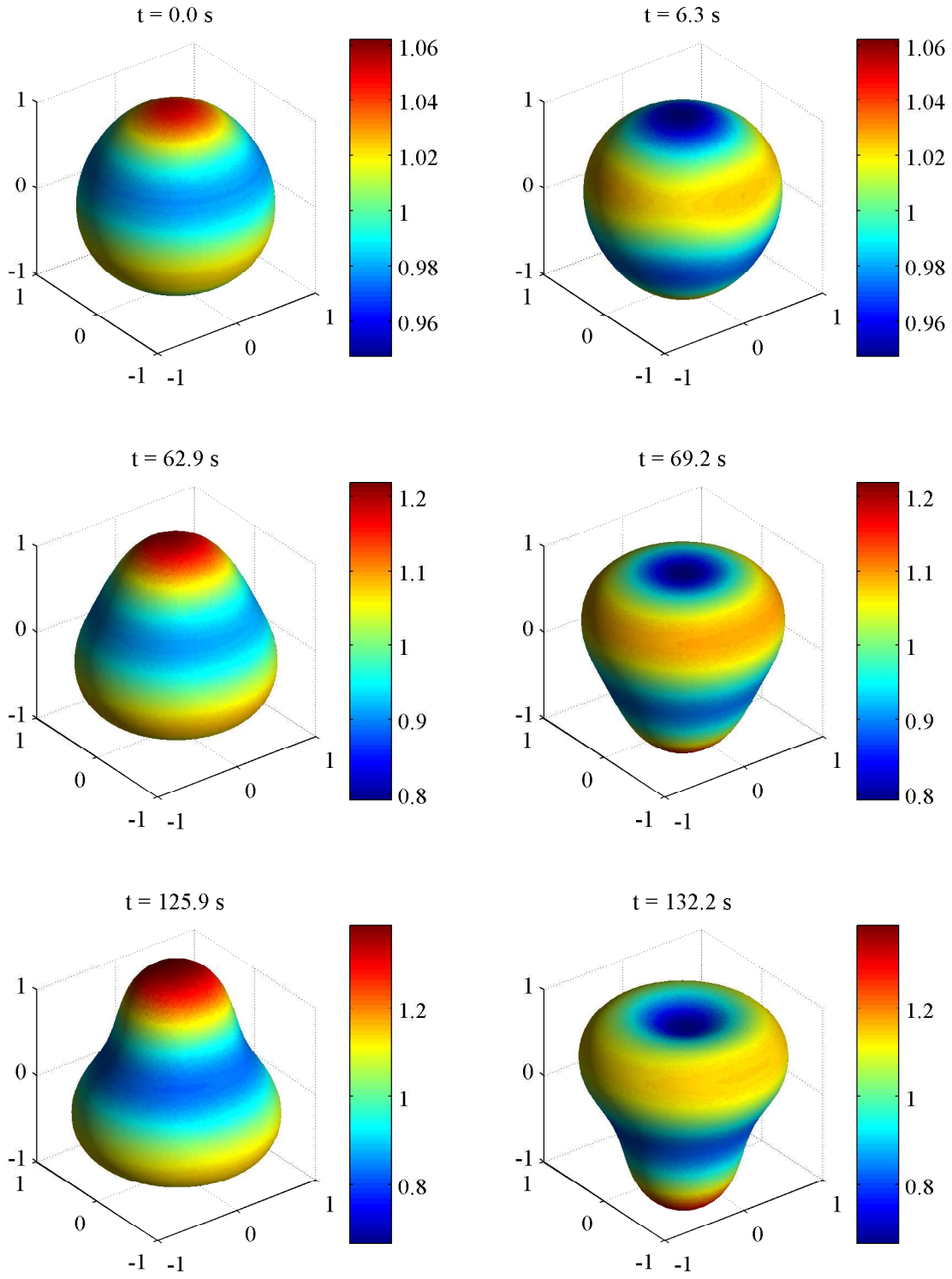

Figure 6.7: Several snapshots from the case 1 simulation where the membrane was initialized with a $(3, 0)$-mode and the forcing amplitude is set to $\tau = 0.45$. Colour map depicts the distance from the origin.

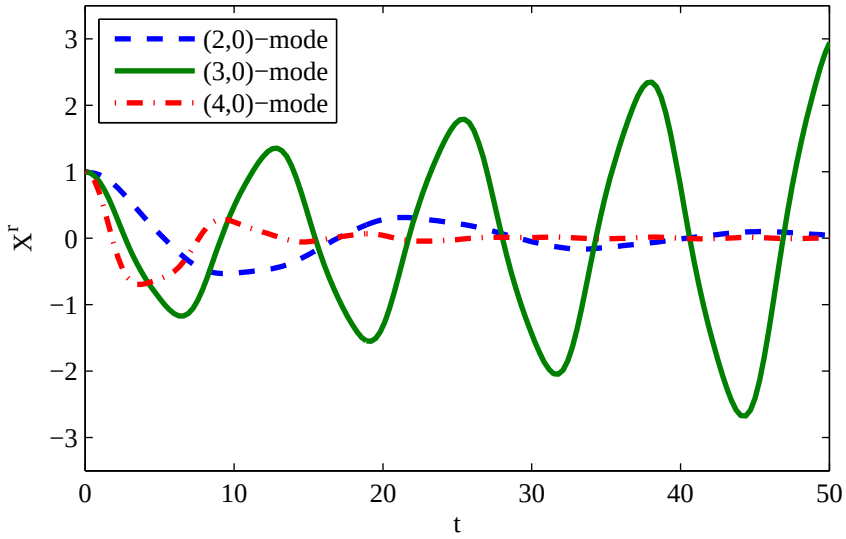

Figure 6.8: Radial amplitude projection X^r for the numerical result from case 1, with the spherical shell perturbed by three different (m, k)-modes. The results are all rescaled to start at $X^r = 1$.

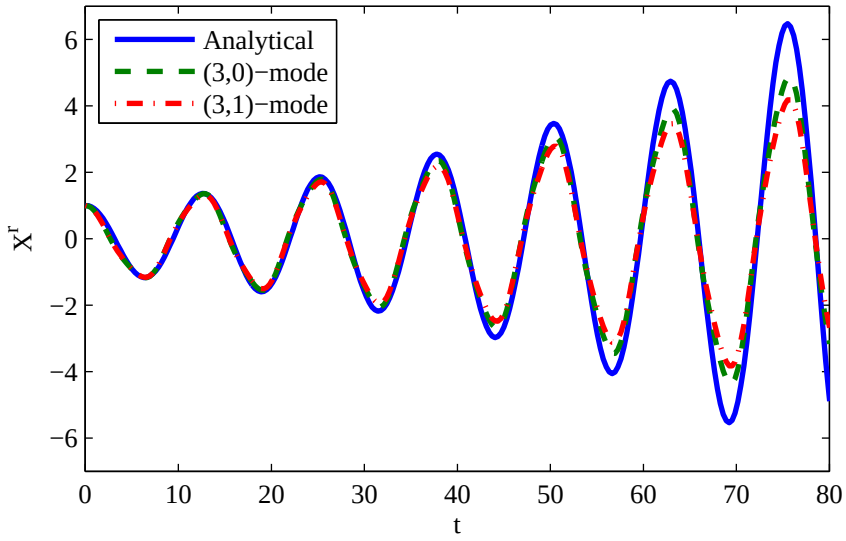

Figure 6.9: Radial amplitude projection X^r in case 1, showing a simulated spherical shell perturbed by a $(3, 0)$-mode (dashed) and a $(3, 1)$-mode (dash-dot). The exact result from the linear analysis is shown as a solid line. All curves are rescaled to start at $X^r = 1$.

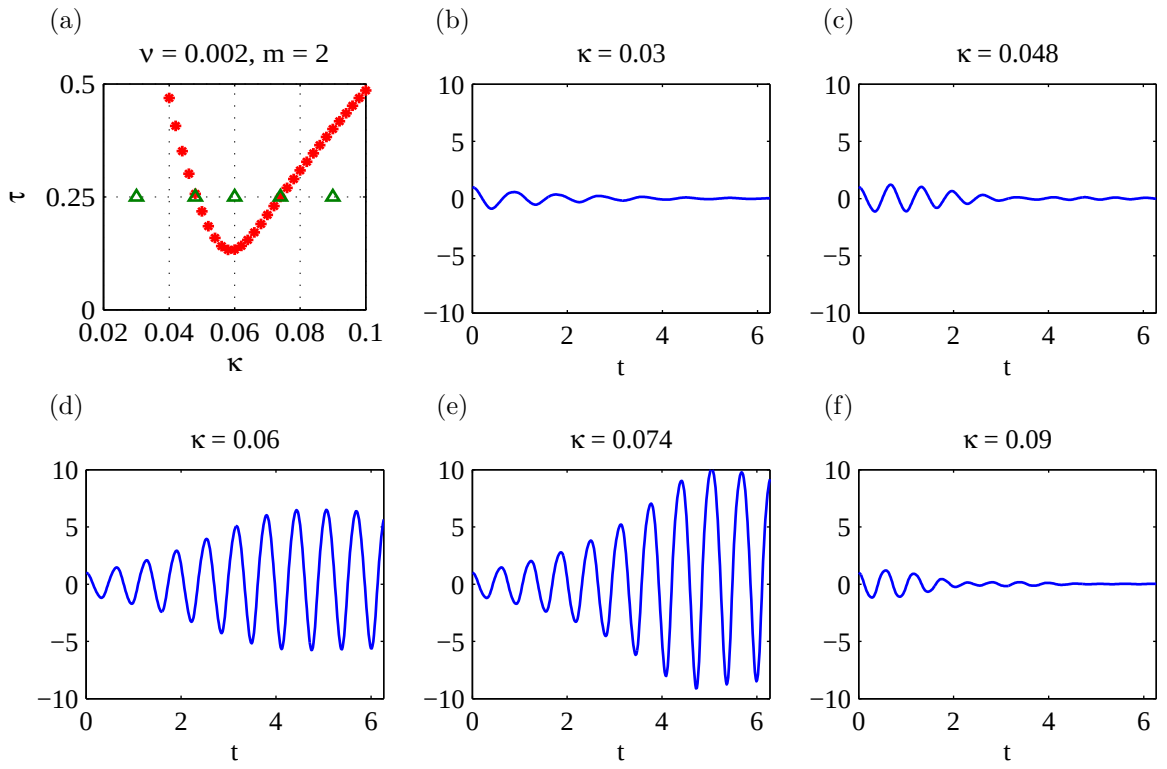

Figure 6.10: (a) Ince-Strutt diagram for $m = 2$ and $\nu = 0.002$ but with varying κ. The parameters used are denoted by △, with the centre point $\kappa = 0.06$ corresponding to case 2. (b)–(f) Radial projection of $\boldsymbol{X}$ from simulations for a range of κ values. The membrane was initialized with a $(2, 0)$-mode and all curves are rescaled to start at $X^r = 1$.

again. The computed stability boundaries do not correspond exactly with the analytical results, particularly for the upper stability limit $\kappa \approx 0.074$; however, the match is still reasonable considering that the analysis is linear.

Finally, we show in figure 6.11 plots of the radial amplitude projection in cases 1–4, perturbing the spherical shell in each case with a mode that we know from the analysis to be unstable. The forcing amplitude is set to $\tau = 0.45$ in all four cases. Snapshots of the membrane evolution are also given for each simulation to illustrate the growth of the given modes. All simulations exhibit the expected unstable growth in solution amplitude, although we stress that the numerical results do not lead to unbounded growth (or blow-up) in the amplitude as suggested by the linear analysis. We attribute this discrepancy in behaviour to nonlinear effects that become important later in the simulation and limit the solution growth when the amplitude of oscillations become large enough. We also note that the correct frequency response is observed in all four tests, with cases 1–3 exhibiting the

expected period-doubling subharmonic response, while case 4 oscillates with a harmonic response.

6.5 Application to Cardiac Fluid Dynamics

This study of parametric forcing of immersed elastic shells was originally motivated by the actively-beating heart muscle fibres that interact with surrounding blood and tissue. Heart muscle contractions are initiated by complex waves of electrical signals that propagate through the heart wall, which should be contrasted with the spatially-uniform coordinated contractions analyzed in this chapter. Furthermore, the heart chambers have an irregular shape and a thick wall that differ significantly from a spherical shell with zero thickness. Nonetheless, it is natural to ask whether our analysis of spherical immersed elastic shells with a periodic internal forcing could still yield any useful insights into the nature of the complex fluid-structure interaction between a beating heart and the surrounding fluid.

To this end, we consider an immersed spherical shell with parameters that correspond to the human heart under two conditions: first, a normal healthy heart; and second, an abnormal heart undergoing a much faster heartbeat. We then ask whether our analysis gives rise to resonant behaviour in either case for physiologically relevant heart beat frequencies. There are a wide range of abnormal heart rhythms classified under the heading of *supraventricular tachycardia* or SVT [77, 104], corresponding to a heart rhythm that is either irregular or abnormally rapid and occurs in the heart's upper chambers (called the left and right atria). In contrast with ventricular tachycardias, which are much more dangerous, many SVTs are non-life-threatening and can persist for long periods of time. Therefore, we will focus on SVTs (and the atria) where fluid dynamic instabilities are more likely to have the time to develop.

We next discuss the choice of parameters that is appropriate for applying our IB model to study FSI in the heart. The resting heart rate for a healthy person ranges from 60 to 100 beats per minute (bpm) and both atria and ventricles beat in synchrony. In contrast, a heart characterized by SVT can exhibit two separate beats in the atria and ventricles, and can have an atrial rhythm that lies anywhere between 100 to 600 bpm. A clinical study by Wang et al. [125] surveyed 322 patients suffering from atrial fibrillation (one sub-class of SVT) and obtained measurements of atrial wall stiffness σ varying between 1×10^3 and 2×10^4 dyn cm^{-1}. We have found no evidence to suggest that the stiffness varies significantly between hearts with normal and abnormal rhythms, and so we use the same range of σ for all cases. Although hearts suffering from conditions such as atrial fibrillation are often

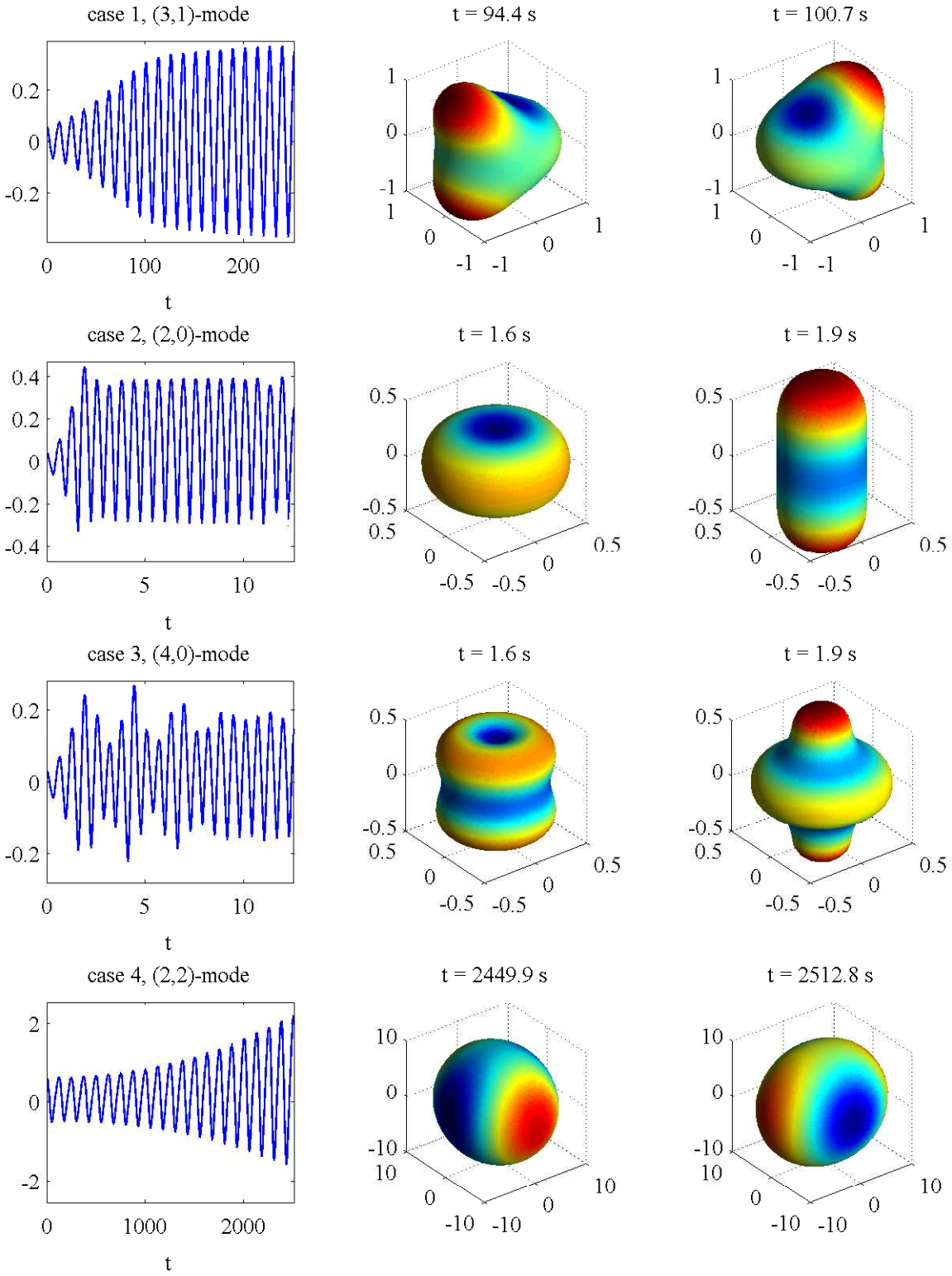

Figure 6.11: Simulation results for all four cases where a spherical shell is perturbed by a mode that is expected to be unstable, with $\tau = 0.45$. The left column shows the radial projection X^r, while snapshots from the corresponding simulations are shown on the right.

characterized by an increased size [125], we elect to use a single representative value of the radius $R = 2.0$ cm for an atrium in both normal and diseased hearts. In terms of the fluid properties, blood has density similar to water with $\rho = 1\ \mathrm{g\,cm^{-3}}$ but has a significantly higher dynamic viscosity of $\mu = 0.04\ \mathrm{g\,cm^{-1}\,s^{-1}}$. We choose a representative SVT rhythm with frequency $\omega = 400$ bpm, which translates into a dimensionless viscosity parameter $\nu = 2.39 \times 10^{-4}$.

Substituting the parameter values and ranges just described into our analytical results from section 6.3 for the first three modes numbered $m = 2, 3, 4$, we obtain the Ince-Strutt plots in figure 6.12. The stability fingers are depicted with the elastic stiffness parameter σ plotted along the horizontal axis, and the results show that parametric instabilities can arise for most values of σ under consideration. Because these resonant instabilities occur over such a wide range of stiffness values covered by the measurements in [125] from the left atrium, it is reasonable to hypothesize that it may be possible for FSI-driven parametric instability to influence the dynamics of the beating heart.

We now delve further into the finger plots in figure 6.12 and remark that experiments suggest the heart muscle is seldom (if ever) completely slack; therefore, we expect that the forcing amplitude parameter τ lies significantly below the threshold value of $\frac{1}{2}$. Indeed, an estimate of $\tau \approx 0.3$ can be extracted from measurements of pressure in the left atrium from [13, Fig. 1]. Figure 6.13 provides an alternate view of the dependence of resonant instabilities on the parameters by depicting the minimum τ giving rise to resonance for a function of elastic stiffness and beat frequency (using modes in the range $m = 2, \ldots, 6$). We are especially interested in the dark (blue) bands that correspond to smaller values of τ and hence more prominent instabilities. Taking a value of $\tau = 0.3$, our analysis predicts "valleys" of instability corresponding to discrete ranges of the parameters ω and σ. For fixed σ, we observe that at low frequency these valleys are very narrow and steep, while as the forcing frequency increases the width of the unstable bands likewise increases. In particular, if we consider an intermediate value of σ for "normal" heart beating in the range of 60–100 bpm, then the unstable bands are relatively small and so resonances would seem to be less likely. On the other hand, if the frequency is increased to 300–600 bpm then we begin to encounter wider valleys that suggest instabilities for a smaller value of τ.

In summary, we have found that resonant instabilities are possible for a wide range of parameters corresponding to both normal and abnormal hearts; furthermore, for higher frequencies corresponding to SVT, instabilities are not only more likely to occur but also persist over wider ranges of parameter space. As suggestive as these results are, we refrain from making any specific claims or predictions regarding resonance in the actual beating

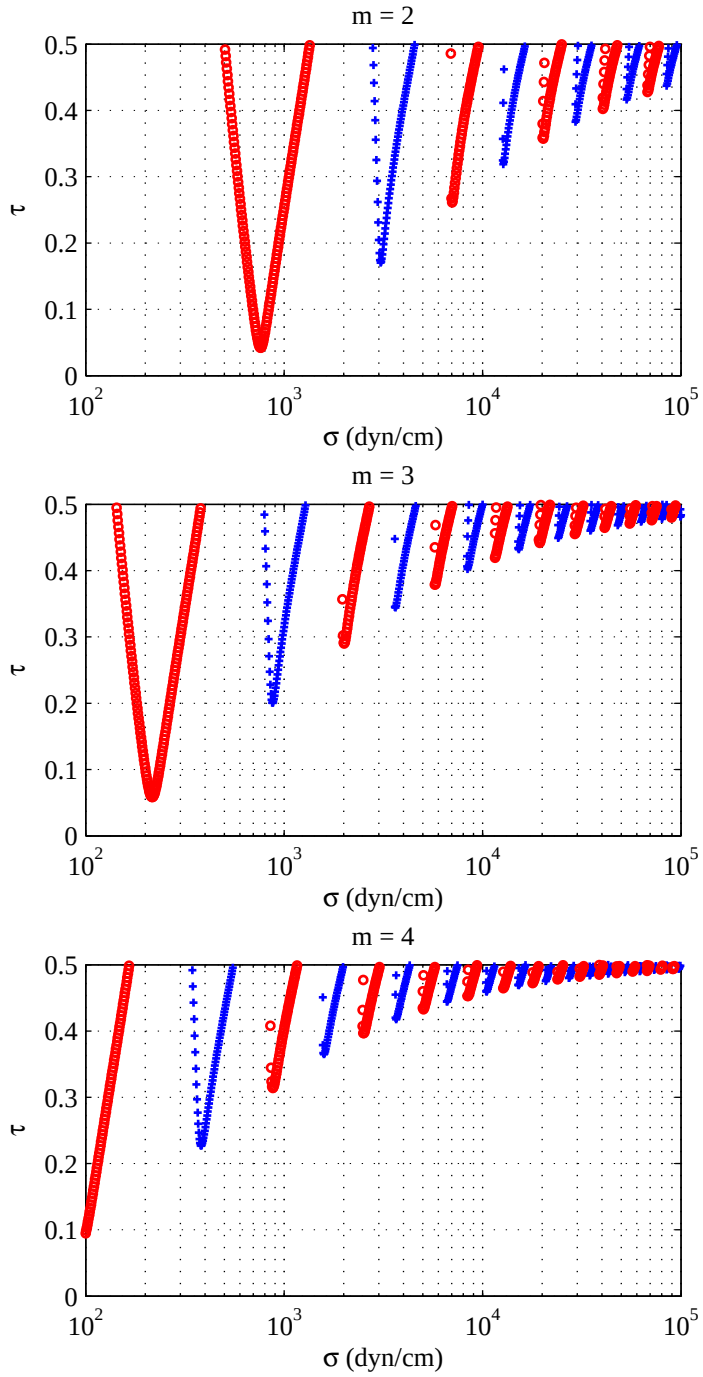

Figure 6.12: Stability contours for physical parameters corresponding to a human heart undergoing an abnormal heart rhythm ($\nu = 2.39 \times 10^{-4}$) for modes $m = 2$ (top), 3 (middle) and 4 (bottom).

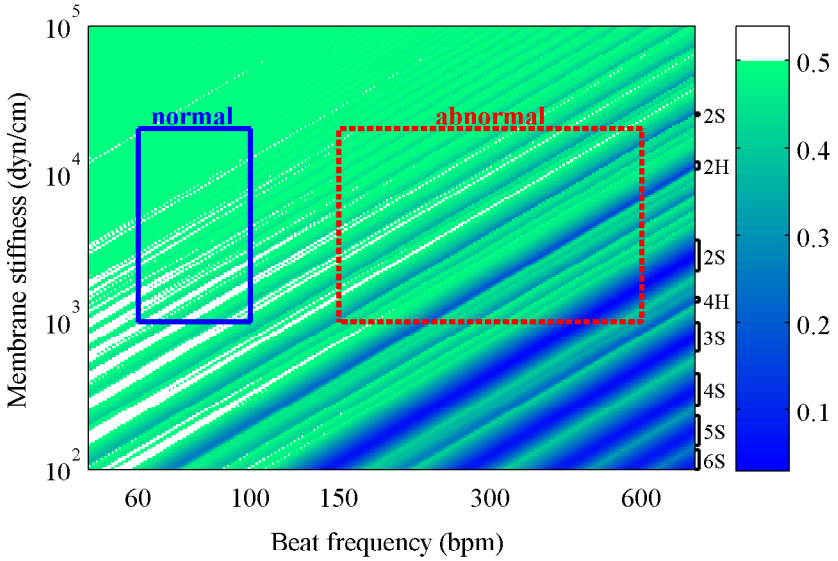

Figure 6.13: Minimum value of τ required for parametric resonance across modes $m = 2, \ldots, 6$. White areas represent parameters for which no physical instability exists. Each dark (blue) band is labelled by its corresponding unstable m-mode and response frequency ('H' for harmonic or 'S' for subharmonic). The boxes indicate parameter ranges for a healthy heart (solid, blue) and for a heart with SVT (dashed, red).

heart since we have made so many simplifications and assumptions here: the applied periodic forcing is oversimplified, nonlinearities are neglected, a spherical shell is a far cry from an atrium, and parameter values are still quite uncertain. Nonetheless, the fact that our analysis predicts resonances for such a wide range of physiologically relevant parameters is compelling enough to suggest that this problem merits further investigation. Moreover, it should be possible to test for the presence of isolated parametric instabilities in carefully designed experiments, and our parameter study above provides guidance in what ranges of parameters are most worthy of investigation.

Chapter 7

Natural Oscillations in Unforced Spherical Shells

We digress from the topic of parametric instabilities in this chapter to consider the natural oscillations of unforced spherical immersed elastic shells. By reducing the Floquet analysis in the previous chapter to the unforced case, setting $\tau = 0$, we obtain a dispersion relation for oscillations of immersed membranes in both inviscid and viscous fluids. Furthermore, we extend the linear inviscid theory to include nonlinear effects and show that nonlinearity has little influence on the membrane oscillations. Finally, we perform an experiment where we measure oscillation frequencies of immersed water balloons and compare them to the frequencies predicted by the aforementioned theories. Although ultimately we find that the experiments do not match closely with the theory, the results nonetheless match qualitatively and we provide a number of possible sources of the discrepancy that are worthy of future study.

The governing equations of the fluid-structure system in the dimensionless delta function formulation are

$$\frac{\partial \boldsymbol{u}}{\partial t} + \boldsymbol{u} \cdot \nabla \boldsymbol{u} = -\nabla p + \nu \Delta \boldsymbol{u} + \boldsymbol{f}, \tag{7.1a}$$

$$\nabla \cdot \boldsymbol{u} = 0, \tag{7.1b}$$

$$\boldsymbol{f}(\boldsymbol{x}, t) = \int_0^{\pi} \int_0^{2\pi} \boldsymbol{F}(\boldsymbol{X}, t)\, \delta(\boldsymbol{x} - \boldsymbol{X}) \sin\eta \, \mathrm{d}\xi \, \mathrm{d}\eta, \tag{7.1c}$$

$$\frac{\partial \boldsymbol{X}}{\partial t} = \boldsymbol{u}(\boldsymbol{X}, t), \tag{7.1d}$$

$$\boldsymbol{F}(\boldsymbol{X}, t) = \kappa \Delta_{\mathrm{S}} \boldsymbol{X}. \tag{7.1e}$$

These equations are the same as in Chapter 6, with the exception of the constant stiffness

in the force density. In the absence of a forcing frequency parameter ω to define a velocity scale, we redefine the dimensionless viscosity as

$$\nu = \frac{\mu}{\rho U R}, \tag{7.2}$$

and the dimensionless stiffness as

$$\kappa = \frac{\sigma}{\rho U^2 R}, \tag{7.3}$$

where U is a characteristic velocity. Moreover, we have a new characteristic time scale R/U, and pressure scale ρU^2.

7.1 Linear Oscillations in an Inviscid Fluid

We have already shown in section 6.2 that the oscillations of an internally forced membrane immersed in an inviscid fluid are governed by the Mathieu equation (6.23). In the absence of any forcing, the Mathieu equation simplifies to the harmonic oscillator equation

$$\frac{\mathrm{d}^2 X^r}{\mathrm{d}t^2} + \frac{\kappa m(m+1)(m-1)(m+2)}{2m+1} X^r = 0,$$

with dimensionless frequency of oscillation λ_0 satisfying

$$\lambda_0^2 = \frac{\kappa m(m+1)(m-1)(m+2)}{2m+1}. \tag{7.4}$$

Substituting the definition of κ from (7.3) and replacing λ_0 with $\omega_0 R/U$ yields

$$\omega_0^2 = \frac{\sigma m(m+1)(m-1)(m+2)}{\rho R^3(2m+1)}, \tag{7.5}$$

which is the dispersion relation for a spherical elastic shell immersed in an inviscid fluid in dimensional form. This is a well-known result that also arises in oscillations of inviscid fluid drops, where σ represents surface tension. Rayleigh [109] derived a similar result for an inviscid drop surrounded by a medium with negligible density, which Lamb [69] generalized to an inviscid drop immersed in another fluid with non-zero density. Lamb's result reduces to (7.5) in the special case where the inner and outer fluids have the same density. Both Rayleigh and Lamb assume axisymmetric drop shapes, however the dispersion relation holds for a degree m spherical harmonic of any azimuth order k [70].

7.2 Linear Oscillations in a Viscous Fluid

We next show how the Floquet analysis in section 6.3 can be applied to derive a linear theory for oscillations of spherical elastic shells immersed in a viscous, incompressible fluid. The derivation of the dispersion relation is similar to the analysis in section 6.3 so that many of the details will be omitted.

We begin with the dimensionless, linearized governing equations that describe the fluid-structure interaction

$$\begin{aligned}
\frac{\partial u^r}{\partial t} &= -\frac{\partial \hat{p}}{\partial r} + \nu\left(\frac{\partial^2 u^r}{\partial r^2} + \frac{2}{r}\frac{\partial u^r}{\partial r} - \frac{m(m+1)}{r^2}u^r - \frac{2}{r^2}\,u^r + \frac{2m(m+1)}{r^2}\,u^\Psi\right),\\
\frac{\partial u^\Psi}{\partial t} &= -\frac{\hat{p}}{r} + \nu\left(\frac{\partial^2 u^\Psi}{\partial r^2} + \frac{2}{r}\frac{\partial u^\Psi}{\partial r} - \frac{m(m+1)}{r^2}u^\Psi + \frac{2}{r^2}\,u^r\right),\\
0 &= \frac{1}{r^2}\frac{\partial}{\partial r}(r^2 u^r) - \frac{m(m+1)}{r}\,u^\Psi,\\
\frac{\partial X^r}{\partial t} &= u^r(1,t),\\
\frac{\partial X^\Psi}{\partial t} &= u^\Psi(1,t),
\end{aligned}$$

where the IB variables are written in terms of vector spherical harmonics as

$$\begin{aligned}
\boldsymbol{u} &= u^r(r,t)\boldsymbol{Y}^c_{m,k} + u^\Psi(r,t)\boldsymbol{\Psi}^c_{m,k},\\
p &= \hat{p}(r,t)Y^c_{m,k},\\
\boldsymbol{X} &= X^r(t)\boldsymbol{Y}^c_{m,k} + X^\Psi(t)\boldsymbol{\Psi}^c_{m,k}.
\end{aligned}$$

The $\boldsymbol{\Phi}_{m,k}$ component is ignored since we already showed in the Chapter 6 that this component is completely uncoupled from the linearized system. Furthermore, if we assume that the $\boldsymbol{\Phi}_{m,k}$ component is initially zero then it will remain zero for all time. It is for this reason that we only consider the $\boldsymbol{Y}_{m,k}$ and $\boldsymbol{\Phi}_{m,k}$ components of velocity and membrane position. We look for solutions of the form

$$u^r(r,t) = e^{\gamma t}\,\breve{u}^r(r),$$

and similarly for the other coefficient functions. Here, $\gamma \in \mathbb{C}$ characterizes the natural modes of the system in terms of decay rate $\Re\{\gamma\}$ and oscillation frequency $\Im\{\gamma\}$. Substituting this

solution form yields the differential-algebraic system

$$\gamma\breve{u}^r = -\frac{\mathrm{d}\breve{p}}{\mathrm{d}r} + \nu\left(\frac{\mathrm{d}^2\breve{u}^r}{\mathrm{d}r^2} + \frac{2}{r}\frac{\mathrm{d}\breve{u}^r}{\mathrm{d}r} - \frac{m(m+1)}{r^2}\breve{u}^r - \frac{2}{r^2}\,\breve{u}^r + \frac{2m(m+1)}{r^2}\,\breve{u}^\Psi\right), \quad (7.6a)$$

$$\gamma\breve{u}^\Psi = -\frac{\breve{p}}{r} + \nu\left(\frac{\mathrm{d}^2\breve{u}^\Psi}{\mathrm{d}r^2} + \frac{2}{r}\frac{\mathrm{d}\breve{u}^\Psi}{\mathrm{d}r} - \frac{m(m+1)}{r^2}\breve{u}^\Psi + \frac{2}{r^2}\,\breve{u}^r\right), \quad (7.6b)$$

$$0 = \frac{1}{r^2}\frac{\mathrm{d}}{\partial r}(r^2\breve{u}^r) - \frac{m(m+1)}{r}\,\breve{u}^\Psi, \quad (7.6c)$$

$$\gamma\breve{X}^r = \breve{u}^r(1), \quad (7.6d)$$

$$\gamma\breve{X}^\Psi = \breve{u}^\Psi(1), \quad (7.6e)$$

which is subject to the jump conditions

$$[\![\breve{u}^r]\!] = 0, \quad (7.7a)$$

$$[\![\breve{u}^\Psi]\!] = 0, \quad (7.7b)$$

$$[\![\breve{p}]\!] = -\kappa(m-1)(m+2)\breve{X}^r, \quad (7.7c)$$

$$\left[\!\!\left[\frac{\mathrm{d}\breve{u}^r}{\mathrm{d}r}\right]\!\!\right] = 0, \quad (7.7d)$$

$$\left[\!\!\left[\frac{\mathrm{d}\breve{u}^\Psi}{\mathrm{d}r}\right]\!\!\right] = \kappa(m-1)(m+2)\breve{X}^\Psi. \quad (7.7e)$$

The solution procedure mirrors that in the previous chapter. The pressure is a solution of Laplace's equation

$$\breve{p}(r) = \begin{cases} \breve{a}\,r^m, & \text{if } r < 1, \\ \breve{b}\,r^{-m-1}, & \text{if } r > 1, \end{cases}$$

where $\breve{a}$ and $\breve{b}$ are unknown constants that will be determined later. Following section 6.3, the radial velocity is

$$\breve{u}^r(r) = \begin{cases} -\dfrac{\mathrm{i}j_m(\mathrm{i}\beta r)}{\nu r}\big(\breve{a}mh_{m+1}(\mathrm{i}\beta) - \breve{b}(m+1)h_{m-1}(\mathrm{i}\beta)\big) - \dfrac{\breve{a}m}{\nu\beta^2}r^{m-1}, & \text{if } r < 1, \\ -\dfrac{\mathrm{i}h_m(\mathrm{i}\beta r)}{\nu r}\big(\breve{a}mj_{m+1}(\mathrm{i}\beta) - \breve{b}(m+1)j_{m-1}(\mathrm{i}\beta)\big) + \dfrac{\breve{b}(m+1)}{\nu\beta^2}r^{-m-2}, & \text{if } r > 1, \end{cases} \quad (7.8)$$

where

$$\beta = \sqrt{\gamma/\nu} \quad \text{with} \quad \Re\{\beta\} > 0, \quad (7.9)$$

and the tangential velocity is

$$\breve{u}^{\Psi}(r) = \begin{cases} -\dfrac{\mathrm{i}}{\nu}\left(\dfrac{j_m(\mathrm{i}\beta r)}{r} + \mathrm{i}\beta j_m'(\mathrm{i}\beta r)\right)\left(\breve{a}\,\dfrac{h_{m+1}(\mathrm{i}\beta)}{m+1} - \breve{b}\,\dfrac{h_{m-1}(\mathrm{i}\beta)}{m}\right) - \dfrac{\breve{a}}{\nu\beta^2}r^{m-1}, & \text{if } r<1, \\ -\dfrac{\mathrm{i}}{\nu}\left(\dfrac{h_m(\mathrm{i}\beta r)}{r} + \mathrm{i}\beta h_m'(\mathrm{i}\beta r)\right)\left(\breve{a}\,\dfrac{j_{m+1}(\mathrm{i}\beta)}{m+1} - \breve{b}\,\dfrac{j_{m-1}(\mathrm{i}\beta)}{m}\right) - \dfrac{\breve{b}}{\nu\beta^2}r^{-m-2}, & \text{if } r>1. \end{cases} \tag{7.10}$$

The membrane evolution equations reduce to the algebraic expressions

$$\begin{aligned} \gamma\breve{X}^r &= -\frac{\mathrm{i}\breve{a}m}{\nu}h_m(\mathrm{i}\beta)j_{m+1}(\mathrm{i}\beta) + \frac{\mathrm{i}\breve{b}(m+1)}{\nu}j_m(\mathrm{i}\beta)h_{m-1}(\mathrm{i}\beta), \\ \gamma\breve{X}^{\Psi} &= -\frac{\mathrm{i}\breve{a}}{(m+1)\nu}\big(h_m(\mathrm{i}\beta) + \mathrm{i}\beta h_m'(\mathrm{i}\beta)\big)j_{m+1}(\mathrm{i}\beta) + \frac{\mathrm{i}\breve{b}}{m\nu}\big(j_m(\mathrm{i}\beta) + \mathrm{i}\beta j_m'(\mathrm{i}\beta)\big)h_{m-1}(\mathrm{i}\beta), \end{aligned}$$

from which we find solutions for $\breve{a}$ and $\breve{b}$ to be

$$\begin{aligned} \breve{a} &= -\frac{\mathrm{i}\nu^2\beta^3}{m}\,\frac{j_m(\mathrm{i}\beta) + \mathrm{i}\beta j_m'(\mathrm{i}\beta)}{j_{m+1}(\mathrm{i}\beta)}\,\breve{X}^r + \mathrm{i}\nu^2\beta^3(m+1)\,\frac{j_m(\mathrm{i}\beta)}{j_{m+1}(\mathrm{i}\beta)}\,\breve{X}^{\Psi}, \\ \breve{b} &= -\frac{\mathrm{i}\nu^2\beta^3}{m+1}\,\frac{h_m(\mathrm{i}\beta) + \mathrm{i}\beta\, h_m'(\mathrm{i}\beta)}{h_{m-1}(\mathrm{i}\beta)}\,\breve{X}^r + \mathrm{i}\nu^2\beta^3 m\,\frac{h_m(\mathrm{i}\beta)}{h_{m-1}(\mathrm{i}\beta)}\,\breve{X}^{\Psi}. \end{aligned}$$

Next we substitute the above expressions into the jump in pressure (7.7c)

$$\begin{aligned} 0 = &\left[\frac{\zeta^2\beta^4}{2m+1}\left(2 - \frac{m}{m+1}\frac{h_{m+1}(i\beta)}{h_{m-1}(i\beta)} - \frac{m+1}{m}\frac{j_{m-1}(i\beta)}{j_{m+1}(i\beta)}\right) + (m+2)(m-1)\right]\breve{X}^r \\ &+ \frac{\zeta^2\beta^4}{2m+1}\left(1 - m\frac{h_{m+1}(i\beta)}{h_{m-1}(i\beta)} + (m+1)\frac{j_{m-1}(i\beta)}{j_{m+1}(i\beta)}\right)\breve{X}^{\Psi}, \end{aligned} \tag{7.11}$$

and the jump in tangential stress (7.7e)

$$\begin{aligned} 0 = &-i\zeta^2\beta^3\left(\frac{h_m(i\beta)}{(m+1)h_{m-1}(i\beta)} - \frac{j_m(i\beta)}{mj_{m+1}(i\beta)}\right)\breve{X}^r \\ &+ \left[-i\zeta^2\beta^3\left(\frac{h_m(i\beta)}{h_{m-1}(i\beta)} + \frac{j_m(i\beta)}{j_{m+1}(i\beta)}\right) - (m+2)(m-1)\right]\breve{X}^{\Psi}. \end{aligned} \tag{7.12}$$

The dimensionless parameter $\zeta = \frac{\nu}{\sqrt{\kappa}}$ determines the relative importance of the fluid viscosity and membrane stiffness. A similar parameter was introduced in section 5.4 describing the natural modes of the basilar membrane in the cochlea. Recalling the definition of ν in (7.2) and κ in (7.3), ζ can be written in terms of dimensional quantities as

$$\zeta = \frac{\mu}{\sqrt{\rho\sigma R}} = \frac{\sqrt{\rho R^3/\sigma}}{\rho R^2/\mu}. \tag{7.13}$$

Hence, ζ can be interpreted as a ratio of two time scales: a stiffness time scale divided by a viscous time scale.

Equations (7.11) and (7.12) can be written as a matrix equation

$$\mathbf{M}\begin{bmatrix}\breve{X}^r\\ \breve{X}^\Psi\end{bmatrix} = \mathbf{0},$$

where $\mathbf{M}$ is a 2×2 matrix that depends on ζ, β and m. Nontrivial solutions to this system exist only if

$$\det(\mathbf{M}) = 0, \tag{7.14}$$

which defines a dispersion relation for the natural (unforced) oscillations of the fluid-structure system. To calculate the decay rate and oscillation frequency of the natural modes, we find β by numerically solving equation (7.14) for given ζ and m, and then computing γ via (7.9). Figure 7.1 shows the decay rates and oscillation frequencies plotted against ζ for $m = 2$, 3 and 4. As expected, all decay rates are negative which implies that all perturbed membrane configurations tend toward the equilibrium state over time. For small ζ, damping effects are negligible and we observe that solutions are nearly periodic, that is $\Re\{\gamma\} \approx 0$. Moreover, the oscillation frequency approaches the value predicted by the inviscid theory, which is denoted by dashed lines in figure 7.1. For intermediate values of ζ, viscous effects become more significant and as a result the oscillation frequency decreases and solutions decay more rapidly. Finally, for large enough ζ viscosity dominates the system and solutions decay exponentially in time with no oscillations.

7.2.1 Numerical Simulations

To validate the analytical results just derived, we perform numerical simulations of the immersed boundary equations (7.1) with the same 3D code described in Chapter 6. The membrane is given the initial configuration

$$\boldsymbol{X}(\xi,\eta,0) = (1+\epsilon Y^c_{m,k}(\xi,\eta))\hat{\boldsymbol{r}},$$

where

$$\epsilon = \frac{0.1}{\max_{\xi,\eta}\left|Y^c_{m,k}(\xi,\eta)\right|}.$$

Computations are performed for several choices of ν and κ corresponding to $\zeta \in [10^{-2}, 2\times 10^{-1}]$, and for mode numbers $m = 2$, 3 and 4. To visualize the behaviour of a particular mode, we again compute the radial projection

$$X^r(t) = \int_0^\pi\int_0^{2\pi} \boldsymbol{X}\cdot\mathbf{Y}^c_{m,k}\,\sin\eta\,\mathrm{d}\xi\,\mathrm{d}\eta.$$

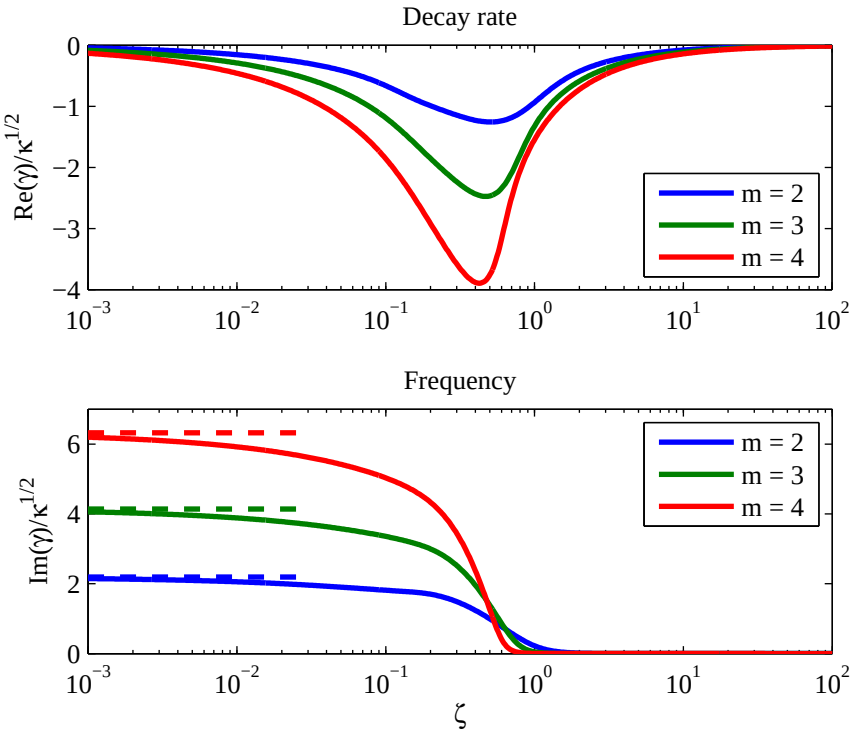

Figure 7.1: Decay rates (top) and oscillation frequency (bottom) of the natural modes for various m and ζ. The horizontal dashed lines in the lower plot indicate the oscillation frequency predicted by the linear inviscid theory (7.4).

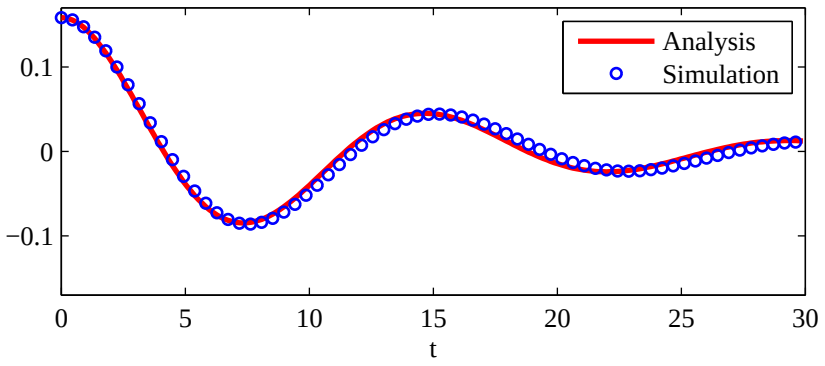

Figure 7.2: Comparison of $X^r(t)$ from a numerical simulation with the analytical results, for parameters $\nu = 0.01$ and $\kappa = 0.05$ ($\zeta = 0.0447$). The membrane is initialized with a (2,0)-mode.

Figure 7.2 plots a simulation using parameters $\nu = 0.01$ and $\kappa = 0.05$, where the membrane is initialized with a $(2, 0)$-mode. The predicted result from the analysis (solid line) is also plotted. We observe a similar qualitative behaviour between analytical and simulated results, however the simulation appears to have a slightly longer period. For a quantitative comparison, we approximate the decay rate and oscillation frequency from simulations by performing a least-squares fit to the function

$$X^{r*}(t) = \epsilon e^{c_r t}\left(\cos(c_i t) - \frac{c_r}{c_i}\sin(c_i t)\right),$$

which satisfies the initial conditions

$$X^{r*}(0) = \epsilon \quad \text{and} \quad \left.\frac{\mathrm{d}X^{r*}}{\mathrm{d}t}\right|_{t=0} = 0,$$

and the fitting parameters give

$$\frac{\gamma}{\sqrt{\kappa}} \approx (c_r + \mathrm{i}c_i)\sqrt{\frac{\rho R^3}{\sigma}}.$$

The least-squares fit is performed over the first complete oscillation and the results are plotted in figure 7.3 where the points indicate the numerical result and solid lines are from the analysis. The simulations follow the analytical results closely as ζ varies, however the decay rate and the oscillation frequency are slightly under-estimated by the numerical simulation. There are several factors that could account for this discrepancy, such as nonlinearity in the governing equations, interference due to periodic copies of the elastic shell, or errors introduced through the regularized Dirac delta function.

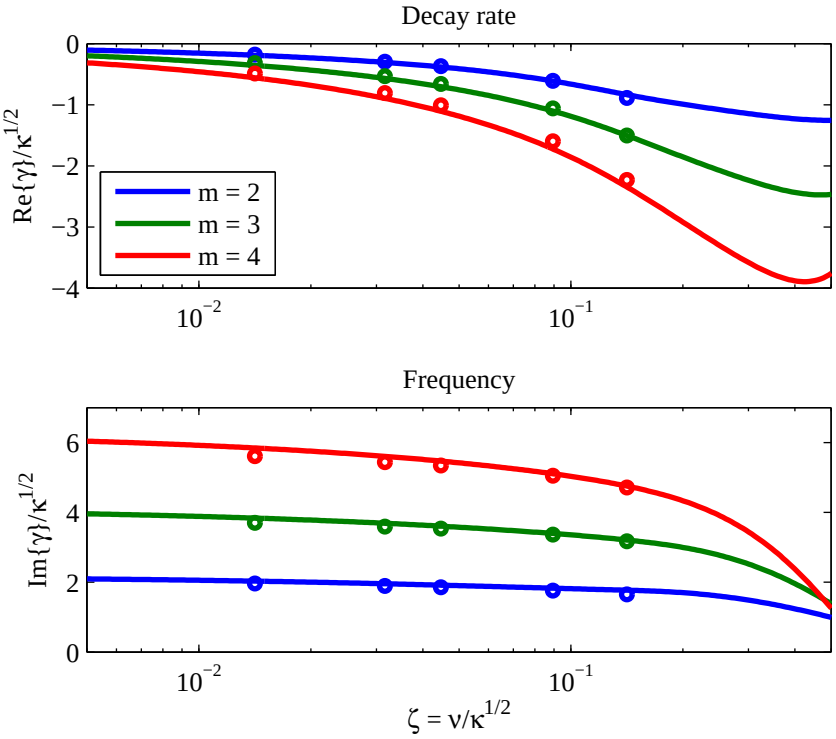

Figure 7.3: Decay rates and oscillation frequencies from numerical simulations denoted by ∘. The results from the linear viscous theory (solid curves) are plotted for comparison.

7.3 Nonlinear Oscillations in an Inviscid Fluid

In order to determine the relevance of nonlinearity in the membrane oscillation frequencies, we next extend the inviscid linear theory in section 7.1 to consider nonlinear effects. In particular, we incorporate the convective terms in the Navier-Stokes equations (7.1a) as well as previously neglected terms arising from the Dirac delta function in the singular forcing (7.1c). For simplicity, we assume the fluid to be irrotational and replace velocity with a potential function $\psi(\boldsymbol{x}, t)$ such that $\boldsymbol{u} = \nabla\psi$ and ψ satisfies

$$\Delta\psi = 0, \tag{7.15}$$

$$\frac{\partial\psi}{\partial t} + \frac{1}{2}|\nabla\psi|^2 = -p + p_0, \tag{7.16}$$

away from the membrane. The first equation is the incompressibility condition and the latter is Bernoulli's equation [70] where p_0 is the equilibrium pressure satisfying $[\![p_0]\!] = -2\kappa$. The pressure jump across the membrane is derived in [67] and also in Chapter 6 but we write it again for convenience as

$$\frac{1}{\sin\eta}\left\|\frac{\partial \boldsymbol{X}}{\partial\xi} \times \frac{\partial \boldsymbol{X}}{\partial\eta}\right\| [\![p]\!] = \hat{\boldsymbol{n}} \cdot \boldsymbol{F}. \tag{7.17}$$

Because the fluid is inviscid, we are only concerned with the radial component of the membrane position vector; that is, $\boldsymbol{X} = X\,\hat{\boldsymbol{r}}$ where $X(\xi, \eta, t)$ is the radial distance from the origin. At the membrane-fluid interface, we impose the no-penetration condition, which in terms of the potential function is

$$\hat{\boldsymbol{n}} \cdot \left(\frac{\partial \boldsymbol{X}}{\partial t} - \nabla\psi|_{r=X}\right) = 0. \tag{7.18}$$

In the absence of viscosity, we assume that solutions do not decay but instead are periodic functions of time with dimensionless frequency λ:

$$\begin{aligned}
\psi(\boldsymbol{x}, t) &= \psi(\boldsymbol{x}, t + 2\pi/\lambda), \\
p(\boldsymbol{x}, t) &= p(\boldsymbol{x}, t + 2\pi/\lambda), \\
\boldsymbol{X}(\boldsymbol{x}, t) &= \boldsymbol{X}(\boldsymbol{x}, t + 2\pi/\lambda).
\end{aligned}$$

Nonlinear oscillations of elastic fibres in an inviscid two-dimensional fluid have been investigated by Cortez and Varela [19]. Moreover, Tsamopoulos and Brown [120] performed a nonlinear analysis of axisymmetric drops and bubbles in inviscid fluids. Both studies employ the Lindstedt-Poincaré technique [92], which will be the method used in this analysis. The

Lindstedt-Poincaré method finds an approximate relationship between the membrane perturbation size ϵ and the oscillation frequency λ, for which we assume a regular asymptotic expansion

$$\lambda = \lambda_0 + \epsilon\lambda_1 + \epsilon^2\lambda_2 + \dots,$$

where λ_0 is the frequency from the linear theory (7.4) and the remaining λ_j for $j = 1, 2, \dots$ are to be determined. Next, we perform the following change of variables to simplify the problem: let $t = t^\star/\lambda$ so that solutions are 2π-periodic in time, and then let $r = Xr^\star$ so that the membrane location is determined by $r^\star = 1$. We then drop the superscript $\star$ to simplify notation. Upon substituting Bernoulli's equation (7.16) into the pressure jump (7.17), we arrive at a system of equations governing the oscillations:

$$\Delta\psi = 0, \tag{7.19a}$$

$$0 = \left[\!\!\left[\lambda\frac{\partial\psi}{\partial t} + \frac{|\nabla\psi|^2}{2X^2} - p_0\right]\!\!\right] \left\|\frac{\partial \boldsymbol{X}}{\partial\eta}\times\frac{\partial\boldsymbol{X}}{\partial\xi}\right\|^2 + \left(\frac{\partial\boldsymbol{X}}{\partial\eta}\times\frac{\partial\boldsymbol{X}}{\partial\xi}\right)\cdot\Delta_{\mathrm{S}}\boldsymbol{X}\sin\eta, \tag{7.19b}$$

$$0 = \left(\frac{\partial\boldsymbol{X}}{\partial\eta}\times\frac{\partial\boldsymbol{X}}{\partial\xi}\right)\cdot\left(\lambda\frac{\partial\boldsymbol{X}}{\partial t} - \frac{1}{X}\,\nabla\psi|_{r=1}\right), \tag{7.19c}$$

where

$$\hat{\boldsymbol{n}} = \frac{\frac{\partial\boldsymbol{X}}{\partial\eta}\times\frac{\partial\boldsymbol{X}}{\partial\xi}}{\left\|\frac{\partial\boldsymbol{X}}{\partial\eta}\times\frac{\partial\boldsymbol{X}}{\partial\xi}\right\|}.$$

Consider an initial membrane configuration deformed by an axisymmetric mode given by

$$\boldsymbol{X}(\xi,\eta,0) = \left(1 + \epsilon Y_{m,0}(\xi,\eta)\right)\hat{\boldsymbol{r}}$$

for $|\epsilon| \ll 1$. We look for a perturbation expansion of the potential function

$$\psi = \epsilon\psi_1 + \epsilon^2\psi_2 + \epsilon^3\psi_3 + \dots,$$

where each ψ_j satisfies Laplace's equation (7.19a). Furthermore, we expand the membrane configuration as

$$X = 1 + \epsilon X_1 + \epsilon^2 X_2 + \dots.$$

Next, we examine the governing equations at each power of ϵ starting with the $O(\epsilon)$ quantities governed by

$$\Delta\psi_1 = 0, \tag{7.20a}$$

$$0 = \left[\!\!\left[\lambda_0\frac{\partial\psi_1}{\partial t}\right]\!\!\right] - \kappa(m+2)(m-1)X_1, \tag{7.20b}$$

$$0 = \lambda_0\frac{\partial X_1}{\partial t} - \left.\frac{\partial\psi_1}{\partial r}\right|_{r=1}, \tag{7.20c}$$

and employ a spherical harmonic decomposition for the remaining unknowns

$$\psi_1(r,\theta,\phi,t) = \psi_m^{(1)}(r,t)Y_{m,0}(\theta,\phi) \quad \text{and} \quad X_1(\xi,\eta,t) = X_m^{(1)}(t)Y_{m,0}(\xi,\eta).$$

The potential function satisfies Laplace's equation (7.20a), hence

$$\psi_m^{(1)}(r,t) = \begin{cases} a_m^{(1)}(t)\, r^m, & \text{if } r < 1, \\ b_m^{(1)}(t)\; r^{-m-1}, & \text{if } r > 1, \end{cases}$$

where the unknown functions $a_m^{(1)}(t)$ and $b_m^{(1)}(t)$ are found from the no-penetration condition (7.20c) as

$$a_m^{(1)}(t) = \frac{\lambda_0}{m}\frac{\mathrm{d}X_m^{(1)}}{\mathrm{d}t} \quad \text{and} \quad b_m^{(1)}(t) = -\frac{\lambda_0}{m+1}\frac{\mathrm{d}X_m^{(1)}}{\mathrm{d}t}.$$

Substituting the potential function $\psi_m^{(1)}$ into the pressure jump (7.20b) yields

$$\frac{\mathrm{d}^2X_m^{(1)}}{\mathrm{d}t^2} + \frac{\kappa m(m+1)(m+2)(m-1)}{\lambda_0^2(2m+1)}X_m^{(1)} = 0.$$

Using the definition of λ_0 in (7.4), the coefficient multiplying $X_m^{(1)}$ in the second term reduces to one and hence the solutions to this ODE are 2π-periodic, as required. Thus, the solution for $X_m^{(1)}$ subject to initial conditions

$$X_m^{(1)}(0) = 1 \quad \text{and} \quad \left.\frac{\mathrm{d}X_m^{(1)}}{\mathrm{d}t}\right|_{t=0} = 0,$$

is $X_m^{(1)}(t) = \cos(t)$, so that the leading-order potential function is

$$\psi_1(r,\theta,\phi,t) = \begin{cases} -\sin t\, \dfrac{\lambda_0}{m}\, r^m\, Y_{m,0}(\theta,\phi), & \text{if } r < 1, \\ \sin t\, \dfrac{\lambda_0}{m+1}\; r^{-m-1}\, Y_{m,0}(\theta,\phi), & \text{if } r > 1. \end{cases}$$

In order to find the frequency correction λ_1, we now examine $O(\epsilon^2)$ quantities and represent the unknown functions as spherical harmonic expansions

$$\psi_2(r,\theta,\phi,t) = \sum_{n=2}^{\infty}\sum_{\ell=-n}^{n}\psi_{n,\ell}^{(2)}(r,t)Y_{n,\ell}(\theta,\phi) \quad \text{and} \quad X_2(\xi,\eta,t) = \sum_{n=2}^{\infty}\sum_{\ell=-n}^{n}X_{n,\ell}^{(2)}(t)Y_{n,\ell}(\xi,\eta),$$

with the coefficients $\psi_{n,\ell}^{(2)}$ given by

$$\psi_{n,\ell}^{(2)} = \begin{cases} a_{n,\ell}^{(2)}(t)\, r^n, & \text{if } r < 1, \\ b_{n,\ell}^{(2)}(t)\, r^{-n-1}, & \text{if } r > 1. \end{cases}$$

To find expressions for functions $a^{(2)}_{n,\ell}(t)$ and $b^{(2)}_{n,\ell}(t)$ we take the inner product of equation (7.19c) with the spherical harmonic $Y_{n,\ell}$ to obtain

$$a^{(2)}_{n,\ell}(t) = \frac{\lambda_0}{n}\frac{\mathrm{d}X^{(2)}_{n,\ell}}{\mathrm{d}t} - \frac{\lambda_1}{n}\sin t\,\langle Y_{m,0}, Y_{n,\ell}\rangle - \frac{\lambda_0}{2n}\sin(2t)\langle Y^2_{m,0}, Y_{n,\ell}\rangle,$$
$$b^{(2)}_{n,\ell}(t) = -\frac{\lambda_0}{n+1}\frac{\mathrm{d}X^{(2)}_{n,\ell}}{\mathrm{d}t} + \frac{\lambda_1}{n+1}\sin t\,\langle Y_{m,0}, Y_{n,\ell}\rangle + \frac{\lambda_0}{2(n+1)}\sin(2t)\langle Y^2_{m,0}, Y_{n,\ell}\rangle,$$

where $\langle\cdot,\cdot\rangle$ is the inner product defined by

$$\langle f, g\rangle = \int_0^{\pi}\int_0^{2\pi} f\,\overline{g}\,\sin\phi\,\mathrm{d}\theta\,\mathrm{d}\phi.$$

Furthermore, taking the inner product of the jump condition (7.19b) with $Y_{n,\ell}$ yields

$$\frac{\mathrm{d}b^{(2)}_{n,\ell}}{\mathrm{d}t} - \frac{\mathrm{d}a^{(2)}_{n,\ell}}{\mathrm{d}t} - \frac{\kappa(n+2)(n-1)}{\lambda_0}X^{(2)}_{n,\ell} + \frac{2m+1}{m(m+1)}\lambda_1\cos t\,\langle Y_{m,0}, Y_{n,\ell}\rangle$$
$$+ \frac{m^2+m-1}{\lambda_0}\big(1+\cos(2t)\big)\langle Y^2_{m,0}, Y_{n,\ell}\rangle + \frac{\lambda_0}{4(m+1)^2}\big(1-\cos(2t)\big)\langle|\boldsymbol{\Psi}_{m,0}|^2, Y_{n,\ell}\rangle = 0.$$

Substituting the functions $a^{(2)}_{n,\ell}(t)$ and $b^{(2)}_{n,\ell}(t)$ into the above equation leads to the second-order ODE

$$\begin{aligned}\frac{\mathrm{d}^2X^{(2)}_{n,\ell}}{\mathrm{d}t^2} + \frac{\kappa n(n+1)(n+2)(n-1)}{\lambda_0^2(2n+1)}X^{(2)}_{n,\ell} &= 2\frac{\lambda_1}{\lambda_0}\cos t\,\langle Y_{m,0}, Y_{n,\ell}\rangle + \cos(2t)\langle Y^2_{m,0}, Y_{n,\ell}\rangle \\ &+ \frac{m^2+m-1}{\lambda_0^2}\frac{n(n+1)}{2n+1}\big(1+\cos(2t)\big)\langle Y^2_{m,0}, Y_{n,\ell}\rangle \\ &+ \frac{1}{(m+1)^2}\frac{n(n+1)}{4(2n+1)}\big(1-\cos(2t)\big)\langle|\boldsymbol{\Psi}_{m,0}|^2, Y_{n,\ell}\rangle.\end{aligned} \tag{7.21}$$

If $n = m$ and $\ell = 0$, then the first term on the right-hand side of (7.21) will lead to non-periodic, unbounded solutions to $X^{(2)}_{n,\ell}$ since $\cos t$ is a homogeneous solution. For this reason we set $\lambda_1 = 0$ to eliminate that term and hence guarantee 2π-periodic solutions.

The nonlinear projection terms in (7.21) can be expressed as

$$\langle Y^2_{m,0}, Y_{n,\ell}\rangle = (-1)^{\ell}\sqrt{\frac{(2m+1)^2(2n+1)}{4\pi}}\begin{pmatrix} m & m & n\\ 0 & 0 & 0\end{pmatrix}\begin{pmatrix} m & m & n\\ 0 & 0 & -\ell\end{pmatrix},$$

$$\langle|\boldsymbol{\Psi}_{m,0}|^2, Y_{n,\ell}\rangle = \begin{cases} -m(m+1)\sqrt{\dfrac{(2m+1)^2(2n+1)}{4\pi}}\begin{pmatrix} m & m & n\\ 1 & -1 & 0\end{pmatrix}\begin{pmatrix} m & m & n\\ 0 & 0 & 0\end{pmatrix}, & \text{if } \ell = 0,\\ 0, \quad \text{otherwise,}\end{cases}$$

where each 2×3 array is a Wigner 3-j symbol [113] and represents a scalar quantity. In general, the 3-j symbol is a function of six variables

$$\begin{pmatrix} m_1 & m_2 & m_3 \\ k_1 & k_2 & k_3 \end{pmatrix},$$

and is nonzero when all of the following conditions on m_j and k_j are met:

- $k_1 + k_2 + k_3 = 0$,
- $m_1 + m_2 + m_3$ is an integer, and is even if $k_1 = k_2 = k_3 = 0$,
- $|m_1 - m_2| \leq m_3 \leq m_1 + m_2$ and,
- $|k_j| \leq m_j$ for each $j = 1$, 2 or 3.

Hence the right-hand side of ODE (7.21) is nonzero if $\ell = 0$ and n is even with $2 \leq n \leq 2m$. For example, if the membrane is initialized with a $(2,0)$-mode, then

$$\frac{\mathrm{d}^2 X_{2,0}^{(2)}}{\mathrm{d}t^2} + X_{2,0}^{(2)} = \frac{23}{56}\sqrt{\frac{5}{\pi}}\cos(2t) - \frac{9}{56}\sqrt{\frac{5}{\pi}}, \tag{7.22a}$$

$$\frac{\mathrm{d}^2 X_{4,0}^{(2)}}{\mathrm{d}t^2} + \frac{25}{3}X_{4,0}^{(2)} = \frac{403}{378\sqrt{\pi}}\cos(2t) + \frac{425}{378\sqrt{\pi}}, \tag{7.22b}$$

while for all other (n,ℓ) we have

$$\frac{\mathrm{d}^2 X_{n,\ell}^{(2)}}{\mathrm{d}t^2} + \frac{\kappa n(n+1)(n+2)(n-1)}{\lambda_0^2(2n+1)}X_{n,\ell}^{(2)} = 0. \tag{7.22c}$$

The initial $O(\epsilon)$ perturbation transfers energy to the $O(\epsilon^2)$ terms via nonlinear interactions. In the above ODEs (7.22), we see that only the $(2,0)$- and $(4,0)$-modes are excited by the nonlinear terms and so we assume that solutions to the remaining $O(\epsilon^2)$ equations, governed by the homogeneous equation (7.22c), are zero since they are not driven by the $X_{2,0}^{(1)}(t)$ term.

Continuing with the example, we take the inner product of the $O(\epsilon^3)$ terms of equations (7.19b) and (7.19c) with $Y_{2,0}$ to obtain the ODE

$$\frac{\mathrm{d}^2 X_{2,0}^{(3)}}{\mathrm{d}t^2} + X_{2,0}^{(3)} = \left(\sqrt{\kappa}\frac{\pi\sqrt{30}}{6}\lambda_2 + \kappa\frac{3531}{784}\right)\cos t + \kappa\frac{8364}{4704}\cos(3t).$$

Again, we must eliminate the $\cos t$ term on the right-hand side to ensure periodicity by setting

$$\lambda_2 = -\frac{3531\sqrt{30}}{3920\pi}\sqrt{\kappa}$$

Therefore, the frequency of the membrane oscillation up to $O(\epsilon^2)$ is

$$\lambda = \lambda_0 \left(1 - \frac{7061}{3136\pi}\,\epsilon^2\right) \approx \lambda_0(1 - 0.7167\,\epsilon^2).$$

Following the same procedure, a membrane initialized with a $(3,0)$-mode oscillates with frequency

$$\lambda = \lambda_0 \left(1 - \frac{529881455}{198772992\pi}\epsilon^2\right) \approx \lambda_0(1 - 0.8485\,\epsilon^2).$$

Similarly, for a $(4,0)$-mode

$$\lambda = \lambda_0 \left(1 - \frac{60326472574591}{18039224403200\pi}\epsilon^2\right) \approx \lambda_0(1 - 1.0645\,\epsilon^2).$$

In the above examples, we see that nonlinear terms decrease the oscillation frequency of an immersed shell, but this effect is on the order of ϵ^2 which is small for even moderately small perturbations ϵ.

For an initial configuration perturbed by a non-axisymmetric mode, that is $k \neq 0$, the inner product in the last term of (7.21) is replaced by $\langle |\mathbf{\Psi}_{m,k}|^2, Y_{n,\ell}\rangle$ which is nonzero for an infinite number of (n,ℓ). This introduces a new challenge in the analysis which we do not consider in this thesis, but is nonetheless worthy of possible future study.

7.4 An Experimental Study of Immersed Water Balloons

In this section, we present an experiment with immersed water balloons where we consider natural, 2-mode oscillations for a range of balloon types and inflation radii R. The goal of this experiment is corroborate the theoretical results presented in the previous sections using data.

7.4.1 Materials and Methods

We use three types of latex balloons, each with various characteristics. The first type, which we label "A", is a regular party balloon with maximum inflated radius of 15 cm. The second, "B", is a "punch" balloon which also has a maximum inflated radius of 15 cm but is thicker than type "A". Lastly, balloon "C" is a large party balloon which can be as large as 45 cm radially when fully inflated and is thicker than the previous two (see table 7.1).

Our IB model of an immersed spherical shell uses a simple force density which leads to the Young-Laplace equation

$$[\![p]\!] = \frac{2\sigma}{R}, \tag{7.23}$$

Identifier	Description	Thickness (cm)	Maximum inflated radius (cm)
A	Regular party balloon	0.0203	15
B	"Punch" balloon	0.0279	15
C	Large party balloon	0.0381	45

Table 7.1: List of balloon types used in the oscillation experiment.

Balloon Type	R (cm)	$[\![p]\!]$ (dyn/cm^2)	σ (dyn/cm)
A	6	30990	92970
A	9	21900	98550
A	12	25900	155400
B	9	25300	113850
B	12	21720	130320
B	15	20500	153750
C	15	19850	148875
C	20	14970	149700
C	25	12530	156625

Table 7.2: Pressure difference and effective membrane stiffness corresponding to the sample data. The pressure difference is measured with a digital manometer and the effective membrane stiffness is calculated with the Young-Laplace equation.

at equilibrium. However, rubber is often treated as a Mooney-Rivlin type material [89] and follows a pressure curve

$$[\![p]\!] = 2s_1 \frac{d_0}{R_0}\left(\frac{R_0}{R} - \left(\frac{R_0}{R}\right)^7\right)\left(1 - \frac{s_{-1}}{s_1}\left(\frac{R}{R_0}\right)^2\right),$$

where R_0 and d_0 are the radius and thickness of the balloon prior to inflation respectively, and s_1 and s_{-1} are material constants. In order to compare the experimental results to our IB model, we interpret σ as an *effective stiffness* that varies with inflation radius R, instead of an actual material stiffness. To measure the effective stiffness, we fill the balloon with air and use a digital manometer to measure the pressure difference between the interior of the ballon and the atmosphere. We then calculate σ with the aforementioned Young-Laplace equation (7.23) assuming the balloon is a sphere. The pressure measurements and effective stiffnesses are summarized in table 7.2.

We perform the experiment in the Simon Fraser University swimming pool, where we inflated each balloon to a desired radius and then lightly squeeze the balloon on opposite sides in order to excite a 2-mode. The oscillations are filmed using a Nikon Coolpix AW120 Waterproof Camera with the image capture rate set to 30 frames per second. A few snapshots covering a single oscillation are shown in figure 7.4.

According to equations (7.8) and (7.10), the fluid velocity decays at rate $O(r^{-4})$ for a 2-mode as r increases. At a distance R away from the membrane, the velocity is about 6% smaller than that at the membrane. Therefore to reduce any boundary effects we ensure that the balloon is at least a distance R from either the pool floor or upper surface.

The video data is analyzed with the image processing toolbox in MATLAB. For a single movie frame, we first isolate the balloon from the rest of the image using a colour-based segmentation technique [85]. An example of an image segmentation is shown in figure 7.5. We then convert the segmented balloon image to a binary image (black and white) and extract the edge using MATLAB's `bwboundaries`. From this curve we can then calculate the maximum diameter of the balloon.

7.4.2 Results and Discussion

Figure 7.6 shows a plot of the maximum diameter for a complete video sequence from which the period of oscillation can be estimated by the length of time between alternating local maxima in the plot. The plot shows a fairly consistent period throughout, however there is a clear downward trend in the maximum radius which can be attributed to the balloon drifting away from the camera.

Using typical parameters for water, $\rho = 1.00\ \mathrm{g\,cm^{-3}}$ and $\mu = 0.01\ \mathrm{g\,cm^{-1}\,s^{-1}}$, we find that the dimensionless parameter ζ is small, with $\zeta \in [5.05 \times 10^{-6}, 1.34 \times 10^{-5}]$. This implies that the elastic force dominates the system and fluid viscosity is negligible. Hence, the experimental results can be predicted by the inviscid theory of oscillation. The results of the experiment are summarized in table 7.3 along with the predicted results from the linear inviscid theory, linear viscous theory, and the nonlinear inviscid theory. At its greatest extent, the diameter of the balloon can be up to 13% larger than the equilibrium diameter, hence

$$\epsilon \approx \frac{0.13}{\max|Y_{2,0}|} = 0.13\sqrt{\frac{4\pi}{5}} \approx 0.20609.$$

It is for this reason that we use a representative value of $\epsilon = 0.2$ for the nonlinear theory in table 7.3. We plot both experimental and analytical results in figure 7.7 which clearly shows that there is a relatively large discrepancy between the experimental and theoretical results, however the error appears to be consistent within each balloon type. This suggests a shortcoming in either our mathematical model or experimental procedure.

Lund and Dalziel [79] performed an experiment where a small water-filled balloon with maximum inflated radius of 6.5 cm is placed on a support inside a water tank. The balloon

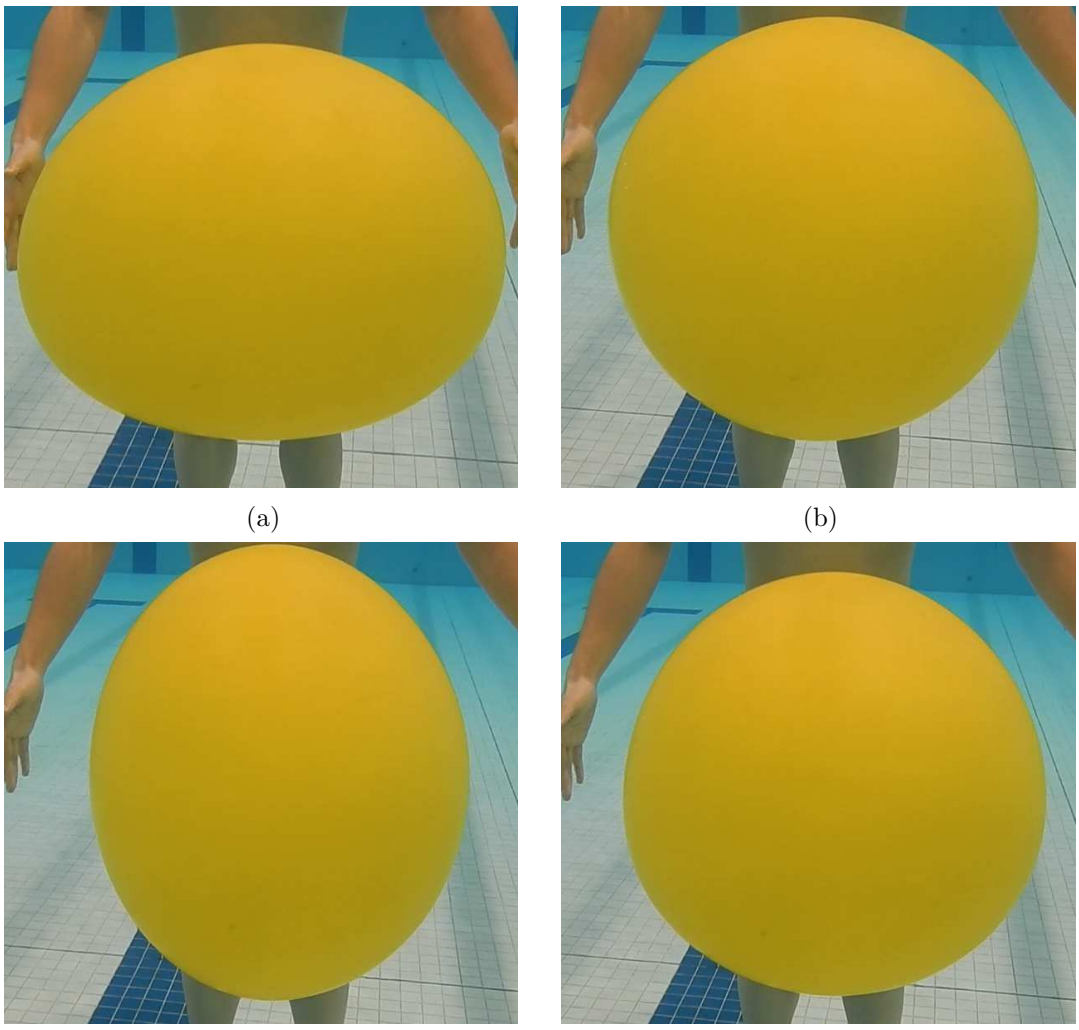

(a) (b)

(c) (d)

Figure 7.4: A sequence of images showing an oscillation of an immersed water balloon of type C with $R = 25$ cm.

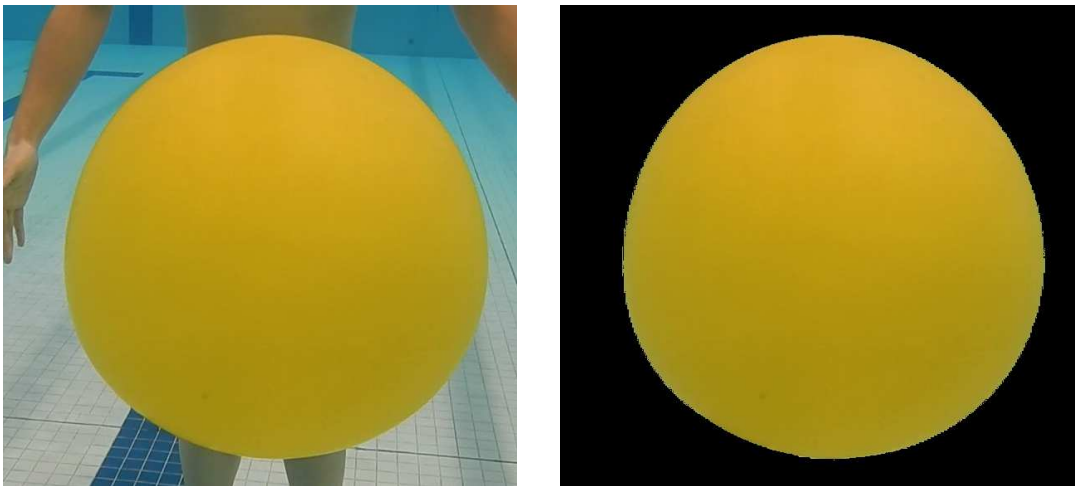

(a) (b)

Figure 7.5: An example of the colour-based segmentation technique applied to a single video frame. (a) Original image. (b) Segmented image.

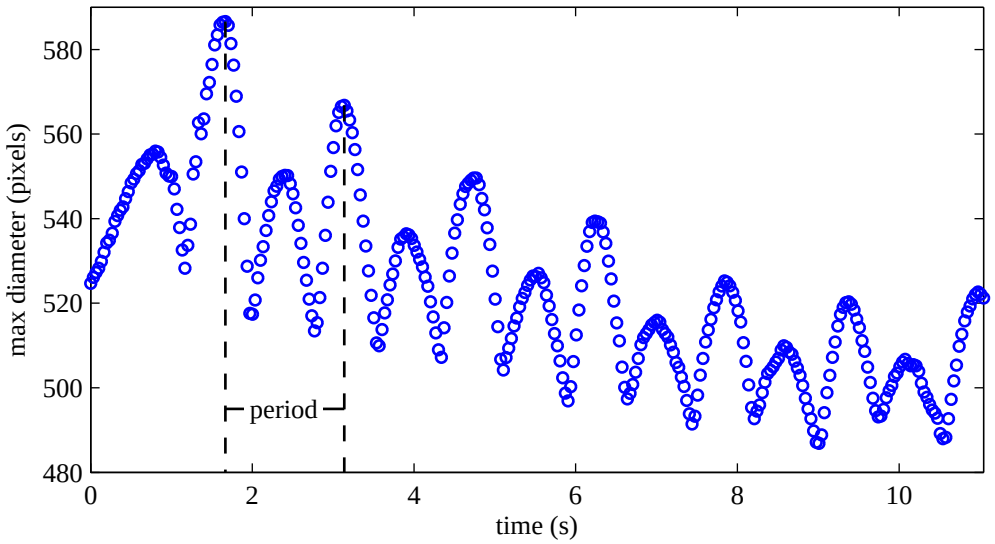

Figure 7.6: Maximum diameter measured in pixels for a single experiment (Balloon type C, $R = 25$ cm). The period of oscillation is estimated as the time between alternating local maxima. The downward trend in diameter is due to the balloon drifting away from the camera after it is released.

Type, R (cm)	Frequency (1/s) Experiment	Inviscid Theory	Viscous Theory	Nonlinear Theory ($\epsilon = 0.2$)
A, 6	31.4	45.45	45.35	44.15
A, 9	18.9	25.47	25.42	24.74
A, 12	13.8	20.78	20.74	20.18
B, 9	15.7	27.38	27.33	26.59
B, 12	11.1	19.03	18.99	18.48
B, 15	9.4	14.79	14.76	14.36
C, 15	8.6	14.55	14.53	14.13
C, 20	5.5	9.48	9.46	9.21
C, 25	4.2	6.94	6.93	6.74

Table 7.3: Balloon oscillation frequencies measured from the experiment. The predicted frequencies from the linear inviscid theory, the linear viscous theory, and the nonlinear theory are also shown for comparison.

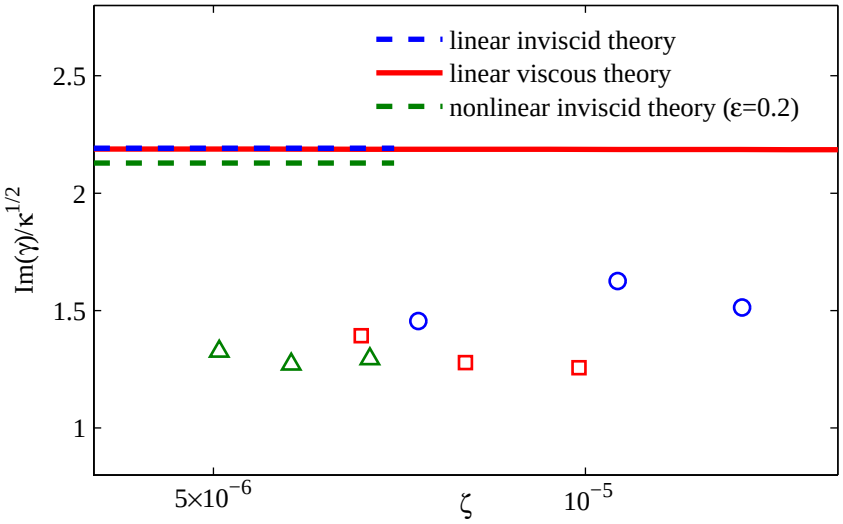

Figure 7.7: Comparison of analytical and experimental frequencies plotted against ζ on a log scale. The experimental results are scaled to be dimensionless and are denoted by balloon type: A ○, B □, and C △.

was periodically forced by a rod attached to a speaker. The pressure difference was measured with a water column manometer that is connected to the balloon through the small support in the tank. The balloon oscillations were captured with a high-resolution camera and the oscillation frequency and spatial wavenumber were measured from the resulting footage. Their result shows good agreement with Lamb's inviscid linear theory of oscillation for a range of wavenumbers $6 \leq m \leq 13$. Comparing our experiment with that by Lund and Dalziel [79], there are several notable differences that may account for the discrepancy in our result:

- Balloon perturbation — The experimental setup by Lund and Dalziel [79] allowed consistent small amplitude surface waves so that their experimental results remain within the linear regime. Our initial perturbations may be too large such that the simple force density (7.1e) in our model may not be suitable to describe the elastic force for large balloon deformations. A nonlinear elasticity, for example neo-Hookean or Mooney-Rivlin, may be required in our model to accurately capture the behaviour of our balloon oscillations.

- Pressure measurement — The pressure data in table 7.2 was measured by filling the balloon with air while our oscillation experiments were performed underwater. The fact that the pressure data was taken in a completely different environment could introduce an error in our effective stiffness σ.

- Boundary effects — The boundary effects due to the arms and body of the balloon holder may impede the velocity field near the balloon and decrease the oscillation frequency. Lund and Dalziel [79] placed the balloon on a small stationary support to minimize boundary effects.

Any or all of these factors may contribute to the discrepancy between our analytical and experimental results and resolving this discrepancy is ongoing work.

Chapter 8

Conclusions

In this thesis, we have demonstrated the existence of parametric instabilities in a spherical elastic shell immersed in an incompressible viscous fluid, wherein the motion is driven by periodic contractions of the shell. A mathematical model was derived using an immersed boundary framework that captures the full two-way interaction between the elastic material and the surrounding fluid. A Floquet analysis of the linearized governing equations is performed using an expansion in terms of vector spherical harmonics. We obtained results regarding the stability of the internally forced system with and without viscosity, and showed with the aid of Ince-Strutt diagrams that fluid-mechanical resonance exists regardless of whether viscous damping is present. Numerical simulations of the full IB model were performed that confirm the presence of these parametric resonances. Moreover, in Chapter 5 we propose an IB model of the cochlea, for the purpose of investigating the relevance of parametric resonance as a novel mechanism for amplification of basilar membrane oscillations. A summary of our findings and concluding remarks on the cochlea can be found in section 5.7.

Because our original motivation for considering this problem derived from the study of periodic contractions driving blood flow in the heart, we also discussed the relevance of our stability analysis to cardiac fluid dynamics. Indeed, our analysis suggests that periodic resonances can occur in an idealized spherical shell geometry for physical parameters corresponding to the heart and provides possible parameter ranges to investigate in an experimental study that could test for resonant solutions. These results are preliminary and much more work needs to be done to determine whether fluid-structure driven resonances can actually play a role in cardiac flows.

In Chapter 7, we considered the natural oscillations of unforced spherical membranes.

We derived a dispersion relation for an oscillating membrane that gives the decay rate and oscillation frequency depending on the fluid parameters, membrane stiffness and spherical harmonic mode number. We also performed a nonlinear analysis without viscosity and derived a correction term to the oscillation frequency up to $O(\epsilon^2)$ for a perturbation amplitude $|\epsilon| \ll 1$. Lastly, we presented an experiment of the oscillations of immersed water balloons and compared the data to the analytical results. Although the experimental data do not match the analytical results, the discrepancy between the two is consistent and resolving this issue is ongoing work.

8.1 Future Work

Our cochlea model in Chapter 5 proposes a novel hypothesis that parametric resonance contributes to the active process that amplifies basilar membrane oscillations and is the contribution in this thesis that has the greatest potential impact. Future work and extensions to our cochlea model are discussed in section 5.7.

One major step in bringing our results in Chapter 6 closer to the actual heart is to generalize our time-periodic (but spatially uniform) driving force to include the effect of spiral waves of contraction that are initiated through electrical signals propagating in the heart wall [30]. Including such spatiotemporal variations in the driving force would naturally couple together the radial and angular VSH components, but generalizing the analysis to handle this fully coupled problem could lead to significant new insights into a more realistic model of FSI in the beating heart.

One possible area of application is the study of cell membrane protrusions appearing in the process of cell locomotion, which although still not well understood are thought to be a mechanism for cells to move by deforming their membrane. Cottet et al. [21] considered parametric resonance as a possible cause of cell membrane protrusions, but a thorough analysis has yet to be done. Another possible biological application is cellular cytokinesis which is the separation of the cell cytoplasm into two daughter cells. It has been observed that an asymmetric cell division may lead to a shape instability and cause cytokinesis to fail [114]. Hence it is interesting to consider if parametric resonance contributes to these instabilities. Cellular dynamics have already been investigated extensively using an IB approach [28, 102] and so analyzing membrane protrusions and cytokinesis in the IB framework appears to offer significant promise.

The results in this thesis can benefit the scientific computing community with the development of a 3D FSI benchmark problem. A common test case that is often employed to

validate numerical algorithms in FSI problems involves an oscillating spherical elastic shell immersed in a fluid [20, 35, 108], however these tests are not compared to any benchmark problem. Using the approximate analytical solution derived in this thesis, together with the IB implementation by Wiens [127, 128], we can design and validate a benchmark problem to which FSI software developers can compare their simulations. We proposed one such benchmark computation problem in [63].

Chapters 6 and 7 focussed on spherical membranes but it is worth exploring other geometries such as a (periodic) cylinder or a torus. The former would be a simple extension of the analysis by Cortez et al. [18]. Both of these geometries allow unidirectional fluid flow and provide an ideal setting to study new areas of application, for example fluid flow via valveless pumping which may explain blood flow in the early developmental stages of the human embryo [76, 98].

Bibliography

[1] M. Abramowitz and I. A. Stegun. *Handbook of Mathematical Functions With Formulas, Graphs and Mathematical Tables*. Dover Publications, New York, 1965.

[2] J. B. Allen. Two-dimensional cochlea fluid model: New results. *J. Acoust. Soc. Am.*, **61**:110–119, 1977.

[3] J. F. Ashmore. Cochlear outer hair cell motility. *Physiol. Rev.*, **88**:173–210, 2008.

[4] J. F. Ashmore, P. Avan, W. E. Brownell, P. Dallos, K. Dierkes, R. Fettiplace, K. Grosh, C. M. Hackney, A. J. Hudspeth, F. Jülicher, B. Lindner, P. Martin, J. Meaud, C. Petit, J. Santos-Sacchi, J. R. S. Sacchi, and B. Canlon. The remarkable cochlear amplifier. *Hearing Res.*, **266**:1–17, 2010.

[5] W. Baker. Axisymetric modes of vibration of thin spherical shell. *J. Acoust. Soc. Am.*, **33**(12):1749–1758, 1961.

[6] A. Baricz. *Generalized Bessel Functions of the First Kind*. Springer-Verlag, New York, 2010.

[7] R. G. Barrera, G. A. Estevez, and J. Giraldo. Vector spherical harmonics and their application to magnetostatics. *Eur. J. Phys.*, **6**:287–294, 1985.

[8] M. V. Bartuccelli, G. Gentile, and K. V. Georgiou. On the dynamics of a vertically driven damped planar pendulum. *Proc. R. Soc. London A*, **457**:3007–3022, 2001.

[9] M. F. Beatty. Small amplitude radial oscillations of an incompressible, isotropic elastic spherical shell. *Math. Mech. Solids*, **16**(5):492–512, 2011.

[10] T. B. Benjamin and F. Ursell. The stability of the plane free surface of a liquid in vertical periodic motion. *Proc. R. Soc. London A*, **225**(1163):505–515, 1954.

[11] R. P. Beyer. A computational model of the cochlea using the immersed boundary method. *J. Comput. Phys.*, **98**:145–162, 1992.

[12] R. N. Bracewell. *The Fourier Transform and Its Applications*. McGraw-Hill, New York, 2000.

[13] E. Braunwald, E. C. Brockenbrough, C. J. Frahm, and J. Ross. Left atrial and left ventricular pressures in subjects without cardiovascular disease: Observations in eighteen patients studied by transseptal left heart catheterization. *Circulation*, **24**(2):267–269, 1961.

[14] W. E. Brownell, C. R. Bader, D. Bertrand, and Y. de Ribaupierre. Evoked mechanical responses of isolated cochlear outer hair cells. *Science*, **227**(4683):194–196, 1985.

[15] R. S. Chadwick, A. Inselberg, and K. Johnson. Mathematical model of the cochlea II: Results and conclusions. *SIAM J. Appl. Math.*, **30**(1):164–179, 1976.

[16] A. R. Champneys. Dynamics of parametric excitation. In R. A. Meyers, editor, *Encyclopedia of Complexity and Systems Science*, pages 2323–2345. Springer, New York, 2009.

[17] A. J. Chorin. A numerical method for solving incompressible viscous flow problems. *J. Comput. Phys.*, **135**:185–125, 1967.

[18] R. Cortez, C. S. Peskin, J. M. Stockie, and D. Varela. Parametric resonance in immersed elastic boundaries. *SIAM J. Appl. Math.*, **65**(2):494–520, 2004.

[19] R. Cortez and D. Varela. The dynamics of an elastic membrane using the impulse method. *J. Comput. Phys.*, **138**(1):224–247, 1997.

[20] G.-H. Cottet and E. Maitre. A level set method for fluid-structure interactions with immersed surfaces. *Math. Model. Methods Appl. Sci.*, **16**(3):415–438, 2006.

[21] G.-H. Cottet, E. Maitre, and T. Milcent. An Eulerian method for fluid-structure coupling with biophysical applications. In P. Wesseling, E. Oñate, and J. Périaux, editors, *European Conference on Computational Fluid Dynamics*. Delft, The Netherlands, 2006.

[22] P. Dallos. The active cochlea. *J. Neurosci.*, **12**(12):4575–4585, 1992.

[23] E. de Boer. The "inverse problem" solved for a three-dimensional model of the cochlea. I. Analysis. *J. Acoust. Soc. Am.*, **98**(2):896–903, 1995.

[24] A. J. Devaney and E. Wolf. Multipole expansions and plane wave representations of the electromagnetic field. *J. Math. Phys.*, **15**(2):234–245, 1974.

[25] R. Dillon, L. J. Fauci, A. L. Fogelson, and D. Gaver III. Modeling biofilm processes using the immersed boundary method. *J. Comput. Phys.*, **129**(1):57–73, 1996.

[26] B. Epp, J. L. Verhey, and M. Mauermann. Modeling cochlear dynamics: Interrelation between cochlea mechanics and psychoacoustics. *J. Acoust. Soc. Am.*, **128**(4):1870–1883, 2010.

[27] M. Faraday. On a peculiar class of acoustical figures; and on certains forms assumed by groups of particles upon vibrating elastic surfaces. *Philos. Trans. R. Soc. London*, **121**:299–340, 1831.

[28] L. J. Fauci and R. Dillon. Biofluidmechanics of reproduction. *Annu. Rev. Fluid Mech.*, **38**:371–394, 2006.

[29] B. U. Felderhof. Jittery velocity relaxation of an elastic sphere immersed in a viscous incompressible fluid. *Phys. Rev. E*, **89**(3):033001, 2014.

[30] R. FitzHugh. Impulses and physiological states in theoretical models of nerve membrane. *Biophys. J.*, **1**(6):445–466, 1961.

[31] M. G. Floquet. Sur les équations différentielles linéaires à coefficients périodiques. *Ann. Sci. l'École Norm. Supérieure*, **12**:47–88, 1883.

[32] A. Friedman and B. Hu. Bifurcation for a free boundary problem modeling tumor growth by Stokes equation. *SIAM J. Math. Anal.*, **39**(1):174–194, 2007.

[33] B. D. Froese and J. K. Wiens. MatIB's User Guide. July 2013. Available at github.com/eldila/MatIB.

[34] C. D. Geisler. *From Sound to Synapse: Physiology of the Mammalian Ear.* Oxford University Press, New York, 1998.

[35] E. Givelberg. Modeling elastic shells immersed in fluid. *Commun. Pure Appl. Math.*, **57**(3):283–309, 2004.

[36] E. Givelberg and J. Bunn. A comprehensive three-dimensional model of the cochlea. *J. Comput. Phys.*, **191**(2):377–391, 2003.

[37] T. Gold. Hearing. II. The physical basis of the action of the cochlea. *Proc. R. Soc. London B*, **135**(881):492–498, 1948.

[38] T. Gold and R. J. Pumphrey. Hearing. I. The cochlea as a frequency analyzer. *Proc. R. Soc. London B*, **135**(881):462–491, 1948.

[39] B. E. Griffith, R. D. Hornung, D. M. McQueen, and C. S. Peskin. An adaptive, formally second order accurate version of the immersed boundary method. *J. Comput. Phys.*, **223**(1):10–49, 2007.

[40] P. Grinfeld. Small oscillations of a soap bubble. *Stud. Appl. Math.*, **128**:30–39, 2011.

[41] A. Y. Gunawan, J. Molenaar, and A. A. F. van de Ven. Does shear flow stabilize an immersed thread? *Eur. J. Mech. - B/Fluids*, **24**(3):379–396, 2005.

[42] W. W. Hansen. A new type of expansion in radiation problems. *Phys. Rev.*, **47**(2):139–143, 1935.

[43] S. Hayek. Vibration of a spherical shell in an acoustic medium. *J. Acoust. Soc. Am.*, **40**(2):342–348, 1966.

[44] H. L. F. Helmholtz. *The Sensations of Tone: As a Physiological Basis for the Theory of Music*. Longmans, Green and Co., New York, 1875.

[45] E. L. Hill. The theory of vector spherical harmonics. *Am. J. Phys.*, **22**(4):211–214, 1954.

[46] R. F. Hoskins. *Delta Functions: Introduction to Generalised Functions*. Horwood Publishing, Chichester, UK, second edition, 2009.

[47] J. Howard and A. J. Hudspeth. Compliance of the hair bundle associated with gating of mechanoelectrical transduction channels in the bullfrog's saccular hair cell. *Neuron*, **1**(3):189–199, 1988.

[48] W.-X. Huang and H. J. Sung. An immersed boundary method for fluid-flexible structure interaction. *Comput. Methods Appl. Mech. Engrg.*, **198**(33-36):2650–2661, 2009.

[49] A. J. Hudspeth. Making an effort to listen: mechanical amplification in the ear. *Neuron*, **59**(4):530–545, 2008.

[50] A. J. Hudspeth, F. Jülicher, and P. Martin. A critique of the critical cochlea: Hopf – a bifurcation – is better than none. *J. Neurophysiol.*, **104**:1219–1229, 2010.

[51] A. Inselberg and R. S. Chadwick. Mathematical model of the cochlea I: Formulation and solution. *SIAM J. Appl. Math.*, **30**(1):149–163, 1976.

[52] P. Jäckel and T. Mullin. A numerical and experimental study of codimension-2 points in a parametrically excited double pendulum. *Proc. R. Soc. London A*, **454**(1980):3257–3274, 1998.

[53] R. W. James. The spectral form of the magnetic induction equation. *Proc. R. Soc. London A*, **340**:287–299, 1974.

[54] D. W. Jordan and P. Smith. *Nonlinear Ordinary Differential Equations An Introduction to Dynamical Systems*. Oxford University Press, Oxford, third edition, 1999.

[55] A. Kalnins and P. M. Naghdi. Axisymmetric vibrations of shallow elastic spherical shells. *J. Acoust. Soc. Am.*, **32**(3):342–347, 1960.

[56] J. B. Keller and J. Neu. Asymptotic analysis of a viscous cochlear model. *J. Acoust. Soc. Am.*, **77**(6):2107–2110, 1985.

[57] D. T. Kemp. Stimulated acoustic emissions from within the human auditory system. *J. Acoust. Soc. Am.*, **64**(5):1386–1391, 1978.

[58] A. Kern, C. Heid, W. H. Steeb, N. Stoop, and R. Stoop. Biophysical parameters modification could overcome essential hearing gaps. *PLoS Comput. Biol.*, **4**(8):e1000161, 2008.

[59] Y. Kim and C. S. Peskin. 3-D parachute simulation by the immersed boundary method. *Comput. Fluids*, **38**(6):1080–1090, 2009.

[60] Y. Kim and J. Xin. A two-dimensional nonlinear nonlocal feed-forward cochlear model and time domain computation of multitone interactions. *Multiscale Model. Simul.*, **4**(2):664–690, 2005.

[61] C. Kleinstreuer. *Biofluid Dynamics: Principles and Selected Applications*. CRC Press, Boca Raton, 2006.

[62] W. Ko and J. M. Stockie. An immersed boundary model of the cochlea with parametric forcing. *SIAM J. Appl. Math.* Accepted, April 2015.

[63] W. Ko and J. M. Stockie. Parametric resonance in spherical immersed elastic shells. *SIAM J. Appl. Math.* Submitted, April 2015.

[64] K. Kumar and L. S. Tuckerman. Parametric instability of the interface between two fluids. *J. Fluid Mech.*, **279**:49–68, 1994.

[65] K. A. Kuo and H. E. M. Hunt. The vibrations of bubbles and balloons. *Acoust. Aust.*, **40**(3):183–187, 2012.

[66] K. A. Kuo, H. E. M. Hunt, and J. R. Lister. Vibration of pressurised, elastic, spherical shells. In *20th International Congress on Sound and Vibration*, pages 1–7. Bangkok, Thailand, 2013.

[67] M.-C. Lai and Z. Li. A remark on jump conditions for the three-dimensional Navier-Stokes equations involving an immersed moving membrane. *Appl. Math. Lett.*, **14**:149–154, 2001.

[68] M.-C. Lai and C. S. Peskin. An immersed boundary method with formal second-order accuracy and reduced numerical viscosity. *J. Comput. Phys.*, **160**(2):705–719, 2000.

[69] H. Lamb. *Hydrodynamics*. Cambridge University Press, 1932.

[70] L. D. Landau and E. M. Lifshitz. *Fluid Mechanics*. Pergamon Press, Oxford, 1959.

[71] M. B. Lesser and D. A. Berkley. Fluid mechanics of the cochlea. Part 1. *J. Fluid Mech.*, **51**(3):497–512, 1972.

[72] R. J. LeVeque and Z. Li. Immersed interface methods for Stokes flow with elastic boundaries or surface tension. *SIAM J. Sci. Comput.*, **18**(3):709–735, 1997.

[73] R. J. LeVeque, C. S. Peskin, and P. D. Lax. Solution of a two-dimensional cochlea model using transform techniques. *SIAM J. Appl. Math.*, **45**(3):450–464, 1985.

[74] R. J. LeVeque, C. S. Peskin, and P. D. Lax. Solution of a two-dimensional cochlea model with fluid viscosity. *SIAM J. Appl. Math.*, **48**(1):191–213, 1988.

[75] M. J. Lighthill. *Mathematical Biofluiddynamics*. Society for Industrial and Applied Mathematics, Philadelphia, 1975.

[76] S. Lim and E. Jung. Three-dimensional simulations of a closed valveless pump system immersed in a viscous fluid. *SIAM J. Appl. Math.*, **70**(6):1999–2022, 2010.

[77] M. S. Link. Clinical practice. Evaluation and initial treatment of supraventricular tachycardia. *N. Engl. J. Med.*, **367**(15):1438–1448, 2012.

[78] A. E. H. Love. The small free vibrations and deformation of a thin elastic shell. *Philos. Trans. R. Soc. London A*, **179**:491–546, 1888.

[79] H. M. Lund and S. B. Dalziel. Bursting water balloons. *J. Fluid Mech.*, **756**:771–815, 2014.

[80] F. Mammano and R. Nobili. Biophysics of the cochlea: Linear approximation. *J. Acoust. Soc. Am.*, **93**(6):3320–3332, 1993.

[81] D. Manoussaki and R. S. Chadwick. Effects of geometry on fluid loading in a coiled cochlea. *SIAM J. Appl. Math.*, **61**(2):369–386, 2000.

[82] D. Manoussaki, E. K. Dimitriadis, and R. S. Chadwick. Cochlea's graded curvature effect on low frequency waves. *Phys. Rev. Lett.*, **96**:088701, 2006.

[83] V. S. Markin and A. J. Hudspeth. Modeling the active process of the cochlea: phase relations, amplification, and spontaneous oscillation. *Biophys. J.*, **69**(1):138–147, 1995.

[84] E. Mathieu. Memoire sur le mouvement vibratoire d'une membrane de forme elliptique. *J. Math. Pures Appliq. Série 2*, **13**:137–203, 1868.

[85] MathWorks Inc. Color-based segmentation using the L*a*b* color space. Last accessed: January 11, 2015. URL: www.mathworks.com/examples/image/2087.

[86] L. A. Miller and C. S. Peskin. When vortices stick: An aerodynamic transition in tiny insect flight. *J. Exp. Biol.*, **207**(17):3073–3088, 2004.

[87] Y. Mori and C. S. Peskin. Implicit second-order immersed boundary methods with boundary mass. *Comput. Methods Appl. Mech. Engrg.*, **197**(25-28):2049–2067, 2008.

[88] H. W. Müller. Linear aspects of the Faraday instability. In *A Perspective Look at Nonlinear Media: From Physics to Biology and Social Sciences*, volume 503 of *Lecture Notes in Physics*, pages 45–60. Springer-Verlag, Berlin, 1998.

[89] I. Müller and H. Struchtrup. Inflating a rubber balloon. *Math. Mech. Solids*, **7**(5):569–577, 2002.

[90] R. C. Naidu and D. C. Mountain. Basilar membrane tension calculations for the gerbil cochlea. *J. Acoust. Soc. Am.*, **121**(2):994–1002, 2007.

[91] A. H. Nayfeh. *Introduction to Perturbation Techniques*. Wiley, New York, 1981.

[92] A. H. Nayfeh and D. T. Mook. *Nonlinear Oscillations*. Wiley, New York, 1979.

[93] S. T. Neely. Finite difference solution of a two-dimensional mathematical model of the cochlea. *J. Acoust. Soc. Am.*, **69**(5):1386–1393, 1981.

[94] F. I. Niordson. Free vibrations of thin elastic spherical shells. *Int. J. Solids Struct.*, **20**(7):667–687, 1984.

[95] R. Nobili, F. Mammano, and J. F. Ashmore. How well do we understand the cochlea? *Trends Neurosci.*, **21**(4):159–167, 1998.

[96] E. S. Olson, H. Duifhuis, and C. R. Steele. Von Békésy and cochlear mechanics. *Hearing Res.*, **293**(1-2):31–43, 2012.

[97] Online CBSE Textbooks. Neural control and coordination. Last accessed: February 22, 2015. URL: cbsetextbooks.weebly.com/21-neural-control-and-coordination.html.

[98] J. T. Ottesen. Valveless pumping in a fluid-filled closed elastic tube-system: One-dimensional theory with experimental validation. *J. Math. Biol.*, **46**:309–332, 2003.

[99] P.-O. Persson and G. Strang. A simple mesh generator in MATLAB. *SIAM Rev.*, **46**:329–345, 2004.

[100] C. S. Peskin. *Partial differential equations in biology (lecture notes)*. Courant Institute of Mathematical Sciences, New York University, New York, 1976.

[101] C. S. Peskin. Numerical analysis of blood flow in the heart. *J. Comput. Phys.*, **25**:220–252, 1977.

[102] C. S. Peskin. The immersed boundary method. *Acta Numer.*, **11**:1–39, 2002.

[103] C. S. Peskin and B. F. Printz. Improved volume conservation in the computation of flows with immersed elastic boundaries. *J. Comput. Phys.*, **105**:33–46, 1993.

[104] R. E. Phillips and M. K. Feeney. *The Cardiac Rhythms: A Systematic Approach to Interpretation*. Saunders, Philadelphia, 1973.

[105] F. J. Poulin, G. R. Flierl, and J. Pedlosky. Parametric instability in oscillatory shear flows. *J. Fluid Mech.*, **481**:329–353, 2003.

[106] C. Pozrikidis. Boundary-integral modeling of cochlear hydrodynamics. *J. Fluids Struct.*, **24**(3):336–365, 2008.

[107] S. Ramamoorthy, N. V. Deo, and K. Grosh. A mechano-electro-acoustical model for the cochlea: Response to acoustic stimuli. *J. Acoust. Soc. Am.*, **121**(5):2758–2773, 2007.

[108] S. Ramanujan and C. Pozrikidis. Deformation of liquid capsules enclosed by elastic membranes in simple shear flow: large deformations and the effect of fluid viscosities. *J. Fluid Mech.*, **361**:117–143, 1998.

[109] L. Rayleigh. On the capillary phenomena of jets. *Proc. R. Soc. London*, **29**:71–97, 1879.

[110] T. Reichenbach and A. J. Hudspeth. A ratchet mechanism for amplification in low-frequency mammalian hearing. *Proc. Natl. Acad. Sci. U. S. A.*, **107**(11):4973–4978, 2010.

[111] T. Reichenbach and A. J. Hudspeth. The physics of hearing: Fluid mechanics and the active process of the inner ear. *Rep. Prog. Phys.*, **77**:076601, 2014.

[112] T. Reichenbach, A. Stefanovic, F. Nin, and A. J. Hudspeth. Waves on Reissner's membrane: A mechanism for the propagation of otoacoustic emissions from the cochlea. *Cell Rep.*, **1**(4):374–384, 2012.

[113] M. Rotenberg, R. Bivins, N. Metropolis, and J. K. Wooten Jr. *The 3-j and 6-j Symbols*. The Technology Press, Cambridge, 1959.

[114] J. Sedzinski, M. Biro, A. Oswald, J.-Y. Tinevez, G. Salbreux, and E. Paluch. Polar actomyosin contractility destabilizes the position of the cytokinetic furrow. *Nature*, **476**(7361):462–466, 2011.

[115] C. Semler and M. P. Païdoussis. Nonlinear analysis of the parametric resonances of a planar fluid-conveying cantilevered pipe. *J. Fluids Struct.*, **10**:787–825, 1996.

[116] D. A. Sonstegard. Effects of a surrounding fluid on the free, axisymmetric vibrations of thin elastic spherical shells. *J. Acoust. Soc. Am.*, **45**(2):506–510, 1969.

[117] J. M. Stockie and S. I. Green. Simulating the motion of flexible pulp fibres using the immersed boundary method. *J. Comput. Phys.*, **147**:147–165, 1998.

[118] J. M. Stockie and B. T. R. Wetton. Stability analysis for the immersed fiber problem. *SIAM J. Appl. Math.*, **55**(6):1577–1591, 1995.

[119] D. Terzopoulos and K. Fleischer. Deformable models. *Vis. Comput.*, **4**(6):306–331, 1988.

[120] J. A. Tsamopoulos and R. A. Brown. Nonlinear oscillations of inviscid drops and bubbles. *J. Fluid Mech.*, **127**:519–537, 1983.

[121] S. Verhulst, T. Dau, and C. A. Shera. Nonlinear time-domain cochlear model for transient stimulation and human otoacoustic emission. *J. Acoust. Soc. Am.*, **132**(6):3842–3848, 2012.

[122] S. Vogel. *Life in Moving Fluids*. Princeton University Press, second edition, 1994.

[123] G. von Békésy. Zur Theorie des Hörens; Die Schwingungsform der Basilarmembran. *Phys. Z.*, **29**:793–810, 1928.

[124] G. von Békésy. *Experiments in Hearing*. McGraw-Hill, New York, 1960.

[125] W. Wang, D. Buehler, A. M. Martland, X. D. Feng, and Y. J. Wang. Left atrial wall tension directly affects the restoration of sinus rhythm after Maze procedure. *Eur. J. Cardio-thoracic Surg.*, **40**:77–82, 2011.

[126] X. Wang. Instability analysis of some fluid-structure interaction problems. *Comput. Fluids*, **32**:121–138, 2003.

[127] J. K. Wiens. *An Efficient Parallel Immersed Boundary Algorithm, with Application to the Suspension of Flexible Fibers*. Ph.D. thesis, Simon Fraser University, 2014.

[128] J. K. Wiens and J. M. Stockie. An efficient parallel immersed boundary algorithm using a pseudo-compressible fluid solver. *J. Comput. Phys.*, **281**:917–941, 2015.

[129] J. Wu and F. Zhou. Asymptotic behaviour of solutions of a free boundary problem modeling the growth of tumors with fluid-like tissue under the action of inhibitors. *Trans. Am. Math. Soc.*, **365**(8):4181–4207, 2013.

[130] J. Xin. Dispersive instability and its minimization in time-domain computation of steady-state responses of cochlear models. *J. Acoust. Soc. Am.*, **115**(5):2173–2177, 2004.

[131] S. Xu and Z. J. Wang. Systematic derivation of jump conditions for the immersed interface method in three-dimensional flow simulation. *SIAM J. Sci. Comput.*, **27**(6):1948–1980, 2006.

[132] T. Yen. Forced vibrations of submerged spheroidal shells. *J. Acoust. Soc. Am.*, **41**(3):618–626, 1967.

[133] G. Zweig. Finding the impedance of the organ of Corti. *J. Acoust. Soc. Am.*, **89**(3):1229–1254, 1991.

Appendix A

Bessel Functions and Spherical Bessel Functions

This thesis makes extensive use of both Bessel functions (in Chapter 4) and spherical Bessel functions (in Chapters 6 and 7). Many useful properties and recurrence relations for both types of Bessel functions can be found in the classic handbook by Abramowitz and Stegun [1] and are reproduced in this appendix. To avoid repetition, this discussion of Bessel functions and spherical Bessel functions is consolidated by considering *generalized Bessel functions* [6].

Consider the ODE

$$z^2 w''(z) + azw'(z) + (z^2 - m(m+d-1))w(z) = 0. \tag{A.1}$$

If $d = 1$, we have Bessel's ODE with two linearly independent solutions denoted $J_m(z)$ and $Y_m(z)$, called the mth-order *Bessel functions* of the first and second kind respectively. There is another pair of linearly independent solutions called *Hankel functions* of the first and second kind (or Bessel functions of the third and fourth kind)

$$H_m^{(1)}(z) = J_m(z) + \mathrm{i}Y_m(z),$$
$$H_m^{(2)}(z) = J_m(z) - \mathrm{i}Y_m(z).$$

If $d = 2$ in ODE (A.1), the solutions are called mth-order *spherical Bessel functions* of the first and second kind, which are denoted by j_m and y_m respectively. The Bessel functions and spherical Bessel functions are related by

$$j_m(z) = \sqrt{\frac{\pi}{2z}} J_{m+\frac{1}{2}}(z),$$
$$y_m(z) = \sqrt{\frac{\pi}{2z}} Y_{m+\frac{1}{2}}(z).$$

The *spherical Hankel functions* of the first and second kind are defined in an analogous way

$$h_m^{(1)}(z) = j_m(z) + \mathrm{i}y_m(z),$$
$$h_m^{(2)}(z) = j_m(z) - \mathrm{i}y_m(z).$$

Note that the ODE (A.1) can be generalized further to incorporate modified Bessel functions and modified spherical Bessel functions [6].

We present a list of properties of generalized Bessel functions that are used in this thesis, using $w_m(z)$ to denote any solution to ODE (A.1) and $d \in \{1, 2\}$.

- Recurrence relation for generalized Bessel functions

$$w_{m+1}(z) = \left(\frac{2m+d-1}{z}\right) w_m(z) - w_{m-1}(z). \tag{A.2}$$

- Derivative of generalized Bessel functions

$$w'_m(z) = \frac{m}{z} w_m(z) - w_{m+1}(z), \tag{A.3}$$
$$w'_m(z) = w_{m-1}(z) - \left(\frac{m+d-1}{z}\right) w_m(z), \tag{A.4}$$
$$w'_m(z) = \frac{1}{2}(w_{m-1}(z) - w_{m+1}(z)) - \left(\frac{d-1}{2z}\right) w_m(z). \tag{A.5}$$

- Derivative of a product of a power function and a generalized Bessel function

$$\left(z^{m+2} w_{m+1}(\beta z)\right)' = \beta z^{m+2} w_m(\beta z), \tag{A.6}$$
$$\left(z^{1-m} w_{m-1}(\beta z)\right)' = -\beta z^{1-m} w_m(\beta z), \tag{A.7}$$

  where $\beta \in \mathbb{C}$.

- Integral of a product of a power function and a generalized Bessel function

$$\int w_m(\beta z) z^{m+2} \mathrm{d}z = \frac{1}{\beta} z^{m+2} w_{m+1}(\beta z) + C, \tag{A.8}$$
$$\int w_m(\beta z) z^{1-m} \mathrm{d}z = -\frac{1}{\beta} z^{1-m} w_{m+1}(\beta z) + C, \tag{A.9}$$

  where $\beta \in \mathbb{C}$ and C is an arbitrary constant of integration.

- Second derivative of a generalized Bessel function

$$w''_m(z) = \left(\frac{d^2 - 1 - 2z^2}{4z^2}\right) w_m(z) - \left(\frac{d-1}{2z}\right)(w_{m-1}(z) - w_{m+1}(z)) + \frac{1}{4}(w_{m-2}(z) + w_{m+2}(z)). \tag{A.10}$$

The following combinations between (spherical) Bessel functions and (spherical) Hankel functions of different orders can be simplified dramatically

$$J_{m+1}(z)H_m^{(1)}(z) - J_m(z)H_{m+1}^{(1)}(z) = \frac{2\mathrm{i}}{\pi z}, \tag{A.11}$$

$$j_{m+1}(z)h_m^{(1)}(z) - j_m(z)h_{m+1}^{(1)}(z) = \frac{\mathrm{i}}{z^2}. \tag{A.12}$$

Lastly, the Wronskian of a (spherical) Bessel function and a (spherical) Hankel function can be simplified

$$J_m(z)H_m^{(1)\prime}(z) - J_m'(z)H_k^{(1)}(z) = \frac{2\mathrm{i}}{\pi z}, \tag{A.13}$$

$$j_m(z)h_m^{(1)\prime}(z) - j_m(z)h_m^{(1)\prime}(z) = \frac{\mathrm{i}}{z^2}. \tag{A.14}$$

More properties of Bessel and spherical Bessel functions can be found in [1].

Appendix B

Spherical Harmonics and Vector Spherical Harmonics

Owing to the spherical geometry and the rotational symmetry of the elastic membrane in Chapters 6 and 7, we decompose solutions in terms of spherical harmonics and vector spherical harmonics. For the reader's convenience we provide a brief description of these functions and a list of properties used in this thesis.

The *spherical harmonics* are eigenfunctions of the spherical Laplacian

$$\Delta_{\mathrm{S}} Y_{m,k} = \frac{1}{\sin\phi}\frac{\partial}{\partial\phi}\left(\sin\phi\,\frac{\partial Y_{m,k}}{\partial\phi}\right) + \frac{1}{\sin^2\phi}\frac{\partial^2 Y_{m,k}}{\partial\theta^2} = -m(m+1)Y_{m,k},$$

hence these functions greatly simplify problems that involve the Laplacian operator. For example, given a scalar function $f(r)$, the Laplacian of $f(r)Y_{m,k}$ is

$$\Delta(f(r)Y_{m,k}) = \left(\frac{1}{r^2}\frac{\mathrm{d}}{\mathrm{d}r}\left(r^2\frac{\mathrm{d}f}{\mathrm{d}r}\right) - \frac{m(m+1)}{r^2}\,f\right)Y_{m,k}, \tag{B.1}$$

which reduces to a differential operator with respect to r only. The normalized spherical harmonic of degree m and order k is

$$Y_{m,k}(\theta,\phi) = (-1)^k\sqrt{\frac{2m+1}{4\pi}\frac{(m-k)!}{(m+k)!}}\,e^{\mathrm{i}k\theta}\,P_{m,k}(\cos\phi),$$

where $P_{m,k}(x)$ is the *associated Legendre polynomial* of degree m and order k [1]. The set $\{Y_{m,k}\}$ forms an orthonormal basis in L^2 with respect to the inner product

$$\langle g, h\rangle = \int_0^{\pi}\int_0^{2\pi} g\,\overline{h}\,\sin\phi\,\mathrm{d}\theta\,\mathrm{d}\phi,$$

where the bar denotes the complex conjugate. This property permits any scalar field in L^2 to be written as a linear combination of spherical harmonics.

The *vector spherical harmonics* (or VSH) are an extension of spherical harmonics to vector-valued functions. Several definitions are proposed literature [7, 42, 45, 53], however the definitions presented by Hill [45] and Barrera et al. [7] are the most prominent in the fluid mechanics literature. Hill [45] defines VSH in terms of spherical harmonics by

$$\begin{aligned}
\boldsymbol{V}_{m,k} &= -\sqrt{\frac{m+1}{2m+1}}\, Y_{m,k}\, \hat{\boldsymbol{r}} + \frac{\mathrm{i}k}{\sqrt{(m+1)(2m+1)}\sin\phi}\, Y_{m,k}\, \hat{\boldsymbol{\theta}} \\
&\qquad + \frac{1}{\sqrt{(m+1)(2m+1)}} \frac{\partial Y_{m,k}}{\partial \phi}\, \hat{\boldsymbol{\phi}}, \\
\boldsymbol{X}_{m,k} &= -\frac{\mathrm{i}}{\sqrt{m(2m+1)}} \frac{\partial Y_{m,k}}{\partial \phi}\, \hat{\boldsymbol{\theta}} - \frac{k}{\sqrt{m(2m+1)}\sin\phi}\, Y_{m,k}\, \hat{\boldsymbol{\phi}}, \\
\boldsymbol{W}_{m,k} &= \sqrt{\frac{m}{2m+1}}\, Y_{m,k}\, \hat{\boldsymbol{r}} + \frac{\mathrm{i}k}{\sqrt{m(2m+1)}\sin\phi}\, Y_{m,k}\, \hat{\boldsymbol{\theta}} \\
&\qquad + \frac{1}{\sqrt{m(2m+1)}} \frac{\partial Y_{m,k}}{\partial \phi}\, \hat{\boldsymbol{\phi}}.
\end{aligned}$$

The above are eigenfunctions of the spherical Laplacian operator that satisfies

$$\begin{aligned}
\Delta_{\mathrm{S}} \boldsymbol{V}_{m,k} &= -(m+1)(m+2)\boldsymbol{V}_{m,k}, \\
\Delta_{\mathrm{S}} \boldsymbol{X}_{m,k} &= -m(m+1)\boldsymbol{X}_{m,k}, \\
\Delta_{\mathrm{S}} \boldsymbol{W}_{m,k} &= -m(m-1)\boldsymbol{W}_{m,k}.
\end{aligned}$$

In this thesis we instead use the basis presented by Barrera et al. [7]

$$\begin{aligned}
\boldsymbol{Y}_{m,k}(\theta,\phi) &= Y_{m,k}\hat{\boldsymbol{r}}, \\
\boldsymbol{\Psi}_{m,k}(\theta,\phi) &= r\nabla Y_{m,k} = \frac{\mathrm{i}k}{\sin\phi} Y_{m,k}\hat{\boldsymbol{\theta}} + \frac{\partial Y_{m,k}}{\partial \phi}\hat{\boldsymbol{\phi}}, \\
\boldsymbol{\Phi}_{m,k}(\theta,\phi) &= \hat{\boldsymbol{r}} \times \boldsymbol{\Psi}_{m,k} = \frac{\partial Y_{m,k}}{\partial \phi}\hat{\boldsymbol{\theta}} - \frac{\mathrm{i}k}{\sin\phi} Y_{m,k}\hat{\boldsymbol{\phi}}.
\end{aligned}$$

The VSH basis by Barrera et al. is related to Hill's by

$$\begin{aligned}
\boldsymbol{Y}_{m,k} &= -\sqrt{\frac{m+1}{2m+1}}\boldsymbol{V}_{m,k} + \sqrt{\frac{m}{2m+1}}\boldsymbol{W}_{m,k}, \\
\boldsymbol{\Psi}_{m,k} &= m\sqrt{\frac{m+1}{2m+1}}\boldsymbol{V}_{m,k} + (m+1)\sqrt{\frac{m}{2m+1}}\boldsymbol{W}_{m,k}, \\
\boldsymbol{\Phi}_{m,k} &= \mathrm{i}\sqrt{m(2m+1)}\boldsymbol{X}_{m,k}.
\end{aligned}$$

For a scalar function $f(r)$, the gradient of a scalar field is given by

$$\nabla(f(r)Y_{m,k}) = \frac{\mathrm{d}f}{\mathrm{d}r}\boldsymbol{Y}_{m,k} + \frac{f}{r}\boldsymbol{\Psi}_{m,k}. \tag{B.2}$$

The divergence and curl of a vector $\boldsymbol{u} = u^r(r)\boldsymbol{Y}_{m,k} + u^\Phi(r)\boldsymbol{\Psi}_{m,k} + u^\Psi(r)\boldsymbol{\Phi}_{m,k}$ are

$$\nabla \cdot \boldsymbol{u} = \left(\frac{1}{r^2}\frac{\mathrm{d}}{\mathrm{d}r}(r^2 u^r) - \frac{m(m+1)}{r}\, u^\Phi\right) Y_{m,k}, \tag{B.3}$$

$$\nabla \times \boldsymbol{u} = -\frac{m(m+1)}{r}\, u^\Psi\, \boldsymbol{Y}_{m,k} - \frac{1}{r}\frac{\mathrm{d}}{\mathrm{d}r}(r u^\Psi)\, \boldsymbol{\Psi}_{m,k} + \left(-\frac{1}{r}u^r + \frac{1}{r}\frac{\mathrm{d}}{\mathrm{d}r}(r u^\Phi)\right) \boldsymbol{\Phi}_{m,k}. \tag{B.4}$$

Observe that the divergence of a vector has no contribution from the u^Ψ term because $\boldsymbol{\Phi}_{m,k}$ is always divergence free

$$\nabla \cdot \boldsymbol{\Phi}_{m,k} = 0.$$

Using (B.2), (B.3) and (B.4), we derive the vector Laplacian

$$\begin{aligned}
\Delta \boldsymbol{u} &= \nabla(\nabla \cdot \boldsymbol{u}) - \nabla \times (\nabla \times \boldsymbol{u}), \\
&= \left(\frac{\mathrm{d}^2 u^r}{\mathrm{d}r^2} + \frac{2}{r}\frac{\mathrm{d}u^r}{\mathrm{d}r} - \frac{m(m+1)}{r^2}\, u^r - \frac{2}{r^2}\, u^r + \frac{2m(m+1)}{r^2}\, u^\Phi\right) \boldsymbol{Y}_{m,k} \\
&\qquad + \left(\frac{\mathrm{d}^2 u^\Phi}{\mathrm{d}r^2} + \frac{2}{r}\frac{\mathrm{d}u^\Phi}{\mathrm{d}r} - \frac{m(m+1)}{r^2}\, u^\Phi + \frac{2}{r^2}\, u^r\right) \boldsymbol{\Psi}_{m,k} \\
&\qquad + \left(\frac{\mathrm{d}^2 u^\Psi}{\mathrm{d}r^2} + \frac{2}{r}\frac{\mathrm{d}u^\Psi}{\mathrm{d}r} - \frac{m(m+1)}{r^2}\, u^\Psi\right) \boldsymbol{\Phi}_{m,k}.
\end{aligned} \tag{B.5}$$

The set $\{\boldsymbol{Y}_{m,k}, \boldsymbol{\Psi}_{m,k}, \boldsymbol{\Phi}_{m,k}\}$ forms an orthogonal basis in L^2 because

$$\begin{aligned}
\langle \boldsymbol{Y}_{m,k}, \boldsymbol{Y}_{m',k'} \rangle &= \delta_{mm'}\delta_{kk'}, \\
\langle \boldsymbol{\Psi}_{m,k}, \boldsymbol{\Psi}_{m',k'} \rangle &= m(m+1)\delta_{mm'}\delta_{kk'}, \\
\langle \boldsymbol{\Phi}_{m,k}, \boldsymbol{\Phi}_{m',k'} \rangle &= m(m+1)\delta_{mm'}\delta_{kk'}, \\
\langle \boldsymbol{Y}_{m,k}, \boldsymbol{\Psi}_{m',k'} \rangle &= 0, \\
\langle \boldsymbol{\Psi}_{m,k}, \boldsymbol{\Phi}_{m',k'} \rangle &= 0, \\
\langle \boldsymbol{\Phi}_{m,k}, \boldsymbol{Y}_{m',k'} \rangle &= 0,
\end{aligned}$$

where $\langle \cdot, \cdot \rangle$ is the L^2 inner product

$$\langle \boldsymbol{g}, \boldsymbol{h} \rangle = \int_0^\pi \int_0^{2\pi} \boldsymbol{g} \cdot \overline{\boldsymbol{h}}\, \sin\phi \, \mathrm{d}\theta \, \mathrm{d}\phi,$$

and $\delta_{mm'}$ is the Kronecker delta.